

**Carbon and titanium-based composites cathode for improving the performance  
of Li-S batteries**

**碳基和钛基复合正极对锂硫电池性能的提升**

A Thesis Submitted to

University of Liverpool

in Partial Fulfillment of the Requirements for

the Degree of Doctor of Philosophy

in the Department of Electrical Engineering and Electronics

by

**Xianwei GENG**

BEng Electrical and Electronic Engineering

Xi'an Jiaotong-Liverpool University

& University of Liverpool, 2023

## Abstract

Over a century, the rapid development of human beings has aggravated the pollution of the environment, and the fossil fuels on the earth are about to be exhausted. However, traditional lithium-ion batteries have fully tapped their energy storage potential in research and commercialization. The energy density of about 150-200 Wh·Kg<sup>-1</sup> cannot meet the needs of large-scale power equipment, especially with the current demand for electric vehicles. The lithium-sulfur batteries thus appear, which use a metallic lithium anode and a sulfur cathode system. It has a high theoretical specific capacity of 1675 mAh·g<sup>-1</sup> and a high theoretical energy density of 2600 Wh·Kg<sup>-1</sup>, which can meet the current market power battery requirements of more than 600 Wh·Kg<sup>-1</sup>. The active material sulfur also has features of low price and environmental protection. However, The insulation of sulfur, the volume expansion of sulfur during charging and discharging, and the “shuttle effect” of polysulfides are the three major shortcomings of lithium-sulfur batteries, limiting large-scale application. Preparing suitable host materials to overcome these shortcomings helps improve the cycle and rate performance significantly.

In the thesis, in order to solve the above issues, the author first used carbon-based and titanium-based electrode materials mixed with sulfur to improve the comprehensive performance of lithium-sulfur batteries. The enhancement of conductivity by titanium carbide and carbon nanotubes and the role of titanium dioxide in trapping polysulfides are explained as a fundamental study at the beginning. The battery with TiC-TiO<sub>2</sub>/SWCNT/S mixture electrode has a specific capacity of 1324.2 mAh·g<sup>-1</sup> at 0.1 C

and  $711.2 \text{ mAh}\cdot\text{g}^{-1}$  at 4 C. Its excellent rate performance and cycle performance fully illustrate the function of different materials and meaning of selecting suitable host materials. On this basis, to increase the sulfur loading and sulfur content of the electrode, a special carbon-based material carbon nanocage and a titanium-based material MXene were prepared, which were composited with sulfur as electrodes (MXene/CNC/S). The carbon nanocages and MXene in the composite have a synergistic effect and complement each other. Particularly, CNC can act as a layer separator to reduce the stacking of MXene while the agglomeration of CNC is significantly relieved by MXene intersected. Under the conditions of  $1.5 \text{ mg}\cdot\text{cm}^{-2}$  sulfur loading and 80 % high sulfur content, the battery maintained a specific capacity of 64.6 % and  $823.8 \text{ mAh}\cdot\text{g}^{-1}$  after 100 cycles of charging and discharging at 0.1 C with stable cycle performance, which owns a higher energy density with more commercial sense. Based on the further optimization of the material itself and the simplification of the material preparation process, the sulfydryl-doped functionalized MXene material was prepared. At the same time, the chemical adsorption process of sulfur was introduced in the process of charging and discharging instead of the traditional physical adsorption, which contributed to suppressing the "shuttle effect". The first 1 C high-current discharge specific capacity reached  $880 \text{ mAh}\cdot\text{g}^{-1}$ , and after 500 cycles, the electrode also had a capacity retention rate of more than 81 %.

In summary, this project mainly focuses on preparing and modifying cathode materials for lithium-sulfur batteries. The first work is a preliminary basic investigation, focusing on finding suitable host materials and applying and analyzing their

performance-enhancing effects. The second and third works emphasize preparing complex materials and material modification to improve some parameters based on high performance.

## 摘要

最近一个多世纪以来，人类的高速发展加剧了环境的污染，地球上的化石能源也即将枯竭。然而，锂离子电池的储能潜力已经在研发和商业化中挖掘充分，约 $150\text{-}200\text{ Wh}\cdot\text{Kg}^{-1}$ 的能量密度无法满足大型动力设备，特别是目前飞速增长的电动汽车的需求。锂硫电池因此出现，其使用了金属锂负极和硫正极体系，拥有 $1675\text{ mAh}\cdot\text{g}^{-1}$ 的高理论比容量和 $2600\text{ Wh}\cdot\text{Kg}^{-1}$ 的高理论能量密度，能够满足目前市场动力电池超过 $600\text{ Wh}\cdot\text{Kg}^{-1}$ 的要求。活性物质硫还有价格低和环境保护的特点硫的绝缘性，充放电过程中硫的体积膨胀和多硫化物的穿梭效应是锂硫电池的三大缺点，限制了大规模的应用。制备合适的宿主材料来克服这些缺点，对提升锂硫电池的循环和倍率性能有重要的意义。

在本文中，为了解决以上缺点，作者先采用了碳基和钛基与硫混合的电极材料提升了锂硫电池的综合性能。其中在一开始解释了碳化钛和碳纳米管对导电性的提升以及二氧化钛对多硫化物捕捉的作用作为基础性的研究。TiC-TiO<sub>2</sub>/SWCNT/S混合电极的电池在 $0.1\text{ C}$ 具有 $1324.2\text{ mAh}\cdot\text{g}^{-1}$ ，在 $4\text{ C}$ 时具有 $711.2\text{ mAh}\cdot\text{g}^{-1}$ 的比容量。其优异的倍率性能和循环性能充分说明了不同材料的作用和挑选合适宿主材料的意义。在此基础上，为了提升电极的载硫量和含硫量，制备了特殊的碳基材料碳纳米笼和钛基材料MXene，与硫复合作为电极(MXene/CNC/S)。该复合材料中的碳纳米笼与MXene起到了协同作用，实现优势互补。特别地，CNC可以起到分隔的作用，减少MXene的堆积，同时相互交错的MXene可以显著减轻CNC的团聚。在 $1.5\text{ mg}\cdot\text{cm}^{-2}$ 的载硫量与 $80\%$ 高含硫量的条件下，该电池在 $0.1\text{ C}$ 充放电在100的循环后保持了 $64.6\%$ 和 $823.8\text{ mAh}\cdot\text{g}^{-1}$ 的比容量，具有稳定的循环性能,这样拥有更高的能量密度和商业化意义。基于对材料本身

的进一步优化和材料制备工艺的简化, 巯基掺杂功能化的MXene材料被制备出来, 同时在充放电过程中引入硫的化学吸附过程代替传统的物理吸附, 有助于更好地抑制“穿隧效应”。第一次1 C大电流放电比容量达到880 mAh·g<sup>-1</sup>, 循环500次后, 电极还拥有超过81 %的容量保持率。

总而言之, 该项目的研究方向主要关注于锂硫电池正极材料的制备和改性。第一项工作作为前期基础实验, 先着重寻找和合适的宿主材料, 应用和分析其对性能的提升作用。第二项工作则和第三项工作则分别侧重于制备复杂材料和材料修饰, 来在高性能的基础上, 对一些指标进行一定提升。

## **Acknowledgements**

The four years of PhD research are a precious final period in my life. I have received generous assistance from the people accompanying me in my project. Without their continuous help and careful guidance, it would have been impossible to finish the work presented now.

At first, I would like to deliver my sincere gratitude to my supervisor Prof. Pengfei Song, Prof. Li Yang and Prof. Cezhou Zhao in Xi'an Jiaotong Liverpool University around me. They always play the role in patient and genial supervisors and offer many supports to let me focus on my academic investigation without any disturbance. I genuinely thank their advice for my research, which stimulated plenty of inspiration for me and let me obtain much knowledge and achievements of this project. Their concerns about my life and career are amiable, and I will always remember those affecting moments during the PhD period.

I would also appreciate the supervisor Dr. Ivona Mitrovic at the University of Liverpool for his inspiring instructions for my experiment. I also want to gratitude to Prof. Chun Zhao for providing favorable suggestions in his research direction, which helps me consider the experiment more comprehensively.

In addition, my gratefulness also belongs to my unitive group: Dr. Ruowei Yi, Dr. Chenguang Liu, Dr. Yingchao Zhao, Dr. Yudan Yuan, Ms. Yi Sun, Mr. Xiangfei Lin, and Mr. Jiawei Ren. They share many experiences to provide references for my experiment.

Moreover, I would like to thank my colleagues: Dr. Qian Zhang, Dr. Shuhui Tao,

Mr. Yixin Cao, Mr. Shiqi Zhao, Ms. Yingqi Fan, Ms. Chang Liu, Ms. Tingwei Gao, Mr. Songjia Kong, Mr. Tianchang Wang. This harmonious family gave me momentous happiness and motivation to study and research for a memorable PhD time.

Finally, profound appreciation is offered to my parents, who are always willing to selflessly support me in overcoming various difficulties during work and life. Although far away physically, it is on my side in the spiritual distance.

Xianwei Geng

Mar. 2023



## List of publications

### Journal Articles

[1] **Xianwei Geng**, Chenguang Liu, Chun Zhao, Zhongjie Jiang, Eng Gee Lim, Yongjie Wang, Ivona Mitrovic, Li Yang, and Pengfei Song, Sulfydryl-modified MXene as a sulfur host for highly stable Li-S batteries, *Electrochimica Acta*, 2023, 441: 141877.

[2] **Xianwei Geng**, Chenguang Liu, Yi Sun, Yingchao Zhao, Ruwei Yi, Pengfei Song, Chun Zhao, Ivona Mitrovic, Li Yang d, and Cezhou Zhao, A  $Ti_3C_2T_x$  MXene - carbon nanocage - sulfur cathode with high conductivity for improving the performance of Li-S batteries, *Journal of Alloys and Compounds*, 2022, 895: 162586.

[3] **Xianwei Geng**, Ruwei Yi, Xiangfei Lin, Chenguang Liu, Yi Sun, Yingchao Zhao, Yinqing Li, Ivona Mitrovic, Rui Liu, Li Yang d, and Cezhou Zhao, A high conductive TiC-TiO<sub>2</sub>/SWCNT/S composite with effective polysulfides adsorption for high performance Li-S batteries, *Journal of Alloys and Compounds*, 2021, 851: 156793.

[4] **Xianwei Geng**, Ruwei Yi, Zhiming Yu, Cezhou Zhao, Yinqing Li, Qiuping Wei, Chenguang Liu, Yinchao Zhao, Bing Lu, and Li Yang, Isothermal sulfur condensation into carbon nanotube/ nitrogen-doped graphene composite for high performance lithium-sulfur batteries. *Journal of Materials Science: Materials in Electronics*, 2018, 29(12): 10071-10081.

[5] Yi Sun, Yudan Yuan, **Xianwei Geng**, Chi Han, Shenkai Lu, Ivona Mitrovic, Li Yang, Pengfei Song, and Cezhou Zhao, Biochar-derived material decorated by MXene/reduced graphene oxide using one-step hydrothermal treatment as high-performance supercapacitor electrodes, *Carbon*, 2022, 199: 224-232.

[6] Ruowei Yi, Chenguang Liu, Yinchao Zhao, Laurence J. Hardwick, Yinqing Li, **Xianwei Geng**, Qian Zhang, Li Yang, and Cezhou Zhao A light-weight free-standing graphene foam-based interlayer towards improved Li-S cells, *Electrochimica Acta*, 2019, 299: 479-488.

[7] Yi Sun, Ruowei Yi, Yinchao Zhao, Chenguang Liu, Yudan Yuan, **Xianwei Geng**, Weixuan Li, Zhichen Feng, Ivona Mitrovic, Li Yang, and Cezhou Zhao, Improved pseudocapacitances of supercapacitors based on electrodes of nitrogen-doped Ti<sub>3</sub>C<sub>2</sub>T<sub>x</sub> nanosheets with in-situ growth of carbon nanotubes, *Journal of Alloys and Compounds*, 2021, 859: 158347.

[8] Ruowei Yi, Xiangfei Lin, Yinchao Zhao, Chenguang Liu, Yinqing Li, Laurence J. Hardwick, Li Yang, Cezhou Zhao, **Xianwei Geng**, and Qian Zhang, Fabrication of a light-weight dual-function modified separator towards high-performance lithium-sulfur batteries, *ChemElectroChem*, 2019, 6(14): 3648-3656.

[9] Yixin Cao, Chun Zhao, Tianshi Zhao, Yi Sun, Zhengjun Liu, Xianyao Li, Li Yin, Jiangmin Gu, Hao Ren, **Xianwei Geng**, Jian Yao and Lixing Kang, Brain-Like Optoelectronic Artificial Synapse with Ultralow Energy Consumption Based on MXene Floating-Gate for Emotion Recognition, *Journal of Materials Chemistry C*, 2023.

## Patents

[1] **Xiawei Geng**, Li Yang, Pengfei Song, Yi Sun, Chenguang Liu, A preparation method of sulfydryl-modified MXene-sulfur composite and its lithium-sulfur batteries, Patent Application No.: 202210299269.9

[2] **Xiawei Geng**, Li Yang, Pengfei Song, Yi Sun, Chenguang Liu, Preparation method and application of MXene- Carbon nanocages - sulfur composite, Patent Application No.: 202110439488.8

[3] **Xiawei Geng**, Chun Zhao, Cezhou Zhao, Li Yang, Li Yin, A type of fluorine and rubidium-doped perovskite solar cell, Patent Application No.: 201920970530.7

[4] **Xiawei Geng**, Chun Zhao, Cezhou Zhao, Li Yang, Li Yin, Encapsulated solar cell, Patent Application No.: 201920253119.8

[5] Ruowei Yi, Li Yang, Cezhou Zhao, Yinchao Zhao, Chenguang Liu, **Xianwei Geng**, Three-dimensional dendritic nitrogen-doped graphene nanotube and its preparation method, Patent Application No.: 201711170934.X

[6] Ruowei Yi, Li Yang, Cezhou Zhao, Chenguang Liu, Yinchao Zhao, **Xianwei Geng**, Method for manufacturing interlayer of conductive polymer compound for lithium-sulfur batteries, Patent Application No.: 201711170978.2

[7] Ruowei Yi, Li Yang, Cezhou Zhao, Chenguang Liu, Yinchao Zhao, **Xianwei Geng**, Lithium-sulfur battery using nitrogen-doped graphene foam sheet as interlayer and its preparation, Patent Application No.: 201711006380.X

[8] Li Yang, Ce Zhou Zhao, Ruowei Yi, Chenguang Liu, Yinchao Zhao, and **Xianwei Geng**, "Positive electrode material of one-dimensional sulfur-conductive high polymer

lithium-sulfur battery and preparation method”, Patent Application No.:  
201711170947.7

[9] Ruowei Yi, Li Yang, Cezhou Zhao, Yudan Yuan, Chenguang Liu, Yinchao Zhao,  
**Xianwei Geng**, Xiangfei Lin, Composite separator for lithium-sulfur battery and its  
preparation method and application, Patent Application No.: 201811442542.9

## List of Figures

<b>Figure 1.1</b> The working principle of a lithium-ion battery with graphite anode and LiCoO <sub>2</sub> cathode [6].	2
<b>Figure 1.2</b> Development of cathode materials, lithium-ion and some new battery systems [11].	3
<b>Figure 1.3</b> Relationship between discharge capacity, capacity retention, and thermal stability for different Ni-containing cathodes [11].	4
<b>Figure 1.4</b> Energy density comparisons of lithium-ion batteries (general LiNi <sub>1/3</sub> Co <sub>1/3</sub> Mn <sub>1/3</sub> O <sub>2</sub> cathodes and graphite anodes) and lithium-sulfur batteries.	5
<b>Figure 1.5</b> Schematic plot of a Li-S battery with the charge or discharge process [24].	7
<b>Figure 1.6</b> Normalized chromatographic peaks of different polysulfide components (R = CH <sub>3</sub> ) from HPLC results during Li-S batteries (a) discharge, (b) charge and corresponding reaction mechanisms; (c) three parts of discharge reaction (d), two parts of charge reaction [26].	8
<b>Figure 1.7</b> The ideal charge-discharge diagram of polysulfides during the charge-discharge [28].	10
<b>Figure 1.8</b> The plot of the main interior and exterior disadvantages of Li-S batteries [36].	11
<b>Figure 1.9</b> The schematic of complex factors leading to the growth of dendritic lithium during cycling [37].	12
<b>Figure 1.10</b> (a) Presentation of the SEI morphology in LiNO <sub>3</sub> containing electrolytes	

with and without  $\text{Li}_2\text{S}_8$ . (b) Cycling performance of Li-S batteries with electrolyte adding  $\text{Li}_2\text{S}_8$  and  $\text{LiNO}_3$  in a DOL: DME [35]. ..... 13

**Figure 1.11** (a) Demonstration of a  $\text{MoS}_2$ -coated Li anode; (b) cross-section and (c) top view SEM images deposited  $\text{MoS}_2$  on Li metal; (d) top view SEM image of the lithiated  $\text{MoS}_2$  on Li metal [40]. ..... 14

**Figure 1.12** Cyclic performance of Li-S batteries with two different discharge cutoff voltages. The 1st-6th cycles were tested at  $0.2 \text{ mA} \cdot \text{cm}^{-2}$  [45]. ..... 16

**Figure 1.13** Cyclic capacity of Li-S batteries with four different electrolyte components [DME: DOL = (a) 4:1, (b) 2:1, (c) 1:1, (d) 1:2, and (e) 1:4] [46]. ..... 16

**Figure 1.14** (a) Cycle performance and (b) discharge curves of Li-S batteries with different electrolytes [49]. ..... 17

**Figure 1.15** Graphical representation of liquid electrolyte Li-S batteries and (b) solid electrolyte Li-S batteries [50]. ..... 18

**Figure 1.16** (a) Charge-discharge curves and (b) cyclic performances at 0.05 C. (c) Rate performance from 0.05 C to 0.5 C; (d) EIS curves [51]. ..... 19

**Figure 1.17** The milestone of Li-S battery development from the past to the present [55]. ..... 20

**Figure 1.18** Descriptions of the PEI-CDots modified cathode at different charge-discharge phases [70]. ..... 22

**Figure 1.19** (a) First discharge/charge curves at 0.25 C, (b) EIS spectra of as-prepared batteries, (c) cycling performance at 0.25 C, (d) rate performance from 0.1 to 4 C current density [71]. ..... 23

<b>Figure 1.20</b> Description of the preparation for microporous carbon-sulfur composite [72].	24
<b>Figure 1.21</b> (a) Illustration of the synthesis, (b) optical image in the flat and bent situation and (c) SEM image of a CNT-based sulfur cathode [56].	25
<b>Figure 1.22</b> (a) Demonstration of the fabrication process to AGNs via self-assembly of GO; (b) FESEM and (c) TEM images of AGNs [76].	27
<b>Figure 1.23</b> (a,b) Optical images of the RGO-S film. (c) Front and (d) cross-sectional SEM images of the RGO-S film. (e, f) TEM images of the RGO-S film [78].	28
<b>Figure 1.24</b> Preparation process of the 3D-NGS composite [79].	29
<b>Figure 1.25</b> Illustration of the preparation process of the 3DCGS composite [30].	30
<b>Figure 1.26</b> (a) Schematic of preparation for the Fe <sub>3</sub> C@N-GE-CNT. XRD patterns of (b) Na <sub>4</sub> Fe(CN) <sub>6</sub> ·10H <sub>2</sub> O, (c) Na <sub>4</sub> Fe(CN) <sub>6</sub> , and (d) Fe <sub>3</sub> C@N-GE-CNT. (e-i) FESEM images of Fe <sub>3</sub> C@N-GE-CNT. (j) Presentation of carbon nanotubes grown from graphene [81].	31
<b>Figure 1.27</b> Illustration of the fabrication procedure of the electrocatalyst Li-S cathode [84].	32
<b>Figure 1.28</b> (a) Fabrication process of TiC-TiO <sub>2</sub> /S composite and (b) long cycle performance at 0.5 C [85].	33
<b>Figure 1.29</b> Illustration of the Ti <sub>3</sub> AlC <sub>2</sub> MAX exfoliation and the fabrication of S/Ti <sub>3</sub> C <sub>2</sub> MXene [89].	34
<b>Figure 1.30</b> Synthesis procedures of MXene, HPCSs, HPCSs@MXene and their sulfur composites [93].	35

<b>Figure 1.31</b> Fabrication process of a crumpled nitrogen-doped N-Ti <sub>3</sub> C <sub>2</sub> T <sub>x</sub> /sulfur (N-Ti <sub>3</sub> C <sub>2</sub> T <sub>x</sub> /S) cathode [94].	35
<b>Figure 1.32</b> Schematic of fabrication steps of a type of 3D MXene sulfur cathode [96].	36
<b>Figure 1.33</b> Preparation of the NG/S–TiO <sub>2</sub> and the experiment of lighting up two LEDs with batteries [102].	37
<b>Figure 1.34</b> Long-term cycle performance of MnO <sub>2</sub> /S. (a) Over 1200 cycles at 0.2 C, (b) over 1500 cycles at 0.2 C, (c) at 2 C for 2000 cycles with a periodic slow rate [105].	38
<b>Figure 1.35</b> Schematic of the preparation for the HPCN-S cathode [106].	39
<b>Figure 1.36</b> (a) Cycle performance with different separators at 1 C for 800 cycles (2.5 mg·cm <sup>-2</sup> ). (b) at 0.1 C for 200 cycles (6.0 mg·cm <sup>-2</sup> ).	40
<b>Figure 1.37</b> Front and cross-sectional structure of (a) S@PPy composite and (b) PPy@S@PPy composite; (c) the function of the external PPy layer after adsorbing the dissolved polysulfides [109].	41
<b>Figure 1.38</b> (a) The demonstration of SPGs. (b) and (c) SEM images of SPGs. (d) Cyclic performance of SPGs as the cathode [108].	42
<b>Figure 1.39</b> Comparison of different cathodes in several important aspects (one up arrow: slight promotion, two up arrows: large promotion).	46
<b>Figure 2.1</b> Diffraction peak and information content that can be extracted [2].	64
<b>Figure 2.2</b> Structure of a typical X-ray photoelectron spectrometer [3].	66
<b>Figure 2.3</b> Equipment structure with the main parts of an SEM microscope [5].	68



<b>Figure 2.4</b> Structure and photograph of TEM [6].	69
<b>Figure 2.5</b> Structure of the volumetric method equipment of BET [7].	70
<b>Figure 2.6</b> Demonstration of a typical Raman microscope system [9].	71
<b>Figure 2.7</b> Illustration of the reduction and oxidation peaks in a CV [11].	73
<b>Figure 2.8</b> A simple equivalent circuit for electrode [13].	74
<b>Figure 3.1</b> Schematic diagram for preparing TiC-TiO <sub>2</sub> /SWCNT/S composite.	80
<b>Figure 3.2</b> Schematic of assembling for (a) coin cell and (b) pouch cell; Optical image of (c-d) coin cell and (e) pouch cell.	81
<b>Figure 3.3</b> SEM images of (a) TiC/S, (b) TiO <sub>2</sub> /S and (c) SWCNT/S.	83
<b>Figure 3.4</b> (a) The first charge-discharge curves, (b) Cycle performance at 0.1 C, (c) Cycle performance at 1 C and (d) Rate performance of four different cathodes for coin cells.	86
<b>Figure 3.5</b> (a) The first charge-discharge curves, (b) cycle performance at 0.1 C of four different cathodes for pouch cells.	88
<b>Figure 3.6</b> (a) SEM image of TiC-TiO <sub>2</sub> /SWCNT/S 2, corresponding EDS elemental mapping images of (b) C, (c) O, (d) S, (e) Ti.	90
<b>Figure 3.7</b> FE-SEM images of (a) TiC, (b) TiC-TiO <sub>2</sub> , (c) TiC-TiO <sub>2</sub> /S and (d) TiC-TiO <sub>2</sub> /SWCNT/S 2.	91
<b>Figure 3.8</b> The high-resolution TEM images of (a) as-purchased TiC, (b) as-purchased TiO <sub>2</sub> and (c) surface oxidized TiC-TiO <sub>2</sub> .	91
<b>Figure 3.9</b> (a) TEM image of TiC-TiO <sub>2</sub> /S composite; (b) STEM image with STEM EDS mapping area and (c) its enlarged view; STEM EDS mapping of (d) C, (e) O, (f)	

Ti and (g) S. ....	92
<b>Figure 3.10</b> (a) TEM image of TiC-TiO <sub>2</sub> /SWCNT/S 2 composite; (b) STEM image with STEM EDS mapping area and (c) The enlarged view of marked area in (b);STEM EDS elemental mapping of (d) C, (e) O, (f) Ti, (g) S. ....	93
<b>Figure 3.11</b> Raman spectra of (a) purchased TiC and TiO <sub>2</sub> ; (b) three distinct materials; (c) XRD patterns of four different materials; XPS spectra of (d) TiC-TiO <sub>2</sub> /SWCNT 2, its (e) C 1s and (f) Ti 2p. ....	97
<b>Figure 3.12</b> TGA curves of TiC-TiO <sub>2</sub> /S, TiC-TiO <sub>2</sub> /SWCNT/S 1 and TiC-TiO <sub>2</sub> /SWCNT/S 2 composites. ....	98
<b>Figure 3.13</b> (a) N <sub>2</sub> adsorption-desorption isotherm and (b) pore-size distribution curves of TiC-TiO <sub>2</sub> /SWCNT 10. ....	99
<b>Figure 3.14</b> (a) First charge-discharge curves; (b) Charge-discharge performance at 0.1 C, (c) Charge-discharge performance at 1 C large current density and (d) Rate performance from 0.1 C to 4 C of four different cathodes for their coin cells. ....	103
<b>Figure 3.15</b> Charge and discharge profiles at 0.1 C, 0.2 C, 0.5 C, 1 C, 2 C and 4 C for (a) TiC-TiO <sub>2</sub> /SWCNT/S 2, (b) TiC-TiO <sub>2</sub> /S and (c) TiC/S. ....	104
<b>Figure 3.16</b> CV plots for the first four cycles of (a) TiC-TiO <sub>2</sub> /S, (b) TiC-TiO <sub>2</sub> /SWCNT/S 1 and (c) TiC-TiO <sub>2</sub> /SWCNT/S 2; (d) CV curves for the 4th cycle of different cathodes. ....	106
<b>Figure 3.17</b> EIS spectra of TiC-TiO <sub>2</sub> /SWCNT/S 2, TiC-TiO <sub>2</sub> /S and TiO <sub>2</sub> /S cathodes (inset – corresponding equivalent circuit).....	107
<b>Figure 3.18</b> (a) First charge-discharge curves; (b) Charge-discharge performance at 0.1	

C of four different cathodes for their pouch cells. ....	108
<b>Figure 4.1</b> Synthesis procedure of (a) CNC/S, (b) MXene/S and (c) MXene/CNC/S. .....	120
<b>Figure 4.2</b> (a) XRD patterns of four different materials; (b) Raman spectra of MXene and MXene/CNC 7:3. ....	124
<b>Figure 4.3</b> (a) XRD patterns of MXene/S, CNC/S and S; (b) Raman spectrum of CNC. .....	124
<b>Figure 4.4</b> FE-SEM images of (a) CNC, (b) MXene, (c) MXene/CNC 7:3 and (d) MXene/CNC/S 7:3. Corresponding EDS mappings of (d) area for elements of (e) C, (f) Ti, (g) O and (h) S, respectively.....	126
<b>Figure 4.5</b> FE-SEM images of (a) CNC/S and (b) MXene/S. (c-f) Corresponding EDS mapping of (b) area for (c) C, (d) Ti, (e) O and (f) S elements.....	126
<b>Figure 4.6</b> TEM images of (a) CNC, (b) MXene, (c) MXene/CNC 7:3 and (d) MXene/CNC/S 7:3. (e) STEM EDS area (d); corresponding STEM EDS mapping for (f) C, (g) Ti, (h) O and (i) S elements. ....	129
<b>Figure 4.7</b> TEM images of (a) MXene and (b) CNC/S. (c) STEM image of CNC/S, (d) enlarged STEM EDS area from (c), (e-g) corresponding STEM EDS mapping of C, O and S elements. ....	129
<b>Figure 4.8</b> TEM image of (a) MXene/S and (b) STEM EDS area of MXene/S, (c-f) corresponding STEM EDS mapping of C, Ti, O and S elements. ....	130
<b>Figure 4.9</b> SAED patterns of (a) CNC, (b) MXene, (c) MXene/CNC 7:3 and (d) MXene/CNC/S 7:3.....	130

<b>Figure 4.10</b> (a) The XPS survey spectra for MXene and MXene/CNC 7:3; XPS spectra for MXene/CNC 7:3 of (b) C 1s, (c) O 1s and (d) Ti 2p.....	132
<b>Figure 4.11</b> The XPS spectra for MXene of (a) C 1s, (b) O 1s and (c) Ti 2p. (d) The XPS survey spectra, (e) S 2p narrow scans for MXene/S, CNC/S and MXene/CNC/S 7:3. ....	133
<b>Figure 4.12</b> (a) N <sub>2</sub> adsorption/desorption isotherm of CNC, MXene and MXene/CNC 7:3; Insert: CNC/S, MXene/S and MXene/CNC/S 7:3. (b) Specific surface area comparison of six different composites. ....	135
<b>Figure 4.13</b> Pore size distribution of (a) CNC, MXene and MXene 7:3 and (b) CNC/S, MXene/S and MXene/CNC/S 7:3 after melting sulfur. ....	135
<b>Figure 4.14</b> TGA curves of Mxene/S, CNC/S composite and MXene/CNC/S 7:3 composite. Insert: enlarged area. ....	136
<b>Figure 4.15</b> (a) First discharge-charge curves of six different cathodes at 0.1 C; (b) The galvanostatic charge-discharge curves for MXene/CNC/S 7:3 at various cycle times; (c) Cyclic performances for six different cathodes at 0.1 C; (d) Rate performances for six different cathodes.....	139
<b>Figure 4.16</b> Cyclic performance of six different cathodes at the large current density of 1 C.....	140
<b>Figure 4.17</b> Cyclic capacity of MXene/CNC/S 7:3 towards active sulfur and the whole composite. ....	140
<b>Figure 4.18</b> (a) CV curves of the MXene/CNC/S 7:3 composite cathode at the scan rate of 0.1 mV·s <sup>-1</sup> for the 1-4th cycle. (b) Comparison of CV curves of the second cycle for	

MXene/CNC/S 7:3, CNC/S and MXene/S. ....	143
<b>Figure 4.19</b> CV curves of (a) CNC/S and (b) MXene/S cathode at a scan rate of 0.1 mV·s <sup>-1</sup> for 1-4th cycles. ....	143
<b>Figure 4.20</b> Nyquist plots of MXene/CNC/S 7:3, CNC/S and MXene/S. Insert: equivalent circuit. ....	144
<b>Figure 4.21</b> Proposed mechanism of synergistic effect between MXene and CNC. ....	147
<b>Figure 4.22</b> (a) First charge-discharge curves; (b) charge-discharge performance at 0.1 C, (c) charge-discharge performance at 1 C large current density and (d) rate performance from 0.1 C to 4 C of different sulfur loading and sulfur content for MXene/CNC/S. ....	150
<b>Figure 4.23</b> (a) First charge-discharge curves; (b) charge-discharge performance at 0.1 C, (c) charge-discharge performance at 1 C large current density and (d) rate performance from 0.1 C to 4 C of the different E/S ratio for MXene/CNC/S. ....	153
<b>Figure 5.1</b> The schematic diagrams of different MXene and their corresponding sulfur-growing composites. ....	168
<b>Figure 5.2</b> (a-d) SEM images of pristine MXene, N-MXene, N, S-MXene and 3D MXene; (e-h) MXene/S, N-MXene/S, N, S-MXene/S and 3D MXene/S. ....	172
<b>Figure 5.3</b> (a) First charge-discharge curves; (b) Charge-discharge performance at 0.1 C, (c) Charge-discharge performance at 1 C large current density and (d) Rate performance from 0.1 C to 4 C of four different cathodes. ....	174
<b>Figure 5.4</b> XRD patterns of (a) MXene, MXene/S, MXeneSH(CH) 15 and S-MXeneSH(CH) 15; (b) MXeneSH(MPTS) 15, S-MXeneSH(MPTS) 15 and sublimed	

sulfur. .... 177

**Figure 5.5** FE-SEM images of (a) pristine MXene sheets and (b) MXene/S composite; (c) TEM image of pristine MXene sheets. Scale bars: (a) 1  $\mu\text{m}$ ; (b) 2  $\mu\text{m}$ ; (c) 100 nm. .... 179

**Figure 5.6** FE-SEM images of (a) MXeneSH(CH) 15 and (b) S-MXeneSH(CH) 15; Corresponding EDS mappings of (c-g) MXeneSH(CH) 15 and (h-l) S-MXeneSH(CH) 15. Scale bars: (a-b) 1  $\mu\text{m}$ ; (c-l) 2  $\mu\text{m}$ . .... 179

**Figure 5.7** TEM images of (a) MXeneSH(CH) 15 and (b) S-MXeneSH(CH) 15; STEM EDS mapping areas of (c) MXeneSH(CH) 15 and (i) S-MXeneSH(CH) 15; Corresponding STEM EDS mapping of (d-h) MXeneSH(CH) 15 and (j-n) S-MXeneSH(CH) 15. Scale bar: 100 nm. .... 180

**Figure 5.8** FE-SEM images of (a) MXeneSH(MPTS) 15 and (b) S-MXeneSH(MPTS) 15; TEM images of (c) MXeneSH(MPTS) 15 and (d) S-MXeneSH(MPTS) 15; STEM EDS mapping area of (e) MXeneSH(MPTS) 15 and (k) S-MXeneSH(MPTS) 15; Corresponding STEM EDS mapping of (f-j) MXeneSH(MPTS) 15 and (l-p) S-MXeneSH(MPTS) 15. Scale bars: (a-b) 1  $\mu\text{m}$ ; (c-p) 100 nm. .... 180

**Figure 5.9** Full scan of XPS survey for five different materials. .... 183

**Figure 5.10** XPS C 1s patterns of (a) MXeneSH(CH) 15, (c) MXeneSH(MPTS) 15, (e) S-MXeneSH(CH) 15 and (g) S-MXeneSH(MPTS) 15 ; XPS S 2p patterns of (b) MXeneSH(CH) 15, (d) MXeneSH(MPTS) 15, (f) S-MXeneSH(CH) 15 and (h) S-MXeneSH(MPTS) 15. .... 184

**Figure 5.11** The UV-vis spectra for polysulfides at different discharge voltages with a

current rate of 0.1 C. (a) MXene/S, (b) S-MXeneSH(CH) 15. (c) S-MXeneSH(MPTS) 15. Inserts: separators taken from disassembled batteries at corresponding voltages. (d) TGA curves of S-MXeneSH(CH) 15, S-MXeneSH(MPTS) 15 and MXene/S. .... 188

**Figure 5.12** (a) Nitrogen adsorption-desorption isotherms and (b) Pore-size distributions of four different composites. .... 189

**Figure 5.13** (a) Nitrogen adsorption-desorption isotherms and (b) pore-size distributions of pristine MXene. .... 190

**Figure 5.14** (a) First discharge-charge curves of three different batteries at 0.1 C; (b) The discharge-charge curves with different current densities of S-MXeneSH(CH) 15; (c) Cyclic performances of three different batteries at 0.1 C; (d) Rate performances of three different batteries. (e) Cyclic performance of three different batteries at the large current density of 1 C. .... 192

**Figure 5.15** (a) CV curves of the S-MXeneSH(CH) 15 composite at the scan rate of 0.1  $\text{mV}\cdot\text{s}^{-1}$  for the 1-4th cycle. (b) Comparison of CV curves of the second cycle for S-MXeneSH(CH) 15, S-MXeneSH(MPTS) 15 and MXene/S composites. .... 194

**Figure 5.16** CV curves of (a) S-MXeneSH(MPTS) 15 and (b) MXene/S composites. .... 194

**Figure 5.17** Nyquist plots of S-MXeneSH(CH) 15, S-MXeneSH(MPTS) 15 and MXene/S composites. Insert: equivalent circuit. .... 195

**Figure 5.18** Nyquist plots of MXeneSH(CH) 15, MXeneSH(MPTS) 15 and MXene composites. Insert: equivalent circuit. .... 196

**Figure 5.19** FE-SEM images of (a) MXeneSH(CH) 5 and (b) S-MXeneSH(CH) 5

composites. Scale bar: 2  $\mu\text{m}$ . .....198

**Figure 5.20** (a) Nitrogen adsorption-desorption isotherms and (b) pore-size distributions of four composites with different CH mixing ratios. ....199

**Figure 5.21** (a) Cyclic performances at 0.1 C and (c) 1 C; (b) Rate performances of four different batteries with different CH mixing ratios. ....200



## List of Tables

<b>Table 3.1</b> Relationship among weight, molar mass and molecular weight for SWCNT and TiC in TiC-TiO <sub>2</sub> /SWCNT/S 2 composite.....	94
<b>Table 4.1</b> Comparison of different cycle performance and retention rates for three different batteries. ....	141
<b>Table 5.1</b> Comparison of different performances for four different cathodes.....	175
<b>Table 5.2</b> Tested resistivity and converted conductivity of different materials. ....	197

## Table of Contents

Abstract.....	II
Acknowledgements.....	VII
List of publications .....	IX
List of Figures .....	XIII
List of Tables.....	XXV
Table of Contents .....	XXVI
List of Acronyms.....	XXX
Chapter 1 : Literature reviews.....	1
1.1 Introduction of lithium-ion and Li-S batteries .....	1
1.1.1 Lithium-ion batteries and cathode materials.....	1
1.1.2 The background and advantages of Li-S batteries .....	5
1.1.3 The mechanism and challenges of Li-S batteries .....	7
1.2 Current research reviews of Li-S batteries.....	12
1.2.1 Li anode .....	12
1.2.2 Electrolyte .....	14
1.2.3 S-based cathode .....	19
1.3 Host materials of S-based cathode.....	20
1.3.1 Carbon-based materials.....	20
1.3.2 Titanium-based materials .....	31
1.3.3 Other materials.....	36
1.4 Research aims and objectives .....	43

1.5 References.....	48
Chapter 2 : Experimental section .....	63
2.1 Structure and morphology characterization .....	63
2.1.1 X-ray Diffraction (XRD) .....	63
2.1.2 X-ray photoelectron spectroscopy (XPS) .....	64
2.1.3 Scanning Electron Microscope (SEM) .....	66
2.1.4 Transmission Electron Microscopy (TEM) .....	68
2.1.5 Brunauer-Emmett-Teller (BET).....	69
2.1.6 Raman Spectroscopy.....	71
2.2 Electrochemical tests .....	71
2.2.1 Galvanostatic charge and discharge .....	71
2.2.2 Cyclic voltammetry (CV) .....	72
2.2.3 Electrochemical impedance spectroscopy (EIS).....	73
2.3 References.....	75
Chapter 3 : 1D SWCNT/ TiC-TiO <sub>2</sub> / sulfur cathode for improving conductivity and overcoming volume expansion of Li-S batteries .....	77
3.1 Introduction.....	77
3.2. Experiment part.....	78
3.2.1 Preparation of TiC/S, TiO <sub>2</sub> /S and SWCNT/S composite .....	78
3.2.2. Fabrication of TiC-TiO <sub>2</sub> /S and TiC-TiO <sub>2</sub> /SWCNT/S composite .....	79
3.2.3. Electrode preparation, fabrication of coin cell and pouch cell .....	80
3.2.4. Materials characterization and electrochemical measurements .....	81

3.3 Results and discussion .....	83
3.3.1 Comparison of TiC/S, TiO <sub>2</sub> /S and SWCNT/S composites .....	83
3.3.2 Optimized TiC-TiO <sub>2</sub> /S and TiC-TiO <sub>2</sub> /SWCNT/S composites .....	88
3.4 Conclusions.....	108
3.5 References.....	110
Chapter 4 : 3D MXene/carbon nanocage/sulfur cathode with synergistic effect for dual-functional of high conductivity and strong polysulfides adsorption towards Li-S batteries.....	116
4.1 Introduction.....	116
4.2. Experiment part.....	118
4.2.1 Fabrication of Ti <sub>3</sub> C <sub>2</sub> T <sub>x</sub> MXene.....	118
4.2.2 Preparation of carbon nanocage (CNC).....	118
4.2.3 Preparation of MXene/CNC and MXene/CNC/S composite.....	119
4.2.4 Materials characterization and electrochemical measurements.....	120
4.3. Results and discussion .....	122
4.3.1 Comparison of CNC/S, MXene/S and MXene/CNC/S composites ...	122
4.3.2 Parameters investigation for MXene/CNC/S composite .....	147
4.4 Conclusions.....	153
4.5 References.....	155
Chapter 5 : Functionalized MXene/sulfur cathode with covalent adsorption mechanism for minimizing the “shuttle effect” of Li-S batteries .....	162
5.1 Introduction.....	162

5.2. Experiment part.....	164
5.2.1 Preparation of MXene/S, N-MXene/S, N,S-MXene/S and 3D MXene/S .....	164
5.2.2 Preparation of two different sulfydryl-functionalized MXene/S electrodes .....	166
5.2.3 Materials characterization and electrochemical measurements .....	168
5.3 Results and discussion .....	170
5.3.1 Comparison of N-MXene/S, N,S-MXene/S and 3D MXene/S composites .....	170
5.3.2 Comparison of different sulfydryl-modified methods .....	175
5.4 Conclusions.....	201
5.5 References.....	202
Chapter 6 : Conclusion and Future perspectives .....	207
6.1 Conclusion .....	207
6.2 Future Perspectives .....	209

## List of Acronyms

Abbreviations	Complete spelling
LIBs	Li-ion batteries
Li	Lithium
Li-S	Lithium-sulfur
EVs	Electric vehicles
LCO	$\text{LiCoO}_2$
LMO	$\text{LiMn}_2\text{O}_4$
NCM	$\text{Li}(\text{Ni}_x\text{Co}_y\text{Mn}_{1-x-y})\text{O}_2$
NCA	$\text{LiNiCoAlO}_2$
XRD	X-ray diffraction
SEM	Scanning electron microscopy
FE-SEM	Field emission scanning electron microscopy
TEM	Transmission electron microscopy
STEM	Scanning transmission electron microscopy
EDS	Energy dispersive spectrometer
XPS	X-ray photoelectron spectroscopy
TGA	Thermogravimetric analysis
BET	Brunauer-Emmett-Teller
BJH	Barrett-Joyner-Halenda

UV-vis	Ultraviolet-visible
CV	Cyclic voltammetry
EIS	Electrochemical impedance spectroscopy
DC	Direct current
AC	Alternating current
Z	Faraday impedance
NMP	N-methyl pyrrolidinone
PVDF	Polyvinylidene fluoride
DOL	Dioxolane
DME	Dimethoxyethane
LiTFSI	Lithium bis (trifluoromethane sulfonyl) imide
DI	Deionized
MAX	$Ti_3AlC_2$
MXene	2D metal carbides
Li	Lithium
S	Sulfur
HCl	Hydrogen chloride
LiF	Lithium fluoride
Al	Aluminum
Ar	Argon

0D	Zero-dimensional
1D	One-dimensional
2D	Two-dimensional
3D	Three-dimensional
TiC	Titanium carbide
TiO <sub>2</sub>	Titanium dioxide
RGO	Reduced graphene oxide
SWCNT	Single-walled carbon nanotube
HNO <sub>3</sub>	Nitric acid
CNC	Carbon nanocage
CH	Cysteamine hydrochloride
MPTS	3-mercaptopropyltrimethoxysilane
MXeneSH(CH)	MXene modified by cysteamine hydrochloride
MXeneSH(MPTS)	MXene modified by 3-mercaptopropyltrimethoxysilane



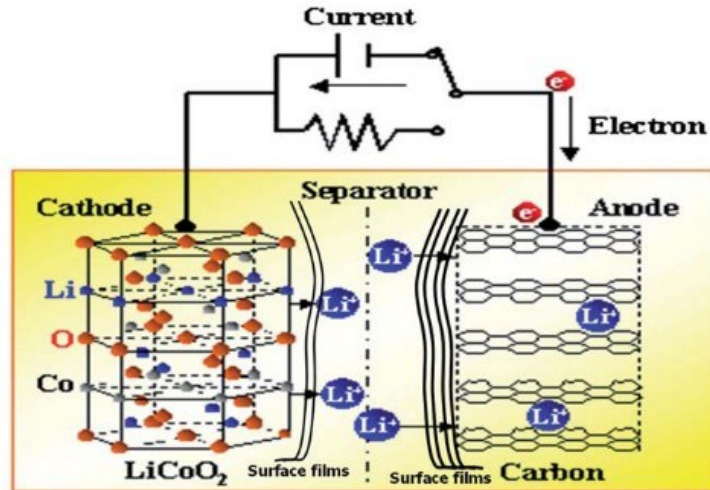
# **Chapter 1 : Literature reviews**

## **1.1 Introduction of lithium-ion and Li-S batteries**

### **1.1.1 Lithium-ion batteries and cathode materials**

The flourishing economy and human activities bring increasing demand for energy. In order to face the issue of global warming and the limited source of fossil fuels, various battery systems were invented for meeting chemical energy storage. Plumbic acid and zinc manganese batteries mainly existed in the early years. Lithium-ion batteries (LIBs) own a higher energy density than two before since lithium has low atomic weight and high electrode potential. Its technologies are mature and it has become predominant in the development of society in recent years [1].

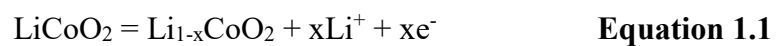
The history of lithium-ion batteries could trace back to the 1950s. The fundamental research began to prove lithium metal might own good stability in fused salts, organic solution and liquid  $\text{SO}_2$ , which could be used as nonaqueous electrolytes [2]. In the following 1970s, scholars found that it could obtain superconductivity by intercalating electrons into the lattice (e.g. metallic layers) and revealed that this process would absorb enormous energy, laying the foundation for energy storage [3]. By 1991, Japanese Sony started to market commercial LIBs, using the transition metal oxides to assemble lithium cobalt oxide ( $\text{LiCoO}_2$ ) as a cathode and graphite as an anode [4]. The cathode and anode structure separated by a polyolefin separator for LIBs is basically established, making the intercalation and deintercalation process safe [5].



**Figure 1.1** The working principle of a lithium-ion battery with graphite anode and LiCoO<sub>2</sub> cathode [6].

As shown in **Figure 1.1**, when charged at an applied voltage, the lithium ions begin to escape from the positive material, enter the electrolyte, and travel through the separator to the negative material. After capturing an electron, lithium-ion is reduced to a lithium atom, intercalated in the negative lattice and stored in the negative material. During the discharge process, the lithium atom in the negative electrode loses an electron to become lithium-ion, which enters the electrolyte and migrates through the separator to the positive electrode.

The charge process in positive electrode:



The charge process in negative electrode:



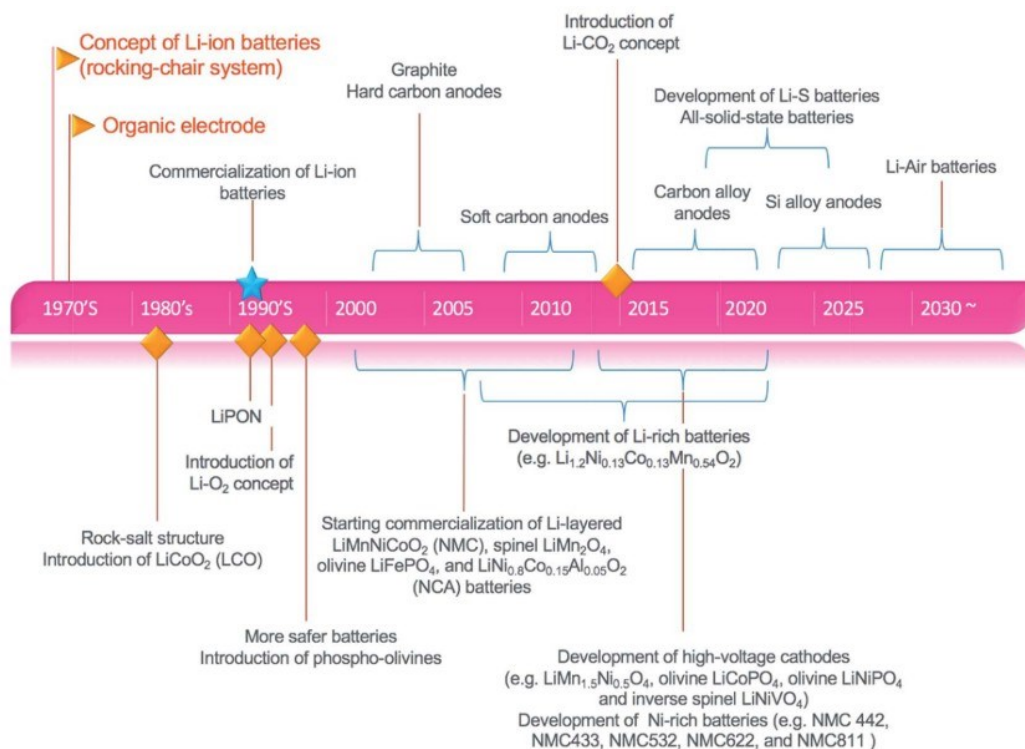
The whole charge process:



Compared with early batteries, the LIBs may provide more than three times the

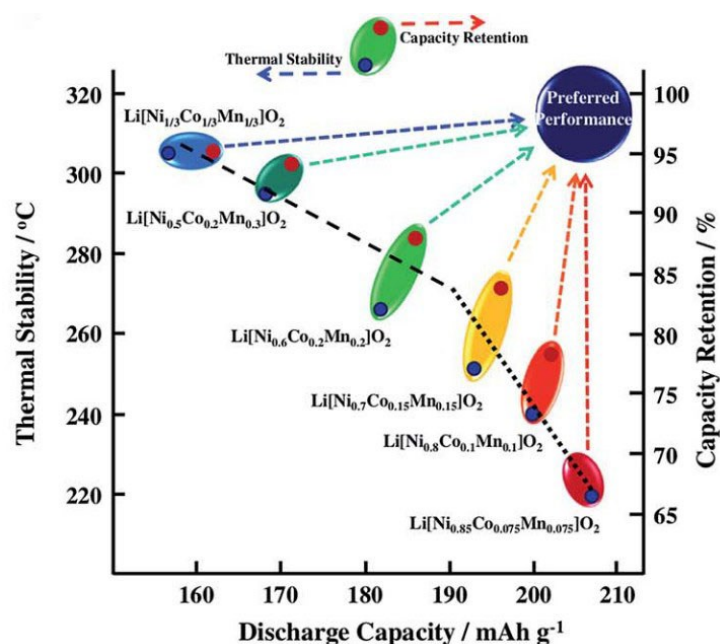
energy density and the intercalation reactions are still applied to commercial secondary lithium batteries up to now [7]. Under the safe mechanism of LIBs, Ni-MH batteries were replaced for electric vehicles (EVs) due to their low energy density. LIBs also brought the flourishing of portable electrical devices. In the 2010s, LIBs entered the era of rapid commercialization [8].

The cathode materials of LIBs have been explored for nearly half a century since they are the most important part of batteries. The concept of LIBs was first put forward in the 1970s. Whittingham applied metal dichalcogenides as an intercalation compound, and  $\text{TiS}_2$  was the earliest cathode material at that time [9]. Before the commercialization of Sony in the early 1980s, Mizushima et al. discovered  $\text{Li}_x\text{CoO}_2$  with an ordered rock-salt structure as a novel cathode material [10].



**Figure 1.2** Development of cathode materials, lithium-ion and some new battery systems [11].

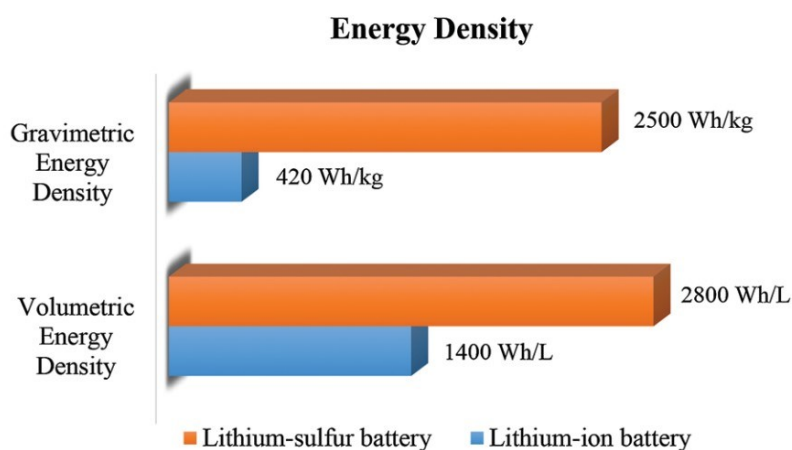
Later, Ni and Mn were tried to replace Co to minimize the overlap with the O<sup>2-</sup>: 2p band and reduce the cost [12]. Due to the synergetic effects, a mixed transition metal cathodes Li(Ni<sub>x</sub>Co<sub>y</sub>Mn<sub>y1-x-y</sub>)O<sub>2</sub> (0 ≤ x ≤ 1, 0 ≤ y ≤ 1, and 0 ≤ x + y ≤ 1) (NCM) gradually caught the interest in the 2000s. NCM can deliver over 200 mAh·g<sup>-1</sup> when the battery is charged between 2.8 V and 4.6 V and is cheaper than LiCoO<sub>2</sub> [13]. In the last decade, the rapid development of electric vehicles has contributed to an interest in Ni-rich layered oxide batteries for NCM cathodes with a higher capacity (e.g. Li[Ni<sub>0.8</sub>Co<sub>0.1</sub>Mn<sub>0.1</sub>]O<sub>2</sub> (NCM811)), which presents 215-220 mAh·g<sup>-1</sup>[14]. Another type of cathode is the high stable LiFePO<sub>4</sub>, which is environmentally friendly and cheaper but has low Li<sup>+</sup> diffusion and more loss of capacity [15].



**Figure 1.3** Relationship between discharge capacity, capacity retention, and thermal stability for different Ni-containing cathodes [11].

### 1.1.2 The background and advantages of Li-S batteries

Nowadays, LIBs have become the main force of power batteries in the EVs industry because of their successful commercialization process. However, China has achieved more than 30 % EV occupancy in the market this year, and people have expected a higher distance per charge to meet daily life. Unlike portable electronic devices and household appliances, EVs require significant battery performance improvement, including fast-charging performance and energy density [16]. As is known to all, traditional LiBs using graphite anode and insertion cathodes provide attainable energy densities of approach to about  $260 \text{ Wh}\cdot\text{kg}^{-1}$  in practice. They provide energy densities when changing them to high-voltage cathodes such as  $\text{LiNiCoAlO}_2$  (NCA), NCM811, and  $\text{LiNiMnO}_4$  (LNMO) of around 354, 338 and  $351 \text{ Wh}\cdot\text{kg}^{-1}$ , respectively. An urgent aim is that EVs should own over 600-800 km endurance mileage, and the commercial energy density requires exceeding  $500 \text{ Wh}\cdot\text{kg}^{-1}$  by 2030 [17]. Nevertheless, only certain specific sites could be intercalated by lithium ions, and thus the theoretical energy density of LIBs is typically restricted to approximately  $420 \text{ Wh}\cdot\text{kg}^{-1}$  or  $1400 \text{ Wh}\cdot\text{L}^{-1}$  [18].



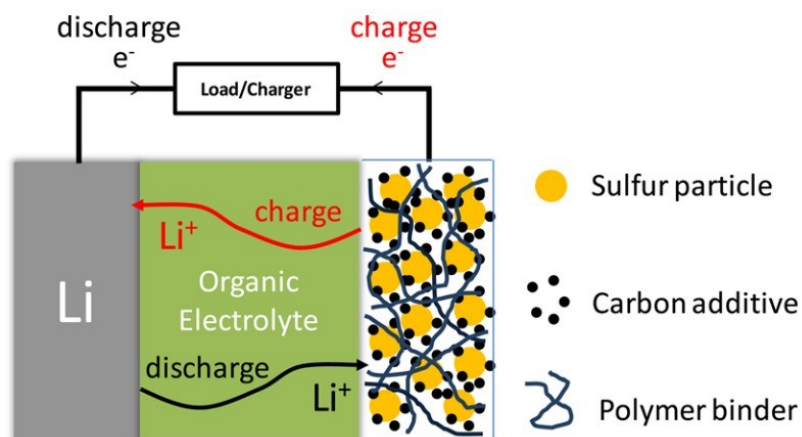
**Figure 1.4** Energy density comparisons of lithium-ion batteries (general

LiNi<sub>1/3</sub>Co<sub>1/3</sub>Mn<sub>1/3</sub>O<sub>2</sub> cathodes and graphite anodes) and lithium-sulfur batteries.

Therefore, researchers must transfer their intention to new systems with a breakthrough in energy density beyond LIBs. Owing to the high energy density, abundance in the universe, and economic elemental sulfur, lithium-sulfur (Li-S) battery has been considered to be a promising choice. When the elemental sulfur reduces to lithium sulfide (Li<sub>2</sub>S) completely, sulfur can theoretically deliver a specific capacity of 1675 mAh·g<sup>-1</sup> and an energy density of 2600 Wh·Kg<sup>-1</sup>, which are three to five times higher than traditional LIBs [19]. Since 1962 firstly discovered in Herbet and Ulam in a U.S. patent [20], Li-S batteries have been deemed potential for powering portable electronics. The redox reaction mechanism with non-topological property between a sulfur cathode and a lithium metal anode give Li-S batteries high theoretical capacity. At the same time, the lithium metal has a feature of a low reduction potential (-3.04 V) versus standard hydrogen electrode (SHE, vs Li/Li<sup>+</sup>) and a high theoretical specific capacity of 3860 mAh·g<sup>-1</sup> because of its low density (0.534 g·cm<sup>-3</sup>) [21]. The side of the lithium anode does not need conductive additives and binder, which is also beneficial to the high energy density in practical applications. On the other hand, the cheap raw material of the sulfur cathode can reduce the budget of EVs as the cost of precursor and transition metal gradually increases. Compared to LIBs with heavy metal, Li-S contribute to reducing environmental pollution due to the non-toxic element sulfur. In general, Li-S batteries are suitable for power batteries for EVs, marine and even aerospace fields.

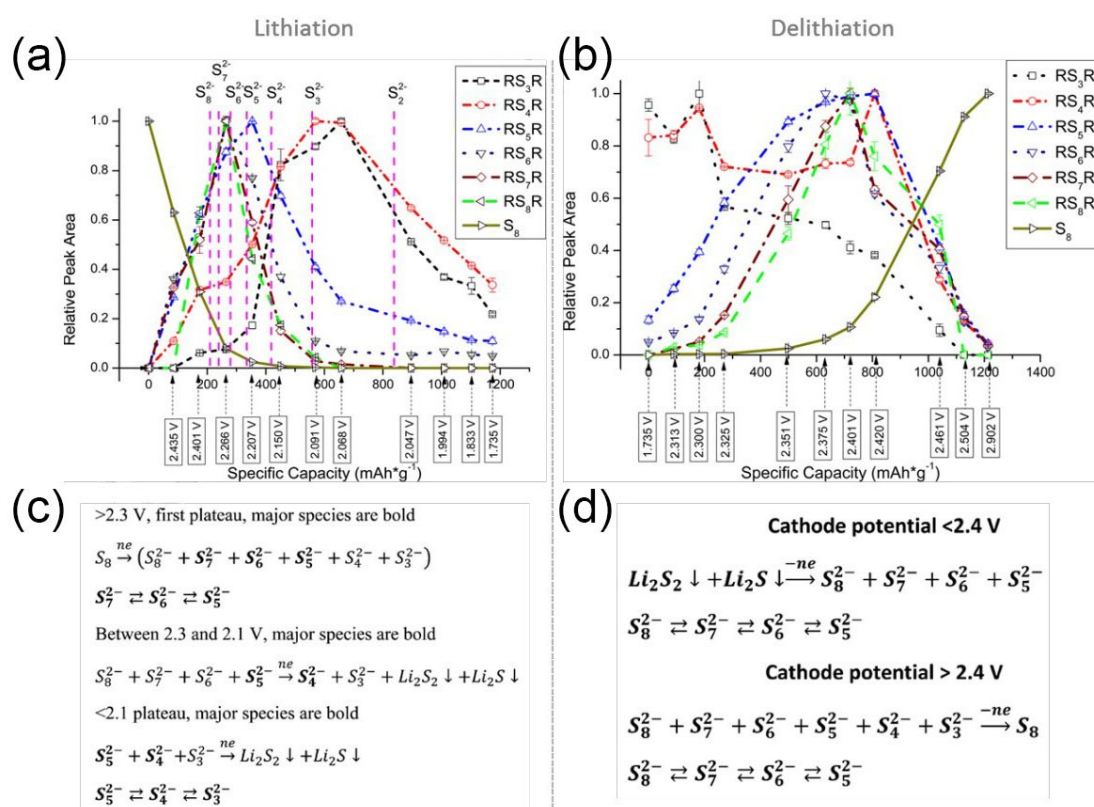
### 1.1.3 The mechanism and challenges of Li-S batteries

Different from the lithium-ion intercalation and de-intercalation mechanism of commercial lithium-ion batteries, the charge and discharge of Li-S batteries proceeded by breaking and bonding the S-S chemical bond in the middle of the S<sub>8</sub> molecule [22]. In the earliest 1975, Li-S batteries were developed for off-peak energy storage, which applied molten LiCl-KCl electrolyte and operated at 400 °C [23], but now Li-S batteries work at room temperature. S-containing cathode, Li metal anode and organic electrolyte constitute the basic structure of Li-S batteries. On the side of cathode, conductive carbon additive and polymer binder are mixed with active sulfur. The working process begins at discharge since sulfur is in the charged situation. During the discharge process, Li metal is oxidized at the negative electrode to generate lithium ions and electrons. The lithium ions then travel to the positive electrode via the electrolyte internally while the electrons transfer to the positive electrode by the external electrical circuit, and thus an electrical current is produced [24]. During the charge process, the lithium ions and electrons travel adversely. The whole redox reaction for the battery is reflected below:



**Figure 1.5** Schematic plot of a Li-S battery with the charge or discharge process [24].

The average potential of this battery is 2.15 V referring to Li/Li<sup>+</sup>, which is evidently lower than graphite-LiMO<sub>2</sub> batteries (>3 V). Since the very high capacity offsets low voltage, the specific energy of it is still large to have commercial value [25]. It seems that the battery reaction is a simple redox reaction, but the process could be decomposed into several complicated transformations of polysulfides, including many chemical equilibriums. After the characterization analysis, the discharge reaction comprises three main parts, while the charge reaction is divided into two parts, as shown in **Figure 1.6c,d**. **Figure 1.6c,d** is the High-Performance Liquid Chromatography (HPLC) to detect the relative content of various types of polysulfides [26].



**Figure 1.6** Normalized chromatographic peaks of different polysulfide components (R = CH<sub>3</sub>) from HPLC results during Li-S batteries (a) discharge, (b) charge and corresponding reaction mechanisms; (c) three parts of discharge reaction (d), two parts



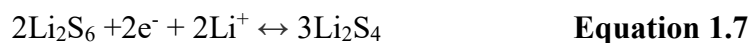
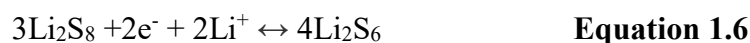
of charge reaction [26].

From another point, the discharge process could be divided into four steps [27].

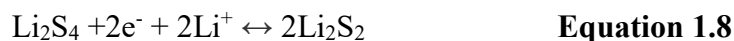
1. Solid-liquid process. The electron transfer velocity, the lithium-ion transfer velocity, and the electron migration velocity at the two-phase interface may influence the speed of this step.



2. Liquid-liquid process. The reason is the reactant and the product, long-chain and short-chain polysulfides, are soluble in the electrolyte. Long-chain polysulfides will be converted to short-chain polysulfides ( $\text{Li}_2\text{S}_3$ ,  $\text{Li}_2\text{S}_4$ ) after receiving electrons during the process.



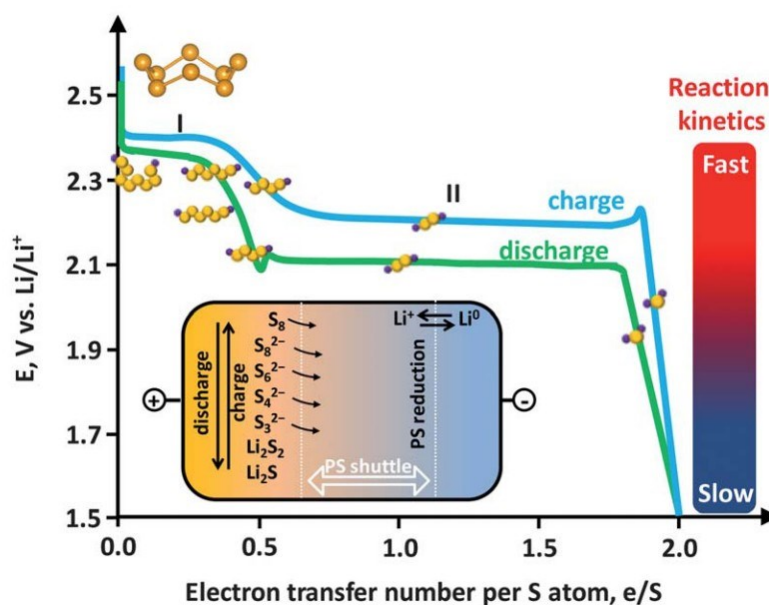
3. Liquid-solid process.  $\text{Li}_2\text{S}_2$  and  $\text{Li}_2\text{S}$  are readily saturated in the electrolyte and deposited on the surface of the anode owing to their poor solubility. The two stages of this deposition process are nucleation and growth. Due to the low electronic conductivity of the two products, it is difficult for electrons to transfer in them.



4. Solid-solid process. The final process does not refer to the diffusion of polysulfides in the electrolyte but still includes the diffusion of lithium ions, which has the most difficult reaction and contributes to around half of the theoretical capacity.



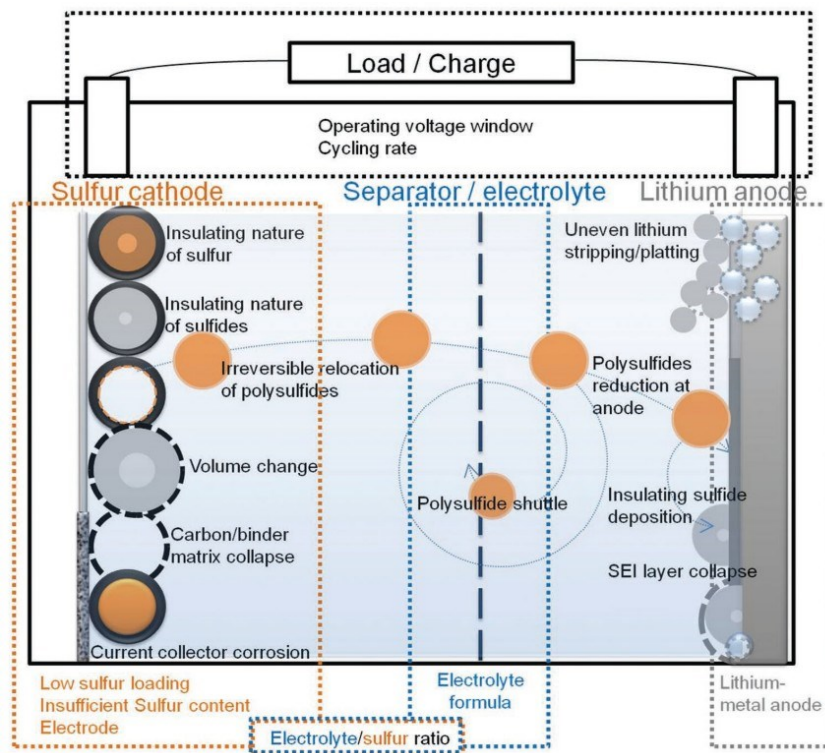
The reaction of completely converting  $\text{Li}_2\text{S}_2$  to  $\text{Li}_2\text{S}$  is difficult and is hindered by sluggish solid diffusion. As a result, the voltage declines rapidly when  $\text{Li}_2\text{S}$  covers the whole electrode, leading to the termination of the discharge process **Figure 1.7** [25].



**Figure 1.7** The ideal charge-discharge diagram of polysulfides during the charge-discharge [28].

Although Li-S batteries have many advantages, there are several problems we must solve to achieve better practical applications. These vital concerns are: (1) the low electrical conductivity of the sulfur ( $5 \times 10^{-30} \text{ S} \cdot \text{cm}^{-1}$ ), and the final product  $\text{Li}_2\text{S}$  ( $10^{-13} \text{ S} \cdot \text{cm}^{-1}$ ) hinders redox reaction, causing low utilization of the active sulfur [29, 30]; (2) in the charge-discharge process, the polysulfide intermediates produced by the positive electrode dissolve into the electrolyte, pass through the separator, diffuse to the negative electrode, and react directly with the metal lithium to form solid  $\text{Li}_2\text{S}_2$  and  $\text{Li}_2\text{S}$ , which are deposited in the negative electrode and cannot return to the positive electrode. This

is called the “shuttle effect”. The result is the irreversible loss of the active sulfur in the battery, decay of capacity and low coulomb efficiency [31, 32]; (3) the volume of sulfur will expand ~80 % after discharging completed, resulting in the damage of the electrode and thus rapid capacity fading [33]; (4) Due to the “shuttle effect”,  $\text{Li}_2\text{S}_2$  and  $\text{Li}_2\text{S}$  are produced on the surface of the anode, damaging solid electrolyte interphase (SEI) on Li anode, which can protect the anode from electrolyte erosion [34]. (5) The growth of lithium dendrites roots from the repeated stripping/plating of a lithium layer during the cycle process is uncontrollable, impaling SEI and causing short-cuts of batteries. This inhomogeneous SEI can further aggravate dendritic lithium growth [35].



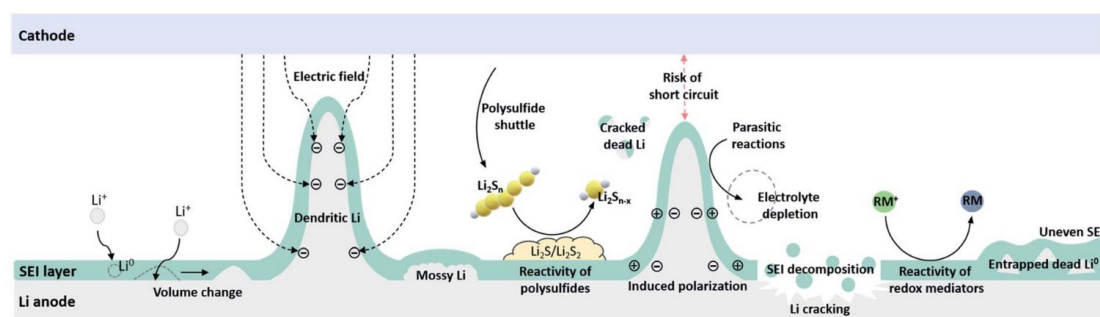
**Figure 1.8** The plot of the main interior and exterior disadvantages of Li-S batteries [36].

## 1.2 Current research reviews of Li-S batteries

### 1.2.1 Li anode

Although metal Li has high theoretical specific capacity and low electrochemical potential, three main issues exist below. Firstly, lithium has high metal activity and serious side effects with dissolved polysulfides which diffuse to the anode side, resulting in low cycle life and coulombic efficiency. Secondly, there is a phenomenon of uneven current density on the anode, leading to dendritic lithium growth and short-cut. Thirdly, the continuous irreversible reaction between lithium and electrolyte is easy to form "dead Li", which results in the loss of active material and decreased battery capacity.

The growth of dendritic lithium and degradation of the Li metal is a complicated phenomenon, which has various effects on the anode reaction, the electrolyte, and the instability of SEI. Some significant related issues are demonstrated in **Figure 1.9**.

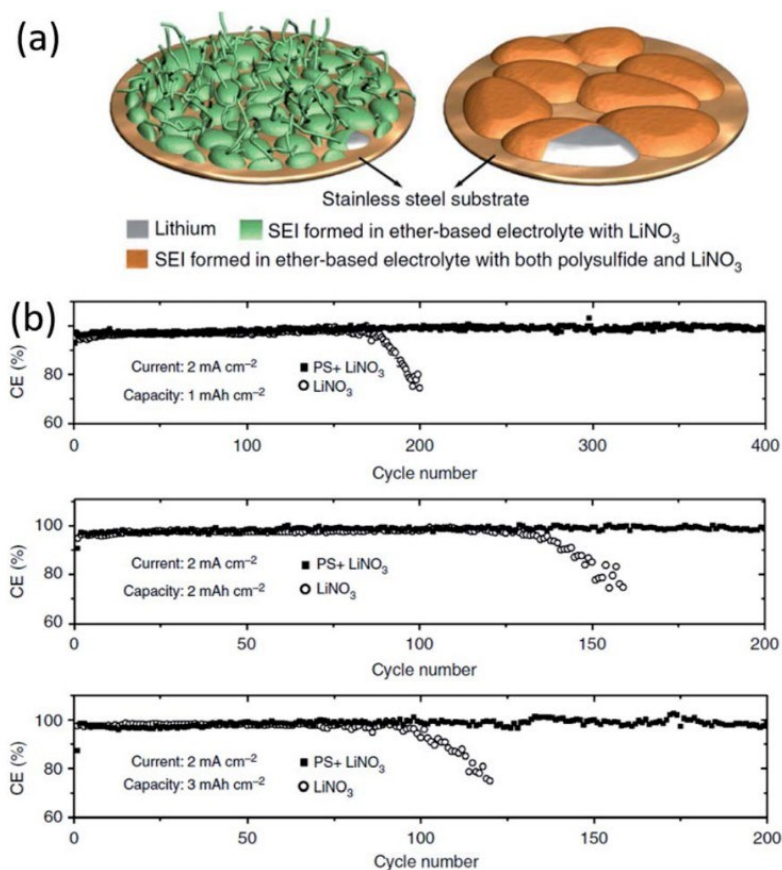


**Figure 1.9** The schematic of complex factors leading to the growth of dendritic lithium during cycling [37].

The formation of micro Li during the cycling is easier during the high-current plating of metals. During the charging process, Li first nucleates on the surface of the inhomogeneous Li metal. The consequent small Li cores serve as charge centers, and

charges accumulate at the sharp ends under the electric field. Then, Li preferentially deposited on these charge centers and accelerated growth [38].

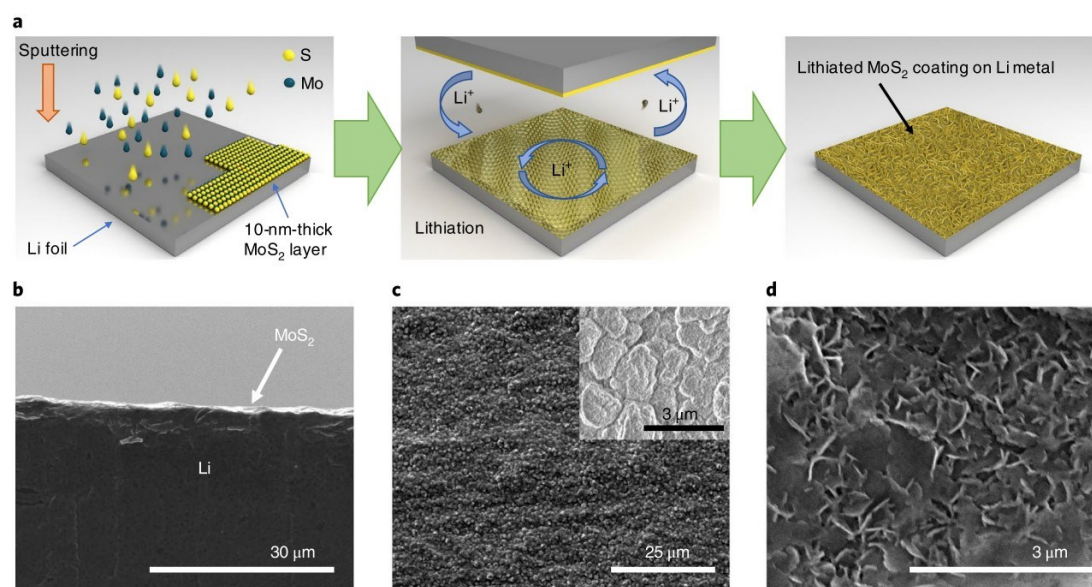
Many significant types of research have been devoted to stabilizing Li metal anodes, including modification of Li metal, building an SEI film and designing Electrolytes [39]. Cui and colleagues discovered a stable and even solid electrolyte interphase film formed because of a synergetic effect of additives in ether-based electrolyte with lithium nitrate and polysulfides, preventing the growth of dendritic lithium and reducing electrolyte decomposition in **Figure 1.10** [35].



**Figure 1.10** (a) Presentation of the SEI morphology in LiNO<sub>3</sub> containing electrolytes with and without Li<sub>2</sub>S<sub>8</sub>. (b) Cycling performance of Li-S batteries with electrolyte adding Li<sub>2</sub>S<sub>8</sub> and LiNO<sub>3</sub> in a DOL: DME [35].

Choi et al. revealed a Li metal anode coated with a tightly adhered MoS<sub>2</sub> layer (10

nm) by the sputtering deposition method in **Figure 1.11**. These uniformly distributed MoS<sub>2</sub> particles may hinder a nonuniform electric resistance for preventing Li dendrite growth and allow rapid diffusion of Li ions on the MoS<sub>2</sub> surface, confirmed by density functional theory (DFT) calculations.



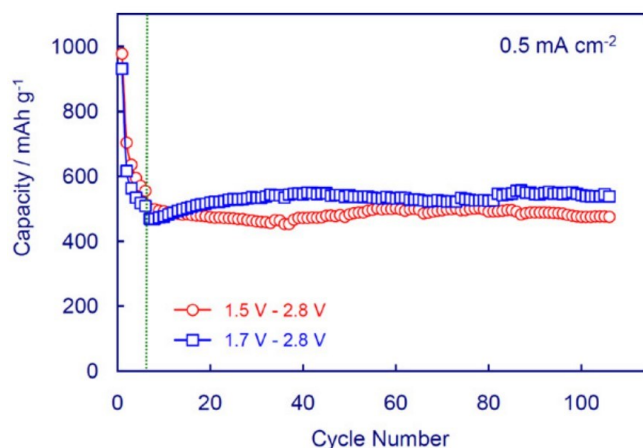
**Figure 1.11** (a) Demonstration of a MoS<sub>2</sub>-coated Li anode; (b) cross-section and (c) top view SEM images deposited MoS<sub>2</sub> on Li metal; (d) top view SEM image of the lithiated MoS<sub>2</sub> on Li metal [40].

### 1.2.2 Electrolyte

The electrolyte is the carrier of ion transport in the battery and the bridge between the cathode and anode, which has a great impact on performance and safety. In order to solve the “shuttle effect” caused by the dissolution of polysulfides in the electrolyte and improve the performance of Li-S batteries, much research has been devoted to studying electrolytes and their additives [41]. Its good ionic conductivity makes organic liquid electrolytes widely used in LIBs. The main components of organic liquid electrolytes are organic solvent and lithium salt. The organic solvent has a great influence on the

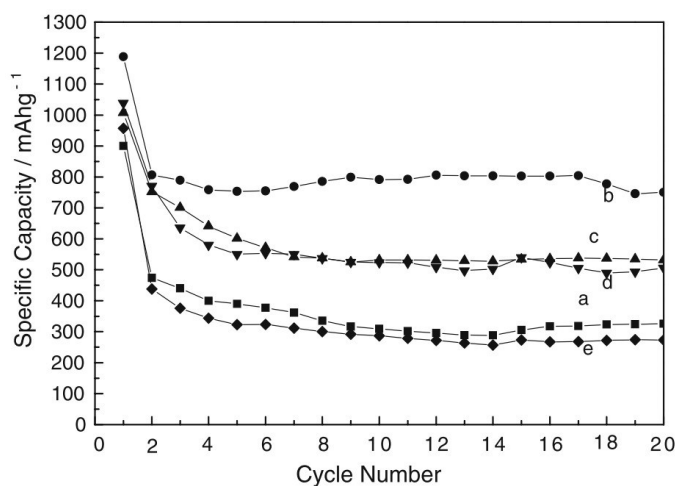
performance of Li-S batteries. The ideal solvent of Li-S batteries should meet three requirements: (1) it has good polysulfides solubility, which is conducive to the full reaction of active material; (2) good chemical stability with polysulfides and lithium anode; (3) it has low viscosity, which is beneficial to the transmission of ions [42]. Based on the above requirements, the current commercial electrolyte of carbonic ester for LIBs is unsuitable for Li-S batteries because of its chemical reaction with polysulfides, so we use the organic ether solvent to replace it [43]. Cyclic and linear ether organic solvents such as 1,3-dioxolane (DOL), 1,2-dimethoxyethane (DME), and tetra(ethylene glycol) dimethyl ether (TEGDME), are suitable for the electrolyte of Li-S batteries, due to their good polysulfide solubility [44]. The general electrolyte for Li-S batteries was lithium bis (trifluoromethane sulfonyl) imide (1.0 M) dissolved in a mixture of a lithium salt ( $\text{Li}[\text{N}(\text{SO}_2\text{CF}_3)_2]$ , LiTFSI) in dioxolane (DOL) and dimethoxyethane (DME) (1:1 by volume) often with a 1.0 wt%  $\text{LiNO}_3$  additive.

During charging and discharging, it is easy to form lithium dendrites that may puncture the separator, so there are potential safety problems. One solution is adding a protective agent to the electrolyte to create a protective layer on the lithium surface. Zhang added  $\text{LiNO}_3$  as an additive to the electrolyte. When the battery voltage exceeds 1.6 V,  $\text{LiNO}_3$  can protect the electrode, generate stable SEI film, reduce the loss of active material and improve the cycle performance [45].



**Figure 1.12** Cyclic performance of Li-S batteries with two different discharge cutoff voltages. The 1st-6th cycles were tested at  $0.2 \text{ mA} \cdot \text{cm}^{-2}$  [45].

Wang et al. explored the influence of the ratio of DOL and DME on battery performance. The results present that the specific discharge capacity of the battery increases with the decrease of DOL, and the discharge voltage increases with the decrease of DME. When DOL: DME=2:1, the battery can maintain a good discharge capacity [46].

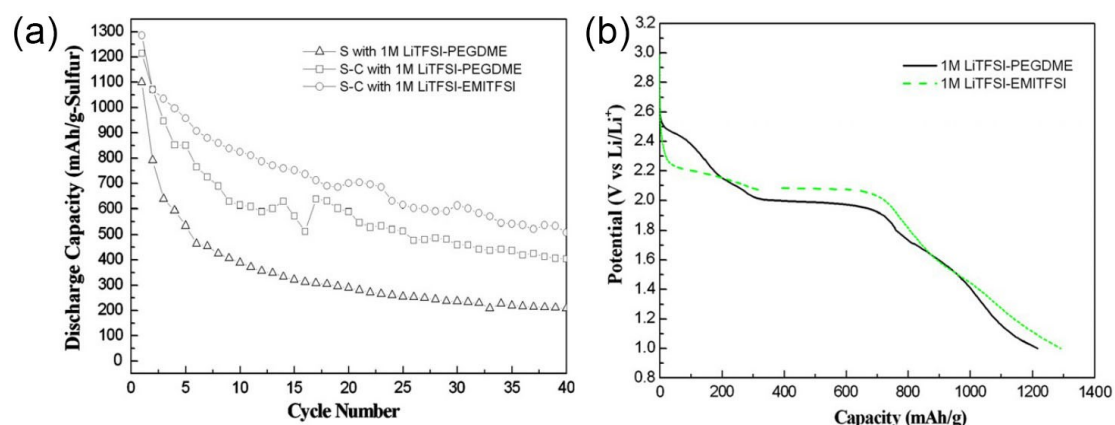


**Figure 1.13** Cyclic capacity of Li-S batteries with four different electrolyte components [DME: DOL = (a) 4:1, (b) 2:1, (c) 1:1, (d) 1:2, and (e) 1:4] [46].

**Ionic Liquid Electrolytes:** The ionic liquid electrolytes consist entirely of ions at room temperature. It has many merits, such as high ionic conductivity and a large

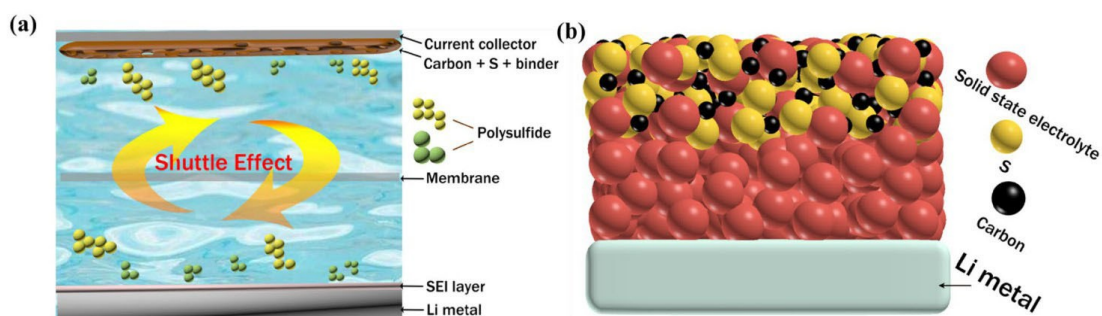


electrochemical stability window. Other admirable features are low volatility, high thermal stability, and a wide liquidus range [47]. However, it also has the weakness of higher viscosities than organic liquids, which leads to low conductivities. Meanwhile, high cost and potential toxicity are considerable [48]. In J. Wang's work, the specific capacity and cycling stability of the S-C cathode with the ionic liquid electrolyte (LiTFSI-EMITFSI) were superior to the cathode tested in an organic solvent electrolyte (LiTFSI-PEGDME) [49].



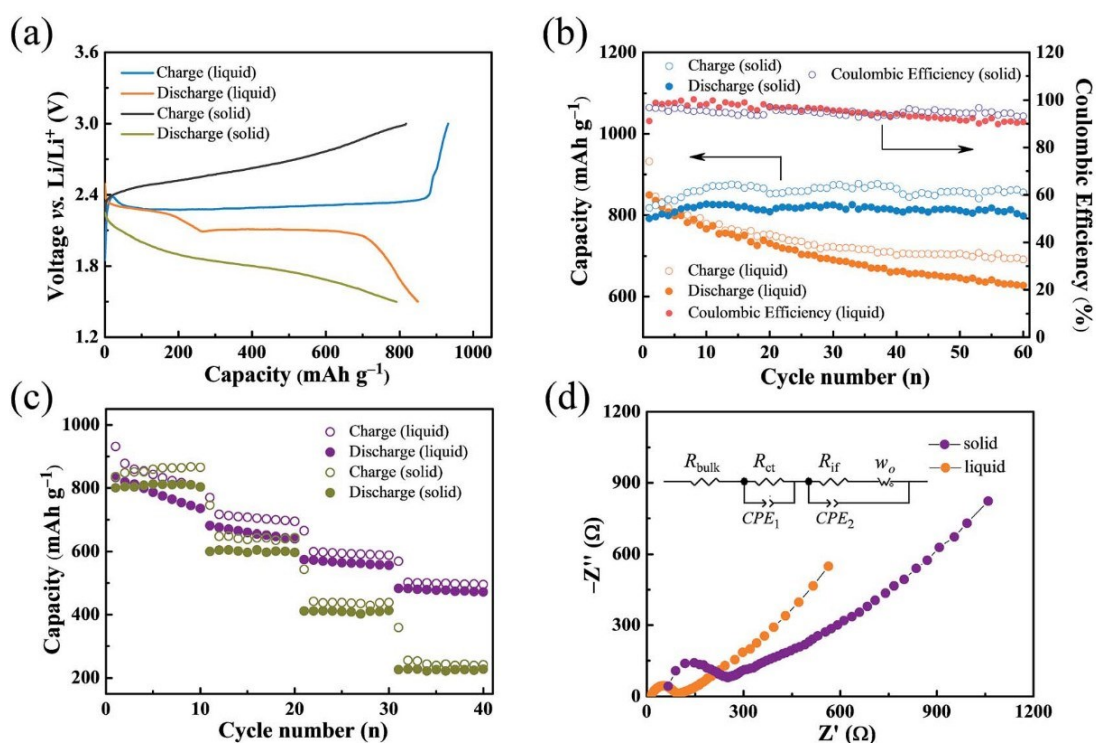
**Figure 1.14** (a) Cycle performance and (b) discharge curves of Li-S batteries with different electrolytes [49].

**All-solid-state electrolytes:** Due to addressing some problems caused by liquid electrolytes, solid electrolytes have become promising alternatives for Li-S batteries. Primarily, solid electrolytes possess a good safety feature than flammable liquid electrolytes. Then, owing to the impenetrability of polysulfides in solid electrolytes, the “shuttle effect” can be inherently eliminated, and polysulfides will be transferred to  $\text{Li}_2\text{S}$  directly. Thirdly, the even Li-ion transference of solid electrolytes are the key to depositing Li uniformly and suppressing lithium dendrite formation.



**Figure 1.15** Graphical representation of liquid electrolyte Li-S batteries and (b) solid electrolyte Li-S batteries [50].

In 2017, Ruochen Xu et al. reported the  $\text{Li}_7\text{P}_{2.9}\text{Mn}_{0.1}\text{S}_{10.7}\text{I}_{0.3}$  solid electrolyte for Li-S batteries, possessing a high ionic conductivity of  $5.6 \text{ mS}\cdot\text{cm}^{-1}$  and a wide voltage stability approach to 5 V (vs  $\text{Li}/\text{Li}^+$ ). The battery showed superior cyclic stability than it with organic liquid electrolyte in **Figure 1.16**. Nevertheless, the all-solid-state battery displayed a worse rate performance at a large current density than the liquid one because of the large interface resistance between the electrodes and electrolyte, which can be reflected by the EIS test in **Figure 1.16d** [51].

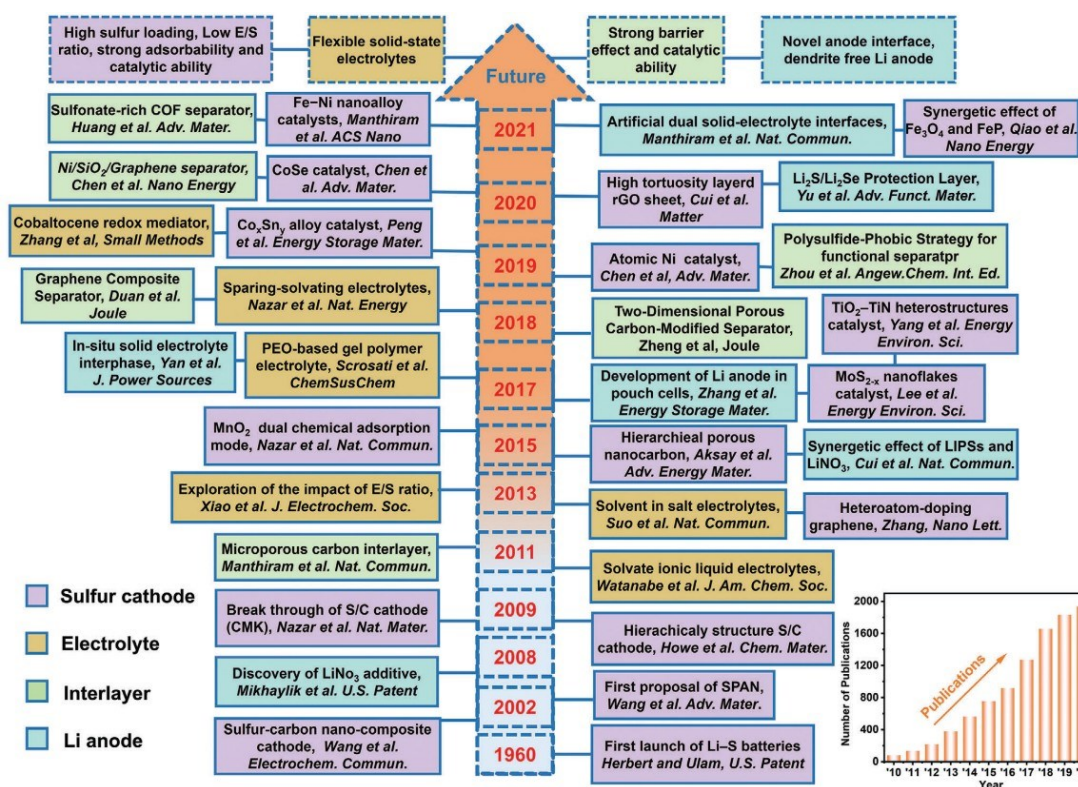


**Figure 1.16** (a) Charge-discharge curves and (b) cyclic performances at 0.05 C. (c) Rate performance from 0.05 C to 0.5 C; (d) EIS curves [51].

### 1.2.3 S-based cathode

Plenty of efforts have been made to overcome the defects of Li-S batteries from the 1960s to now [20]. However, due to the appearance of EVs, LIBs have become a prominent research field and have achieved commercialization worldwide in advance. Since EVs require a higher energy density to meet daily life, academics turn their attention to Li-S batteries again. There was a breakthrough investigation by Nazar's group in 2009. A mesoporous carbon-sulfur composite was applied as the cathode material, achieving a high reversible specific capacity of over 1300 mAh·g<sup>-1</sup> and good long-cycle performance [52]. After that, research on the sulfur cathode began to grow rapidly, mainly including the various materials adopted and the diversity of structural design. Then it develops the research of material surface modification, features of low

cost, environmentally friendly and safe. Numerous methods have been applied to enhance the battery performance, such as a higher specific capacity, energy density, large current long cycle performance and rate performance. Besides the elemental sulfur,  $\text{Li}_2\text{S}$ ,  $\text{S}_{2-4}$ , organic sulfur and liquid sulfur could be applied to cathode materials [53, 54]. In the next part, the various elemental sulfur-based cathode will be discussed for several types in detail.



**Figure 1.17** The milestone of Li-S battery development from the past to the present [55].

### 1.3 Host materials of S-based cathode

#### 1.3.1 Carbon-based materials

To address these challenges, recent efforts have been focused on the designs of the host material for sulfur. Among them, carbon-based materials have been widely used since they can improve conductivity and act as an alternative conducting source for the

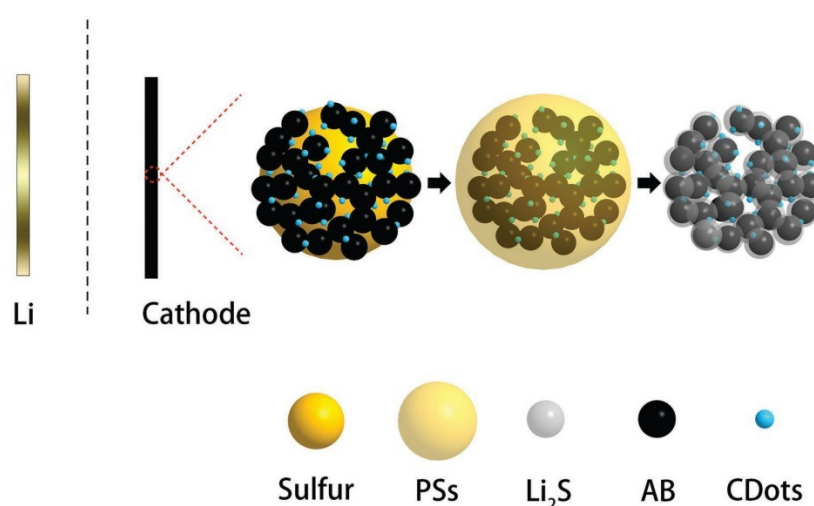
non-conductivity of the sulfur cathode. Another advantage is that the volume expansion is greatly obviated during the cycle. Furthermore, carbon has been widely found on the earth and is readily available through mature fabrication techniques [56]. The combination of sulfur and carbon is typically subjected to an isothermal treatment at 155 °C for 8 to 24 hours under a protected environment to produce the sulfur-carbon composite. Through capillary force, the molten sulfur fills the pores or covers the surface of the carbon host throughout this process. The temperature is selected to produce liquid sulfur with the lowest viscosity at this time [57].

There are now diverse examples of using carbon-based materials in Li-S batteries, including the carbon nanotube-sulfur [30, 58], graphene-sulfur [59, 60] and some other structured porous carbon-sulfur [61-63], acting as the most potential cathode materials profited from an easy preparation method and significantly improved comprehensive performance [64-67]. In order to create the ideal sulfur host, the carbon material must have a uniform pore distribution, enough pore volume and specific surface area, and a robust polysulfides-trapping capacity to provide the desired sulfur distribution, sulfur content, and long-term cycle stability [68]. Consequently, scientists have worked tirelessly to develop and create various carbonaceous materials that may serve as sulfur hosts. We will review these carbon host studies regarding their structure, morphology, and interfacial alteration.

#### (1) zero-dimensional (0D) structure

All of its dimensions are small for materials within the nanoscale, which can be defined as 0D structure. In the case of carbon materials, nano-shells, nanospheres,

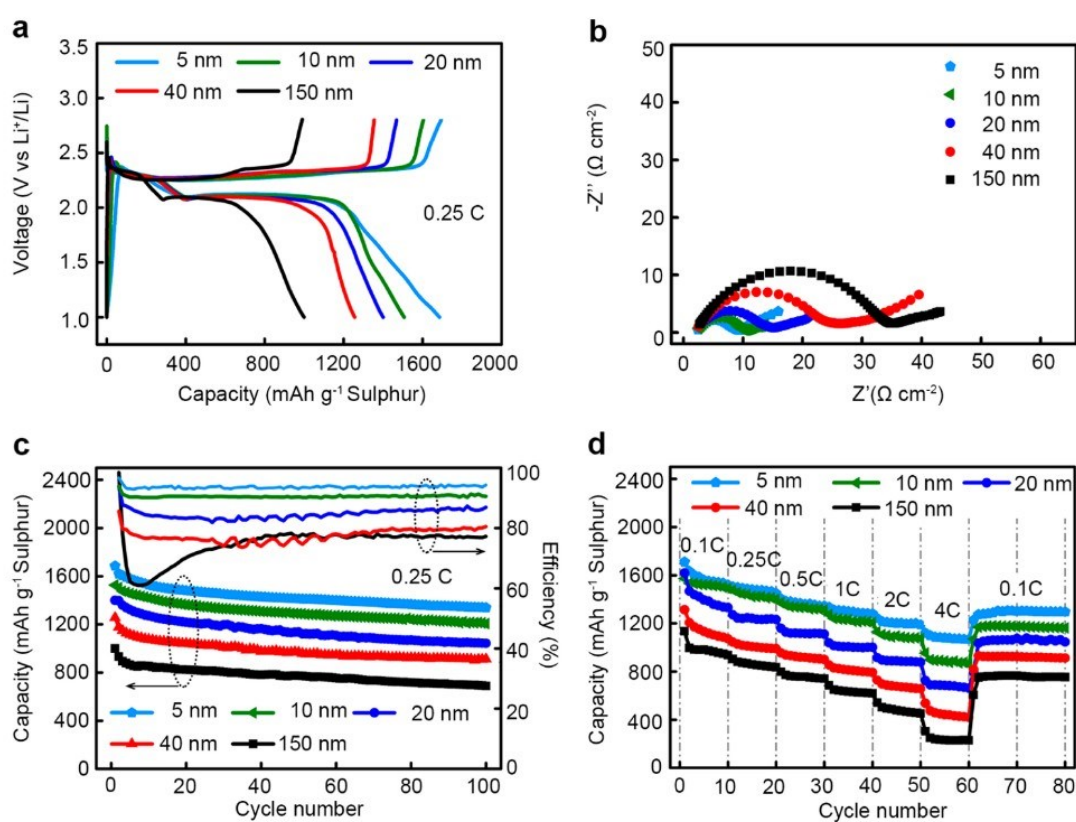
nanocages as well as quantum dots, are often employed 0D materials as sulfur hosts. These structures either surround the sulfur particles independently or enclose them within their micropores and vacant space. For example, Jørg Schuster invented an exceptional spherical at the nanoscale demonstrating high initial discharge capacity up to  $1350 \text{ mAhg}^{-1}$  and good cyclability without sacrificing rate capability as a sulfur host for Li-S batteries. In contrast to bulk porous carbons, the carbon-sulfur sphere electrode did not exhibit appreciable capacity fading with the increasing sulfur content [69]. Yin Hu et al. discovered one-step carbonization of the polyethyleneimine-functionalized carbon dots (PEI-CDots) in 2019 (**Figure 1.18**). The PEI-CDots-modified Li-S battery produces an areal capacity of  $3.3 \text{ mAh}\cdot\text{cm}^{-2}$  at a high current density of  $8 \text{ mA}\cdot\text{cm}^{-2}$  with just 0.07 % capacity loss per cycle over 400 cycles at 6.6 mg sulfur loading. These are attributed to the increased conductivity of Li-ion by zero-dimensional PEI-CDots and enhanced polysulfides adsorption of actives site [70].



**Figure 1.18** Descriptions of the PEI-CDots modified cathode at different charge-discharge phases [70].

Besides the carbon host, researchers look for ways to reduce the size of sulfur

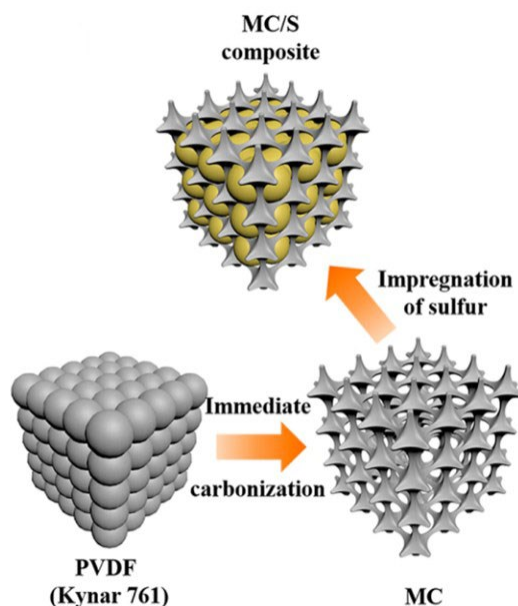
particles to improve the use of active material and increase electrochemical kinetics. In Chen's work, they produced monodispersed S nanoparticles with diameters of 5, 10, 20, 40 and 150 nm on reduced graphene oxide (rGO) surface via sulfur-amine chemistry and adjusting reaction conditions such as solution pH and deposition time. The specific capacity of sulfur approaches the theoretical specific capacity of  $1672 \text{ mAh}\cdot\text{g}^{-1}$  at 0.1 C and  $1089 \text{ mAh}\cdot\text{g}^{-1}$  even at 4 C when the sulfur particle size is reduced to 5 nm [71].



**Figure 1.19** (a) First discharge/charge curves at 0.25 C, (b) EIS spectra of as-prepared batteries, (c) cycling performance at 0.25 C, (d) rate performance from 0.1 to 4 C current density [71].

Even though the sulfur particle at the nanoscale had desirable properties, some researchers persisted in bringing the sulfur size down to less than a S<sub>8</sub> molecule. In 2017, Hu et al. applied a sulfur cathode with an ultra micropore pore size less than 0.7

nm, exhibiting superior electrochemical performance of a capacity of  $507.9 \text{ mAh}\cdot\text{g}^{-1}$  after 500 cycles at 2 C in Li-S batteries and good behavior in Na-S batteries [72].



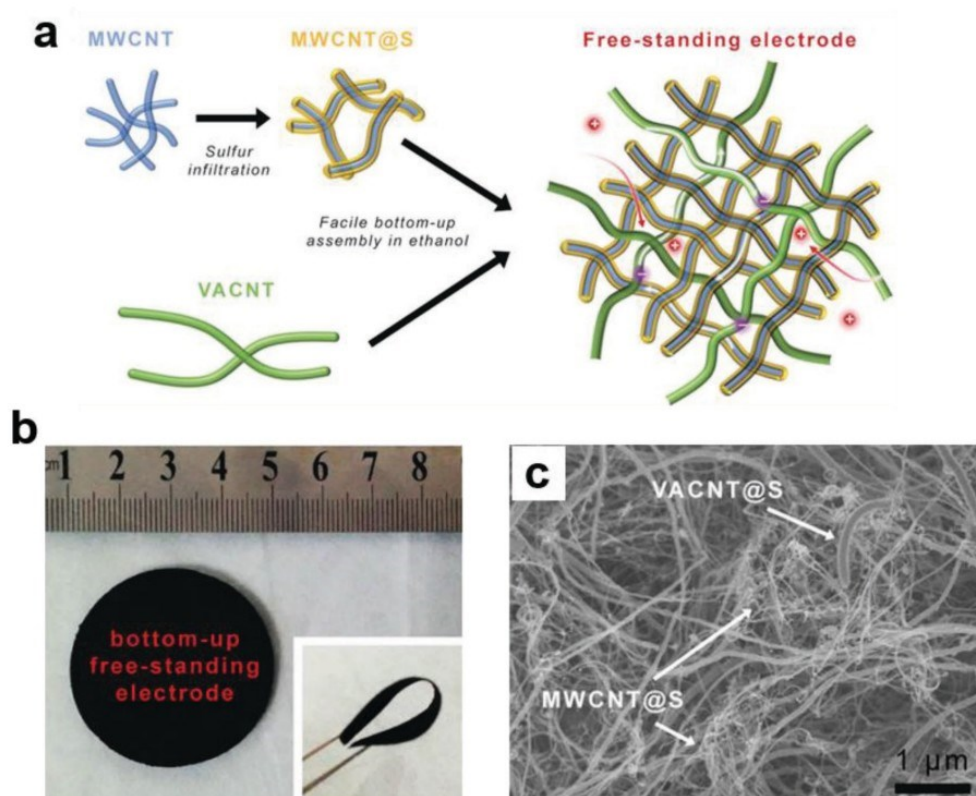
**Figure 1.20** Description of the preparation for microporous carbon-sulfur composite [72].

(2) one-dimensional (1D) structure

The common 1D material for Li-S cathode is the high carbon nanotube (CNT) or carbon nanofiber with high specific surface area (SSA) and conductivity. There are various methods of application for CNT. For instance, M. Hagen and co-workers use vertical-aligned carbon nanotubes directly grown on a nickel foil current collector without a binder. The binder-free cathode contains a high 90 % sulfur in the electrode, almost the highest published [73]. In 2014, Wu and researchers developed mesohollow and microporous carbon nanofibers (MhMpCFs) via the electrospinning method with polymethylmethacrylate (PMMA) and polyacrylonitrile (PAN) as spinning solutions followed by carbonization. The S/MhMpCFs electrode owned a capacity of  $815 \text{ mAh}\cdot\text{g}^{-1}$



<sup>1</sup> after activation and remained  $715 \text{ mAh}\cdot\text{g}^{-1}$  after 70 cycles with 88 % retention [74]. Yuan's group explored a free-standing sulfur cathode, with a short multiwalled carbon nanotube (MWCNT) as a conductive framework for a sulfur host and a superlong vertically aligned carbon nanotube (VACNT) serving as both a long-range conductive connection (**Figure 1.21a**) with favourable flexibility (**Figure 1.21b,c**) [75]. The free-standing CNT-based cathode remained at a reversible capacity of about  $700 \text{ mAh}\cdot\text{g}^{-1}$  after 150 cycles at  $0.38 \text{ mA}\cdot\text{cm}^{-2}$  with a high sulfur loading of  $6.3 \text{ mg}\cdot\text{cm}^{-2}$ .



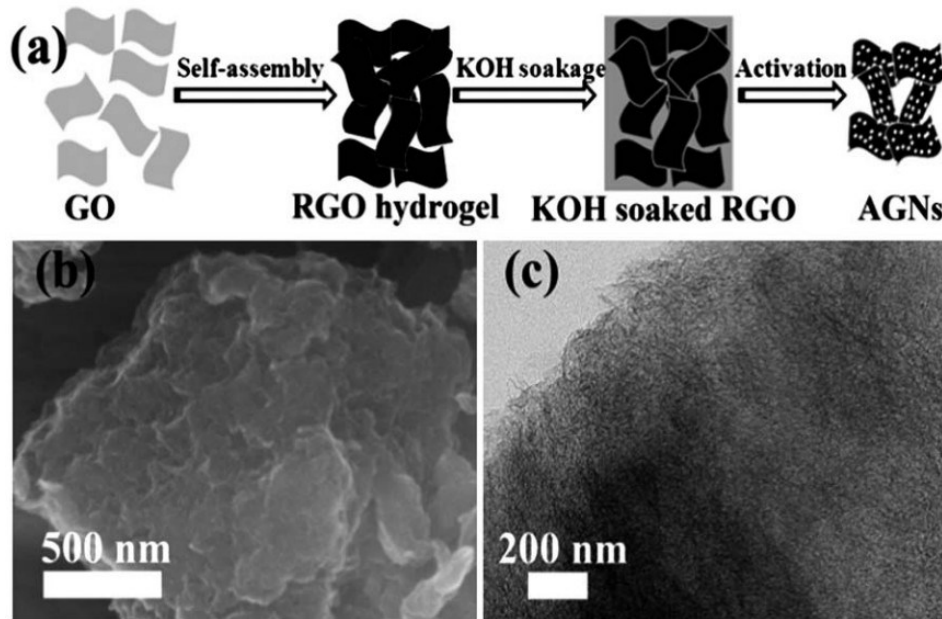
**Figure 1.21** (a) Illustration of the synthesis, (b) optical image in the flat and bent situation and (c) SEM image of a CNT-based sulfur cathode [56].

(3) two-dimensional (2D) structure

The representative 2D carbon materials are graphene and its derivatives. They have received great interest in the realm of Li-S battery cathode due to their distinctive

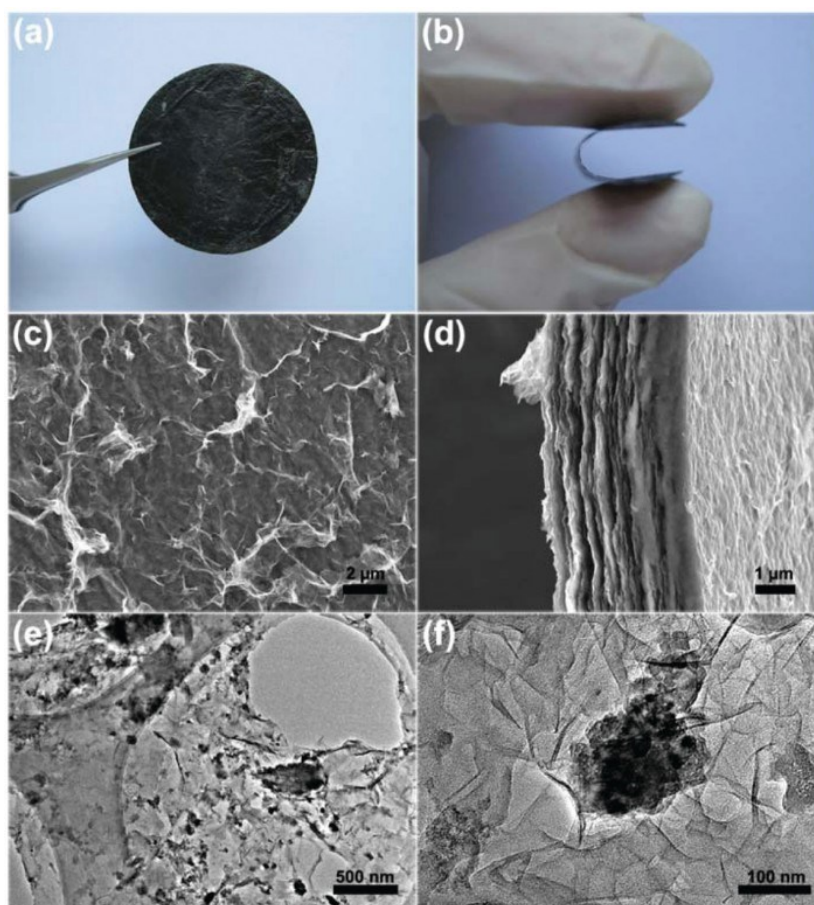
2D structure. Monatomic sp<sup>2</sup> carbon layer graphene has high conductivity, high specific surface area, significant chemical stability and strong mechanical strength. Oxidation and heteroatom doping are modifications of graphene that may be made to alter its properties to match specific needs.

Ten years ago, activated graphene nanosheets (AGNs) were prepared through modified chemical activation of hydrothermally reduced graphene oxide (RGO) hydrogel, which served as potential scaffolds for confining sulfur particles. The AGNs/S composite owned the initial specific capacity of 1379 mAh·g<sup>-1</sup> at 0.2 C and a stable cycle performance [76]. The microporous AGNs framework not only served as an electric medium for the insulating sulfur and encapsulated it, but it also rendered "micro-reactors" for the electrochemical process, allowing for the entrapment of polysulfide intermediates and accommodating volume expansion during the charge-discharge process. These excellent electrochemical properties should contribute to the attractive nanostructure of chemically tailored graphene.



**Figure 1.22** (a) Demonstration of the fabrication process to AGNs via self-assembly of GO; (b) FESEM and (c) TEM images of AGNs [76].

Later, Gu et al. prepared a porous nitrogen and phosphorus dual-doped graphene (p-NP-G) layer with high conductivity through a thermal annealing and hydrothermal process, showing the excellent first capacity of  $1158.3 \text{ mAh}\cdot\text{g}^{-1}$  at 1C, high rate capability of  $633.7 \text{ mAh}\cdot\text{g}^{-1}$  at 2 C [77]. In 2017, Luo and co-workers fabricated a type of free-standing RGO-S film as a cathode via infiltrating sulfur into the solvated RGO films and freeze-drying. High conductivity, a regularly layered structure, and a robust binding between rGO sheets and S nanoparticles are all characteristics of rGO-S composite films. As a result, the nanostructured rGO-S composite films may act directly as a self-supporting cathode for Li-S batteries without the requirement for aluminium current collectors. At 0.1 C current density, it showed a high first capacity of  $1028 \text{ mAh}\cdot\text{g}^{-1}$  and outstanding stability after 300 cycles with 65 % capacity retention [78].

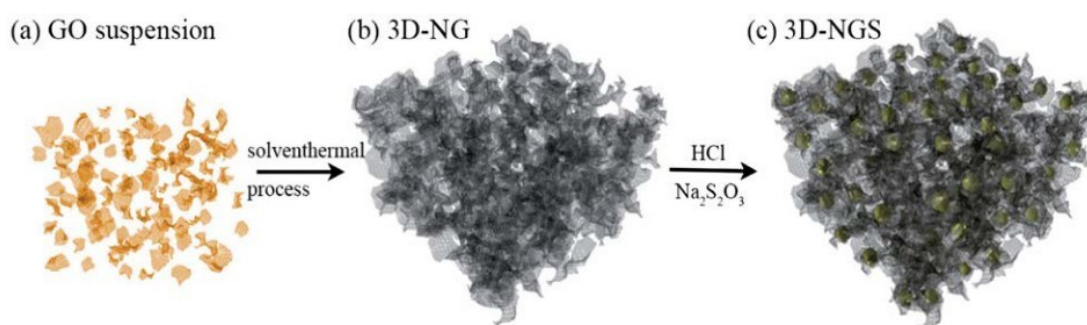


**Figure 1.23** (a,b) Optical images of the RGO-S film. (c) Front and (d) cross-sectional SEM images of the RGO-S film. (e, f) TEM images of the RGO-S film [78].

#### (4) three-dimensional (3D) structure

3D structured carbon hosts of sulfur often offer a large number of meso- and micropores, which may accommodate sulfur while improving electronic conductivity owing to a network of interconnected pores. In Wang's research, the simple one-pot solution reaction route was used to easily prepare the 3D nitrogen-doped graphene sulfur (3D-NGS) cathode, which has a high 87.6 wt% sulfur content, delivering  $792 \text{ mAh}\cdot\text{g}^{-1}$  capacity after 145 cycles at a current density of  $600 \text{ mA}\cdot\text{g}^{-1}$  and the low capacity fading rate of 0.05 % per cycle [79]. This can be ascribed to a structure that facilitates the flow of electrons and reduces the volume impact when cycling. Due to

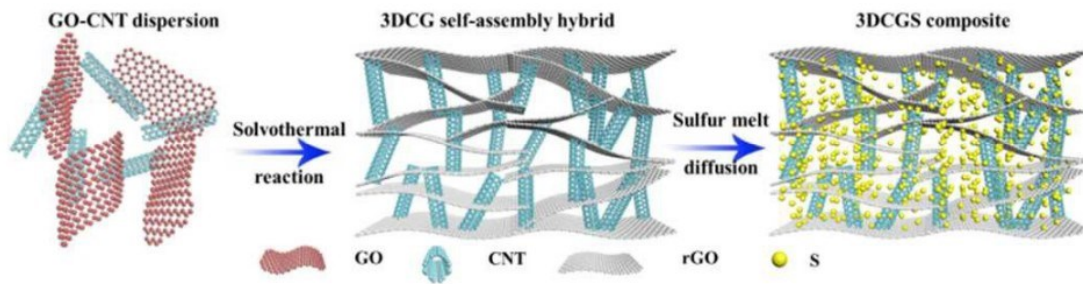
the strong chemical connection between S and the N atoms, N-doping can let Li ions traverse the graphene and limit sulfur.



**Figure 1.24** Preparation process of the 3D-NGS composite [79].

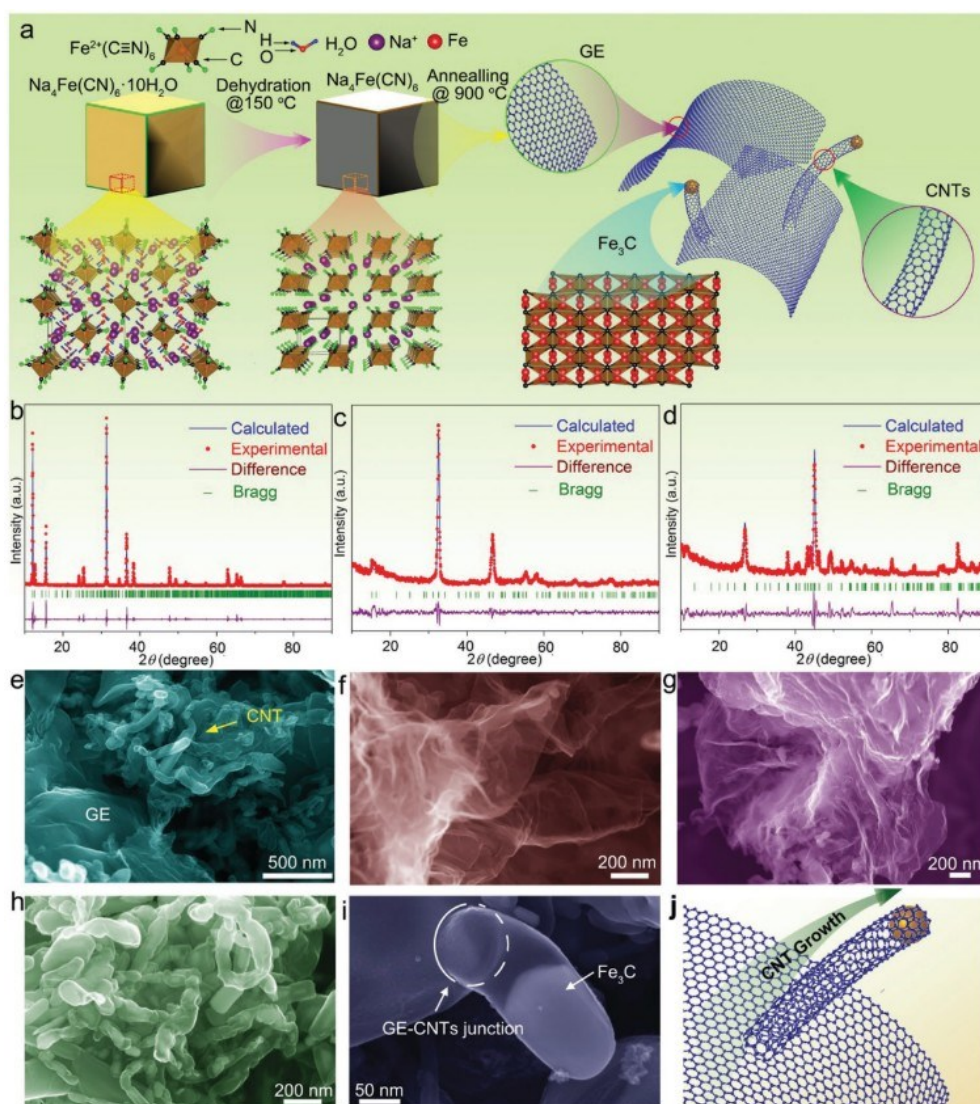
Razaq's group synthesized a particular 3D hollow nitrogen-doped carbon flower (HNCF) with Mo<sub>2</sub>C particles uniformly distributed on its 2D nanosheets by 2020. The Mo<sub>2</sub>C/HNCF efficiently relieved the aggregation of nanosheets and acted as active sites for efficient adsorption and conversion of polysulfides [80]. Its cathode presented a high rate performance and a prominent retention rate of 92 % after 100 cycles at 0.5 C.

He et al. prepared a 3D carbon nanotube/graphene-sulfur (3DCGS) sponge with a high sulfur content of over 80 %. The conductivity of 3DCGS with two types of mesopores is elevated by 324.7% compared to the 3D graphene-sulfur (3DGS) sponge without CNT [30]. The 3DCGS showed a low capacity decay of 0.08 % per cycle, and excellent rate performance, retaining 653.4 mAh·g<sup>-1</sup> at 4 C, which results from strong polysulfides adsorption, maximum optimization speed of charge transportation and full electrolyte penetration.



**Figure 1.25** Illustration of the preparation process of the 3DCGS composite [30].

In Su's work, a simple one-step in-situ growing method was adopted to fabricate 3D nitrogen doped graphene-carbon nanotube ( $\text{Fe}_3\text{C}@N\text{GE-CNT}$ ) with low-cost precursors. It can be characterized as 1D CNT and 2D graphene bonded seamlessly when growing. Consequently, the hybrid has a high capacity of  $1221 \text{ mAh}\cdot\text{g}^{-1}$  at  $0.2 \text{ C}$  current density and outstanding rate performance of  $220 \text{ mAh}\cdot\text{g}^{-1}$  at  $10 \text{ C}$  due to fast penetration and diffusion of electrolytes and great conductivity [81].



**Figure 1.26** (a) Schematic of preparation for the Fe<sub>3</sub>C@N-GE-CNT. XRD patterns of (b) Na<sub>4</sub>Fe(CN)<sub>6</sub>·10H<sub>2</sub>O, (c) Na<sub>4</sub>Fe(CN)<sub>6</sub>, and (d) Fe<sub>3</sub>C@N-GE-CNT. (e-i) FESEM images of Fe<sub>3</sub>C@N-GE-CNT. (j) Presentation of carbon nanotubes grown from graphene [81].

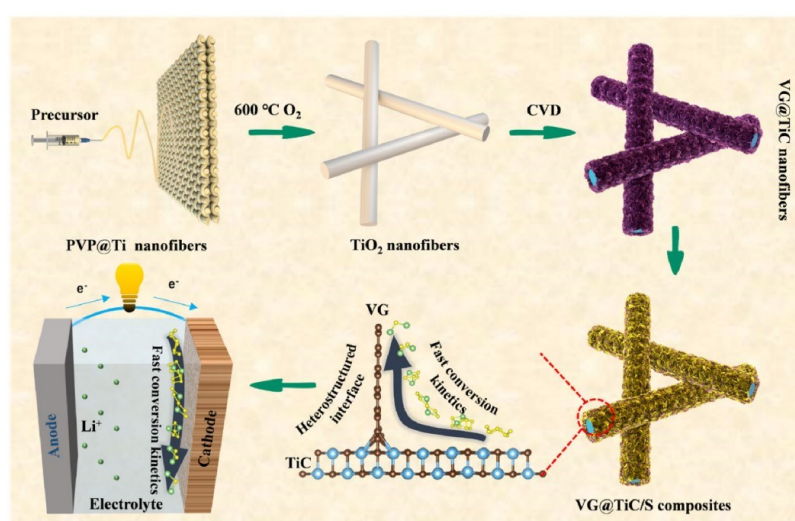
### 1.3.2 Titanium-based materials

Titanium has attracted more and more attention in recent years for several merits. First, it is a non-heavy metal and a nonmagnetic substance, which is beneficial to use in medical equipment. Second, titanium is environmentally friendly and has low density, contributing to reducing the weight of electrode materials. Third, titanium and its

compounds possess a good corrosion resistance, providing convenience for the preparation of stable electrode materials [82].

A 3D titanium nitride (TiN) nanowire array with exposed (200) facets-based electrode could offer highly ordered nanowires to accelerate the efficient transition of redox charge carriers and to promote the redox kinetics of polysulfides further and provide five-coordinated Ti sites on (200) facets to strengthen the adsorption of polysulfides [83].

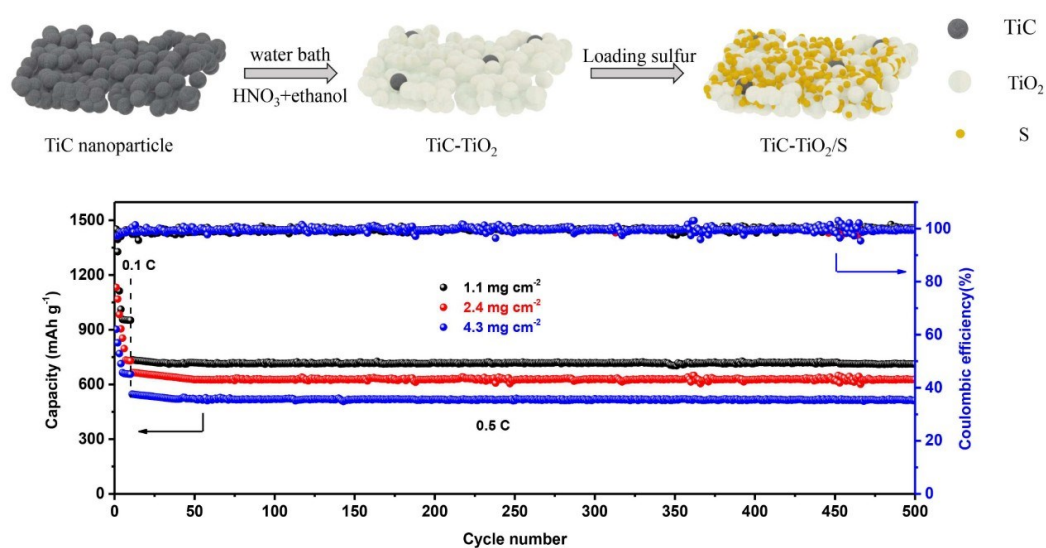
The titanium carbide (TiC) not only shows a high conductivity compensating insulated sulfur but also plays a role in an electrocatalyst for promoting the sulfur redox reaction kinetics. In 2021, Zhang put forward a cathode with TiC nanofibers and in-situ grown graphene [84]. The heterostructured electrocatalysts can improve Li ion and electron transportation, accelerating the transformation kinetics between different sulfur components and inducing homogeneous deposition of final Li<sub>2</sub>S. Its battery displayed an excellent capacity of 971 mAh·g<sup>-1</sup> at 2 C.



**Figure 1.27** Illustration of the fabrication procedure of the electrocatalyst Li-S cathode [84].



The titanium dioxide ( $\text{TiO}_2$ ) can suppress the “shuttle effect” and has a strong polysulfides adsorption as it contains an anion ( $\text{O}^{2-}$ ) with a strong polar surface. Owing to the semiconductor property, Cui and co-workers prepared a microporous  $\text{TiC-TiO}_2/\text{S}$  composite by a facile method to achieve better conductivity, good rate performance, and excellent cycling stability [85]. When charging and discharging at 0.5 C, a stable specific capacity of  $714 \text{ mAh}\cdot\text{g}^{-1}$  can remain for 500 cycles at the sulfur loading exceeding  $1 \text{ mg}\cdot\text{cm}^{-2}$ .

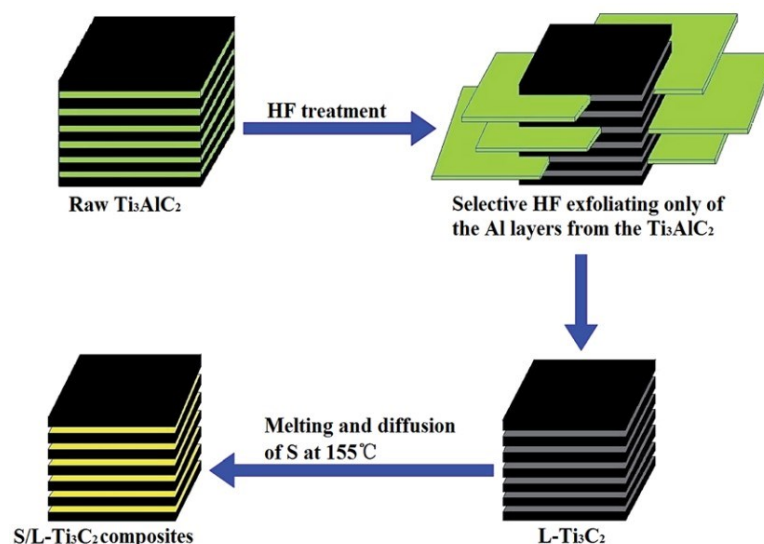


**Figure 1.28** (a) Fabrication process of  $\text{TiC-TiO}_2/\text{S}$  composite and (b) long cycle performance at 0.5 C [85].

A typical two-dimensional layered titanium-based material,  $\text{Ti}_3\text{C}_2\text{T}_x$  MXene, has recently emerged in Li-S battery electrodes. The advantage of the use of MXene in Li-S batteries lies in their metallic conductivity and abundant functional groups ( $-\text{O}$ ,  $-\text{OH}$  and  $-\text{F}$ ), which can adsorb polysulfides and suppress the "shuttle effect" effectively [86, 87].

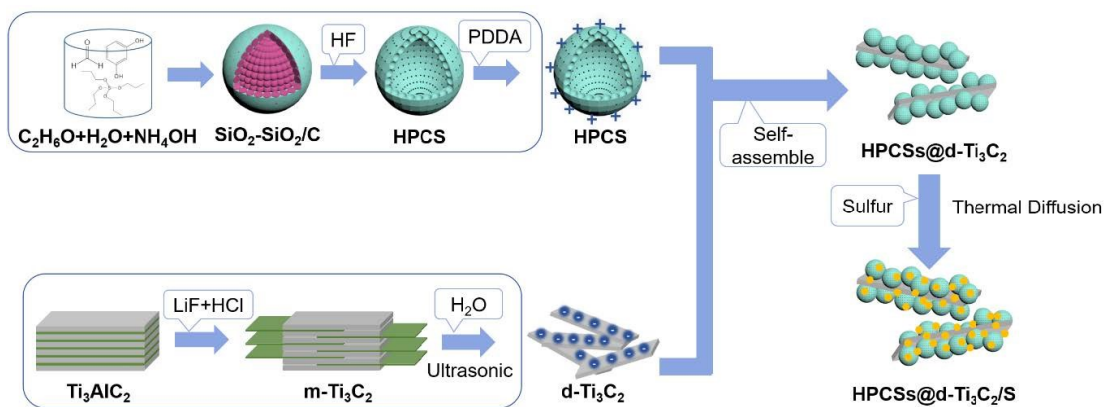
Liang et al. fabricated conductive MXene nanosheets as a sulfur cathode, showing a high  $1200 \text{ mAh}\cdot\text{g}^{-1}$  capacity at 0.2 C and achieving 80 % retention over 400 cycles at

0.5 C [88]. Similarly, Zhao's group synthesized layered MXene for the sulfur cathode and reported a high first discharge capacity of  $1291 \text{ mA h}\cdot\text{g}^{-1}$  around 0.1 C and superb capacity retention of  $970 \text{ mA h}\cdot\text{g}^{-1}$  after 100 cycles [89].



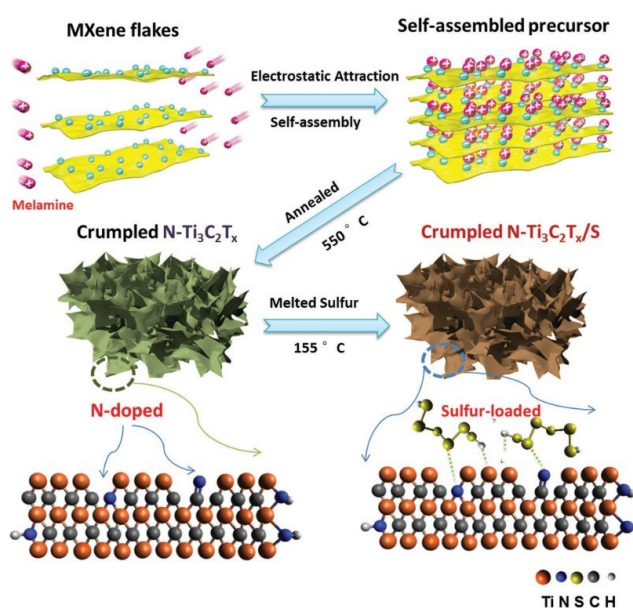
**Figure 1.29** Illustration of the  $\text{Ti}_3\text{AlC}_2$  MAX exfoliation and the fabrication of  $\text{S}/\text{Ti}_3\text{C}_2$  MXene [89].

However, the pristine MXene material tends to stack tightly and reduce the specific surface area, making its advantages less appealing [90, 91]. Therefore, mixing other materials with MXene is a common and effective way to tackle these drawbacks. In Bao's work, they prepared a 3D MXene/reduced graphene oxide hybrid electrode as a sulfur host, presenting a high first capacity of  $1144.2 \text{ mAh}\cdot\text{g}^{-1}$  at 0.5 C and retention of  $878.4 \text{ mAh}\cdot\text{g}^{-1}$  after 300 cycles [92]. In 2020, Qi et al. reported a hollow porous carbon sphere @ MXene composites for Li-S batteries, achieving an excellent long-cycle performance with a low capacity fading rate of 0.069 % per cycle at 1 C [93].



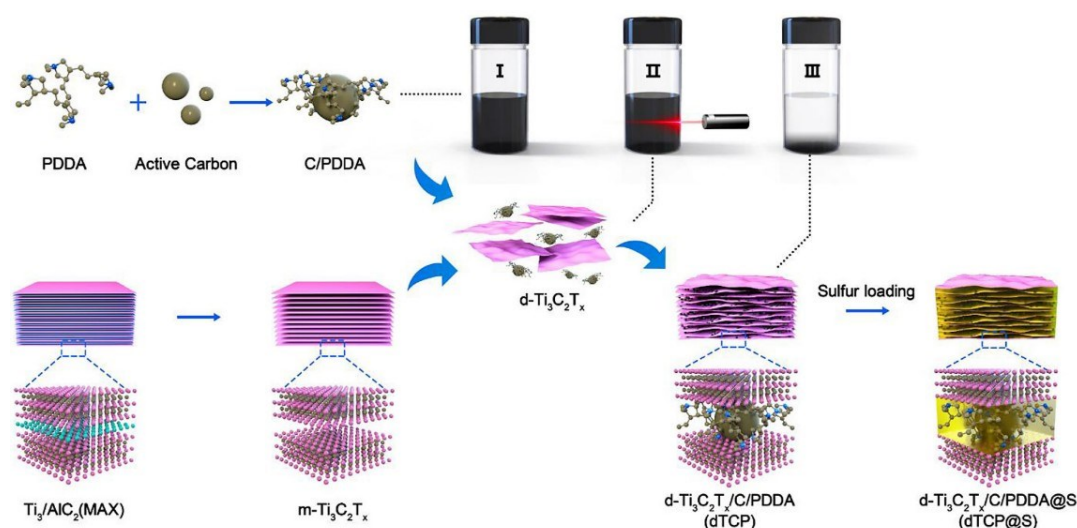
**Figure 1.30** Synthesis procedures of MXene, HPCSs, HPCSs@MXene and their sulfur composites [93].

Similar to nitrogen-doped graphene, nitrogen-doped titanium-based MXene also has many applications for Li-S batteries. The nitrogen-doping introduces heteroatoms into MXene and creates its porous structure, high SSA, and strong binding of physical and chemical dual-adsorption for polysulfides. It owns a fantastic capacity of  $1144 \text{ mAh}\cdot\text{g}^{-1}$  at  $0.2 \text{ C}$  and a superlong stable cycle of  $610 \text{ mAh}\cdot\text{g}^{-1}$  at  $2 \text{ C}$  for 1000 cycles [94].



**Figure 1.31** Fabrication process of a crumpled nitrogen-doped  $N-Ti_3C_2T_x/S$  cathode [94].

Assembling MXene from 2D to 3D is the other strategy to overcome drawbacks [95]. 3D MXene was synthesized by MXene sheets and carbon-poly (diallyl dimethyl ammonium chloride) nanoparticles via a self-assembly way. The 3D MXene not only relieves MXene sheets from stacking itself but also provides a skeleton to accommodate S and lift sulfur utilization [96]. Consequently, its sulfur cathode obtained a good initial capacity of 1016.8 mAh g<sup>-1</sup> at 0.2 C, and excellent long cycling performance, with a 0.075 % low capacity decay rate per cycle after 600 cycles at 1 C current density.



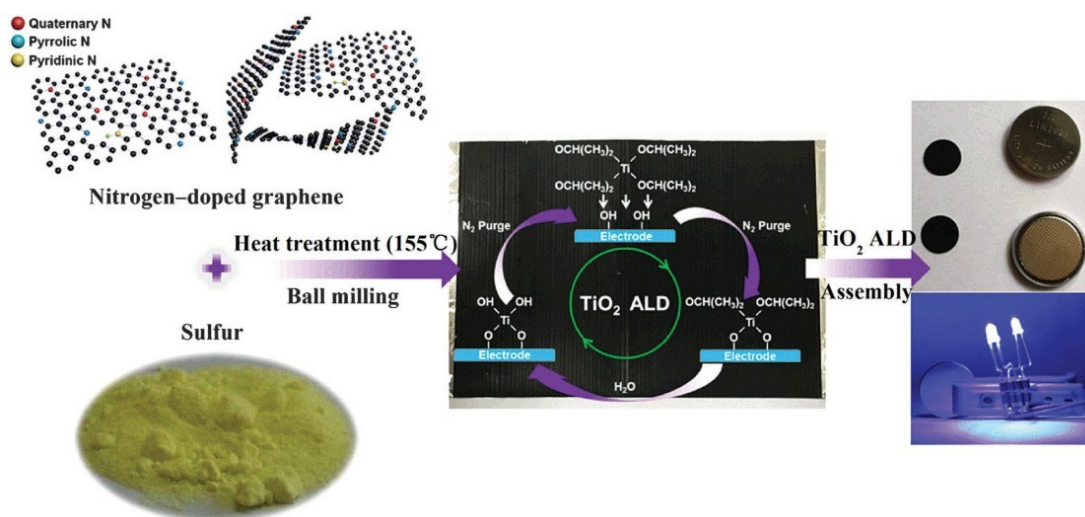
**Figure 1.32** Schematic of fabrication steps of a type of 3D MXene sulfur cathode [96].

### 1.3.3 Other materials

#### Metallic compounds

Metal compounds can be divided into metal sulfide, metal oxide, metal carbide, metal nitride, metal phosphide and so on. Different species of metal compounds have their own advantages and disadvantages. One of the most representative is metal oxides that typically contain an anion ( $O^{2-}$ ) with a strong polar surface [97]. Unlike nanostructured carbon materials, nanostructured metal oxides afford abundant polar active sites to favor the absorption of polysulfides, facilitating the Li-S batteries with

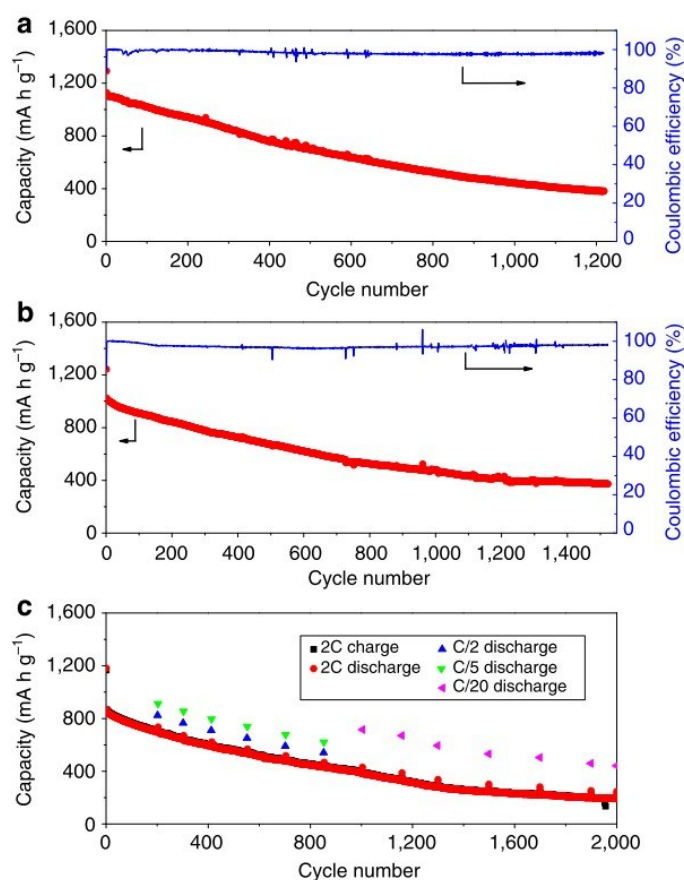
high sulfur utilization and a long life span [83, 98-101]. One good example was reported in Mingpeng Yu's work. They applied atomic layer deposition of titanium dioxide ( $\text{TiO}_2$ ) layers on nitrogen-doped graphene/sulfur (NG/S) electrodes to avoid capacity deterioration. It delivered initial discharge capacity up to  $1069.5 \text{ mAh}\cdot\text{g}^{-1}$  and  $918.3 \text{ mAh}\cdot\text{g}^{-1}$  after 500 cycles at 1 C [102]. Similarly, Xiao Liang's group applied S/vanadium pentoxide ( $\text{V}_2\text{O}_5$ )-graphene composite to obtain a decay rate of 0.048 % per cycle at 0.05 C, and Xiulei Ji's group employed a porous silicon dioxide ( $\text{SiO}_2$ ) embedded within the carbon-sulfur composite to assist the absorption of polysulfides [103, 104].



**Figure 1.33** Preparation of the NG/S–TiO<sub>2</sub> and the experiment of lighting up two LEDs with batteries [102].

Liang et al. adopted a chemical procedure that uses a host ( $\text{MnO}_2$  nanosheets serve as the prototype) to react with originally generated polysulfides to create surface-bound intermediates and to adsorb polysulfides, greatly suppressing the “shuttle effect”[105]. The  $\text{MnO}_2/\text{S}$  composite with 75 wt% high sulfur content delivers a specific capacity of  $1,300 \text{ mAh}\cdot\text{g}^{-1}$  at low current density and an extremely low decay rate of 0.036 % per

cycle after 2,000 cycles.

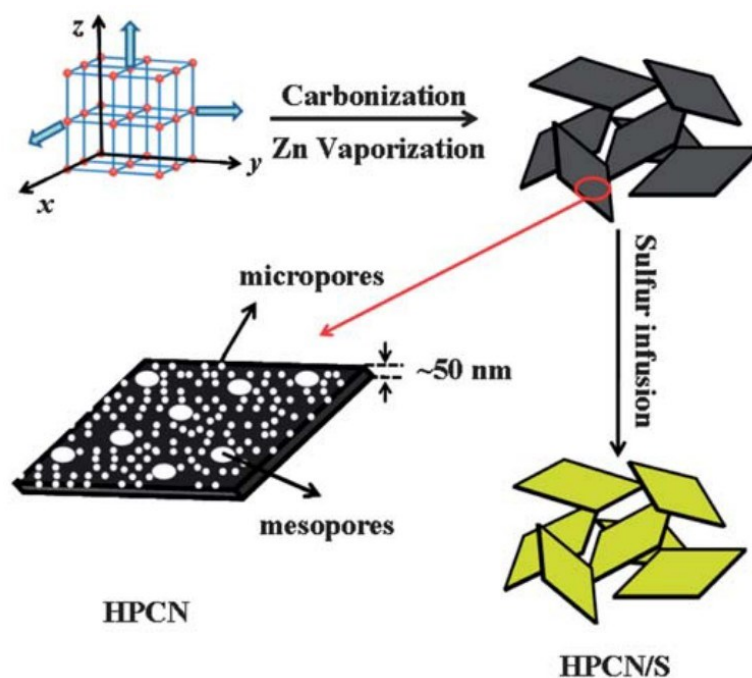


**Figure 1.34** Long-term cycle performance of MnO<sub>2</sub>/S. (a) Over 1200 cycles at 0.2 C, (b) over 1500 cycles at 0.2 C, (c) at 2 C for 2000 cycles with a periodic slow rate [105].

### Metal-organic framework (MOF)

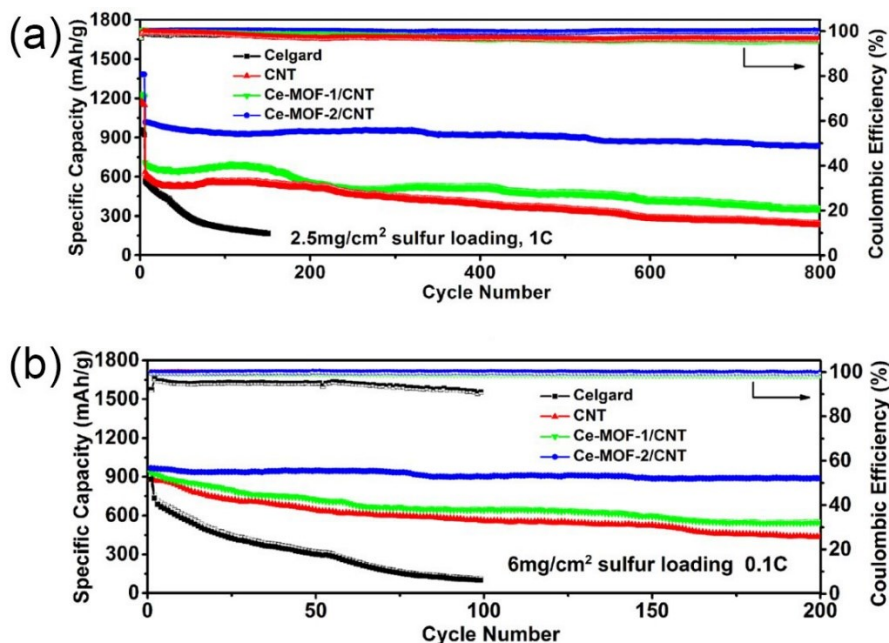
It is generally known that MOF may act as a self-sacrificial template and that when it decomposes under inert circumstances, the organic ligands in the framework structures produce carbon compounds. Another benefit of using a MOF as a precursor is that it is non-volatile and has low solubility, which boosts the yield of carbon products from starting chemicals. Hence, much work has been put into developing carbon materials made from MOFs that have special qualities, including hydrophobic behavior and surface area. Sulfur was reported to be encapsulated in hierarchically porous carbon

nanoplates (HPCN), which were created by pyrolyzing metal-organic frameworks (MOF) in a single process [106]. HPCN-S showed the first discharge capacity of 1177 mAh·g<sup>-1</sup> at 0.1 C. It still delivers a high capacity of 730 mAh·g<sup>-1</sup> after 50 cycles when the current increases to 0.5 C.



**Figure 1.35** Schematic of the preparation for the HPCN-S cathode [106].

In 2019, Hong et al. reported that cerium-based MOFs combined with CNT to form Ce-MOF/CNT composites as separators for Li-S batteries, present superb performance even under high sulfur loading (6 mg·cm<sup>-2</sup>). Under the 2.5 mg·cm<sup>-2</sup> sulfur loading, the first capacity of 1021.8 mAh·g<sup>-1</sup> at 1 C was obtained, which was slowly declined to 838.8 mAh·g<sup>-1</sup> after 800 cycles with merely a 0.022 % decay rate and the Coulombic efficiency approach to 100 %. It can be attributed to the strong adsorption of the Ce-MOF-2 to Li<sub>2</sub>S<sub>6</sub> and the catalytic effect toward transforming polysulfides [107].



**Figure 1.36** (a) Cycle performance with different separators at 1 C for 800 cycles ( $2.5 \text{ mg} \cdot \text{cm}^{-2}$ ). (b) at 0.1 C for 200 cycles ( $6.0 \text{ mg} \cdot \text{cm}^{-2}$ ).

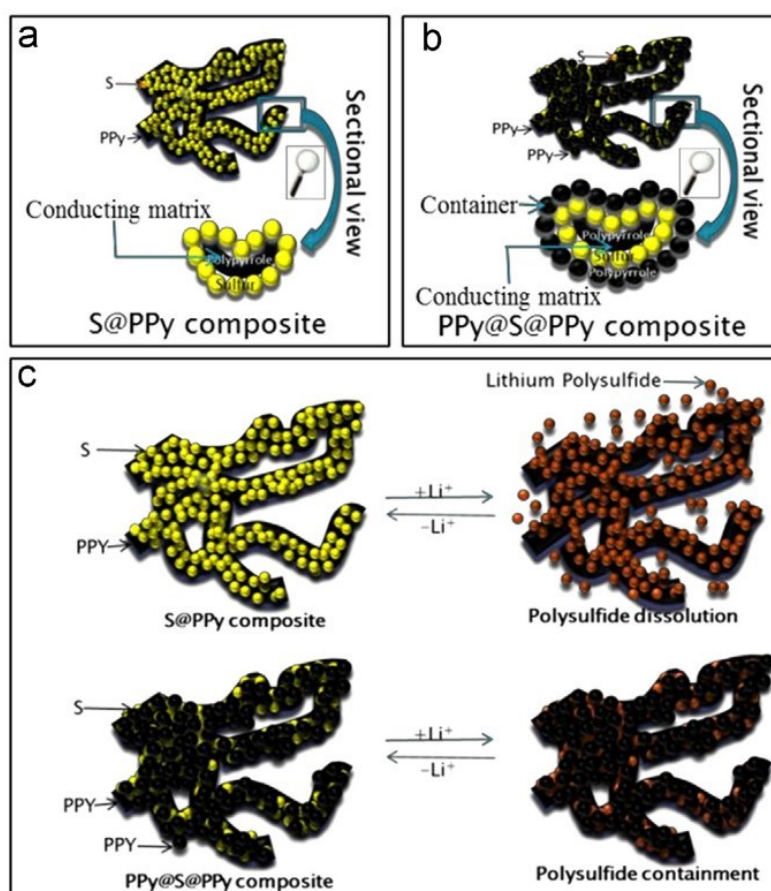
### Polymer-based materials

Other conductive materials, such as conductive polymers, which can effectively adsorb polysulfides through both physical and chemical means, have attracted interest in addition to the conductive carbon host due to their distinctive properties. Polymers including poly(pyrrole) (PPy), poly(thiophene) (PT), poly(aniline) (PANI), and poly(3,4ethylenedioxythiophene) (PEDOT) were adopted to encapsulating elemental sulfur and  $\text{Li}_2\text{S}$  [108]. The basic structure of the polymer is permeable to the lithium ions, so they can diffuse into the interior to react with the sulfur. On the one hand, the wide gap in the polymer body provides buffer space for the volume expansion of sulfur, and the polymer has a certain flexibility, so the volume change in the discharge process will not destroy the outer protective layer of the polymer. On the other hand, due to the chemical interaction between the polysulfides and the polymer chain, the polymer can



absorb the polysulfides, inhibit the “shuttle effect”, and increase the battery capacity.

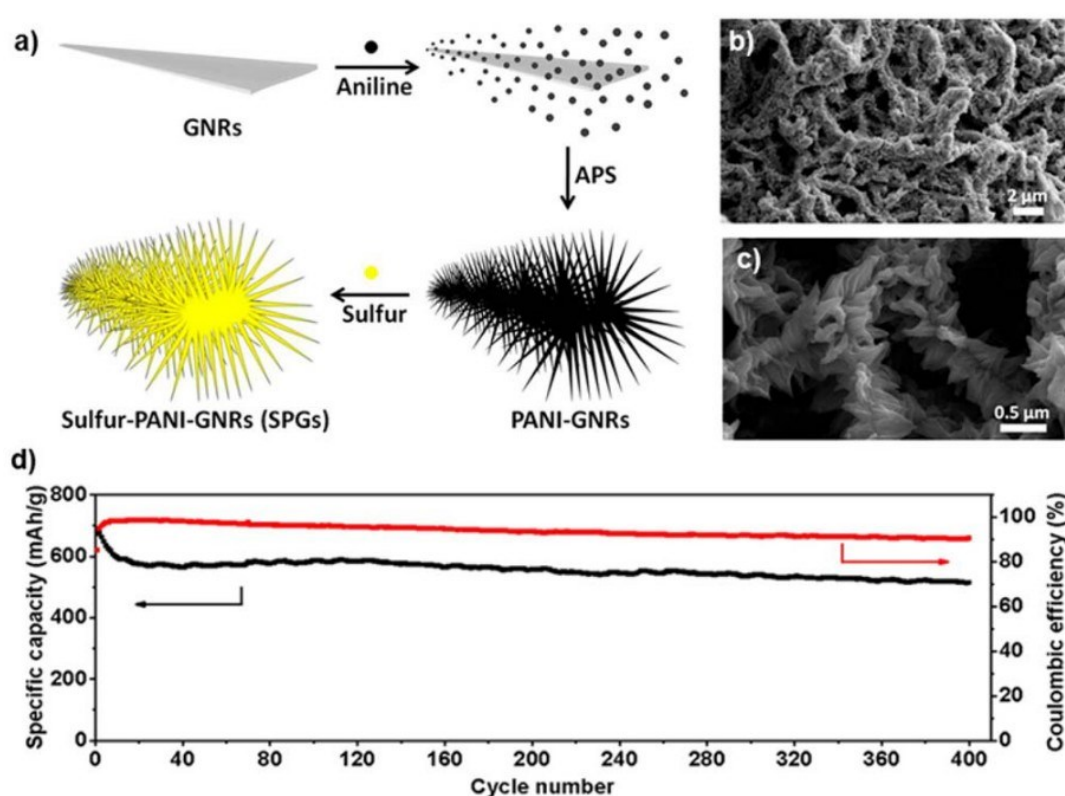
Liang’s group synthesized a PPy@S@PPy composite with a novel three-layer-3D-structure through the oxidic chemical polymerization and precipitation way. The discharge specific capacity of the cathode remained at 554 mAh·g<sup>-1</sup> after 50 cycles, with 68.8 % retention of the first capacity [109].



**Figure 1.37** Front and cross-sectional structure of (a) S@PPy composite and (b) PPy@S@PPy composite; (c) the function of the external PPy layer after adsorbing the dissolved polysulfides [109].

A hierarchical structure composed of sulfur, polyaniline, and graphene nanoribbons (SPGs) was successfully designed and created by Li and co-workers. Graphene nanoribbons (GNRs) significantly enhanced the mechanical characteristics

of the entire system in this composite. Polyaniline graphene nanoribbons (PANI-GNRs) served as an excellent loading platform for sulfur with enhanced electronic conductivity. Due to the synergistic interaction between the PANI, GNRs, and sulfur, electrochemical tests show that the SPGs display superior rate performance and high cycle stability as cathode materials compared to pure elemental sulfur and sulfur-PANI. It has been demonstrated that the SPG composite synthesis yields a useful component to enhance the electrochemical stability of the electrode materials for Li-S batteries.



**Figure 1.38** (a) The demonstration of SPGs. (b) and (c) SEM images of SPGs. (d) Cyclic performance of SPGs as the cathode [108].

#### **1.4 Research aims and objectives**

Compared with traditionally commercial lithium-ion batteries in the energy storage field, Li-S batteries exhibit a high theoretical specific capacity, and superb energy density with low-cost sulfur resources, making it the most promising secondary battery system. However, some issues still need to be solved for commercial applications, such as the non-conductive feature of sulfur, "shuttle effect" of polysulfides, and expansion during the charge-discharge process. To address these challenges, it is proposed to design favorable sulfur host materials in electrodes as a promising approach.

Herein, the thesis will focus on searching and designing appropriate host materials to fabricate high-performance cathodes, mainly using carbon and titanium-based materials. Carbon-based materials can be easily made, improve the conductivity of the sulfur cathode, and obviate volume expansion. Titanium-based materials have low density and good corrosion resistance, providing convenience for the preparation of light and stable electrode materials. Carbon and titanium-based materials are expected to collaborate, achieving a synergistic effect to improve the batteries performance intensively.

The project starts to investigate simple purchased materials, then modified as necessary. Firstly, TiC, TiO<sub>2</sub> and SWCNT were purchased, and simply mixed with

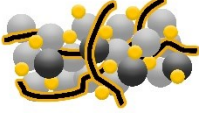

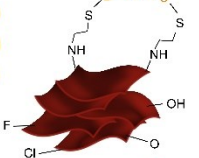

sulfur at the beginning. It is found that through different combination and modification, the capacity and cycling performance of electrodes can be improved significantly. TiC is the simplest carbon titanium compounds with high conductivity. TiO<sub>2</sub> is one of the metal oxides with strong polysulfides adsorption. SWCNT is known to overcome the volume expansion of sulfur with excellent electrical conductivity, but it is too expensive. These three carbon and titanium-based materials have completely different characteristics, therefore, careful designing the composite of the electrodes is needed to guide the cost control and commercial sense. Our results reveal that TiC-TiO<sub>2</sub>/SWCNT/S composite achieves both excellent conductivity and polysulfides adsorption. In particular, 1D SWCNT plays a significant role in connecting different materials to form a conductive network, making the structure more robust. As a result, TiC-TiO<sub>2</sub>/SWCNT/S delivers 1324.2 mAh·g<sup>-1</sup> first specific capacity and remains at 61.7 % capacity after 100 cycles, as well as 711.2 mAh·g<sup>-1</sup> at 4 C large current density.

Chapter 4 turns to investigate a newly-discovered 2D titanium-based layered material, Ti<sub>3</sub>C<sub>2</sub>T<sub>x</sub> MXene and a 3D MXene-carbon nanocage-sulfur composite (MXene/CNC/S) designed for Li-S batteries. This strategy has achieved a high sulfur content of ~80 wt% and a high sulfur loading of ~1.5 mg·cm<sup>-2</sup>. The combination of MXene and CNC presents a synergistic effect of enhancing polysulfides adsorption by MXene and a desirable conductivity from carbon nanocage composite.

Chapter 5 reports a further step to functionalise MXene and its cathodes. Two strategies of sulfhydryl functionalized MXene have been explored successfully via the chemical reaction of cysteamine hydrochloride (CH) or 3-

mercaptopropyltrimethoxysilane (MPTS). It is found that during the cycle process, the produced polysulfides have been chemically instead of physically adsorbed, which can greatly suppress the “shuttle effect” as only low-order polysulfides were generated. Therefore, the S-MXeneSH(CH) 15 cathode possesses a high  $880 \text{ mAh}\cdot\text{g}^{-1}$  at the beginning and 81.3 % retention over 500 stable cycles.

**Figure 1.39** compared the cathodes performance and other properties of three different strategies reported in Chapter 3-5. TiC-TiO<sub>2</sub>/S composite acts as a benchmark because it represents the basic carbon and titanium materials and it can be fabricated by a simple method with a mediocre performance. It is clear that the three designed composite cathodes present excellent behaviors during small and large current density cycling, as well as rate performance.

	TiC-TiO <sub>2</sub> /SWCNT/S	MXene/CNC/S	S-MXeneSH	TiC-TiO <sub>2</sub> /S (control group)
<b>Cathode materials</b>				
<b>Cycle capacity</b>	1st(0.1C): 1324 mAh·g <sup>-1</sup> ↑ 500th(1C): 77.7 % retention↑ Rate(4C): 711 mAh·g <sup>-1</sup> ↑↑	1276 mAh·g <sup>-1</sup> ↑ 59.2 % retention 631 mAh·g <sup>-1</sup> ↑	1367 mAh·g <sup>-1</sup> ↑↑ 81.3 % retention↑↑ 668 mAh·g <sup>-1</sup> ↑	1157 mAh·g <sup>-1</sup> 71.1 % retention 155 mAh·g <sup>-1</sup>
<b>Sulfur loading</b>	~0.5 mg·cm <sup>2</sup>	~1.5 mg·cm <sup>2</sup> ↑	~1.5 mg·cm <sup>2</sup> ↑	~0.5 mg·cm <sup>2</sup>
<b>Electrode capacity/energy</b>	0.861 mAh 1.851 mWh	2.546 mAh↑ 5.474 mWh↑	2.727 mAh↑ 5.863 mWh↑	0.752 mAh 1.617 mWh
<b>Material cost</b>	medium	low↑	low↑	medium
<b>Fabrication process</b>	Temperature: medium↑ Energy Consumption: low↑ Reaction: strong acid	high high strong acid	medium↑ low↑ gentle↑	medium↑ low↑ strong acid
<b>Feature</b>	simply mixture	synergistic effect↑	covalent adsorption↑↑	simply mixture

**Figure 1.39** Comparison of different cathodes in several important aspects (one up arrow: slight promotion, two up arrows: large promotion).

However, other considerations should be addressed for practical applications, for example the energy density, ease of fabrication, energy consumption and safety, with more commercial value close to society etc. Through the synergistic effect between MXene and CNC, MXene/CNC/S achieves a slightly low specific capacity than TiC-TiO<sub>2</sub>/SWCNT/S, but the sulfur loading increases significantly from 0.5 to 1.5 mg·cm<sup>2</sup>, which can greatly elevate the whole electrode capacity and thus energy density of batteries. For the MXene/CNC/S and S-MXeneSH batteries, their energy density is around three times larger than TiC-TiO<sub>2</sub>/SWCNT/S, which has more commercial value.

Another consideration of commercialization is material cost. To this end, raw materials of fabricating MXene/CNC/S and S-MXeneSH are also cheaper than TiC-TiO<sub>2</sub>/SWCNT/S because of the expensive SWCNT. On the other hand, during the fabricating process, MXene/CNC/S involves an annealing process at 800 °C with more energy consumption and higher cost, while TiC-TiO<sub>2</sub>/SWCNT/S and S-MXeneSH are made below 200 °C. Besides, nitric acid is required to oxidize TiC and prepare TiC-TiO<sub>2</sub>/SWCNT/S, while hydrochloric acid is applied to etch impurities of CNC and fabricate MXene/CNC/S. Both strong acids have the safety problems for large-scaled production. As a consequence, the strategy of modified S-MXeneSH stands out if pristine MXene is readily available. Moreover, the covalent bonding occurring at the S-MXeneSH reduces active material loss and capacity fading, which is very different from other strategies with traditional physical adsorption. As a result, the retention rate has been significantly improved, demonstrating a promising approach to commercialized ternary lithium batteries or even lithium iron phosphate batteries.

## 1.5 References

- [1] S. Wu, R. Xu, M. Lu, R. Ge, J. Iocozzia, C. Han, B. Jiang, and Z. Lin, Graphene-Containing Nanomaterials for Lithium-Ion Batteries, *Advanced Energy Materials*, 5 (2015) 1500400.
- [2] R. Jasinski, *High-Energy Batteries*, New York: Plenum Press, (1967).
- [3] F.R. Gamble, J.H. Osiecki, M. Cais, R. Pisharody, F.J. DiSalvo, and T.H. Geballe, Intercalation Complexes of Lewis Bases and Layered Sulfides: A Large Class of New Superconductors, *Science*, 174 (1971) 493-497.
- [4] T.H. Kim, J.S. Park, S.K. Chang, S. Choi, J.H. Ryu, and H.K. Song, The Current Move of Lithium Ion Batteries Towards the Next Phase, *Advanced Energy Materials*, 2 (2012) 860-872.
- [5] J. Broadhead and A. Butherus, Rechargeable nonaqueous battery, United States Patent Application, (1974).
- [6] V. Etacheri, R. Marom, R. Elazari, G. Salitra, and D. Aurbach, Challenges in the development of advanced Li-ion batteries: a review, *Energy & Environmental Science*, 4 (2011) 3243-3262.
- [7] J.M. Tarascon and M. Armand, Issues and challenges facing rechargeable lithium batteries, *Nature*, 414 (2001) 359-367.
- [8] B. Scrosati and J. Garche, Lithium batteries: Status, prospects and future, *Journal of Power Sources*, 195 (2010) 2419-2430.
- [9] M.S. Whittingham, Electrical Energy Storage and Intercalation Chemistry, *Science*, 192 (1976) 1126-1127.



- [10] P.C.J.K. Mizushima, P.C. Jones, P.J. Wiseman and J.B. Goodenough,  $\text{Li}_x\text{CoO}_2$  ( $0 < x < 1$ ): A new cathode material for batteries of high energy density, *Materials Research Bulletin*, 15 (1980) 783-789.
- [11] T. Kim, W. Song, D.Y. Son, L.K. Ono, and Y. Qi, Lithium-ion batteries: outlook on present, future, and hybridized technologies, *Journal of Materials Chemistry A*, 7 (2019) 2942-2964.
- [12] A. Mendiboure, C. Delmas, and P. Hagemuller, New layered structure obtained by electrochemical deintercalation of the metastable  $\text{LiCoO}_2$  ( $\text{O}_2$ ) variety, 19 (1984) 1383-1392.
- [13] K.M. Shaju, G.V.S. Rao, and B.V.R. Chowdari, Performance of layered  $\text{Li}(\text{Ni}_{1/3}\text{Co}_{1/3}\text{Mn}_{1/3})\text{O}_2$  as cathode for Li-ion batteries, *Electrochimica Acta*, 48 (2002) 145-151.
- [14] C.S. Yoon, K.J. Park, U.H. Kim, K.H. Kang, H.H. Ryu, and Y.K. Sun, High-Energy Ni-Rich  $\text{Li}[\text{Ni}_x\text{Co}_y\text{Mn}_{1-x-y}]\text{O}_2$  Cathodes via Compositional Partitioning for Next-Generation Electric Vehicles, *Chemistry of Materials*, 29 (2017) 10436-10445.
- [15] L. Laffont, C. Delacourt, P. Gibot, M.Y. Wu, P. Kooyman, C. Masquelier, and J. M. Tarascon, Study of the  $\text{LiFePO}_4/\text{FePO}_4$  Two-Phase System by High-Resolution Electron Energy Loss Spectroscopy, *Chemistry of Materials*, 18 (2006) 5520-5529.
- [16] M. Hagen, D. Hanselmann, K. Ahlbrecht, R. Maça, D. Gerber, and J. Tübke, Lithium-Sulfur Cells: The Gap between the State-of-the-Art and the Requirements for High Energy Battery Cells, *Advanced Energy Materials*, 5 (2015) 1401986.
- [17] J.B. Goodenough and K.S. Park, The Li-ion rechargeable battery: a perspective,

Journal of the American Chemical Society, 135 (2013) 1167-1176.

[18] Z.W. Seh, Y. Sun, Q. Zhang, and Y. Cui, Designing high-energy lithium-sulfur batteries, *Chemical Society reviews*, 45 (2016) 5605-5634.

[19] S.S. Zhang, Liquid electrolyte lithium/sulfur battery: Fundamental chemistry, problems, and solutions, *Journal of Power Sources*, 231 (2013) 153-162.

[20] U.J. Herbert D, Electric dry cells and storage batteries, US Patent A, 3043896 (1962).

[21] G. Babu, K. Ababtain, K.Y. Ng, and L.M. Arava, Electrocatalysis of lithium polysulfides: current collectors as electrodes in Li/S battery configuration, *Scientific reports*, 5 (2015) 8763.

[22] S. Evers and L.F. Nazar, New approaches for high energy density lithium-sulfur battery cathodes, *Accounts of chemical research*, 46(5) (2012) 1135-1143.

[23] J.R. Birk and R.K. Steunenberg, *Chemical Investigations of Lithium-Sulfur Cells*, 1975, 186-202.

[24] A. Manthiram, Y. Fu, S.H. Chung, C. Zu, and Y.S. Su, Rechargeable lithium-sulfur batteries, *Chemical reviews*, 114 (2014) 11751-11787.

[25] Y. Yang, G. Zheng, and Y. Cui, Nanostructured sulfur cathodes, *Chemical Society reviews*, 42 (2013) 3018-3032.

[26] J. Conder and C. Villevieille, Is the Li-S battery an everlasting challenge for operando techniques?, *Current Opinion in Electrochemistry*, 9 (2018) 33-40.

[27] C. Deng, Z. Wang, L. Feng, S. Wang, and J. Yu, Electrocatalysis of sulfur and polysulfides in Li-S batteries, *Journal of Materials Chemistry A*, 8 (2020) 19704-19728.

- [28] D.W. Wang, Q. Zeng, G. Zhou, L. Yin, F. Li, H.M. Cheng, I. R. Gentle, and G.Q.M. Lu, Carbon-sulfur composites for Li-S batteries: status and prospects, *Journal of Materials Chemistry A*, 1 (2013) 9382-9394.
- [29] Q. Lin, L. Huang, W. Liu, Z. Li, R. Fang, D.W. Wang, Q.H. Yang, and W. Lv, High-performance lithium-sulfur batteries enabled by regulating Li<sub>2</sub>S deposition, *Physical chemistry chemical physics : Physical Chemistry Chemical Physics*, 23 (2021) 21385-21398.
- [30] J. He, Y. Chen, P. Li, F. Fu, Z. Wang, and W. Zhang, Three-Dimensional CNT Graphene-Sulfur Hybrid Sponges with High Sulfur Loading as Superior-Capacity Cathode for Lithium-Sulfur Batteries, *Journal of Materials Chemistry A*, 3 (2015) 18605-18610.
- [31] N. Li, Y. Xie, S. Peng, X. Xiong, and K. Han, Ultra-lightweight Ti<sub>3</sub>C<sub>2</sub>T<sub>x</sub> MXene modified separator for Li-S batteries: Thickness regulation enabled polysulfide inhibition and lithium ion transportation, *Journal of Energy Chemistry*, 42 (2020) 116-125.
- [32] H.K. Seo, Y. Hwa, J.H. Chang, J.Y. Park, J.S. Lee, J. Park, E.J. Cairns, and J. M. Yuk, Direct Visualization of Lithium Polysulfides and Their Suppression in Liquid Electrolyte, *Nano letters*, 20 (2020) 2080-2086.
- [33] Z. Ma, F. Jing, Y. Fan, J. Li, Y. Zhao, and G. Shao, High electrical conductivity of 3D mesoporous carbon nanocage as an efficient polysulfide buffer layer for high sulfur utilization in lithium-sulfur batteries, *Journal of Alloys and Compounds*, 789 (2019) 71-79.

- [34] S.D. Ware, C.J. Hansen, J.P. Jones, J. Hennessy, R.V. Bugga, and K.A. See, Fluoride in the SEI Stabilizes the Li Metal Interface in Li-S Batteries with Solvate Electrolytes, *ACS applied materials & interfaces*, 13 (2021) 18865-18875.
- [35] W. Li, H. Yao, K. Yan, G. Zheng, Z. Liang, Y.M. Chiang, and Y. Cui, The synergetic effect of lithium polysulfide and lithium nitrate to prevent lithium dendrite growth, *Nature communications*, 6 (2015) 7436.
- [36] S.H. Chung and A. Manthiram, Current Status and Future Prospects of Metal-Sulfur Batteries, *Advanced materials*, 31 (2019) 1901125.
- [37] H. Hong, N.A.R.C. Mohamad, K. Chae, F.M. Mota, and D.H. Kim, The lithium metal anode in Li-S batteries: challenges and recent progress, *Journal of Materials Chemistry A*, 9 (2021) 10012-10038.
- [38] C.P. Yang, Y.X. Yin, S.F. Zhang, N.W. Li, and Y.G. Guo, Accommodating lithium into 3D current collectors with a submicron skeleton towards long-life lithium metal anodes, *Nature communications*, 6 (2015) 8058.
- [39] Z.A. Ghazi, Z. Sun, C. Sun, F. Qi, B. An, F. Li, and H.M. Cheng, Key Aspects of Lithium Metal Anodes for Lithium Metal Batteries, *Small*, 15 (2019) 1900687.
- [40] E. Cha, M.D. Patel, J. Park, J. Hwang, V. Prasad, K. Cho, and W. Choi, 2D MoS<sub>2</sub> as an efficient protective layer for lithium metal anodes in high-performance Li-S batteries, *Nature Nanotechnology*, 13 (2018) 337-344.
- [41] S. Zhang, K. Ueno, K. Dokko, and M. Watanabe, Recent Advances in Electrolytes for Lithium-Sulfur Batteries, *Advanced Energy Materials*, 5 (2015) 1500117.
- [42] D.R. Chang, S.H. Lee, S.W. Kim, and H.T. Kim, Binary electrolyte based on

tetra(ethylene glycol) dimethyl ether and 1,3-dioxolane for lithium-sulfur battery, *Journal of Power Sources* 112 (2002) 452–460.

[43] C. Barchasz, J.C. Leprêtre, S. Patoux, and F. Alloin, Electrochemical properties of ether-based electrolytes for lithium/sulfur rechargeable batteries, *Electrochimica Acta*, 89 (2013) 737-743.

[44] M. Galiński, A. Lewandowski, and I. Stępnia, Ionic liquids as electrolytes, *Electrochimica Acta*, 51 (2006) 5567-5580.

[45] S.S. Zhang, Role of  $\text{LiNO}_3$  in rechargeable lithium/sulfur battery, *Electrochimica Acta*, 70 (2012) 344-348.

[46] W. Wang, Y. Wang, Y. Huang, C. Huang, Z. Yu, H. Zhang, A. Wang, and K. Yuan, The electrochemical performance of lithium-sulfur batteries with  $\text{LiClO}_4$  DOL/DME electrolyte, *Journal of Applied Electrochemistry*, 40 (2009) 321-325.

[47] J.W. Park, K. Ueno, N. Tachikawa, K. Dokko, and M. Watanabe, Ionic Liquid Electrolytes for Lithium-Sulfur Batteries, *The Journal of Physical Chemistry C*, 117 (2013) 20531-20541.

[48] J. Scheers, S. Fantini, and P. Johansson, A review of electrolytes for lithium-sulphur batteries, *Journal of Power Sources*, 255 (2014) 204-218.

[49] J. Wang, S.Y. Chew, Z.W. Zhao, S. Ashraf, D. Wexler, J. Chen, S.H. Ng, S.L. Chou, and H.K. Liu, Sulfur-mesoporous carbon composites in conjunction with a novel ionic liquid electrolyte for lithium rechargeable batteries, *Carbon*, 46 (2008) 229-235.

[50] E. Umeshbabu, B. Zheng, and Y. Yang, Recent Progress in All-Solid-State Lithium-Sulfur Batteries Using High Li-Ion Conductive Solid Electrolytes,

Electrochemical Energy Reviews, 2 (2019) 199-230.

[51] R.C. Xu, X.H. Xia, S.H. Li, S.Z. Zhang, X.L. Wang, and J.P. Tu, All-solid-state lithium-sulfur batteries based on a newly designed  $\text{Li}_7\text{P}_{2.9}\text{Mn}_{0.1}\text{S}_{10.7}\text{I}_{0.3}$  superionic conductor, *Journal of Materials Chemistry A*, 5 (2017) 6310-6317.

[52] X. Ji, K.T. Lee, and L.F. Nazar, A highly ordered nanostructured carbon-sulphur cathode for lithium-sulphur batteries, *Nature materials*, 8 (2009) 500-506.

[53] J.G. Wang, K. Xie, and B. Wei, Advanced engineering of nanostructured carbons for lithium-sulfur batteries, *Nano Energy*, 15 (2015) 413-444.

[54] Y. He, Z. Chang, S. Wu, and H. Zhou, Effective strategies for long-cycle life lithium-sulfur batteries, *Journal of Materials Chemistry A*, 6 (2018) 6155-6182.

[55] Y. Huang, L. Lin, C. Zhang, L. Liu, Y. Li, Z. Qiao, J. Lin, Q. Wei, L. Wang, Q. Xie, and D.L. Peng, Recent Advances and Strategies toward Polysulfides Shuttle Inhibition for High-Performance Li-S Batteries, *Advanced Science*, 9 (2022) 2106004.

[56] R. Fang, K. Chen, L. Yin, Z. Sun, F. Li, and H.M. Cheng, The Regulating Role of Carbon Nanotubes and Graphene in Lithium-Ion and Lithium-Sulfur Batteries, *Advanced materials*, 31 (2019) 1800863.

[57] R. Carter, L. Oakes, N. Muralidharan, and C.L. Pint, Isothermal Sulfur Condensation into Carbon Scaffolds: Improved Loading, Performance, and Scalability for Lithium-Sulfur Battery Cathodes, *The Journal of Physical Chemistry C*, 121 (2017) 7718-7727.

[58] M.Q. Zhao, Q. Zhang, J.Q. Huang, G.L. Tian, T.C. Chen, W.Z. Qian, and F. Wei, Towards high purity graphene/single-walled carbon nanotube hybrids with improved

- electrochemical capacitive performance, *Carbon*, 54 (2013) 403-411.
- [59] C. Li, X.L. Sui, Z.B. Wang, Q. Wang, and D.M. Gu, 3D N-doped graphene nanomesh foam for long cycle life lithium-sulfur battery, *Chemical Engineering Journal*, 326 (2017) 265-272.
- [60] H. Yan, M. Cheng, and B. Zhong, Y. Chen, Three-dimensional nitrogen-doped graphene/sulfur composite for lithium-sulfur battery, *Ionics*, 22 (2016) 1999-2006.
- [61] J.L. Shi, H.J. Peng, L. Zhu, W. Zhu, and Q. Zhang, Template growth of porous graphene microspheres on layered double oxide catalysts and their applications in lithium-sulfur batteries, *Carbon*, 92 (2015) 96-105.
- [62] Q. Wu, L. Yang, X. Wang, and Z. Hu, Carbon-Based Nanocages: A New Platform for Advanced Energy Storage and Conversion, *Advanced materials*, 32 (2020) 1904177.
- [63] D. Xiao, Q. Li, H. Zhang, Y. Ma, C. Lu, C. Chen, Y. Liu, and S. Yuan, A sulfur host based on cobalt-graphitic carbon nanocages for high performance lithium-sulfur batteries, *Journal of Materials Chemistry A*, 5 (2017) 24901-24908.
- [64] Z. Li, Y. Huang, L. Yuan, Z. Hao, and Y. Huang, Status and prospects in sulfur-carbon composites as cathode materials for rechargeable lithium-sulfur batteries, *Carbon*, 92 (2015) 41-63.
- [65] C. Nan, Z. Lin, H. Liao, M.K. Song, Y. Li, and E.J. Cairns, Durable carbon-coated Li<sub>2</sub>S core-shell spheres for high performance lithium/sulfur cells, *Journal of the American Chemical Society*, 136 (2014) 4659-4663.
- [66] J. Zhang, N. Yang, X. Yang, S. Li, J. Yao, and Y. Cai, Hollow sulfur@graphene oxide core-shell composite for high-performance Li-S batteries, *Journal of Alloys and*

Compounds, 650 (2015) 604-609.

[67] X. Song, T. Gao, S. Wang, Y. Bao, G. Chen, L.X. Ding, H. Wang, Free-standing sulfur host based on titanium-dioxide-modified porous-carbon nanofibers for lithium-sulfur batteries, *Journal of Power Sources*, 356 (2017) 172-180.

[68] J. Zhang, H. Huang, J. Bae, S.H. Chung, W. Zhang, A. Manthiram, and G. Yu, Nanostructured Host Materials for Trapping Sulfur in Rechargeable Li-S Batteries: Structure Design and Interfacial Chemistry, *Small Methods*, 2 (2017).

[69] J. Schuster, G. He, B. Mandlmeier, T. Yim, K.T. Lee, T. Bein, and L.F. Nazar, Spherical ordered mesoporous carbon nanoparticles with high porosity for lithium-sulfur batteries, *Angewandte Chemie*, 51 (2012) 3591-3595.

[70] Y. Hu, W. Chen, T. Lei, B. Zhou, Y. Jiao, Y. Yan, X. Du, J. Huang, C. Wu, X. Wang, Y. Wang, B. Chen, J. Xu, C. Wang, and J. Xiong, Carbon Quantum Dots-Modified Interfacial Interactions and Ion Conductivity for Enhanced High Current Density Performance in Lithium-Sulfur Batteries, *Advanced Energy Materials*, 9 (2019).

[71] H. Chen, C. Wang, W. Dong, W. Lu, Z. Du, and L. Chen, Monodispersed sulfur nanoparticles for lithium-sulfur batteries with theoretical performance, *Nano letters*, 15 (2015) 798-802.

[72] L. Hu, Y. Lu, T. Zhang, T. Huang, Y. Zhu, and Y. Qian, Ultramicroporous Carbon through an Activation-Free Approach for Li-S and Na-S Batteries in Carbonate-Based Electrolyte, *ACS applied materials & interfaces*, 9 (2017) 13813-13818.

[73] M. Hagen, S. Dörfler, H. Althues, J. Tübke, M.J. Hoffmann, S. Kaskel, and K. Pinkwart, Lithium-sulphur batteries - binder free carbon nanotubes electrode examined



with various electrolytes, *Journal of Power Sources*, 213 (2012) 239-248.

[74] Y. Wu, M. Gao, X. Li, Y. Liu, and H. Pan, Preparation of mesohollow and microporous carbon nanofiber and its application in cathode material for lithium-sulfur batteries, *Journal of Alloys and Compounds*, 608 (2014) 220-228.

[75] Z. Yuan, H.J. Peng, J.Q. Huang, X.Y. Liu, D.W. Wang, X.B. Cheng, and Q. Zhang, Hierarchical Free-Standing Carbon-Nanotube Paper Electrodes with Ultrahigh Sulfur-Loading for Lithium-Sulfur Batteries, *Advanced Functional Materials*, 24 (2014) 6105-6112.

[76] B. Ding, C. Yuan, L. Shen, G. Xu, P. Nie, Q. Lai, and X. Zhang, Chemically tailoring the nanostructure of graphenenanosheets to confine sulfur for high-performance lithium-sulfur batteries, *Journal of Materials Chemistry A*, 1 (2013) 1096-1101.

[77] X. Gu, C.J. Tong, C. Lai, J. Qiu, X. Huang, W. Yang, B. Wen, L.M. Liu, Y. Hou, and S. Zhang, A porous nitrogen and phosphorous dual doped graphene blocking layer for high performance Li-S batteries, *Journal of Materials Chemistry A*, 3 (2015) 16670-16678.

[78] S. Luo, M. Yao, S. Lei, P. Yan, X. Wei, X. Wang, L. Liu, and Z. Niu, Freestanding reduced graphene oxide-sulfur composite films for highly stable lithium-sulfur batteries, *Nanoscale*, 9 (2017) 4646-4651.

[79] C. Wang, K. Su, W. Wan, H. Guo, H. Zhou, J. Chen, X. Zhang, and Y. Huang, High sulfur loading composite wrapped by 3D nitrogen-doped graphene as a cathode material for lithium-sulfur batteries, *Journal of Materials Chemistry A*, 2 (2014) 5018-5023.

- [80] R. Razaq, N. Zhang, Y. Xin, Q. Li, J. Wang, and Z. Zhang, Electrochemical conversion of lithium polysulfides by highly dispersed ultrafine Mo<sub>2</sub>C nanoparticles on hollow N-doped carbon flowers for Li-S batteries, *EcoMat*, 2 (2020) e12020.
- [81] D. Su, M. Cortie, and G. Wang, Fabrication of N-doped Graphene-Carbon Nanotube Hybrids from Prussian Blue for Lithium-Sulfur Batteries, *Advanced Energy Materials*, 7 (2017) 1602014.
- [82] F. Zhang, S. Chen, L. Dong, Y. Lei, T. Liu, and Y. Yin, Preparation of superhydrophobic films on titanium as effective corrosion barriers, *Applied Surface Science*, 257 (2011) 2587-2591.
- [83] C. Zha, X. Zhu, J. Deng, Y. Zhou, Y. Li, J. Chen, P. Ding, Y. Hu, Y. Li, and H. Chen, Facet-tailoring five-coordinated Ti sites and structure-optimizing electron transfer in a bifunctional cathode with titanium nitride nanowire array to boost the performance of Li<sub>2</sub>S<sub>6</sub>-based lithium-sulfur batteries, *Energy Storage Materials*, 26 (2020) 40-45.
- [84] Y. Zhang, P. Zhang, S. Zhang, Z. Wang, N. Li, S.R.P. Silva, and G. Shao, TiC nanofiber/vertical graphene 1D/2D heterostructured as active electrocatalyst for advanced Li-S batteries, *InfoMat*, 3 (2021) 790-803.
- [85] Z. Cui, J. Yao, T. Mei, S. Zhou, B. Hou, J. Li, J. Li, J. Wang, J. Qian, and X. Wang, Strong lithium polysulfides chemical trapping of TiC-TiO<sub>2</sub>/S composite for long-cycle lithium-sulfur batteries, *Electrochimica Acta*, 298 (2019) 43-51.
- [86] C. Zhang, Y. Ma, X. Zhang, S. Abdolhosseinzadeh, H. Sheng, W. Lan, A. Pakdel, J. Heier, and F. Nüesch, Two-Dimensional Transition Metal Carbides and Nitrides

(MXenes): Synthesis, Properties, and Electrochemical Energy Storage Applications, *Energy & Environmental Materials*, 3 (2020) 29-55.

[87] C. Zhang, L. Cui, S. Abdolhosseinzadeh, and J. Heier, Two-dimensional MXenes for lithium-sulfur batteries, *InfoMat*, 2 (2020) 613-638.

[88] X. Liang, A. Garsuch, and L.F. Nazar, Sulfur cathodes based on conductive MXene nanosheets for high-performance lithium-sulfur batteries, *Angewandte Chemie*, 127 (2015) 1-6.

[89] X. Zhao, M. Liu, Y. Chen, B. Hou, N. Zhang, B. Chen, N. Yang, K. Chen, J. Li, and L. An, Fabrication of layered  $Ti_3C_2$  with an accordion-like structure as a potential cathode material for high performance lithium-sulfur batteries, *Journal of Materials Chemistry A*, 3 (2015) 7870-7876.

[90] K. Li, M. Liang, H. Wang, X. Wang, Y. Huang, J. Coelho, S. Pinilla, Y. Zhang, F. Qi, V. Nicolosi, and Y. Xu, 3D MXene Architectures for Efficient Energy Storage and Conversion, *Advanced Functional Materials*, 30 (2020) 2000842.

[91] X. Liang, Y. Rangom, C.Y. Kwok, Q. Pang, and L.F. Nazar, Interwoven MXene Nanosheet/Carbon-Nanotube Composites as Li-S Cathode Hosts, *Advanced materials*, 29 (2017).

[92] W. Bao, X. Xie, J. Xu, X. Guo, J. Song, W. Wu, D. Su, and G. Wang, Confined Sulfur in 3D MXene/Reduced Graphene Oxide Hybrid Nanosheets for Lithium-Sulfur Battery, *Chemistry*, 23 (2017) 12613-12619.

[93] Q. Qi, H. Zhang, P. Zhang, Z. Bao, W. Zheng, W. Tian, W. Zhang, M. Zhou, and Z. Sun, Self-assembled sandwich hollow porous carbon sphere @ MXene composites

- as superior LiS battery cathode hosts, *2D Materials*, 7 (2020) 025049.
- [94] W. Bao, L. Liu, C. Wang, S. Choi, D. Wang, and G. Wang, Facile Synthesis of Crumpled Nitrogen-Doped MXene Nanosheets as a New Sulfur Host for Lithium-Sulfur Batteries, *Advanced Energy Materials*, 8 (2018) 1702485.
- [95] Z. Wu, T. Shang, Y. Deng, Y. Tao, and Q.H. Yang, The Assembly of MXenes from 2D to 3D, *Advanced Science*, 7 (2020) 1903077.
- [96] L. Zhang, J. Bi, Z. Zhao, Y. Wang, D. Mu, and B. Wu, Sulfur@Self-assembly 3D MXene hybrid cathode material for lithium-sulfur batteries, *Electrochimica Acta*, 370 (2021) 137759.
- [97] H.J. Peng, G. Zhang, X. Chen, Z.W. Zhang, W.T. Xu, J.Q. Huang, and Q. Zhang, Enhanced Electrochemical Kinetics on Conductive Polar Mediators for Lithium-Sulfur Batteries, *Angewandte Chemie*, 55 (2016) 12990-12995.
- [98] M.S. Song, S.C. Han, H.S. Kim, J.H. Kim, K.T. Kim, Y.M. Kang, H.J. Ahn, S.X. Dou, and J.Y. Lee, Effects of Nanosized Adsorbing Material on Electrochemical Properties of Sulfur Cathodes for Li/S Secondary Batteries, *Journal of The Electrochemical Society*, 151 (2004) A791-A795.
- [99] C. Zha, F. Yang, J. Zhang, T. Zhang, S. Dong, and H. Chen, Promoting polysulfide redox reactions and improving electronic conductivity in lithium-sulfur batteries via hierarchical cathode materials of graphene-wrapped porous TiO<sub>2</sub> microspheres with exposed (001) facets, *Journal of Materials Chemistry A*, 6 (2018) 16574-16582.
- [100] C. Zha, X. Gu, D. Wu, and H. Chen, Interfacial active fluorine site-induced electron transfer on TiO<sub>2</sub> (001) facets to enhance polysulfide redox reactions for better

liquid  $\text{Li}_2\text{S}_6$ -Based lithium-sulfur batteries, *Journal of Materials Chemistry A*, 7 (2019) 6431-6438.

[101] C. Zha, D. Wu, T. Zhang, J. Wu, and H. Chen, A facile and effective sulfur loading method: Direct drop of liquid  $\text{Li}_2\text{S}_8$  on carbon coated  $\text{TiO}_2$  nanowire arrays as cathode towards commercializing lithium-sulfur battery, *Energy Storage Materials*, 17 (2019) 118-125.

[102] M. Yu, J. Ma, H. Song, A. Wang, F. Tian, Y. Wang, H. Qiu, and R. Wang, Atomic layer deposited  $\text{TiO}_2$  on a nitrogen-doped graphene/sulfur electrode for high performance lithium-sulfur batteries, *Energy & Environmental Science*, 9 (2016) 1495-1503.

[103] X. Liang, C.Y. Kwok, F. Lodi-Marzano, Q. Pang, M. Cuisinier, H. Huang, C.J. Hart, D. Houtarde, K. Kaup, H. Sommer, T. Brezesinski, J. Janek, and L.F. Nazar, Tuning Transition Metal Oxide-Sulfur Interactions for Long Life Lithium Sulfur Batteries: The “Goldilocks” Principle, *Advanced Energy Materials*, 6 (2016) 1501636.

[104] X. Ji, S. Evers, R. Black, and L.F. Nazar, Stabilizing lithium-sulphur cathodes using polysulphide reservoirs, *Nature communications*, 2 (2011) 325.

[105] X. Liang, C. Hart, Q. Pang, A. Garsuch, T. Weiss, and L.F. Nazar, A highly efficient polysulfide mediator for lithium-sulfur batteries, *Nature communications*, 6 (2015) 5682.

[106] G. Xu, B. Ding, L. Shen, P. Nie, J. Han, and X. Zhang, Sulfur embedded in metal organic framework-derived hierarchically porous carbon nanoplates for high performance lithium-sulfur battery, *Journal of Materials Chemistry A*, 1 (2013) 4490.

- [107] X.J. Hong, C.L. Song, Y. Yang, H.C. Tan, G.H. Li, Y.P. Cai, and H. Wang, Cerium Based Metal-Organic Frameworks as an Efficient Separator Coating Catalyzing the Conversion of Polysulfides for High Performance Lithium-Sulfur Batteries, *ACS nano*, 13 (2019) 1923-1931.
- [108] P.T. Dirlam, R.S. Glass, K. Char, and J. Pyun, The use of polymers in Li-S batteries: A review, *Journal of Polymer Science Part A: Polymer Chemistry*, 55 (2017) 1635-1668.
- [109] X. Liang, M. Zhang, M.R. Kaiser, X. Gao, K. Konstantinov, R. Tandiono, Z. Wang, H.K. Liu, S.X. Dou, and J. Wang, Split-half-tubular polypyrrole@sulfur@polypyrrole composite with a novel three-layer-3D structure as cathode for lithium/sulfur batteries, *Nano Energy*, 11 (2015) 587-599.

## Chapter 2 : Experimental section

This section introduces the materials' characterization and the battery testing methods used in this thesis. We will briefly overview their working principles and roles in comprehending the prepared materials.

### 2.1 Structure and morphology characterization

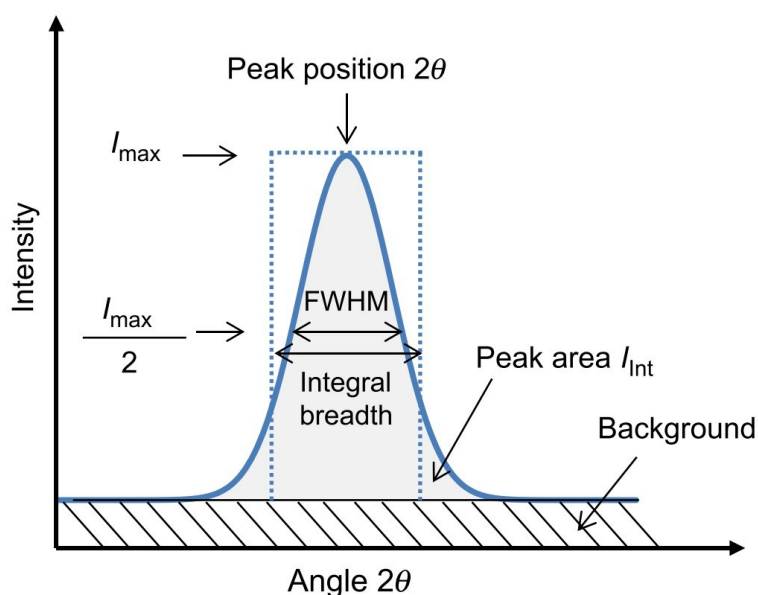
#### 2.1.1 X-ray Diffraction (XRD)

When a monochromatic X-ray is incident on a crystal, since the crystal is composed of cells arranged by atoms regularly, the distance between these atoms is of the same order of magnitude as the wavelength of the incident X-ray, so the X-rays scattered by different atoms interfere with each other, resulting in strong X-ray diffraction in some special directions [1]. The orientation and intensity of the spatial distribution of the diffraction lines are closely related to the crystal structure, which is the basic principle of XRD. A particular number of electrons are typically impacted and run out from the material, accelerated by a strong electric field (> 50 kV), and then crash with a copper plate to create powerful  $K_{\alpha}$  and  $K_{\beta}$  rays. These rays enter the interior and interact with materials with their lattice structure, causing interference between the incident rays and the crystal by altering the incident angle of  $K_{\alpha}$  rays. According to Bragg's law, this incidence angle corresponds to the crystalline structure of the materials' lattice spacing [2].

$$2d\sin\theta = n\lambda \qquad \text{Equation 2.1}$$

The parameter  $\lambda$  represents the wavelength of  $K_{\alpha}$  rays, whereas the lattice spacing between the two atom planes is represented by the parameter  $d$ , which may be utilized

to determine the crystal structure and atom arrangement. Intensity distribution as a function of the  $2\theta$  angle is the typical representation of diffraction data. **Figure 2.1** illustrates the extractable information content. The highest peak  $I_{\max}$  and the integrated intensity  $I_{\text{int}}$  can be determined following background removal. The full width at half maximum (FWHM), which corresponds to the peak breadth at half of the highest intensity, can broadly describe the peak width. Another is integral breadth (IB), referring to the width of a rectangle with the same integrated maximum intensity as the peak under consideration. The distinct peak parameters are utilized, depending on the goal of measurement.



**Figure 2.1** Diffraction peak and information content that can be extracted [2].

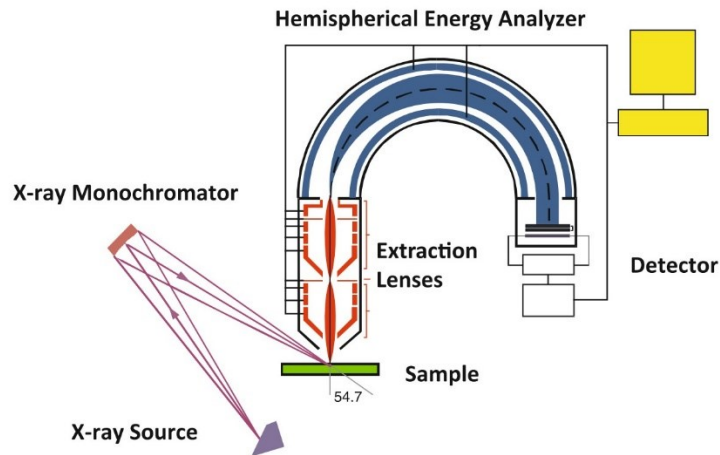
### 2.1.2 X-ray photoelectron spectroscopy (XPS)

The principle of XPS is to radiate the sample with X-rays, causing the inner or valence electrons of atoms or molecules to be excited. Electrons excited by photons are called photoelectrons, and the energy of photoelectrons can be measured. With the kinetic energy of photoelectrons ( $E_b = h\nu$  light energy,  $E_k$  kinetic energy,  $W$  work



function) as the X-axis and the relative intensity (counts/s) as the Y-axis, to make the photoelectron spectra, which can obtain information about the sample (e.g. qualitative and quantitative analysis of elements, chemical bonds and valences, functional groups) [3].

The XPS spectrometer mainly comprises a monoenergetic X-ray source, an electron energy analyzer, and a detector (**Figure 2.2**). The typical X-ray emission from light elements like Mg or Al is practically monoenergetic. Therefore, an X-ray monochromator is not required when they are employed as X-ray source anode materials. First, an electron energy analyzer collects the excited electrons through X-rays. Then, a second plane known as the entrance aperture plane of the analyzer is projected with the picture of the electrons. Finally, an image of the electrons is projected via the energy filter to a third detection plane.



**Figure 2.2** Structure of a typical X-ray photoelectron spectrometer [3].

### 2.1.3 Scanning Electron Microscope (SEM)

Generally, scanning electron microscopy scans the material with a highly concentrated, high-energy electron beam to stimulate certain physical signals, which are collected and amplified to observe surface morphology. These signals include secondary electrons (SE), backscattered electrons (BSE), Auger electrons, and X-ray photons [4].

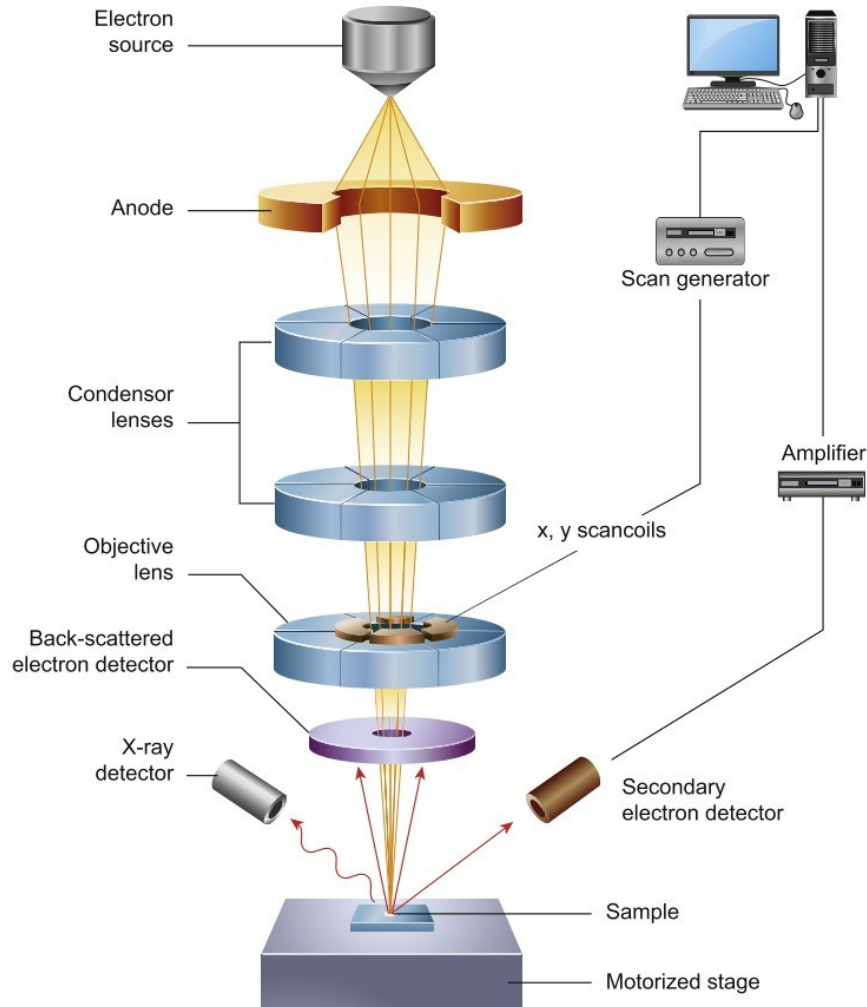
The SE is emitted from a 5-10 nm surface layer with an energy of 0-50 eV. The SE is very sensitive to the surface state and can reflect the surface morphology of the sample effectively. Since SE comes from the surface layer of the sample, the incident electron cannot be scattered many times, so the area of SE generated is mainly related to the size of the incident electron beam spot. The smaller the beam spot, the smaller the area of SE production, so the spatial resolution of SE is higher, generally up to 3-6 nm, even 0.4-2 nm when using a field-emission gun. Therefore, SE is mainly used for morphological observation.

BSE is the large angle scattered electron formed by the incident electron scattered

by the nucleus Rutherford scattering in the sample. Generally, the electron is emitted from the sample at a depth of 0.1-1  $\mu\text{m}$ , and its energy is close to that of the incident electron. As incident electrons enter the sample deeper and have been scattered, BSE comes from a larger region than the secondary electrons, so the resolution of BSE is low, generally 50-200nm, 6nm when using a field-emission gun, which can characterize the sample from the deep surface.

Auger electrons are emitted from the thickness of several atomic layers on the sample surface (about 1nm), and their energy is generally 1000 eV. Auger electrons are often used in surface composition analysis because they can give information about the surface of materials. The equipment for analysis using Auger electrons is called an Auger electrons spectrometer (AES).

When the inner electrons of the sample atom are excited or ionized by the incident electrons, a vacancy occurs in the inner electrons, so the atoms are in a state of high-energy excitation. In this case, the outer electrons transition to the inner layer to fill the vacancy, thus emitting X-ray photons with a certain characteristic energy. An energy dispersive spectrometer (EDS) uses this characteristic energy to analyze the composition of elements in the region [5].

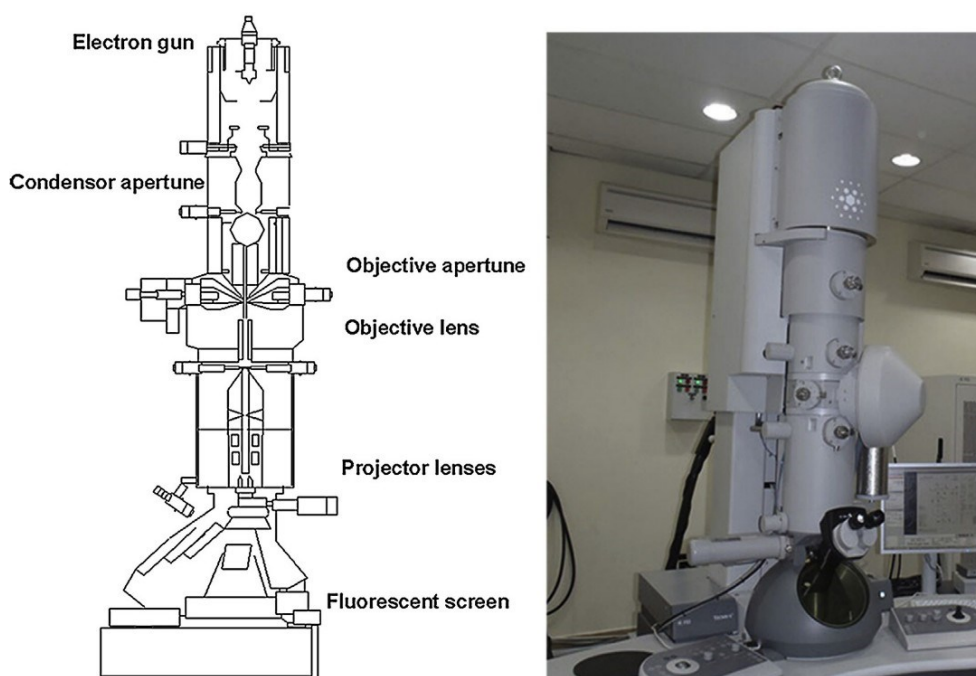


**Figure 2.3** Equipment structure with the main parts of an SEM microscope [5].

### 2.1.4 Transmission Electron Microscopy (TEM)

TEM can observe fine structures smaller than  $0.2 \mu\text{m}$  that cannot be seen under an optical microscope. These structures are called submicron structures or ultrastructures. In 1932, Ruska invented TEM using an electron beam by the high voltage and highly focused condenser as a light source. The wavelength of the electron beam is much shorter than that of visible light and ultraviolet light, and the wavelength of the electron beam is inversely proportional to the square root of the voltage of the transmitting electron beam, meaning the shorter its wavelength generated by the higher the voltage. Its light path resembles optical microscopy, and the appearance is displayed in **Figure**

2.4. The beam will pass through the sample, enter the objective lens, and then be magnified and projected through the lens. On the screen, the magnified image will be gathered. The sample should have a thickness of less than 200 nm since the penetrability of the electron beam is significantly lower than that of X-rays. When electrons pass through a sample, they carry the inherent structural information of the sample and project it onto a screen as pictures or a diffraction spectrum, which has a resolution of 0.2 nm [6].

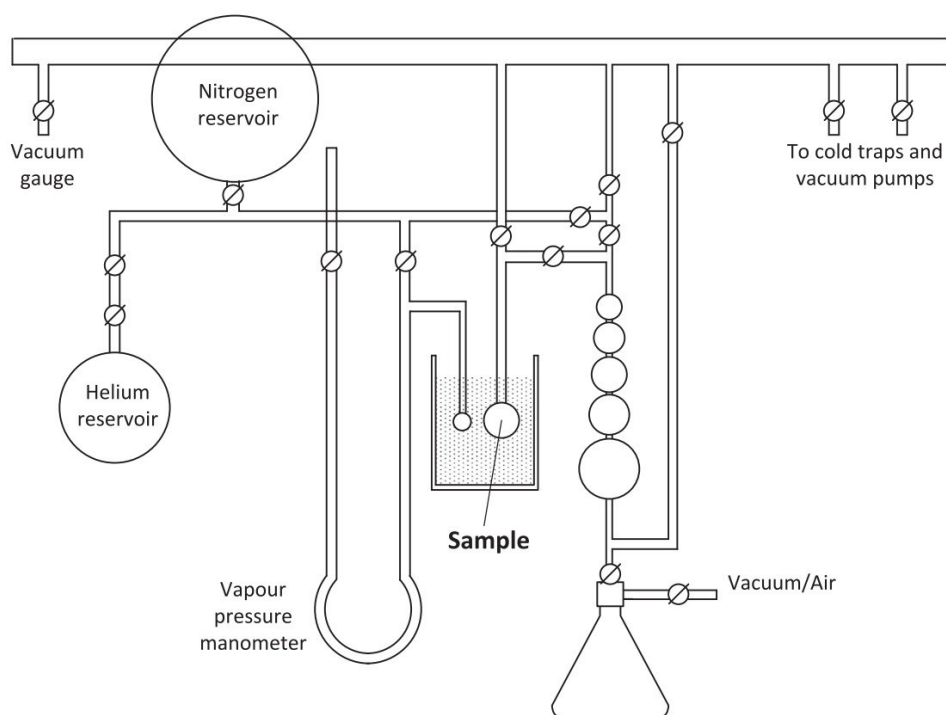


**Figure 2.4** Structure and photograph of TEM [6].

### 2.1.5 Brunauer-Emmett-Teller (BET)

The BET method is based on the principle that physical adsorption occurs on the surface of a substance at low temperatures and is currently recognized as the standard method for measuring the specific surface of a solid. The specific surface determined by the BET method uses nitrogen as an adsorbent and helium or hydrogen as a carrier gas. The two gases are mixed at a constant ratio to reach the specified relative pressure

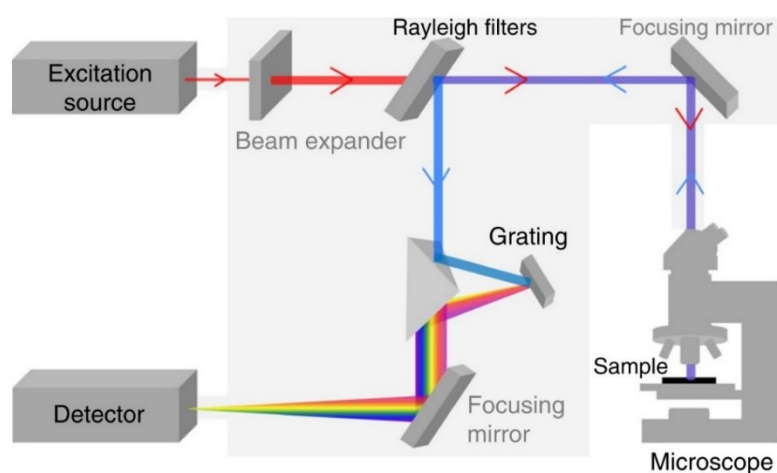
and then flow through solid materials. When the sample tube is put into liquid nitrogen to stabilize temperature, the sample will physically adsorb nitrogen in the gas mixture, while the carrier gas will not be adsorbed. The adsorption peak appears on the screen. When the liquid nitrogen is removed, the sample tube is brought back to room temperature, and the adsorbed nitrogen is desorbed and appears at the desorption peak [7]. Finally, a known volume of pure nitrogen is injected into the mixture to obtain a correction peak. According to the peak area of the correction peak and desorption peak, the adsorption capacity of the sample under this relative pressure can be calculated. By changing the mixture ratio of nitrogen and carrier gas, the adsorption capacity of nitrogen under relative pressure can be measured, and the specific surface can be calculated according to the BET formula. **Figure 2.5** is a volumetric method apparatus for the BET test.



**Figure 2.5** Structure of the volumetric method equipment of BET [7].

## 2.1.6 Raman Spectroscopy

When a photon from incident light impacts a molecule and produces a scattered photon, a method called Raman spectroscopy is used to measure the frequency shift of the inelastically scattered light from the sample [8]. The resulting scattered light may have a frequency that is lower than the original photon, in which case it is referred to as Stokes-Raman scattering. When the frequency is higher, it is called anti-Stokes-Raman scattering. In the latter hypothesis, the molecule bonds will provide energy to the photon when it is originally in an excited vibrational state [9]. Typically, Raman works by detecting changes in the energy of the departing photon. The chemical composition affects the dispersed light change in wavelength. **Figure 2.6** depicts a general schematic of a typical Raman system and lists important technical elements.



**Figure 2.6** Demonstration of a typical Raman microscope system [9].

## 2.2 Electrochemical tests

### 2.2.1 Galvanostatic charge and discharge

A galvanostatic charge-discharge measurement was utilized to reflect the cycle performance of the Li-S batteries. The mass of the active material electrode and the

theoretical capacity of the elemental sulfur were used to calculate the tested current value, which was set in each galvanostatic cell during cycling. The formula could be used to compute the theoretical capacity [10].

$$Q_{\text{theoretical}} = nF/(3.6 \times M) \text{ (mAh} \cdot \text{g}^{-1}) \quad \text{Equation 2.2}$$

The  $n$  in this formula is for the number of  $\text{Li}^+$  per unit of sulfur ( $n = 2$  for a one S atom), the  $F$  stands for the Faraday constant ( $96485 \text{ C} \cdot \text{mol}^{-1}$ ), and the  $M$  stands for the relative mass of the S atom ( $M_s = 32 \text{ g} \cdot \text{mol}^{-1}$ ). Consequently, it is possible to calculate that the elemental sulfur has a theoretical specific capacity of  $1675 \text{ mAh} \cdot \text{g}^{-1}$ . The current rate unit used for the thesis is C ( $1675 \text{ mA} \cdot \text{g}^{-1}$  sulfur), meaning the amount of current required to theoretically discharge or charge each gram of sulfur completely in 1 h. For example, a Li-S battery is fully charged or discharged in 10 hours using the 0.1 C current.

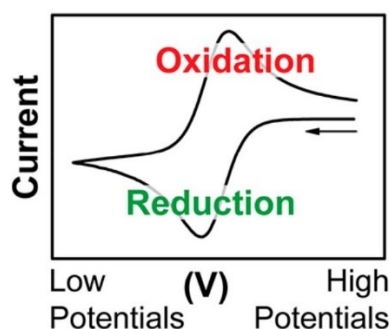
### 2.2.2 Cyclic voltammetry (CV)

The technique frequently used to investigate the redox reaction is cyclic voltammetry. The potential (V), applied to the system, acts as the X-axis parameter in a typical CV profile, while the responding current (I) recorded acts as the Y-axis. The arrow denotes the starting voltage and direction of the initial sweeping.

The cathodic current increases as the working potential of the electrode scan from high to low [11]. Nevertheless, the diffusion layer of the species constantly rises as the concentration of the reactant species adjacent to the electrode progressively decreases over time, in line with the Nernst equation, making it harder for the reactant to reach the electrode surface. As a result, as the scan continues, a diminishing current manifests,



leading to a reduction current peak. Similar events occur when the scan is reversed during oxidation, producing the oxidation peak in **Figure 2.7**.

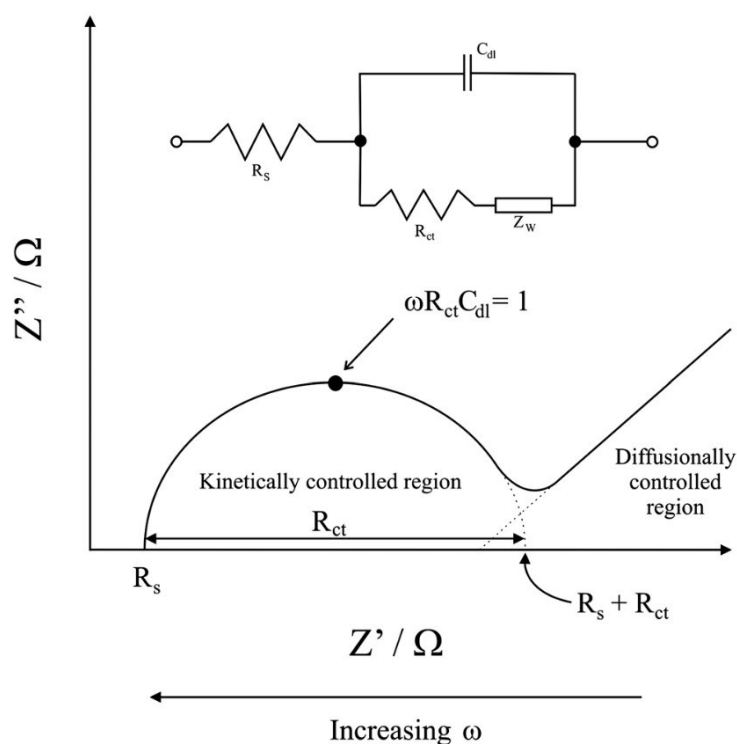


**Figure 2.7** Illustration of the reduction and oxidation peaks in a CV [11].

### 2.2.3 Electrochemical impedance spectroscopy (EIS)

A small amplitude (several to dozens of mV) and low-frequency sinusoidal voltage is superimposed on the external direct current (DC) voltage and used in the electrolytic cell. Then the alternating current (AC) impedance of the polarized electrode in the electrolytic cell is measured so as to determine the electrochemical characteristics of the measured substance in the electrolytic cell. The method is electrochemical impedance spectroscopy, which mainly measures Faraday impedance ( $Z$ ) and its relationship with the electrochemical properties of the measured substance. In this method, the electrochemical process on the polarized electrode corresponds to the equivalent circuit composed of capacitance and impedance. The AC voltage causes an electrochemical reaction on the electrode to produce an AC, which is equal to the AC produced by an equivalent circuit composed of a capacitor and a resistance element. Thus, the electrochemical behavior on the electrode corresponds to the effect of an impedance. Since this impedance is derived from a chemical reaction at the electrode, it is called the Faraday impedance [12].

The similar circuit includes  $R_s$ ,  $R_{ct}$ ,  $C_{dl}$ , and  $Z_w$ , which constitute the simulated circuit system of the working electrode, as represented by a simple equivalent circuit in **Figure 2.8**. Particularly,  $R_s$  refers to solution resistance,  $R_{ct}$  symbolizes the charge transfer resistance,  $C_{dl}$  stands for the double layer charging at the electrode surface, and  $Z_w$  or  $W_o$  is the Warburg impedance [13].



**Figure 2.8** A simple equivalent circuit for electrode [13].

## 2.3 References

- [1] R.E. Dinnebier, and S.J. Billinge, Powder Diffraction: Theory and Practice. Royal society of chemistry, A65 (2008) 51.
- [2] J. Epp, X-ray diffraction (XRD) techniques for materials characterization, Woodhead Publishing, (2016) 81-124.
- [3] R.T. Haasch, X-Ray Photoelectron Spectroscopy (XPS) and Auger Electron Spectroscopy (AES), Practical Materials Characterization, (2014) 93-132.
- [4] K. Akhtar, S.A. Khan, S.B. Khan, and A.M. Asiri, Scanning Electron Microscopy: Principle and Applications in Nanomaterials Characterization, Handbook of materials characterization, (2018) 113-145.
- [5] B.J. Inkson, Scanning electron microscopy (SEM) and transmission electron microscopy (TEM) for materials characterization, Woodhead Publishing, (2016) 17-43.
- [6] C.Y. Tang and Z. Yang, Transmission Electron Microscopy (TEM), (2017) 145-159.
- [7] M. Naderi, Surface Area: Brunauer-Emmett-Teller (BET), (2015) 585-608.
- [8] P.J. Hendra, and P.M Stratton, Laser-Raman spectroscopy, Chemical reviews, 69 (1969) 325-344.
- [9] H.J. Butler, L. Ashton, B. Bird, G. Cinque, K. Curtis, J. Dorney, K. Esmonde-White, N.J. Fullwood, B. Gardner, P.L. Martin-Hirsch, M.J. Walsh, M.R. McAinsh, N. Stone, and F.L. Martin, Using Raman spectroscopy to characterize biological materials, Nature Protocols, 11 (2016) 664-687.
- [10] H. Chen, Study on the  $\text{Li}_{1-x}\text{Ni}_{0.5}\text{Mn}_{1.5}\text{O}_4$  for Lithium Ion Batteries: a First-Principles Theory, International Journal of Electrochemical Science, (2017) 11309-

11315.

[11] N. Elgrishi, K.J. Rountree, B.D. McCarthy, E.S. Rountree, T.T. Eisenhart, and J.L. Dempsey, A Practical Beginner's Guide to Cyclic Voltammetry, *Journal of Chemical Education*, 95 (2017) 197-206.

[12] S. Waluś, C. Barchasz, R. Bouchet, and F. Alloin, Electrochemical impedance spectroscopy study of lithium-sulfur batteries: Useful technique to reveal the Li/S electrochemical mechanism, *Electrochimica Acta*, 359 (2020) 136944.

[13] E.P. Randviir and C.E. Banks, Electrochemical impedance spectroscopy: an overview of bioanalytical applications, *Analytical Methods*, 5 (2013) 1098-1115.

# **Chapter 3 : 1D SWCNT/ TiC-TiO<sub>2</sub>/ sulfur cathode for improving conductivity and overcoming volume expansion of Li-S batteries**

## **3.1 Introduction**

As mentioned in chapter 1, the three main disadvantages of Li-S batteries are the non-conductive feature of sulfur, “shuttle effect” and volume expansion during the charge-discharge process. In order to solve these issues, various methods have been dedicated, and the main focus is to fabricate novel nanostructured composite cathodes. One of the popular choices is carbon material since it exists widely in nature and offers great conductivity, high porosity and surface area. Moreover, carbon has a flexible layered structure, which could wrap small-size active sulfur and effectively reduce the loss of sulfur [1]. Carbon-based materials have become the most promising electrode materials that benefited from a simple preparation process and superior improved capacity performance [2-5]. Another research hotspot is metal oxides that offer abundant polar active sites in favor of the absorption of polysulfides, promoting the Li-S batteries with a stable cycle performance [6-9]. However, most of the metal oxides have poor conductivity and, thus the slow electron transfer speed, which is unfavorable to the utilization of sulfur under the large current density. Hence, a challenge has been to develop a composite that can not only capture polysulfides but also enhance the conductivity of the cathode.

Herein, several different materials are chosen to combine with sulfur to fabricate composite cathodes for improving performance. Carbon-based materials are used for

enhancing conductivity and relieving volume expansion, while metal-based materials are applied for polysulfides adsorption [2, 10, 11]. Firstly, TiC or SWCNT are combined with sulfur to make a highly conductive cathode, and TiO<sub>2</sub> is mixed with sulfur to achieve strong polysulfides adsorption, respectively. Then, a special TiC-TiO<sub>2</sub>/SWCNT/S composite is designed and the 1D SWCNT plays an important role in connecting different materials to form a conductive network, achieving both excellent conductivity and polysulfides adsorption.

The research work was designed and carried out under the supervision of Prof. Li Yang and Prof. Cezhou Zhao. The result shown in this chapter was published on Journal of Alloys and Compounds, 2021. 851: 156793 (DOI: 10.1016/j.jallcom.2020.156793). The manuscript was first drafted by me and corrected by Prof. Li Yang and Prof. Cezhou Zhao. The rest of the authors helped with some supplementary works, including idea guidance, data analysis, and experimental data checking.

## **3.2. Experiment part**

### **3.2.1 Preparation of TiC/S, TiO<sub>2</sub>/S and SWCNT/S composite**

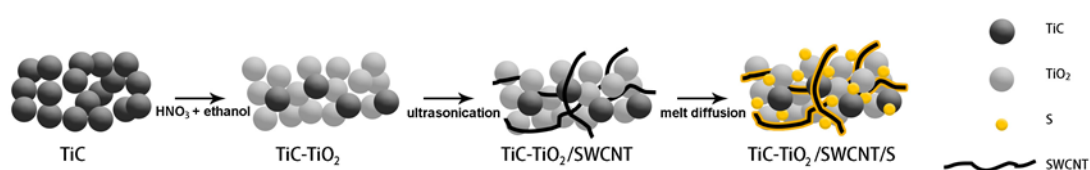
Firstly, 200 mg TiC, TiO<sub>2</sub> or SWCNT were separately mixed with 600 mg sublimed sulfur (1:3 ratio by weight) and under ball-milling for 10 min in order to uniform mixtures. Then, these three mixtures were melted at 155 °C for 10 h in the furnace with the protection of the Ar gas stream. After cooling down to room temperature, the final composites were denoted as TiC/S, TiO<sub>2</sub>/S and SWCNT/S, respectively.

### 3.2.2. Fabrication of TiC-TiO<sub>2</sub>/S and TiC-TiO<sub>2</sub>/SWCNT/S composite

The TiC-TiO<sub>2</sub> composite was synthesized by a simple oxidation reaction. At first, 30 mL nitric acid (HNO<sub>3</sub>, 7 M) and 60 mL ethanol were mixed together and stirred for 5 min. Then, 600 mg TiC was added into the mixed solvent, stirred well and under ultrasonic dispersion for 10 min. Next, the mixture suspension was under magnetically stirred at 60 °C for 12 h. Finally, the suspension was centrifuged, washed with ethanol and Deionized (DI) water for several times. After dried at 80 °C by vacuum drying oven, the TiC-TiO<sub>2</sub> composite was obtained [12]. A half of the composite was prepared for the following sulfur melting, while another half was stored for preparing TiC-TiO<sub>2</sub>/SWCNT/S. For the TiC-TiO<sub>2</sub>/S composites, sulfur loading was also achieved through a melting-diffusion method. At the beginning, sublimed sulfur was mixed into TiC-TiO<sub>2</sub> composite with 3:1 ratio by weight, and then under ball-milling for 10 min in order to mix uniformly and ensure good homogeneity before the process of melting sulfur. The following procedure was applied for melting sulfur in the composites. Firstly, the powder was placed in a porcelain boat and transferred to a quartz tube, then heated at 155 °C for 10 h under the protection of Ar in the furnace. Next, the powder was heated to 200 °C in Ar and kept for 15 min to remove the excess sulfur on the surface. After cooling naturally to room temperature, the resultant composite was denoted as TiC-TiO<sub>2</sub>/S [13].

For TiC-TiO<sub>2</sub>/SWCNT/S composite, 3 wt%, 2 wt% and 1 wt% SWCNT (relative to the mass ratio of TiC-TiO<sub>2</sub>/SWCNT/S) were mixed with TiC-TiO<sub>2</sub> respectively in ethanol via ultrasonic dispersion for 30 min. The suspension was then filtered and dried

to obtain the TiC-TiO<sub>2</sub>/SWCNT composite. These prepared composites and sublimed sulfur (TiC-TiO<sub>2</sub> : S = 1:3 ratio by weight) were placed under the same ball-milling mentioned above. The melting sulfur procedure was the same as TiC-TiO<sub>2</sub>/S, except the addition of SWCNT. The final products were named as TiC-TiO<sub>2</sub>/SWCNT/S 3, TiC-TiO<sub>2</sub>/SWCNT/S 2 and TiC-TiO<sub>2</sub>/SWCNT/S 1, respectively. The schematic of the procedure for preparing TiC-TiO<sub>2</sub>/SWCNT/S composite is shown in **Figure 3.1**.



**Figure 3.1** Schematic diagram for preparing TiC-TiO<sub>2</sub>/SWCNT/S composite.

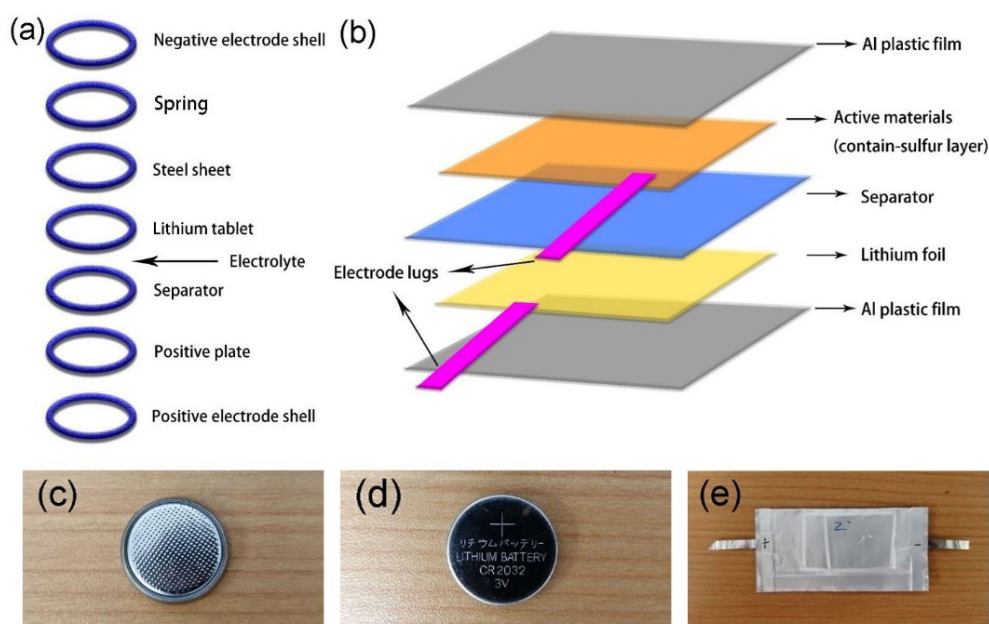
### 3.2.3. Electrode preparation, fabrication of coin cell and pouch cell

To prepare the working electrode, a slurry was obtained by mixing and stirring the composite, conductive agent and binder: namely as-prepared active material, super P (TIMCAL, Switzerland) and polyvinylidene fluoride (PVDF, ARKEMA, Paris French) with the mass ratio of 8:1:1 in N-methyl-2-pyrrolidone (NMP, Aladdin, Shanghai China), respectively. The slurry was coated to the current collector (aluminium foil) by using a coating machine and vacuum dried for 12 h at 60 °C. The electrolyte amount is around 40 μl/mg sulfur, and the sulfur loading ranges from 0.5-1 mg/cm<sup>2</sup>.

Before assembly, the positive shell, negative shell, steel sheet, separator, and shrapnel spring were washed with ethanol and then vacuumed at 50 °C for 2 h. CR2032-type coin cells were manually assembled in a glove box (Vigor Sci-Lab) under Ar-filled atmosphere (water and oxygen content are less than 1 ppm) and used for electrochemical characterization. Prepared electrodes were used as the cathode (13 mm)



and lithium tablets were used as the anode (14 mm), which were separated by the Celgard 2400 separator (18 mm), and the coin cell assembly order was shown in **Figure 3.2a**. The electrolyte was lithium bis (trifluoromethanesulfonyl) imide (1.0 M) dissolved in a mixture of a lithium salt (LiTFSI) in dioxolane (DOL) and dimethoxyethane (DME) (1:1 by volume) with a 1.0 wt% LiNO<sub>3</sub> additive. Pouch cells were fabricated as shown in **Figure 3.2b**. Its surface area of it is about 10.0 cm<sup>2</sup> (2.5 × 4.0 cm), the electrolyte is added with 25 μl/mg sulfur and the sulfur loading is about 1 mg/cm<sup>2</sup>. The separator and electrolyte were sandwiched between the electrodes. In addition, two pieces of electrode lugs were used as current collectors. All of them were sealed in Al-plastic films by a vacuum packing machine.



**Figure 3.2** Schematic of assembling for (a) coin cell and (b) pouch cell; Optical image of (c-d) coin cell and (e) pouch cell.

### 3.2.4. Materials characterization and electrochemical measurements

The microstructure and morphology of different composites were characterized by

scanning electron microscope (SEM), field emission scanning electron microscope (FE-SEM), scanning transmission electron microscopy (STEM) and selected area electron diffraction (SAED). The SEM was investigated by JEOL JSM-6510. The FE-SEM was performed with S-4700 type manufactured by HITACHI. The TEM was carried out by FEI Tecnai G2 F20 with STEM and SAED function. Powder X-ray diffraction (XRD) patterns of these composites were collected on an X-ray diffractometer (BRUKER D8 ADVANCE) from 10 ° to 80 ° with Cu K $\alpha$  radiation. Raman spectroscopy was performed on a HORIBA XploRA system with a 532 nm laser. Thermogravimetric analysis (TGA, NETZSCH STA 449 F3) was performed from 28-500 °C at a heating rate of 10 °C per minute in N<sub>2</sub> atmosphere to determine the content of elemental sulfur. X-ray photoelectron spectroscopy (XPS, ESCALAB 250Xi, Thermo scientific) was used to characterize surface functional groups and chemical bonding states. The specific surface area and the pore size distribution of the product were tested by the Brunauer-Emmett-Teller (BET; 3H-2000PS2) through recording N<sub>2</sub> adsorption-desorption isotherms at 77.3 K.

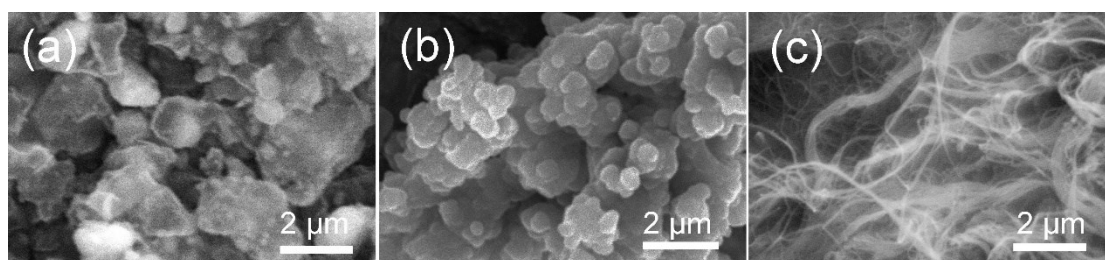
For electrochemical tests, galvanostatic charge/discharge tests were performed in the potential range of 1.7-2.8 V at 22 °C by using a Neware CT-4008 battery-testing instrument. Cyclic voltammetry (CV) was conducted at a scan rate of 0.1 mV·s<sup>-1</sup> in a voltage range of 1.7-2.8 V, and electrochemical impedance spectroscopy (EIS) was used in the frequency ranging from 5 mHz to 100 kHz with Autolab PGSTAT302N electrochemical workstation.

### 3.3 Results and discussion

#### 3.3.1 Comparison of TiC/S, TiO<sub>2</sub>/S and SWCNT/S composites

Since Li-S batteries have three main drawbacks of volume expansion, insulated sulfur and “shuttle effect”, choosing suitable host materials for the sulfur cathode is difficult and necessary to solve these issues and obtain high performance. Hence, high-conductive TiC and SWCNT are considered to improve the conductivity while TiO<sub>2</sub> is applied for polysulfides adsorption. In order to analyze the mechanism of these improvements clearly, different host materials are mixed with sulfur separately at first.

The rough morphology of three simple composites is depicted in **Figure 3.3**. **Figure 3.3a** shows an irregular bulk shape of TiC/S because sulfur melting is based on the sharp and irregular purchased TiC particles (**Figure 3.7a**). Meanwhile, TiO<sub>2</sub>/S presents a sphere structure in **Figure 3.3b** due to the round particles of the original TiO<sub>2</sub> in **Figure 3.8b**. In **Figure 3.3c**, SWCNT/S owns a totally different feature seems as pristine SWCNT, since sulfur can melt into the micropores in SWCNT via melting infiltrated[14].



**Figure 3.3** SEM images of (a) TiC/S, (b) TiO<sub>2</sub>/S and (c) SWCNT/S.

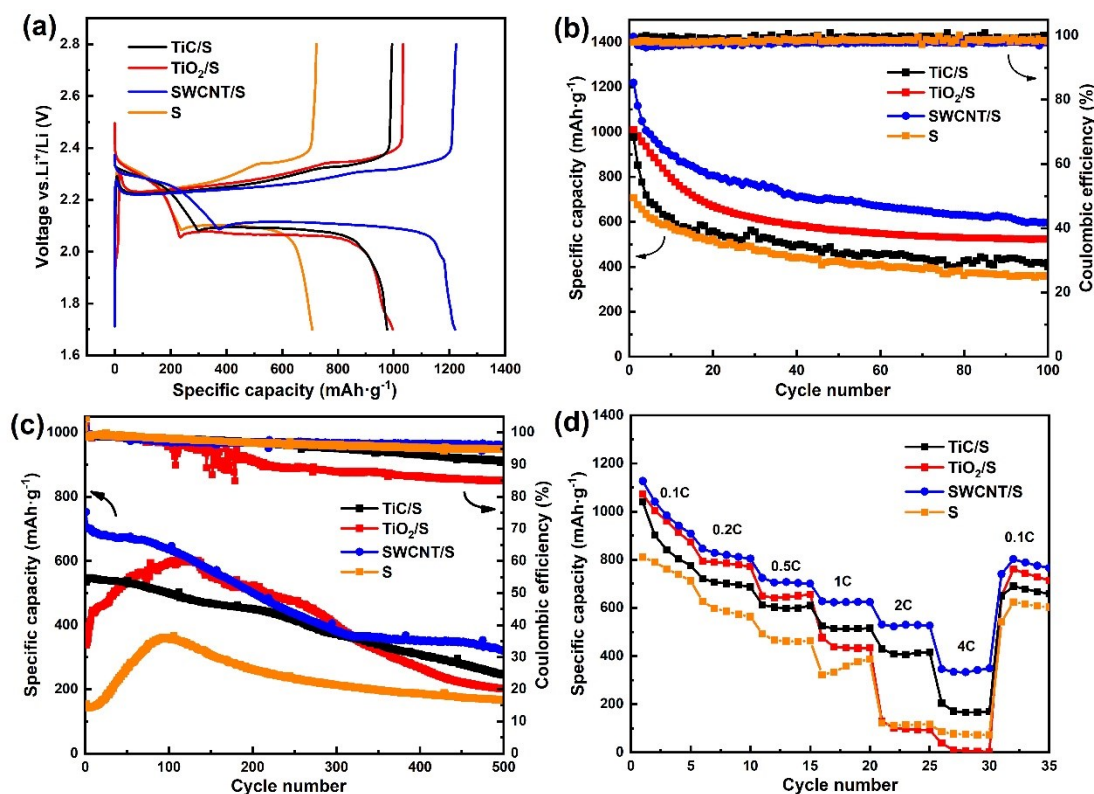
Owing to the great difference of the three composites in morphology, their coin cells display performances with different merits and drawbacks. Considering the insulate feature of active sulfur, we firstly mixed conductive TiC into sulfur to prepare

the TiC/S cathode. In **Figure 3.4a**, compared to the pure sulfur (S) cathode with a specific capacity of only  $707.6 \text{ mAh}\cdot\text{g}^{-1}$  at the initial cycle, TiC/S shows a relatively higher value of  $976.5 \text{ mAh}\cdot\text{g}^{-1}$  owing to enhanced conductivity. TiC and S cathodes present a similar shape of charge-discharge curves with two distinct discharge platforms and two charge platforms. In **Figure 3.4b**, the capacities of these two cathodes also decay at a fast speed, dropping to  $401.7 \text{ mAh}\cdot\text{g}^{-1}$  and  $358.0 \text{ mAh}\cdot\text{g}^{-1}$  after 100 cycles at  $0.1 \text{ C}$ , respectively. Therefore, in order to lessen capacity decay and improve polysulfides adsorption, we chose to fabricate the  $\text{TiO}_2/\text{S}$  composite. It achieves the first capacity of about  $1000 \text{ mAh}\cdot\text{g}^{-1}$  with a longer second discharge platform and obtains a satisfactory capacity retention rate (51.8 %) after 100 cycles because metal oxide  $\text{TiO}_2$  owns a strong ability of polysulfides adsorption [15]. Finally, a special porous carbon material SWCNT was used for a similar performance test. The prepared SWCNT/S electrode displays the highest performance of the four electrodes. At the first cycle, it demonstrates the longest charge-discharge platforms with  $1219.6 \text{ mAh}\cdot\text{g}^{-1}$  capacity (up to 72.8 % sulfur utilization, corresponding to  $1675 \text{ mAh}\cdot\text{g}^{-1}$  theoretical specific capacity of sulfur), which may result from the higher conductivity of SWCNT than TiC, and the smaller-sized sulfur particles in the composite (no obvious large particles seen in **Figure 3.3c**). Due to the porous structure of SWCNT, this carbon material also possesses the ability of polysulfides adsorption to some extent. As a result, it still remains at  $595.9 \text{ mAh}\cdot\text{g}^{-1}$  capacity of SWCNT/S when 100 cycles are finished.

For the  $1 \text{ C}$  large current charge-discharge test, four different materials render a slightly different result in **Figure 3.4c**. Due to the high conductivity and sulfur

utilization of the SWCNT/S composite, it achieves the highest capacity of 752.1 mAh·g<sup>-1</sup> at the first cycle at 1 C large current density. The difference is that the TiC/S composite just owns 534.6 mAh·g<sup>-1</sup> initial capacity. Although TiC is also a type of conductive material, its larger particle feature of TiC leads to its larger particle size of TiC/S composite and relatively low sulfur utilization. However, TiO<sub>2</sub>/S cannot release an effective capacity with only 338.4 mAh·g<sup>-1</sup> at the beginning of cycling. It is because TiO<sub>2</sub>/S still has a large particle structure and TiO<sub>2</sub> is a semiconductor, resulting in low conductivity and low sulfur utilization. Interestingly, its capacity gradually increases to around 600 mAh·g<sup>-1</sup> with the full infiltration of the electrolyte during the cycling process. The pure sulfur cathode also presents the same trend as the low conductivity of sulfur. Towards the long cycle performance after 300 times charge-discharge, the relatively stable SWCNT/S remains 320.7 mAh·g<sup>-1</sup> for 500 cycles. Comparatively, TiC/S and TiO<sub>2</sub>/S decay fast to just over 200 mAh·g<sup>-1</sup>. As expected, the pure sulfur cathode displays the lowest performance all the time because of the low sulfur utilization and conductivity.

In terms of rate performance (**Figure 3.4d**), the SWCNT/S composite can obtain first-class behavior, retaining 346.8 mAh·g<sup>-1</sup> at 4 C large current density, because sulfur disperses in a nanoscale in the SWCNT/S composite (seen in **Figure 3.3c**) and it benefits to exert excellent conductivity of SWCNT, but the SWCNT is obviously more expensive than other materials. TiC/S drops to 204.4 mAh·g<sup>-1</sup> at 4 C on account of the underutilized conductivity of TiC. Insulated TiO<sub>2</sub>/S only remains a little capacity below 100 mAh·g<sup>-1</sup> when the current density magnifies to over 2 C.



**Figure 3.4** (a) The first charge-discharge curves, (b) Cycle performance at 0.1 C, (c) Cycle performance at 1 C and (d) Rate performance of four different cathodes for coin cells.

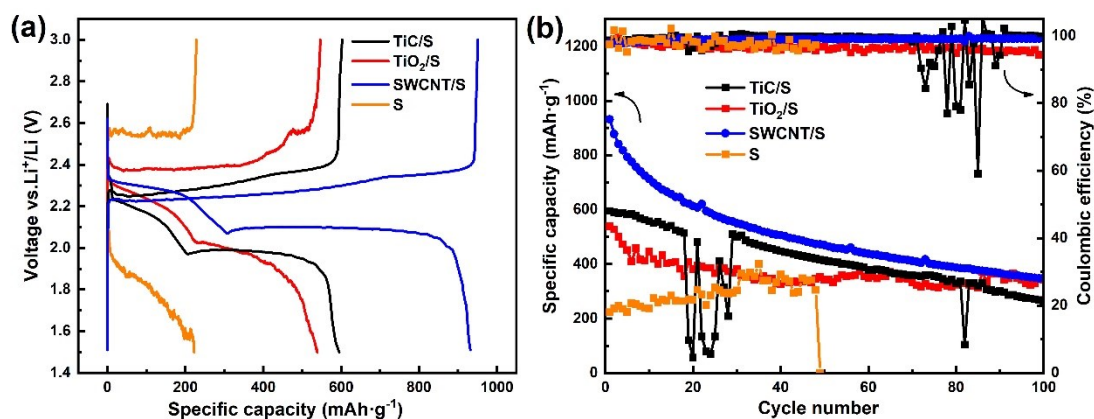
After a clear investigation and distinction of different host materials for coin cells, it turns to the investigation and application of their pouch cells. Compared to the coin cells in general laboratory, pouch cells with active material of large area might show relatively low performance due to non-uniform slurry coating, insufficient electrolyte infiltration or micro-short phenomenon of cells [16, 17]. Through several times experiments, the pouch cells of pure sulfur cathode were assembled successfully, but they demonstrate a terrible charge-discharge curve with no discharge plateaus, unstable voltage, large polarization and only 222.5 mAh·g<sup>-1</sup> initial discharge capacity in **Figure 3.5a**. This may be explained that the transfer speed of electrons is very slow among

non-conductive sulfur in the large electrode. During the discharge process, the reduction reaction is unstable and insufficient, leading to fluctuating voltage and large polarization. At the end of discharge, most active sulfur is underutilized, causing extremely low capacity. The oxidation reaction of the charge process is a similar situation. Adding TiC and TiO<sub>2</sub> into sulfur, these negative phenomena are ameliorated apparently though TiC/S and TiO<sub>2</sub>/S just own 595.0 mAh·g<sup>-1</sup> and 538.4 mAh·g<sup>-1</sup> capacity at the primary cycle, respectively. Owing to a finer melting between SWCNT and sulfur, SWCNT/S has a high usage of sulfur and a high capacity of 931.7 mAh·g<sup>-1</sup> for its pouch cells.

For the cycling performance at 0.1 C in **Figure 3.5b**, the capacity of the pure sulfur cathode shows a gradual increment until the 35th cycles approach to 400 mAh·g<sup>-1</sup> and start to attenuate later. Due to voltage instability and severe short circuits, it breaks down at the 48th cycle. With the addition of TiO<sub>2</sub>, the stability of TiO<sub>2</sub>/S pouch cells is strengthened, displaying 342.9 mAh·g<sup>-1</sup> with a 63.7 % high retention rate after 100 cycles, which profits from strong polysulfides adsorption of TiO<sub>2</sub>. Although TiC/S has a higher initial capacity, it decays faster and appears in some micro-short circuits during charge-discharge, giving rise to huge volatilities of capacity around the 25th and 82th cycles.

In general, coin cells of Li-S batteries are fabricated, achieving high performance relatively easily in the laboratory, but the success in pouch cells is the road to commercialization. Although a large number of academic research at home and abroad have made remarkable achievements in coin cells, research on practical applications of

pouch cells is progressing slowly. Therefore, we should also pay attention to the protection of metal Li, further optimization of host materials, electrolyte types and their amounts to fabricate large-scaled pouch cells with commercial potential.



**Figure 3.5** (a) The first charge-discharge curves, (b) cycle performance at 0.1 C of four different cathodes for pouch cells.

### 3.3.2 Optimized TiC-TiO<sub>2</sub>/S and TiC-TiO<sub>2</sub>/SWCNT/S composites

We explored three different host materials of sulfur for Li-S batteries and compared their different nature for improving performance in the last part. However, the single purchased material as the sulfur host exists defects, and it enhances the performance fairly limited. In brief, TiC just helps to increase conductivity and elevate capacity in earlier cycles, while it cannot reduce the loss of polysulfides. The TiO<sub>2</sub> is an opposed situation. Although SWCNT contributes to both high conductivity and polysulfides adsorption, the exorbitant price limits its application. Therefore, developing their strength together may be a feasible way to avoid evident defects, and to enhance the whole performance.

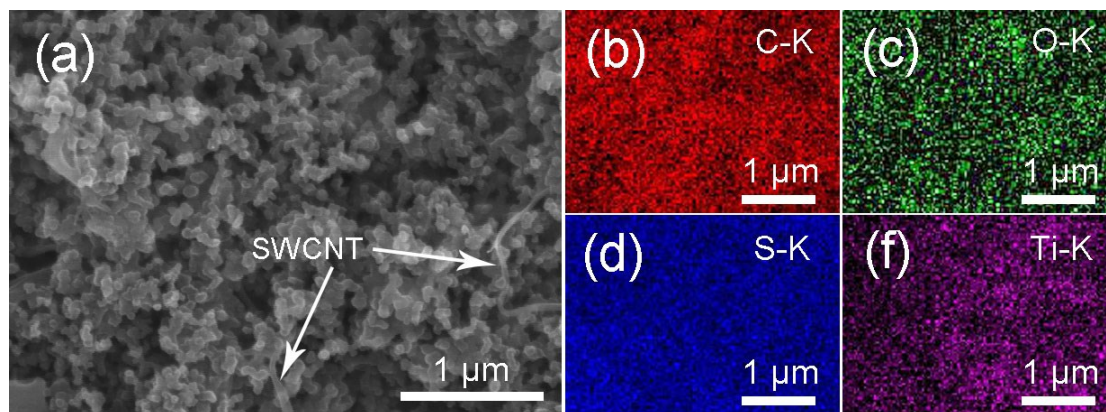
In this part, a TiC-TiO<sub>2</sub>/S composite was fabricated at first to achieve relatively high comprehensive performance. Then, a small amount of SWCNT was mixed into it



to form the TiC-TiO<sub>2</sub>/SWCNT/S composites to further improve the performance to a great extent. We demonstrated a facile process to fabricate the titanium carbide - titanium dioxide/single-walled carbon nanotube/sulfur composite (TiC-TiO<sub>2</sub>/SWCNT/S) to address this challenge. At the beginning, a simple oxidation reaction was carried out for turning TiC to TiC-TiO<sub>2</sub> composite. Then, SWCNT was mixed with TiC-TiO<sub>2</sub> through an ultrasonic dispersion technique to form the TiC-TiO<sub>2</sub>/SWCNT composite. Finally, sulfur was deposited on the TiC-TiO<sub>2</sub>/SWCNT composite by a melting-diffusion method and the final composite TiC-TiO<sub>2</sub>/SWCNT/S was produced. Compared with previous work [13, 15], TiC-TiO<sub>2</sub>/SWCNT/S presents a higher capacity in large current density (850.7 mAh·g<sup>-1</sup> at 1 C for the first cycle) and has a better rate performance (711.2 mAh·g<sup>-1</sup> at 4 C) with improved conductivity. Another attractive feature is less conductive agent (super p) used during the slurry preparation process compared to previous study [13, 15]. We improved the conductivity by modifying the composite materials with less conductive agent, namely the mass ratio of the composite: conductive agent: binder is 8:1:1 in keeping with our last part rather than the previous reported 7:2:1 [13, 15]. This strategy is more cost effective and excellent performance with application potential achieved by increasing the energy density for the whole battery.

To investigate the microstructures and morphologies of the modified cathodes, SEM and TEM images of different materials are conducted. **Figure 3.6a** presents the low magnification SEM image of TiC-TiO<sub>2</sub>/SWCNT/S 2 composite, which offers a large field of view of this composite. The corresponding EDS elemental mapping

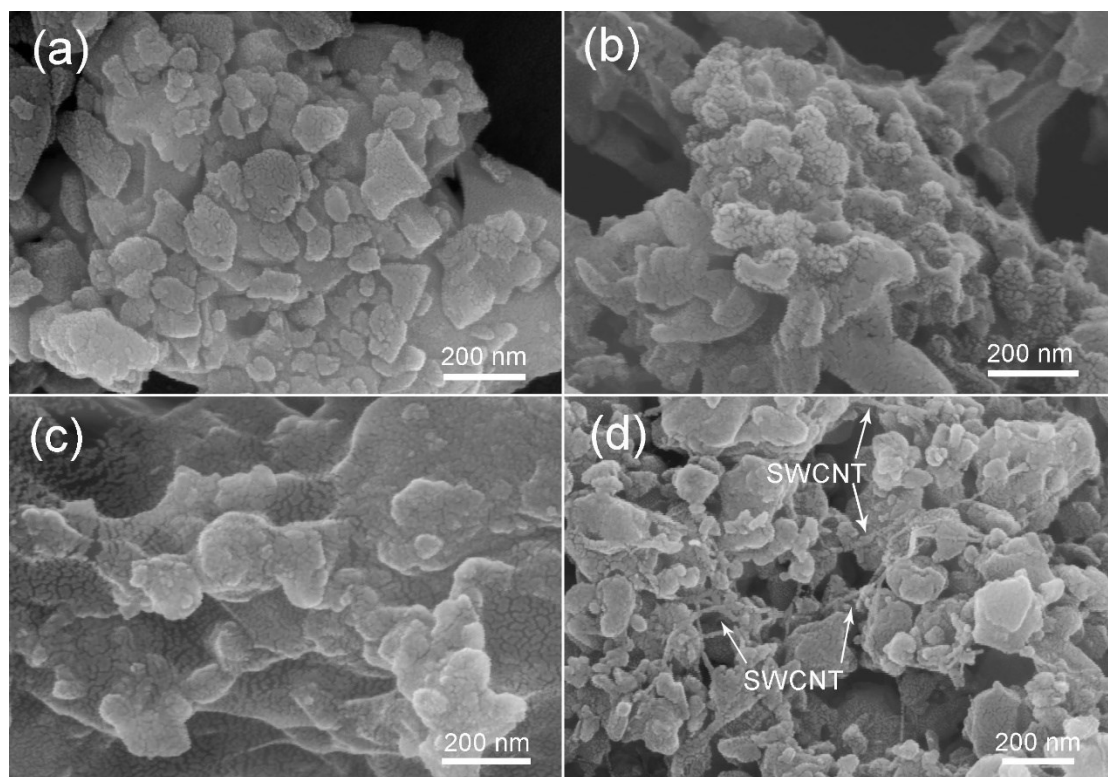
images of C, O, S and Ti in this large view are shown in **Figure 3.6b-e**. It is clear that all the elements are dispersed well in the composite, demonstrating the uniform distribution of sulfur, SWCNT and TiC-TiO<sub>2</sub> in the composite.



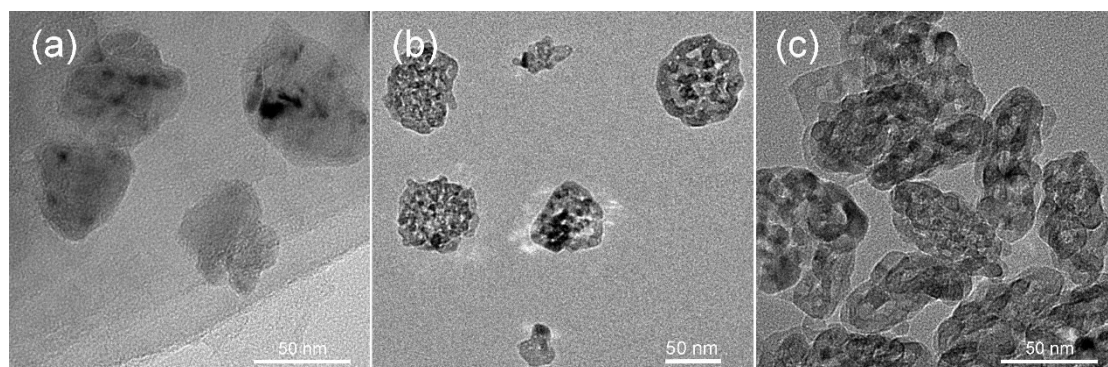
**Figure 3.6** (a) SEM image of TiC-TiO<sub>2</sub>/SWCNT/S 2, corresponding EDS elemental mapping images of (b) C, (c) O, (d) S, (e) Ti.

High-resolution FE-SEM and TEM images are further used to characterize the composite. **Figure 3.7a** and **Figure 3.8a** are the as-purchased TiC particles. After growing TiO<sub>2</sub> to form TiC-TiO<sub>2</sub>, the surface becomes more rounded shape and most areas of the surface develop a porous structure (see **Figure 3.7** and **Figure 3.8c**). When the melted sulfur process is carried out, these TiC-TiO<sub>2</sub> particles are aggregated and inter-linked by a large amount of sulfur particles (**Figure 3.7c**). In **Figure 3.7d**, it is seen that a few batches of SWCNT are intertwined to the particles and the TiC-TiO<sub>2</sub>/SWCNT/S 2 composite is formed. It is interesting that the addition of these SWCNTs preventing a full coating of non-conductive sulfur, thus enhances the dispersion of TiC-TiO<sub>2</sub>/S particles and a high conductive network is built to improve the performance of batteries, and this structure is also beneficial to high utilization of sulfur. Actually SWCNT was reported in favor of forming a flexible and free-standing

structure [18, 19], so it is expected SWCNT would make the composite more robust and may overcome volume expansion of sulfur by this intertwine structure.



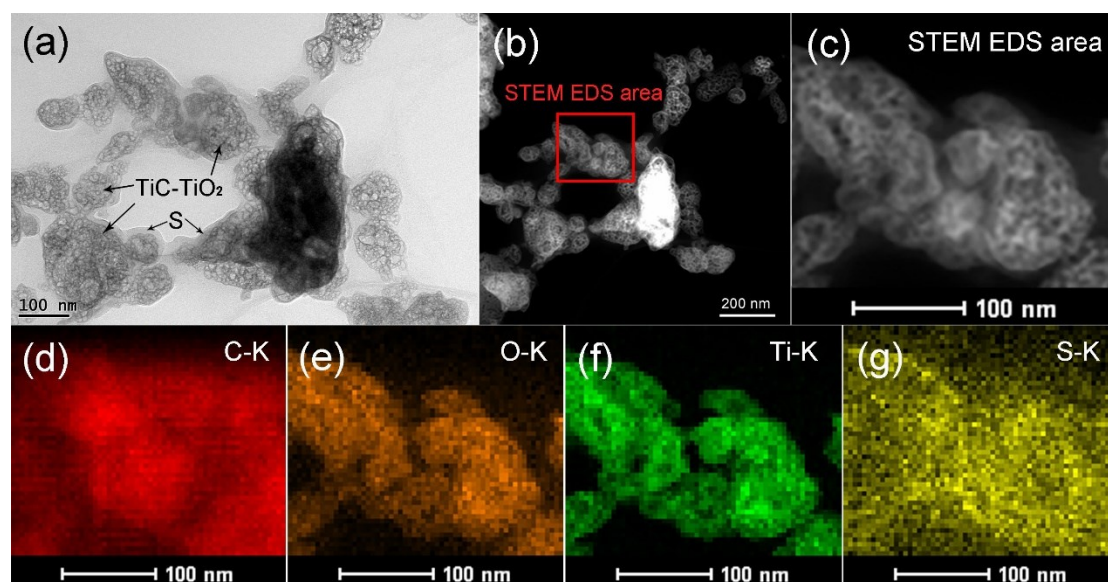
**Figure 3.7** FE-SEM images of (a) TiC, (b) TiC-TiO<sub>2</sub>, (c) TiC-TiO<sub>2</sub>/S and (d) TiC-TiO<sub>2</sub>/SWCNT/S 2.



**Figure 3.8** The high-resolution TEM images of (a) as-purchased TiC, (b) as-purchased TiO<sub>2</sub> and (c) surface oxidized TiC-TiO<sub>2</sub>.

For the local details, TEM and STEM EDS mapping images are obtained. As seen in **Figure 3.9a**, for TiC-TiO<sub>2</sub>/S composites, the size of TiC-TiO<sub>2</sub> particles is range from

50-100 nm. Attractively, all these particles are wrapped with a thin sulfur layer as confirmed by an evidence from the STEM EDS sulfur elemental mapping of **Figure 3.9g**. A uniform distribution in the composite is also observed from other elemental mapping images of C, O, Ti shown in **Figure 3.9d-f**.

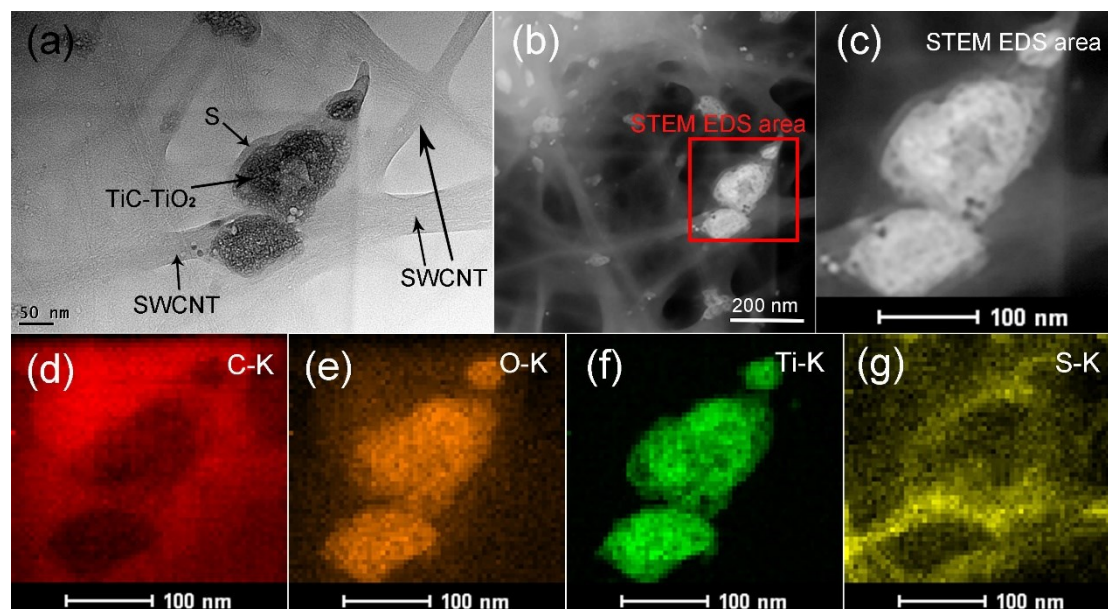


**Figure 3.9** (a) TEM image of TiC-TiO<sub>2</sub>/S composite; (b) STEM image with STEM EDS mapping area and (c) its enlarged view; STEM EDS mapping of (d) C, (e) O, (f) Ti and (g) S.

**Figure 3.10a** shows the TEM images of TiC-TiO<sub>2</sub>/SWCNT/S 2 composite. Compared to **Figure 3.9**, the original TiC-TiO<sub>2</sub> particles with wrapped sulfur layer remain unchanged. The added SWCNTs serves as a network to link the TiC-TiO<sub>2</sub> particles. Moreover, there are some sulfur nanoparticles growing on the SWCNT surface [14, 20], which is supported by **Figure 3.10g**. Similarly, as shown in the STEM image (**Figure 3.10b-c**) and STEM EDS mapping results (**Figure 3.10d-g**), all the elements also distribute uniformly in the composite. Noticeably, the content of carbon is concentrated around the TiC-TiO<sub>2</sub>/S particles due to the SWCNT is surrounding them

(Figure 3.10d) while the distribution of titanium has a clear boundary (Figure 3.10f).

In general, it is clear that SWCNTs intertwine the TiC-TiO<sub>2</sub>/S tightly, which may benefit for ready electrons transport among different materials.



**Figure 3.10** (a) TEM image of TiC-TiO<sub>2</sub>/SWCNT/S 2 composite; (b) STEM image with STEM EDS mapping area and (c) The enlarged view of marked area in (b);STEM EDS elemental mapping of (d) C, (e) O, (f) Ti, (g) S.

**Figure 3.11a** is the Raman spectra of purchased TiC and TiO<sub>2</sub> powders, which are served as the baselines to compare the as-prepared TiC-TiO<sub>2</sub> composite. Their characteristic peaks are showed as black line (TiC) and red line (TiO<sub>2</sub>) respectively. In **Figure 3.11b**, for the as-prepared TiC-TiO<sub>2</sub> composite there are 4 peaks located at 141.8, 384.5, 506.7, and 619.3 cm<sup>-1</sup>. As the molecular percentage of TiC is 33 % and thus TiO<sub>2</sub> is 67 % in TiC-TiO<sub>2</sub> composite (**Table 3.1**) and the composite presents peaks belong to more abundant materials, all the peaks for TiC cannot be observed.

**Table 3.1** Relationship among weight, molar mass and molecular weight for SWCNT and TiC in TiC-TiO<sub>2</sub>/SWCNT/S 2 composite.

	SWCNT	TiC
Mass (m)	0.06 g	0.6 g
Molar mass (M)	12	60
Molecular weight (n)	$0.06/12 = 0.005$	$0.6/60 = 0.01$

According to the relationship among weight (m), molar mass (M) and molecular weight (n) for the composite (Table S1), namely:  $n = m/M$ .

The molar ratio:

$$n(\text{SWCNT}) : n(\text{TiC}) = m(\text{SWCNT})/M(\text{SWCNT}) : m(\text{TiC})/M(\text{TiC}) = 0.005 : 0.01 \\ = 1 : 2.$$

Thus, it can be calculated that 4.56 at.% element carbon in SWCNT and 9.11 at.% of it in TiC (13.67 at.% for all the C element from XPS result). As a result, there are 9.11 at.% element titanium in TiC and 18.09 at.% of it (27.2 at.%-9.11 at.%) in TiO<sub>2</sub> (27.2 at.% for all the Ti element from XPS result), so the molecular ratio of TiC and TiO<sub>2</sub> is around 1:2 (9.11:18.09). Therefore, it can be calculated that the molecular percentage of TiC in TiC-TiO<sub>2</sub> composite is 33 %, and thus TiO<sub>2</sub> is 67 %.

At the same time, peaks of TiC-TiO<sub>2</sub> composite are close to the characteristic peaks of TiO<sub>2</sub> in **Figure 3.11a** but with a slight shift, reflecting some remaining pristine TiC particles. In **Figure 3.11b**, for the final product TiC-TiO<sub>2</sub>/SWCNT/S 2, there are no visible TiC and TiO<sub>2</sub> characteristic peaks, only sulfur peaks and three extra peaks for SWCNT (D band at 1333.0 cm<sup>-1</sup>, G band at 1586.8 cm<sup>-1</sup> and 2D band at 2665.4 cm<sup>-1</sup>).

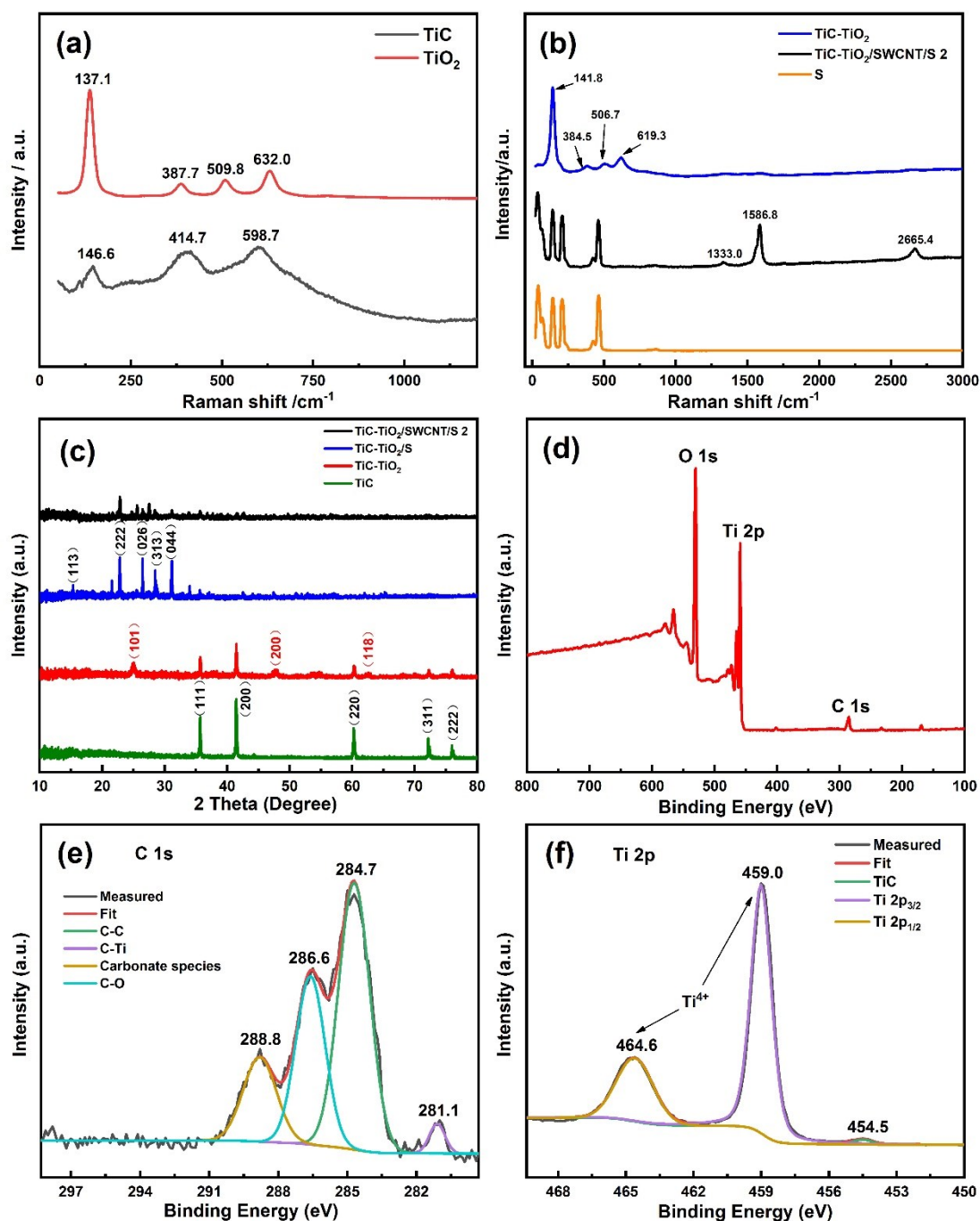
The observation here is consistent that SWCNT is well-known for its distinct and intense Raman characteristic peaks even for a very small content [20-22]. Sulfur is dominant here because it takes nearly three quarters mass ratio in the composite. Moreover, as shown previously in the TEM image, the TiC-TiO<sub>2</sub> particles are typically enclosed by a large amount of sulfur. Although TiC has some chemisorption towards polysulfides [23], polysulfides mainly are adsorbed by surface oxidized TiO<sub>2</sub> in TiC-TiO<sub>2</sub>.

**Figure 3.11c** compares the XRD patterns of four different materials. Specifically, the green line is the diffraction peaks of purchased TiC. For the red line, three new weaker peaks located at 25.0°, 47.9° and 62.7° correspond to the crystal planes (101), (200) and (118) of TiO<sub>2</sub> [24]. The TiC-TiO<sub>2</sub>/S composite mainly shows the diffraction peaks from sulfur such as (113), (222) and (026) because of the high content of sulfur, while all the peaks are weaker in the TiC-TiO<sub>2</sub>/SWCNT/S 2 composite due to the addition of a small amount of SWCNT with broad peaks and the formation of smaller nano sulfur particles according to the BET results (see **Figure 3.13b**) [20, 25].

To determine the chemical composition of the as-prepared materials, XPS analysis was carried out for these composites. **Figure 3.11d** displays the wide scan of TiC-TiO<sub>2</sub>/SWCNT 2 composite (2 wt% SWCNT in whole composite) and three peaks are corresponding to C 1s, O 1s and Ti 2p. According to the peak areas, the atomic content of carbon, oxygen and titanium are calculated as 13.7, 59.1 and 27.2 at.%. According to the relationship of weight (m), molar mass (M) and molecular weight (n) in the composite (see Table S1), it can be calculated that the molecular percentage of TiC in

TiC-TiO<sub>2</sub> composite is 33 % or the molecular ratio of TiC and TiO<sub>2</sub> is around 1:2. For the TiC-TiO<sub>2</sub>/S composite, it can be seen that the conductivity of this composite is insufficient in previous work, because the non-conductive TiO<sub>2</sub> occupies a large proportion, more conductive agent is needed in slurry but the capacity was unsatisfactory at large current density [26, 27]. Similarly, in Fig.7c-d, poor performance is observed in our work for TiC-TiO<sub>2</sub>/S composite with less conductive agent. The peaks at 284.7 eV, 286.6 eV, and 288.8 eV refer to the C-C, C-O bonds and carbonate species while the peak at 281.1 eV could be assigned to C-Ti bond (**Figure 3.11e**) [28-30]. For Ti 2*p* peaks in **Figure 3.11f**, two peaks located at 459.0 eV and 464.6 eV are assigned to the Ti<sup>4+</sup> oxidation state in TiO<sub>2</sub>, whereas an extremely weaker peak located at 454.5 eV might result from a relatively small quantity of Ti-C [13].

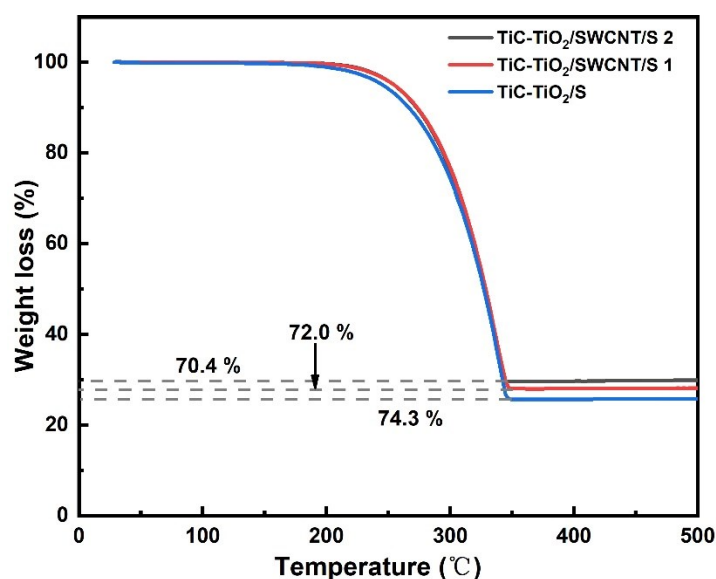




**Figure 3.11** Raman spectra of (a) purchased TiC and TiO<sub>2</sub>; (b) three distinct materials; (c) XRD patterns of four different materials; XPS spectra of (d) TiC-TiO<sub>2</sub>/SWCNT 2, its (e) C 1s and (f) Ti 2p.

The TGA curves of TiC-TiO<sub>2</sub>/S, TiC-TiO<sub>2</sub>/SWCNT/S 1 and TiC-TiO<sub>2</sub>/SWCNT/S 2 composite are presented in **Figure 3.12**. The sulfur contents of TiC-TiO<sub>2</sub>/S, TiC-TiO<sub>2</sub>/SWCNT/S 1 and TiC-TiO<sub>2</sub>/SWCNT/S 2 composite are 74.3 wt%, 72.0 wt% and

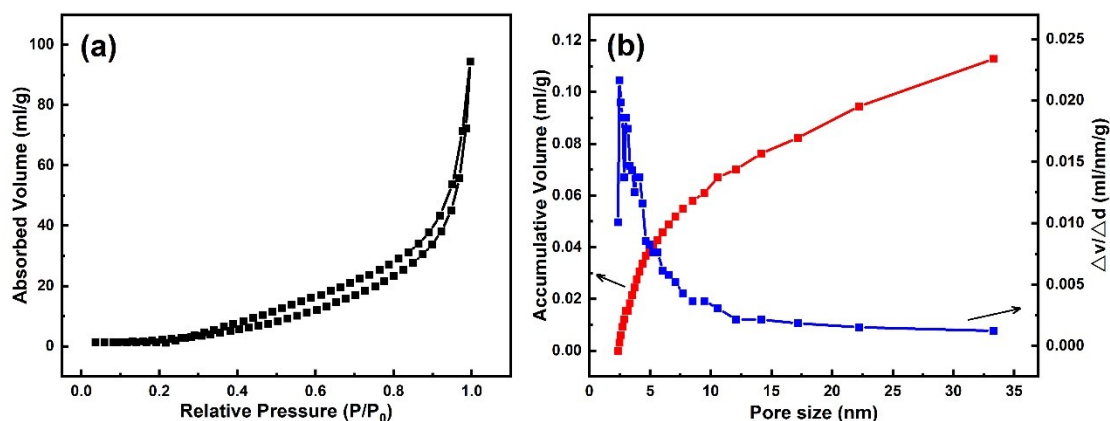
70.4 wt% respectively. It is expected that sulfur content would further decrease with increasing the amount of SWCNT added. Therefore, it is important to balance the content of sulfur and the amount of SWCNT for a practical and cost-effective application. In our study, the slurry ratio is now 8:1:1 rather than the previous reported one 7:2:1 [13, 15], which offers 10 % more electrode material. However, from **Figure 3.12** it is only less than 4 % sulfur in TiC-TiO<sub>2</sub>/SWCNT/S 2 compared to that of TiC-TiO<sub>2</sub>/S. Therefore, adding a small amount of SWCNT (around 2 wt% in TiC-TiO<sub>2</sub>/SWCNT/S 2) has no negative effect to the energy density. On the contrary, there is 8 % more active sulfur in electrode as a whole, making it attractive as high-performance Li-S batteries.



**Figure 3.12** TGA curves of TiC-TiO<sub>2</sub>/S, TiC-TiO<sub>2</sub>/SWCNT/S 1 and TiC-TiO<sub>2</sub>/SWCNT/S 2 composites.

**Figure 3.13** shows the N<sub>2</sub> adsorption-desorption isotherms of TiC-TiO<sub>2</sub>/SWCNT/S 2 composite. In previous work, the pore size distribution for TiC-TiO<sub>2</sub> is at the range of 2-10 nm with 158.99 m<sup>2</sup>·g<sup>-1</sup> large specific surface area. On the

contrary, TiC-TiO<sub>2</sub>/S just has 8.24 m<sup>2</sup>·g<sup>-1</sup> low specific surface area and all the pores are larger than 5 nm because TiC-TiO<sub>2</sub> is almost filled with sulfur in TiC-TiO<sub>2</sub>/S [13]. In our work, the situation of the TiC-TiO<sub>2</sub>/S composite is similar to previous work [13] and it can be calculated that the specific surface area of TiC-TiO<sub>2</sub>/SWCNT/S 2 composite is 12.08 m<sup>2</sup>·g<sup>-1</sup>, which is slightly higher than TiC-TiO<sub>2</sub>/S composite, because of the addition of a small amount of SWCNT. Meanwhile, the formation of smaller nano sulfur particles contributes to this increase of the specific surface area. As a result, it appears a number of 2-5 nm pores again in TiC-TiO<sub>2</sub>/SWCNT/S 2 and the average pore size is calculated to be 9.8 nm.



**Figure 3.13** (a) N<sub>2</sub> adsorption-desorption isotherm and (b) pore-size distribution curves of TiC-TiO<sub>2</sub>/SWCNT 10.

In the aspect of electrochemical performance, the charge-discharge profiles in **Figure 3.14a** show two discharge plateaus and one charge plateau during the process for all the composites. For TiC-TiO<sub>2</sub>/SWCNT/S 2 composite, its discharge platforms appear at about 2.35 V and 2.10 V, corresponding to the reduction peaks of the CV curves in **Figure 3.16c**. All the TiC-TiO<sub>2</sub>/SWCNT/S cathodes display similar shape for the first cycle with less polarization and higher sulfur utilization, since those composites

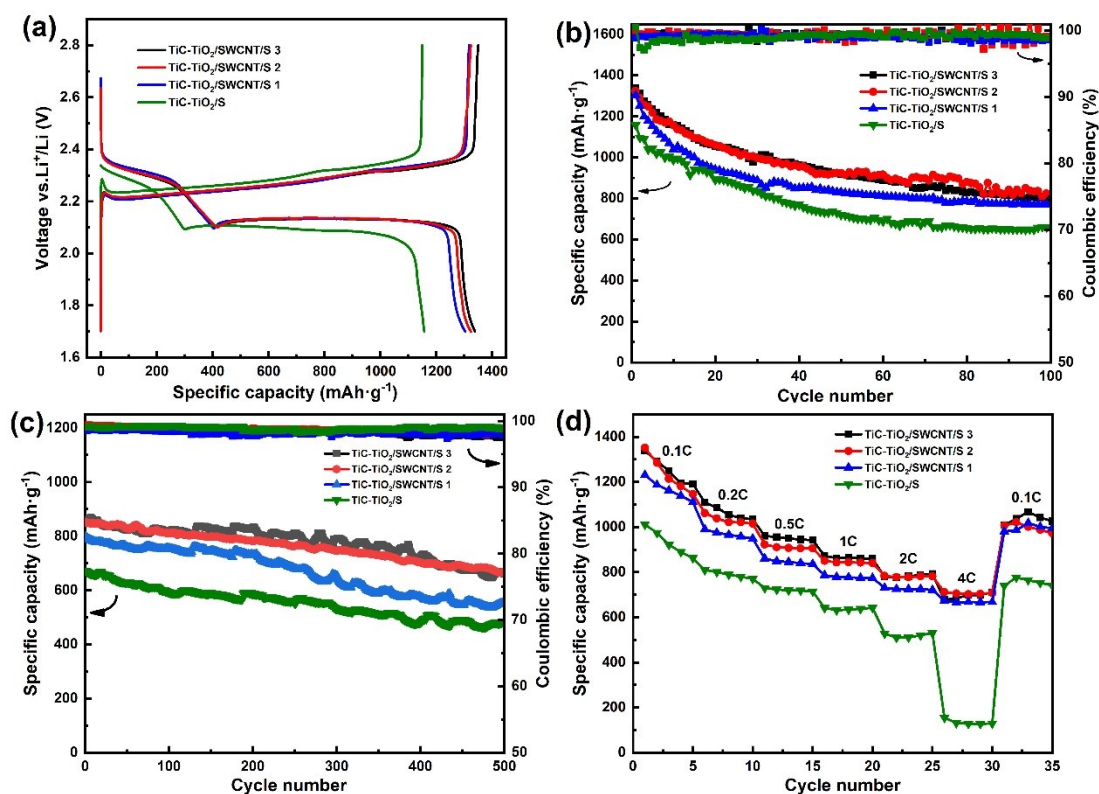
with SWCNT have good conductivity. Moreover, the intertwined networks formed by SWCNT can facilitate the reaction to polysulfides and further reaction of  $\text{Li}_2\text{S}_2$  and  $\text{Li}_2\text{S}$  by offering effective electron tunnels and decreasing charge transfer resistance (verified in Fig.9). However, the profile of  $\text{TiC-TiO}_2/\text{S}$  cathode has a large extent polarization (its discharge platforms appear at about 2.30 V and 2.05 V) as charge transfer resistance is higher without the connection of SWCNT. For the charge platform, different cathodes show a little difference and most of them appear at around 2.25 V. As observed in **Figure 3.14b**, the discharge specific capacities were obtained during cycling for the batteries of five different materials at 0.1 C. A significant high initial capacity of  $1324.2 \text{ mAh}\cdot\text{g}^{-1}$  is delivered by the cell with  $\text{TiC-TiO}_2/\text{SWCNT}/\text{S} 2$  cathode. The capacity maintains at  $817.0 \text{ mAh}\cdot\text{g}^{-1}$  after 100 cycles with a satisfactory retention of about 60 % to the initial value because of the high utilization rate of sulfur in modified crosslinked structure, as well as  $\text{TiO}_2$  with strong adsorption of polysulfides. The cell with  $\text{TiC-TiO}_2/\text{SWCNT}/\text{S} 3$  presents a very similar performance while a slightly low capacity of  $802.5 \text{ mAh}\cdot\text{g}^{-1}$  was observed after cycles. In comparison, the cell with  $\text{TiC-TiO}_2/\text{S}$  composite shows the capacity  $1157.3 \text{ mAh}\cdot\text{g}^{-1}$  and  $657.9 \text{ mAh}\cdot\text{g}^{-1}$  with the capacity retention of 57 % under the same condition. For the simple  $\text{TiC}/\text{S}$  cathode, its capacity decays to just  $534.6 \text{ mAh}\cdot\text{g}^{-1}$  after 100 cycles from the value of  $1202.4 \text{ mAh}\cdot\text{g}^{-1}$  at the beginning due to poor adsorption of polysulfides without  $\text{TiO}_2$ . Clearly, capacity for the cells with the addition of SWCNT were markedly superior to the cells without SWCNT, meanwhile  $\text{TiO}_2$  also plays an important role in the improved cycling capacity as its good adsorption of polysulfides.

Long cycle performance of these cathodes at large current density of 1 C is presented in **Figure 3.14c**. For the initial cycle, both TiC-TiO<sub>2</sub>/SWCNT/S 2 and TiC-TiO<sub>2</sub>/SWCNT/S 3 display a relatively high capacity, with 850.7 mAh·g<sup>-1</sup> and 857.3 mAh·g<sup>-1</sup> at the first cycle, respectively. After charged and discharged for 500 cycles, the capacity is about 666.5 mAh·g<sup>-1</sup> for TiC-TiO<sub>2</sub>/SWCNT/S 2 with 77.7 % retention rate, and the values of TiC-TiO<sub>2</sub>/SWCNT/S 3 are close to TiC-TiO<sub>2</sub>/SWCNT/S 2, while a slightly lower capacity (799.1 mAh·g<sup>-1</sup> at first cycle) is seen in the blue line for the composite with only 5 % SWCNT added. The excellent large current performance found from the SWCNT modified cathodes is explained by that a small amount addition of SWCNT can improve the conductivity of cathode to a great extent. However, our results also reveal that adding too much SWCNT in the composite might not have obvious positive effect on enhancing the conductivity. Although having a relatively slow decay rate, it only achieves 671.0 mAh·g<sup>-1</sup> at first cycle for the TiC-TiO<sub>2</sub>/S composite, which means the conductivity of TiC-TiO<sub>2</sub>/S is insufficient and its conductivity is the lowest among all the composites. On the contrary, for the initial several cycles the cell with TiC/S offers better capacity than the cell with TiC-TiO<sub>2</sub>/S because the conductivity of TiC/S is higher. However, without metal oxide of TiO<sub>2</sub>, the TiC/S cathode alone is lacking the effective adsorption of polysulfide, resulting in a fast decay during whole cycle process as agreed to the performance shown in **Figure 3.14b** at 0.1 C.

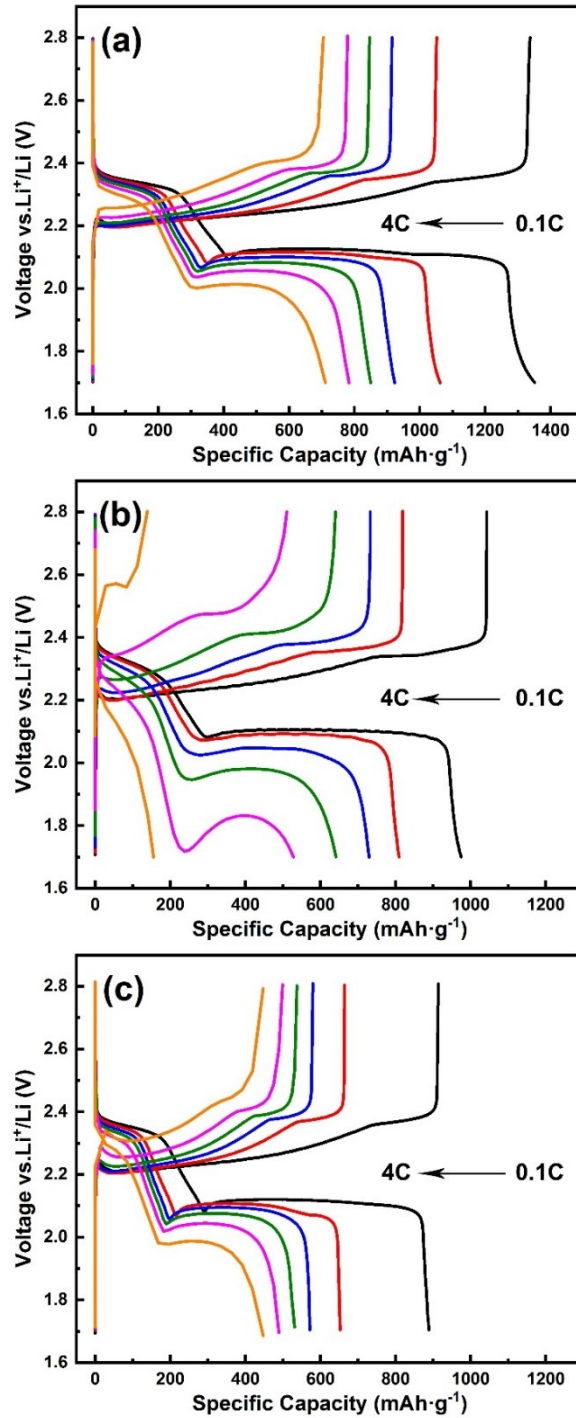
For the rate performance in **Figure 3.14d**, the results are similar to the corresponding cycling performance as seen in **Figure 3.14b-c**. The TiC-

TiO<sub>2</sub>/SWCNT/S 1 cell only dives to 673.2 mAh·g<sup>-1</sup> at a high rate of 4 C and retains 981.2 mAh·g<sup>-1</sup> when the current returns to 0.1 C. As expected, the cells with TiC-TiO<sub>2</sub>/SWCNT/S 2 and TiC-TiO<sub>2</sub>/SWCNT/S 3 cathodes present similar outstanding performance, but two curves can be still independently distinguished. The discharge capacity of TiO<sub>2</sub>/SWCNT/S 2 reaches 711.2 mAh·g<sup>-1</sup> at 4 C and recovers to 1006.9 mAh·g<sup>-1</sup> when the current density resets to 0.1 C, which is significantly higher than 490 mAh·g<sup>-1</sup> at 4 C reported in recent work [13]. This excellent rate performance and the recoverability are associated with the outstanding conductivity and the remarkably robust electrode structure with relieved volume expansion after cycling at high current density (4 C), refer to FE-SEM image in **Figure 3.7d**. For the current density from 0.1, 0.2, 0.5, 1 C to 4 C and back to 0.1 C, the results of TiC-TiO<sub>2</sub>/SWCNT/S 3 are slightly superior to TiC-TiO<sub>2</sub>/SWCNT/S 2 in 0.1 C to 1 C process, because adding SWCNT could improve the conductivity of the cathode and more efficient in accelerating the velocity of the redox reaction in the Li-S cell. However, this improvement is not that significant if considering the cost of adding extra 5 % SWCNT, as well as it will decrease the energy density of the whole cell. Noticeably, the cell with TiC-TiO<sub>2</sub>/S composite just achieves 155.3 mAh·g<sup>-1</sup> at 4 C and its second discharge platform is below 1.8 V at 2 C current density on account of such low conductivity of TiC-TiO<sub>2</sub>/S (**Figure 3.15b**). To further understand the reason, **Figure 3.15** shows a comparison of charge and discharge profiles for rate performance of three electrodes. Due to the large polarization, TiC-TiO<sub>2</sub>/S just shows one discharge platform when current is 4 C (**Figure 3.15b**). On the contrast, although overall capacity of rate performance of TiC/S is lower,

TiC/S with higher conductivity shows a smaller polarization and two full discharge platforms all the time in **Figure 3.15c**. Therefore, TiC/S still remains  $460.4 \text{ mAh}\cdot\text{g}^{-1}$  at 4 C large current density. Furthermore, compared with **Figure 3.15a** and **Figure 3.15c**, TiC-TiO<sub>2</sub>/SWCNT/S 2 and TiC/S present almost the same degree of polarization, indicating that they have similar conductivity, verified in EIS results in **Figure 3.17**. Obviously, both conductivities are markedly higher than TiC-TiO<sub>2</sub>/S and thus the addition of SWCNT into TiC-TiO<sub>2</sub>/S is essential for improving the performance of the Li-S batteries.



**Figure 3.14** (a) First charge-discharge curves; (b) Charge-discharge performance at 0.1 C, (c) Charge-discharge performance at 1 C large current density and (d) Rate performance from 0.1 C to 4 C of four different cathodes for their coin cells.



**Figure 3.15** Charge and discharge profiles at 0.1 C, 0.2 C, 0.5 C, 1 C, 2 C and 4 C for

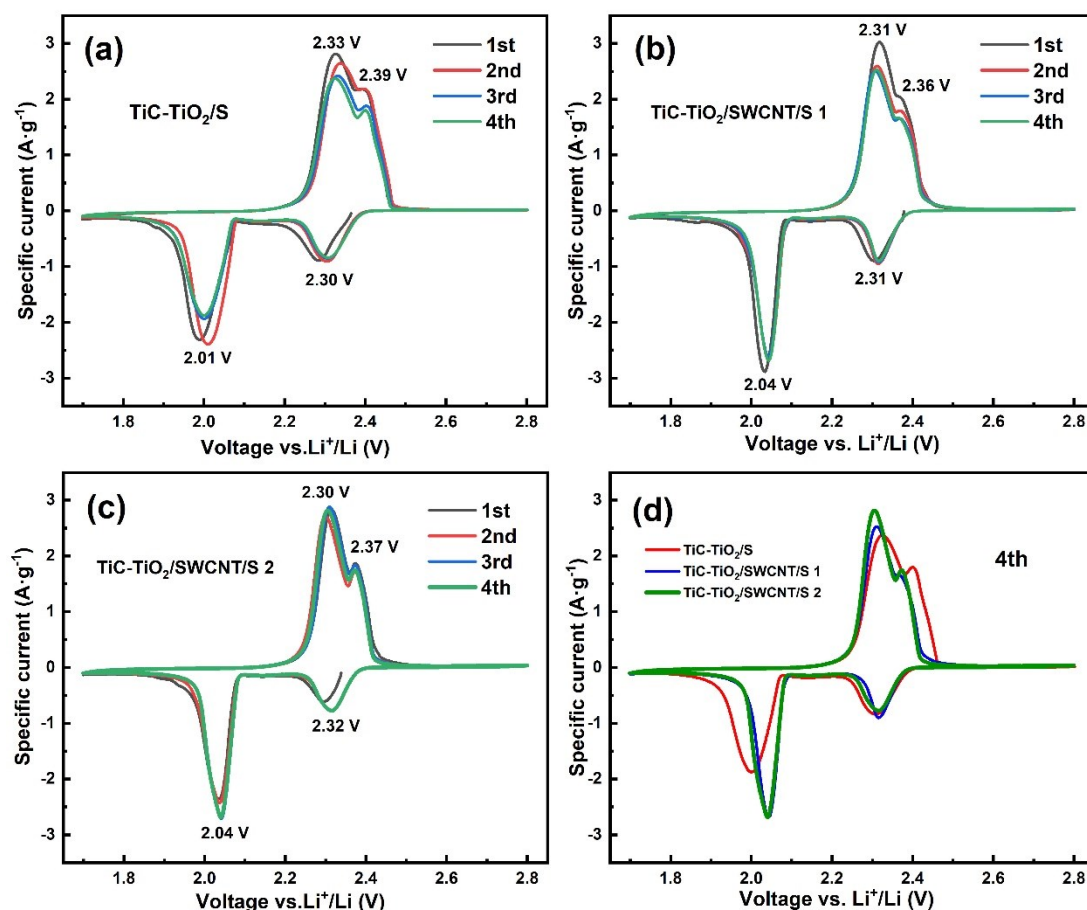
(a) TiC-TiO<sub>2</sub>/SWCNT/S 2, (b) TiC-TiO<sub>2</sub>/S and (c) TiC/S.

Here, we can observe that performance improvement of the multiple host material is remarkably superior to the single host material. For example, both cycle performance and rate performance of TiC-TiO<sub>2</sub>/S are higher than TiC/S and TiO<sub>2</sub>/S (comparing



**Figure 3.4** and **Figure 3.14**), which use a low-cost method to achieve as high performance as SWCNT/S. In addition, mixing a small amount of SWCNT (~2 %) into TiC-TiO<sub>2</sub>/S to form TiC-TiO<sub>2</sub>/SWCNT/S 2 can greatly further enhance the performance without excessively higher cost.

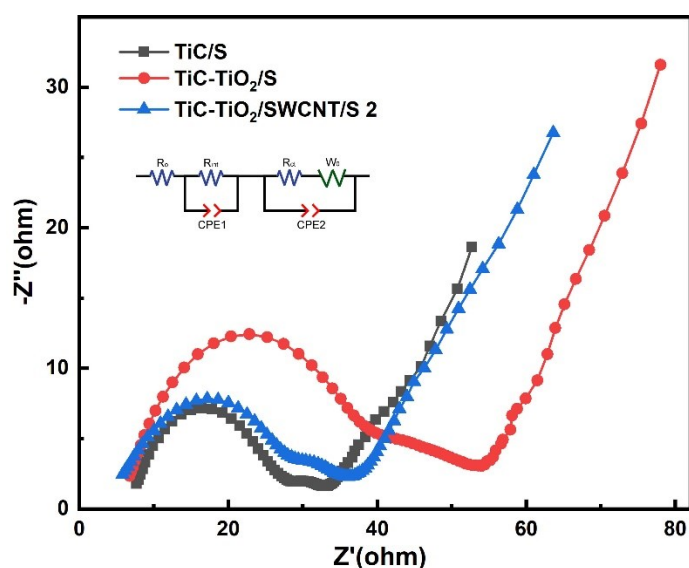
CV curves of three different batteries are shown in **Figure 3.16**. For TiC-TiO<sub>2</sub>/SWCNT/S 2, two reduction peaks are seen at 2.32 V and 2.04 V, corresponding to the reduction of elemental sulfur to high-order lithium polysulfides and the further reduction of high-order lithium polysulfides into Li<sub>2</sub>S<sub>2</sub> and Li<sub>2</sub>S during the discharge process. Two peaks at 2.30 V and 2.37 V refer to two oxidation process during charge process [10]. Starting point appears around 2.36 V at first cycle for all the batteries is associated with the self-discharge phenomenon of the cell after standing. If compared with **Figure 3.16a-c**, it is clear that the redox peaks are gradually sharper and better overlapping feature for the initial several cycles with the addition of SWCNT. Among these three cathodes, the shape and the position of redox peaks of TiC-TiO<sub>2</sub>/SWCNT/S 2 are the sharpest and the closest to the theoretical values. On the other hand, these peaks have almost no shifts on the following cycles for TiC-TiO<sub>2</sub>/SWCNT/S 2, indicating the stable reaction pathway for the redox process. Meanwhile, with the addition SWCNT, the level of polarization gradually decreases and two oxidation peaks have become more pronounced. To compare more clearly, the CV curves for the 4th cycle presenting a relative stable condition of these three different batteries is illustrated in **Figure 3.16d**. All these CV results are in a good agreement with charge-discharge curves shown in **Figure 3.14a**.



**Figure 3.16** CV plots for the first four cycles of (a) TiC-TiO<sub>2</sub>/S, (b) TiC-TiO<sub>2</sub>/SWCNT/S 1 and (c) TiC-TiO<sub>2</sub>/SWCNT/S 2; (d) CV curves for the 4th cycle of different cathodes.

EIS test can further demonstrate the impedance of cathodes. In **Figure 3.17**, the semicircle in the high-frequency region can be ascribed to the internal impedance of the cathode ( $R_{int}$ ), and a small arc of a semicircle located in the medium frequency range refers to the charge-transfer resistance ( $R_{ct}$ ) [13, 31]. The short line in the low-frequency region is generally named as Warburg resistance, denoted as  $W_0$ , which is attributed to the diffusion resistance of lithium ions within the cathode. CPE1 and CPE2 in the equivalent circuit represent the capacitive elements [32]. A corresponding equivalent circuit is inserted. It can be measured that the  $R_{int}$  of TiC-TiO<sub>2</sub>/SWCNT/S 2 is 22.9  $\Omega$ ,

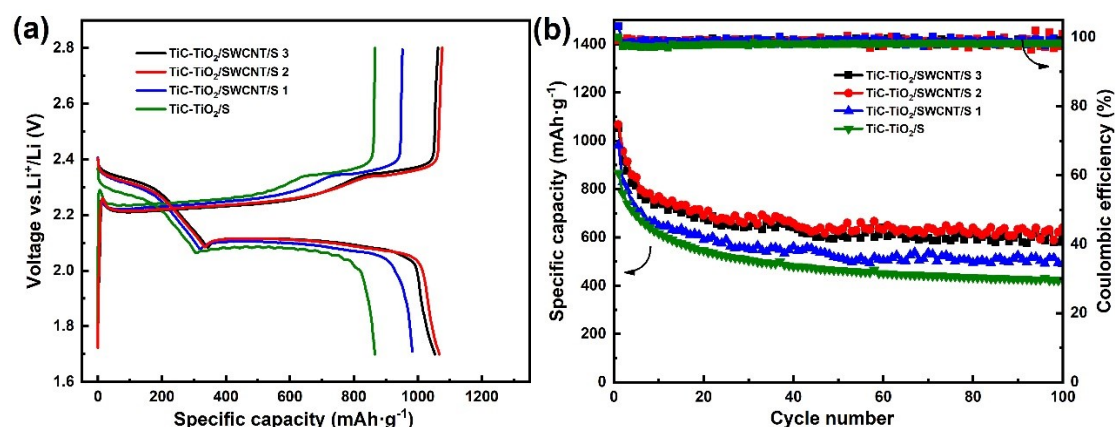
which is smaller than TiC-TiO<sub>2</sub>/S (31.2 Ω) and bigger than TiC/S (16.4 Ω). Meanwhile, the R<sub>ct</sub> of TiC-TiO<sub>2</sub>/SWCNT/S 2 is 9.6 Ω, which is also lower than TiC-TiO<sub>2</sub>/S (16.1 Ω) and even less than TiC/S (10.8 Ω). These phenomena could be explained by surface oxidized TiO<sub>2</sub> leading to a relatively high resistance for TiC-TiO<sub>2</sub>/S. In addition, SWCNT can decrease resistance in TiC-TiO<sub>2</sub>/SWCNT/S 2 by constructing a conductive network [20, 26]. Moreover, a small amount of SWCNT intertwined in TiC-TiO<sub>2</sub>/SWCNT/S 2 composite can break non-conductive sulfur agglomeration in large areas, thus promoting material dispersion and decreasing charge-transfer resistance by providing numerous electron tunnels [33]. The structure can be seen in FE-SEM images in **Figure 3.7c-d** and **Figure 3.10a**.



**Figure 3.17** EIS spectra of TiC-TiO<sub>2</sub>/SWCNT/S 2, TiC-TiO<sub>2</sub>/S and TiO<sub>2</sub>/S cathodes (inset – corresponding equivalent circuit).

In addition, the pouch cell performances of four composites are tested. Compared to some simple cathodes in **Figure 3.5**, these well-mixed composites display conspicuously higher and more stable cycling in **Figure 3.18**. All the composites own

a slightly lower capacity than their coin cells. TiC-TiO<sub>2</sub>/SWCNT/S 2 shows the highest capacity of 1067.6 mAh·g<sup>-1</sup> and retains 639.9 mAh·g<sup>-1</sup> for 100 cycles at 0.1 C, followed by TiC-TiO<sub>2</sub>/SWCNT/S 3 and TiC-TiO<sub>2</sub>/SWCNT/S 1. Without the supported conductivity of SWCNT, there is a larger polarization and lower capacity of TiC-TiO<sub>2</sub>/S.



**Figure 3.18** (a) First charge-discharge curves; (b) Charge-discharge performance at 0.1 C of four different cathodes for their pouch cells.

### 3.4 Conclusions

In summary, we first choose several different types of materials to combine with sulfur to fabricate composite cathodes to improve battery performance and investigate their different features. Based on understanding the merits and drawbacks of TiC, TiO<sub>2</sub> and SWCNT materials, the TiC-TiO<sub>2</sub>/SWCNT/S modified cathode for Li-S batteries was proposed and fabricated with a high conductive network via 1D SWCNT connected. Compared with the TiC-TiO<sub>2</sub>/S cathode, TiC-TiO<sub>2</sub>/SWCNT/S 2 with a small addition of SWCNT delivers 1324.2 mAh·g<sup>-1</sup> specific capacity at first cycle and 817.0 mAh·g<sup>-1</sup> after 100 cycles for 0.1 C, proving its higher conductivity and greater sulfur utilization. For rate performance, it shows 711.2 mAh·g<sup>-1</sup> at 4 C and recovers to 1006.9 mAh·g<sup>-1</sup> when the current returns to 0.1 C. This cathode also reveals good long cycling stability

with  $850.7 \text{ mAh}\cdot\text{g}^{-1}$  initial capacity and 77.7 % retention rate after 500 cycles at 1 C large current density. Another attractive element for this study is that only a small amount of SWCNT (~2 %wt) is needed to enhance the conductivity of the whole composite to a large extent. The overall cycling, rate performance and long cycling stability remain almost identical for adding 2 % or 3 % of SWCNT, indicating 2 wt% SWCNT is sufficient to offer good electrons transferring channels. In addition, pouch cells with TiC-TiO<sub>2</sub>/SWCNT/S 2 cathode were fabricated successfully, presenting  $1067.6 \text{ mAh}\cdot\text{g}^{-1}$  high first capacity and retaining  $639.9 \text{ mAh}\cdot\text{g}^{-1}$  after 100 cycles at 0.1 C. Our results highlight that this strategy is efficient and low-cost to obtain high-performance batteries.

### 3.5 References

- [1] J. Liang, Z.H. Sun, F. Li, and H.M. Cheng, Carbon materials for Li-S batteries: Functional evolution and performance improvement, *Energy Storage Materials*, 2 (2016) 76-106.
- [2] Z. Li, Y. Huang, L. Yuan, Z. Hao, and Y. Huang, Status and prospects in sulfur-carbon composites as cathode materials for rechargeable lithium-sulfur batteries, *Carbon*, 92 (2015) 41-63.
- [3] C. Nan, Z. Lin, H. Liao, M.K. Song, Y. Li, and E.J. Cairns, Durable carbon-coated Li<sub>2</sub>S core-shell spheres for high performance lithium/sulfur cells, *Journal of the American Chemical Society*, 136 (2014) 4659-4663.
- [4] J. Zhang, N. Yang, X. Yang, S. Li, J. Yao, and Y. Cai, Hollow sulfur@graphene oxide core-shell composite for high-performance Li-S batteries, *Journal of Alloys and Compounds*, 650 (2015) 604-609.
- [5] X. Song, T. Gao, S. Wang, Y. Bao, G. Chen, L.-X. Ding, and H. Wang, Free-standing sulfur host based on titanium-dioxide-modified porous-carbon nanofibers for lithium-sulfur batteries, *Journal of Power Sources*, 356 (2017) 172-180.
- [6] M.S. Song, S.C. Han, H.S. Kim, J.H. Kim, K.T. Kim, Y.M. Kang, H.J. Ahn, S.X. Dou, and J.Y. Lee, Effects of Nanosized Adsorbing Material on Electrochemical Properties of Sulfur Cathodes for Li/S Secondary Batteries, *Journal of The Electrochemical Society*, 151 (2004) A791-A795.
- [7] C. Zha, F. Yang, J. Zhang, T. Zhang, S. Dong, and H. Chen, Promoting polysulfide redox reactions and improving electronic conductivity in lithium-sulfur batteries via

hierarchical cathode materials of graphene-wrapped porous TiO<sub>2</sub> microspheres with exposed (001) facets, *Journal of Materials Chemistry A*, 6 (2018) 16574-16582.

[8] C. Zha, D. Wu, T. Zhang, J. Wu, and H. Chen, A facile and effective sulfur loading method: Direct drop of liquid Li<sub>2</sub>S<sub>8</sub> on carbon coated TiO<sub>2</sub> nanowire arrays as cathode towards commercializing lithium-sulfur battery, *Energy Storage Materials*, 17 (2019) 118-125.

[9] C. Zha, X. Zhu, J. Deng, Y. Zhou, Y. Li, J. Chen, P. Ding, Y. Hu, Y. Li, and H. Chen, Facet-tailoring five-coordinated Ti sites and structure-optimizing electron transfer in a bifunctional cathode with titanium nitride nanowire array to boost the performance of Li<sub>2</sub>S<sub>6</sub>-based lithium-sulfur batteries, *Energy Storage Materials*, 26 (2020) 40-45.

[10] D.W. Wang, Q. Zeng, G. Zhou, L. Yin, F. Li, H.M. Cheng, I.R. Gentle, and G.Q.M. Lu, Carbon-sulfur composites for Li-S batteries: status and prospects, *Journal of Materials Chemistry A*, 1 (2013) 9382-9394.

[11] X. Liu, J.Q. Huang, Q. Zhang, and L. Mai, Nanostructured Metal Oxides and Sulfides for Lithium-Sulfur Batteries, *Advanced materials*, 29 (2017) 1601759.

[12] D.E. Gu, Y. Lu, B.C. Yang, and Y.D. Hu, Facile preparation of micro-mesoporous carbon-doped TiO<sub>2</sub> photocatalysts with anatase crystalline walls under template-free condition, *Chemical communications*, 21 (2008) 2453-2455.

[13] Z. Cui, J. Yao, T. Mei, S. Zhou, B. Hou, J. Li, J. Li, J. Wang, J. Qian, and X. Wang, Strong lithium polysulfides chemical trapping of TiC-TiO<sub>2</sub>/S composite for long-cycle lithium-sulfur batteries, *Electrochimica Acta*, 298 (2019) 43-51.

[14] R. Carter, L. Oakes, N. Muralidharan, and C.L. Pint, Isothermal Sulfur

Condensation into Carbon Scaffolds: Improved Loading, Performance, and Scalability for Lithium-Sulfur Battery Cathodes, *The Journal of Physical Chemistry C*, 121 (2017) 7718-7727.

[15] X. Lang, Y. Zhao, K. Cai, L. Li, D. Chen, and Q. Zhang, A Facile Synthesis of Stable TiO<sub>2</sub>/TiC Composite Material as Sulfur Immobilizers for Cathodes of Lithium-Sulfur Batteries with Excellent Electrochemical Performances, *Energy Technology*, 7 (2019) 1900543.

[16] L. Shi, S.M. Bak, Z. Shadike, C. Wang, C. Niu, P. Northrup, H. Lee, A.Y. Baranovskiy, C.S. Anderson, J. Qin, S. Feng, X. Ren, D. Liu, X.-Q. Yang, F. Gao, D. Lu, J. Xiao, and J. Liu, Reaction heterogeneity in practical high-energy lithium-sulfur pouch cells, *Energy & Environmental Science*, 13 (2020) 3620-3632.

[17] O.I.A. Maiga, R. Li, K.F. Ye, B.H. Liu, and Z.P. Li, Sulfide heave: Key factor governing cathode deterioration in pouch Li-S cells, *Electrochimica Acta*, 300 (2019) 150-155.

[18] C.H. Chang, S.H. Chung, and A. Manthiram, Highly flexible, freestanding tandem sulfur cathodes for foldable Li-S batteries with a high areal capacity, *Materials Horizons*, 4 (2017) 249-258.

[19] R. Fang, K. Chen, L. Yin, Z. Sun, F. Li, and H.M. Cheng, The Regulating Role of Carbon Nanotubes and Graphene in Lithium-Ion and Lithium-Sulfur Batteries, *Advanced materials*, 31 (2019) 1800863.

[20] M.Q. Zhao, X.F. Liu, Q. Zhang, G.L. Tian, J.Q. Huang, W. Zhu, and F. Wei, Graphene Single-Walled Carbon Nanotube Hybrids One-Step Catalytic Growth and



- Applications for High-Rate Li-S Batteries, *ACS Nano*, 6 (2012) 10759-10769.
- [21] H.M. Heise, R. Kuckuk, A.K. Ojha, A. Srivastava, V. Srivastava, and B.P. Asthana, Characterisation of carbonaceous materials using Raman spectroscopy: a comparison of carbon nanotube filters, single- and multi-walled nanotubes, graphitised porous carbon and graphite, *Journal of Raman Spectroscopy*, 40 (2009) 344-353.
- [22] M.Q. Zhao, Q. Zhang, J.Q. Huang, G.L. Tian, T.C. Chen, W.Z. Qian, and F. Wei, Towards high purity graphene/single-walled carbon nanotube hybrids with improved electrochemical capacitive performance, *Carbon*, 54 (2013) 403-411.
- [23] H.J. Peng, G. Zhang, X. Chen, Z.W. Zhang, W.T. Xu, J.Q. Huang, and Q. Zhang, Enhanced Electrochemical Kinetics on Conductive Polar Mediators for Lithium-Sulfur Batteries, *Angewandte Chemie*, 55 (2016) 12990-12995.
- [24] K. Thamaphat, P. Limsuwan, and B. Ngotawornchai, Phase Characterization of TiO<sub>2</sub> Powder by XRD and TEM, *Agriculture and Natural Resources*, 42 (2008) 357-361.
- [25] D.N. Futaba, K. Hata, T. Yamada, T. Hiraoka, Y. Hayamizu, Y. Kakudate, O. Tanaike, H. Hatori, M. Yumura, and S. Iijima, Shape-engineerable and highly densely packed single-walled carbon nanotubes and their application as super-capacitor electrodes, *Nature materials*, 5 (2006) 987-994.
- [26] Z. Xiao, Z. Yang, L. Wang, H. Nie, M. Zhong, Q. Lai, X. Xu, L. Zhang, and S. Huang, A Lightweight TiO<sub>2</sub>/Graphene Interlayer, Applied as a Highly Effective Polysulfide Absorbent for Fast, Long-Life Lithium-Sulfur Batteries, *Advanced materials*, 27 (2015) 2891-2898.

- [27] Y. Wang, R. Zhang, J. Chen, H. Wu, S. Lu, K. Wang, H. Li, C.J. Harris, K. Xi, R.V. Kumar, and S. Ding, Enhancing Catalytic Activity of Titanium Oxide in Lithium-Sulfur Batteries by Band Engineering, *Advanced Energy Materials*, 9 (2019) 1900953.
- [28] A. Ignaszak, C. Song, W. Zhu, J. Zhang, A. Bauer, R. Baker, V. Neburchilov, S. Ye, and S. Campbell, Titanium carbide and its core-shelled derivative TiC@TiO<sub>2</sub> as catalyst supports for proton exchange membrane fuel cells, *Electrochimica Acta*, 69 (2012) 397-405.
- [29] X. Guo, G. Zhang, H. Cui, N. Wei, X. Song, J. Li, and J. Tian, Porous TiB<sub>2</sub>-TiC/TiO<sub>2</sub> heterostructures: Synthesis and enhanced photocatalytic properties from nanosheets to sweetened rolls, *Applied Catalysis B: Environmental*, 217 (2017) 12-20.
- [30] D.L. Shieh, S.J. Huang, Y.C. Lin, Y.S. Lin, J.L. Lin, T.F. Yeh, and H. Teng, TiO<sub>2</sub> derived from TiC reaction in HNO<sub>3</sub>: Investigating the origin of textural change and enhanced visible-light absorption and applications in catalysis, *Microporous and Mesoporous Materials*, 167 (2013) 237-244.
- [31] J. Chen, X. Jia, Q. She, C. Wang, Q. Zhang, M. Zheng, and Q. Dong, The preparation of nano-sulfur/MWCNTs and its electrochemical performance, *Electrochimica Acta*, 55 (2010) 8062-8066.
- [32] N.A. Cañas, K. Hirose, B. Pascucci, N. Wagner, K.A. Friedrich, and R. Hiesgen, Investigations of lithium-sulfur batteries using electrochemical impedance spectroscopy, *Electrochimica Acta*, 97 (2013) 42-51.
- [33] A. Anson-Casaos, C. Rubio-Munoz, J. Hernandez-Ferrer, A. Santidrian, A.M. Benito, and W.K. Maser, Capacitive and Charge Transfer Effects of Single-Walled

Carbon Nanotubes in TiO<sub>2</sub> Electrodes, Chemphyschem, 20 (2019) 838-847.

## **Chapter 4 : 3D MXene/carbon nanocage/sulfur cathode with synergistic effect for dual-functional of high conductivity and strong polysulfides adsorption towards Li-S batteries**

### **4.1 Introduction**

In previous chapter 3, a TiC-TiO<sub>2</sub>/SWCNT/S composite was fabricated successfully. As a mixed cathode, it shows a high initial capacity, stable long-cycle performance and excellent rate performance for Li-S batteries. However, compared to some carbon-based cathodes with a superb performance in the academic circle [1], our TiC-TiO<sub>2</sub>/SWCNT/S hybrid cathode only possesses a relatively low sulfur loading (<1 mg·cm<sup>-2</sup>), which is not beneficial to high energy density after battery-packaging for commercial applications. Therefore, we aim to explore a new material system to handle electrodes with high sulfur loading.

In addition, most carbon-based materials have been investigated for many years but can only tackle one main drawbacks of Li-S batteries, conductivity or polysulfides adsorption. Challenges arose in finding solutions to solve all main drawbacks effectively is one of the primary goals of Li-S batteries. An inorganic two-dimensional Ti<sub>3</sub>C<sub>2</sub>T<sub>x</sub> MXene may be a solution, which has emerged in Li-S battery electrodes in recent years. The advantage in the use of MXene in Li-S batteries lies in their metallic conductivity and abundant functional groups (-O, -OH and -F), which can adsorb polysulfides and suppress the "shuttle effect" effectively [2, 3]. Nevertheless, the pristine MXene material tends to stack tightly and reduce the specific surface area,

making its advantages less appealing [4, 5]. Therefore, mixing other materials with MXene is a common and effective way to tackle these drawbacks.

In the present study, we fabricate a 3D  $\text{Ti}_3\text{C}_2\text{T}_x$  MXene-carbon nanocage-sulfur composite (MXene/CNC/S) for Li-S batteries to achieve high conductivity at a high sulfur content (~80 wt%). The combination of MXene and carbon nanocage is attractive due to the synergistic effect. MXene is being used successfully in improving polysulfides adsorption and CNC has excellent conductivity close to acetylene black [6]. Moreover, the fabrication process just has three simple steps and is potentially scaled up in industrial applications. Due to the excellent conductivity and strong polysulfides adsorption, the designed MXene/CNC/S 7:3 shows  $630.5 \text{ mAh}\cdot\text{g}^{-1}$  at 4 C for rate performance and remains  $823.8 \text{ mAh}\cdot\text{g}^{-1}$  after 100 cycles at 0.1 C. Another attractive feature of this work is achieving a high sulfur content of close to 80 % through a synergistic effect of MXene and CNC, as well as a higher sulfur loading ( $\sim 1.5 \text{ mg}\cdot\text{cm}^{-2}$ ) compared to chapter 3. A possible mechanism that might help to understand the excellent electrochemical performance of Li-S batteries is discussed.

Meanwhile, in order to further optimize the process of battery assembling and study material features, parameters research of different sulfur loading, sulfur content and the ratio between electrolyte and sulfur (E/S ratio) were carried out. We try to find the most appropriate sulfur loading and electrolyte ratio for MXene/CNC/S cathode for both outstanding performance and effective application value.

The research work in chapter 4 was designed and carried out under the supervision of Prof. Li Yang, Prof. Cezhou Zhao and Prof. Pengfei Song. The result shown in this

chapter was published on Journal of Alloys and Compounds, 2022, 895: 162586 (DOI: 10.1016/j.jallcom.2021.162586). The manuscript was drafted by me and corrected by Dr. Li Yang, Dr. Cezhou Zhao and Dr. Pengfei Song. The rest of the authors helped with some supplementary works, including idea guidance, data analysis, and experimental data checking.

## **4.2. Experiment part**

### **4.2.1 Fabrication of $Ti_3C_2T_x$ MXene**

$Ti_3C_2T_x$  MXene was synthesized via an acid etching method according to earlier work [7]. Briefly, 2 g lithium fluoride (LiF) was dissolved in 40 mL hydrogen chloride (HCl, 12 M) under magnetic stirring for 30 min to form a homogeneous acid HF solution. 2 g  $Ti_3AlC_2$  powder was added slowly into the above solution and heated to 35 °C for 24 h to etch Al atoms under magnetic stirring. Then, the solution was washed with deionized (DI) water several times by centrifugation at 5500 rpm for 5 min until the pH of the solution approached 6. Next, the ethanol was used as the intercalator for the MXene, and its mixed solution was under ultrasonic for 1.5 h. Later, the delaminated MXene sheets were collected by centrifugation process. Finally, the delaminated  $Ti_3C_2T_x$  MXene solution (about 10 mg·mL<sup>-1</sup>) was obtained with a black-green colour.

### **4.2.2 Preparation of carbon nanocage (CNC)**

A carbon nanocage material was prepared via a simple carbonization and etching method reported in previous work [8]. Briefly, the sodium citrate anhydrous was under ball-milling for 12 h. The white powder with grinding refinement was heated for 2 h at 800 °C under a pure argon atmosphere. Then, 15 wt% HCl solution was used for etching

the carbonized powder for 24 h under magnetic stirring. Next, the CNC powder was achieved by filtrating and washing with DI water several times and then vacuum drying at 80 °C for 6 h.

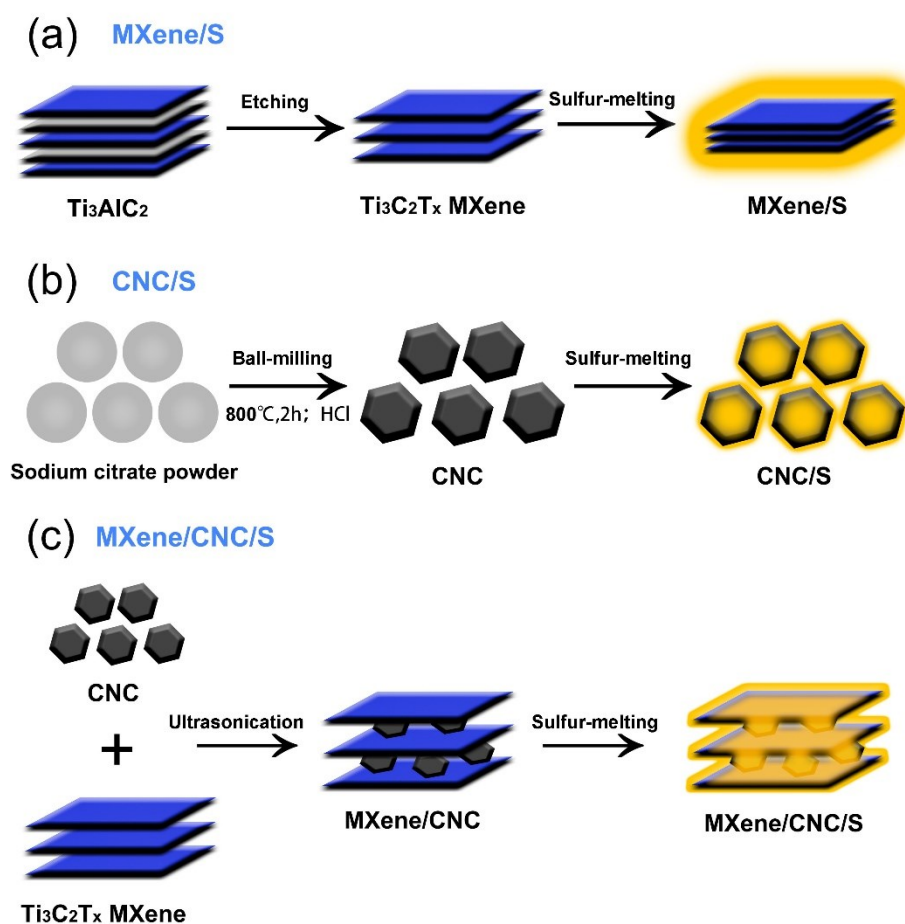
#### 4.2.3 Preparation of MXene/CNC and MXene/CNC/S composite

Firstly, 70 mg CNC was added into 7 mL  $Ti_3C_2T_x$  MXene solution. Secondly, the solution was under ultrasonic treatment for 30 min to effectively disperse MXene and CNC. Thirdly, the solution was dried at 60 °C for 48 h in a vacuum drying oven. The remaining composite powders were denoted as MXene/CNC 7:7. Similarly, 50 mg, 30 mg, and 10 mg CNC were added into 7 mL  $Ti_3C_2T_x$  MXene solution. Their final composites were denoted as MXene/CNC 7:5, MXene/CNC 7:3 and MXene/CNC 7:1, respectively.

A melting-diffusion method was used for growing sulfur for all the composites above. Briefly, sublimed sulfur was mixed into four different composites independently with a 4:1 ratio by weight, and these mixtures were ground thoroughly. After that, the mixtures were put into different reaction stills, and all the reaction stills were filled with argon to prevent the oxidation of MXene. After heating them at 155 °C for 12 h, the final composites were obtained, which were named as MXene/CNC/S 7:7, MXene/CNC/S 7:5, MXene/CNC/S 7:3 and MXene/CNC/S 7:1. The schematic diagrams for the preparation of these materials are shown in **Figure 4.1**

For comparison, MXene/S and CNC/S were fabricated via the same melting-diffusion method. Briefly,  $Ti_3C_2T_x$  MXene solution was dried at 60 °C for 48 h. Then, sulfur was mixed into MXene or CNC powder with a 4:1 ratio by weight. The mixture

was heated at 155 °C for 12 h, and the final form of MXene/S and CNC/S were made.



**Figure 4.1** Synthesis procedure of (a) CNC/S, (b) MXene/S and (c) MXene/CNC/S.

#### 4.2.4 Materials characterization and electrochemical measurements

The microstructure and morphology of MXene/CNC/S composites and other control groups were characterized by scanning electron microscope (SEM, JEOL JSM-6510), field emission scanning electron microscope (FE-SEM, Regulus SU8230), and transmission electron microscope (TEM, FEI Tecnai G2 F20) with scanning transmission electron microscopy (STEM) and selected area electron diffraction (SAED) function. The crystal structures of materials were tested by the X-ray diffraction (XRD, D8 Advance, Bruker, with Cu  $K\alpha$  radiation,  $\lambda = 1.5406 \text{ \AA}$ ) analysis from 4 ° to 75 °. Raman spectroscopy was performed on a HORIBA XploRA system



with a 532 nm laser. Thermogravimetric analysis (TGA, NETZSCH STA 449 F3) was performed from 28-500 °C at a heating rate of 10 °C per minute in the N<sub>2</sub> atmosphere to determine the content of elemental sulfur. X-ray photoelectron spectroscopy (XPS, ESCALAB 250Xi, Thermo scientific) was used to characterize surface functional groups and chemical bonding states. The specific surface area and the pore size distribution of the product were tested by the Brunauer-Emmett-Teller (BET, 3H-2000PS2) through recording N<sub>2</sub> adsorption-desorption isotherms at 77.3 K.

CR2032-type coin cells were assembled in a glove box (Vigor Sci-Lab) under an Ar-filled atmosphere and used for electrochemical characterization. MXene/CNC/S composites were used as the cathode, and lithium tablets were used as the anode, separated by the Celgard 2400 separator. The electrolyte was lithium bis (trifluoromethane sulfonyl) imide (1.0 M) dissolved in a mixture of a lithium salt (LiTFSI) in dioxolane (DOL) and dimethoxyethane (DME) (1:1 by volume) with a 1.0 wt% LiNO<sub>3</sub> additive. To prepare the cathode, a slurry was obtained by mixing and stirring the as-prepared MXene/CNC/S composite, conductive agent (super P) and binder (polyvinyl difluoride) with the mass ratio of 8:1:1 in N-methyl-2-pyrrolidone (NMP). The slurry was coated on the current collector of aluminium foil by the coating machine and vacuum dried for 12 h at 60 °C.

The charge-discharge cycle performance tests of batteries were performed using the Neware CT-4008 battery-testing instrument at a 22 °C constant temperature with the voltage window set at 1.7 - 2.8 V. The cyclic voltammetry (CV) was measured in the voltage range of 1.7 - 2.8 V (vs. Li<sup>+</sup>/Li) at the scan rate of 0.1 mV·s<sup>-1</sup>, and the

electrochemical impedance spectroscopy (EIS) was tested in the frequency ranging from 15 mHz to 100 kHz with an electrochemical workstation (Autolab PGSTAT302N).

After the cathode materials preparation, we investigated sulfur loading, sulfur content and the ratio between electrolyte and sulfur for MXene/CNC/S. Sulfur loading was controlled by the thickness of the slurry coating. The sulfur loading of  $0.5 \text{ mg}\cdot\text{cm}^{-2}$ ,  $1.5 \text{ mg}\cdot\text{cm}^{-2}$  and  $2.5 \text{ mg}\cdot\text{cm}^{-2}$  were adopted, corresponding to low, medium and high sulfur loading, all under the 80 % sulfur content. Especially,  $0.5 \text{ mg}\cdot\text{cm}^{-2}$  sulfur loading and 60 % sulfur content, and  $2.5 \text{ mg}\cdot\text{cm}^{-2}$  sulfur loading and 90 % sulfur content were tested for an extreme situation. These were named as  $2.5 \text{ mg}\cdot\text{cm}^{-2}$  90 % and  $0.5 \text{ mg}\cdot\text{cm}^{-2}$  60 %. The sulfur content was controlled in the sulfur melting process by adjusting the mass ratio between sulfur and host material. During the battery assembling process, we add the amount of electrolyte with  $20 \mu\text{l}\cdot\text{mg}^{-1}$ ,  $40 \mu\text{l}\cdot\text{mg}^{-1}$  and  $60 \mu\text{l}\cdot\text{mg}^{-1}$  sulfur, referring to the weight of active sulfur. All the parameters research focus on MXene/CNC/S composite for the performance of Li-S batteries.

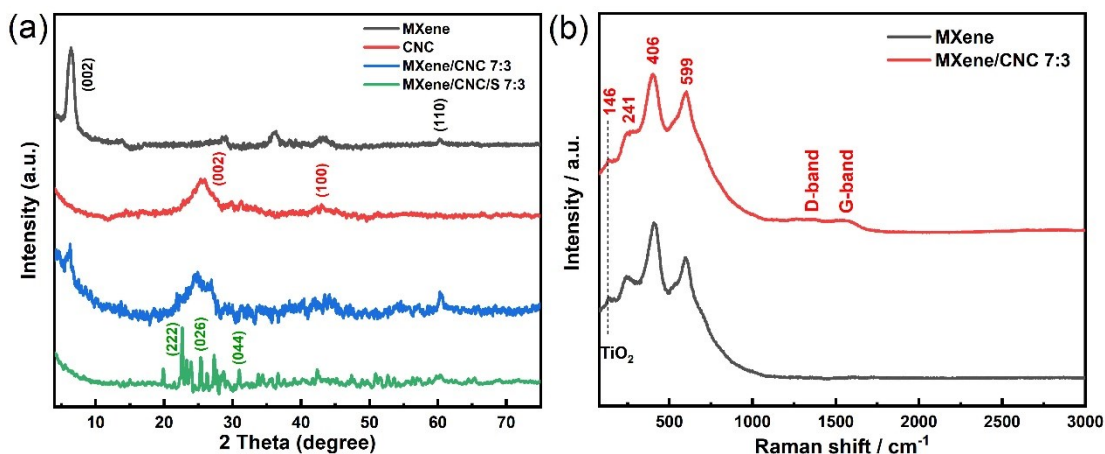
### 4.3. Results and discussion

#### 4.3.1 Comparison of CNC/S, MXene/S and MXene/CNC/S composites

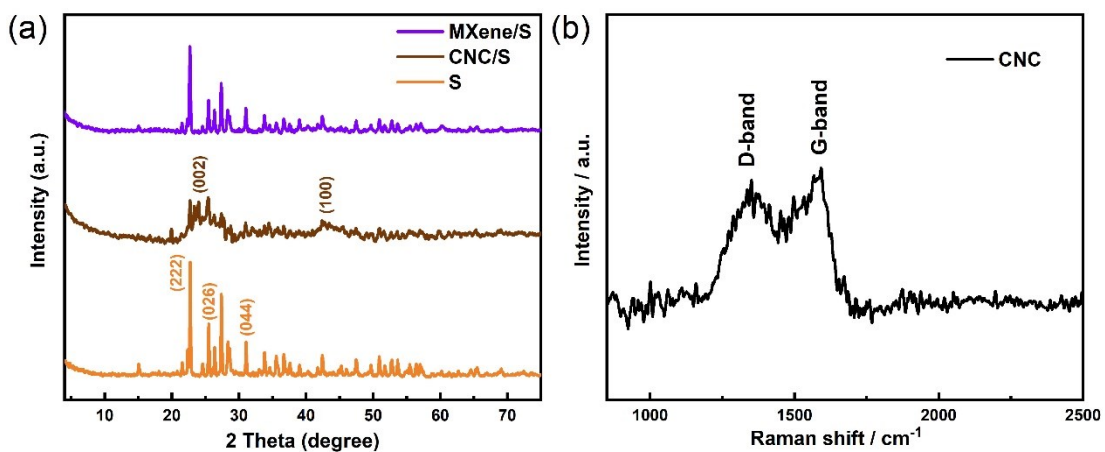
The crystalline structure of as-prepared MXene/CNC/S 7:3 and other samples was characterized by XRD patterns. In **Figure 4.2a**, for the pristine MXene (black line), two characteristic peaks at  $6.4^\circ$  and  $61.3^\circ$  suggest the (002) and (110) crystal planes of  $\text{Ti}_3\text{C}_2\text{T}_x$  MXene [9, 10]. For the pristine CNC (red line), there is a broad peak located at around  $24^\circ$ , which indicates a graphitic (002) facet of carbon [6]. Concerning MXene/CNC (blue line), this broad peak (002) of CNC is visible, suggesting that

MXene and CNC are dispersed uniformly together. The peak at  $6.4^\circ$  for (002) of MXene is less pronounced, whereas the high angle peak at  $61.3^\circ$  is still strong. However, for MXene/CNC/S 7:3 composite (green line), the characteristic peaks of MXene and CNC disappear, the spectrum shows many peaks of sulfur, such as (222), (206) and (044) [11]. These peaks can refer to pure sulfur in **Figure 4.3a**. For comparison, it can be seen that all the sulfur peaks of MXene/S (purple line) are stronger than those of CNC/S (brown line) (**Figure 4.3a**). These results imply that there may have a large amount of crystalline sulfur on the MXene surface of MXene/S composite, while amorphous sulfur particles are dominant on the CNC surface of CNC/S composite [12].

The structure of MXene/CNC 7:3, MXene and CNC are further evaluated by Raman spectroscopy. In **Figure 4.2b**, four strong peaks at 146, 241, 406 and  $599\text{ cm}^{-1}$  are ascribed to the vibration of  $\text{Ti}_3\text{C}_2\text{T}_x$ , and the peak at  $146\text{ cm}^{-1}$  corresponds to the oxidation of MXene [13, 14]. For pure CNC (shown in **Figure 4.3b**), there are two weak peaks: D-band ( $1305\text{ cm}^{-1}$ ) and G-band ( $1570\text{ cm}^{-1}$ ), corresponding to the graphite structure of carbon. The intensity ratio of the D-band and G-band is calculated to be 0.92, indicating a high graphitization of CNC [6]. For MXene/CNC 7:3 composite, the D-band and G-band are weak (**Figure 4.2b**) and other peaks show no markable change (red line) if compared to pure MXene, indicating that the content of MXene is dominant in MXene/CNC 7:3 composite.



**Figure 4.2** (a) XRD patterns of four different materials; (b) Raman spectra of MXene and MXene/CNC 7:3.

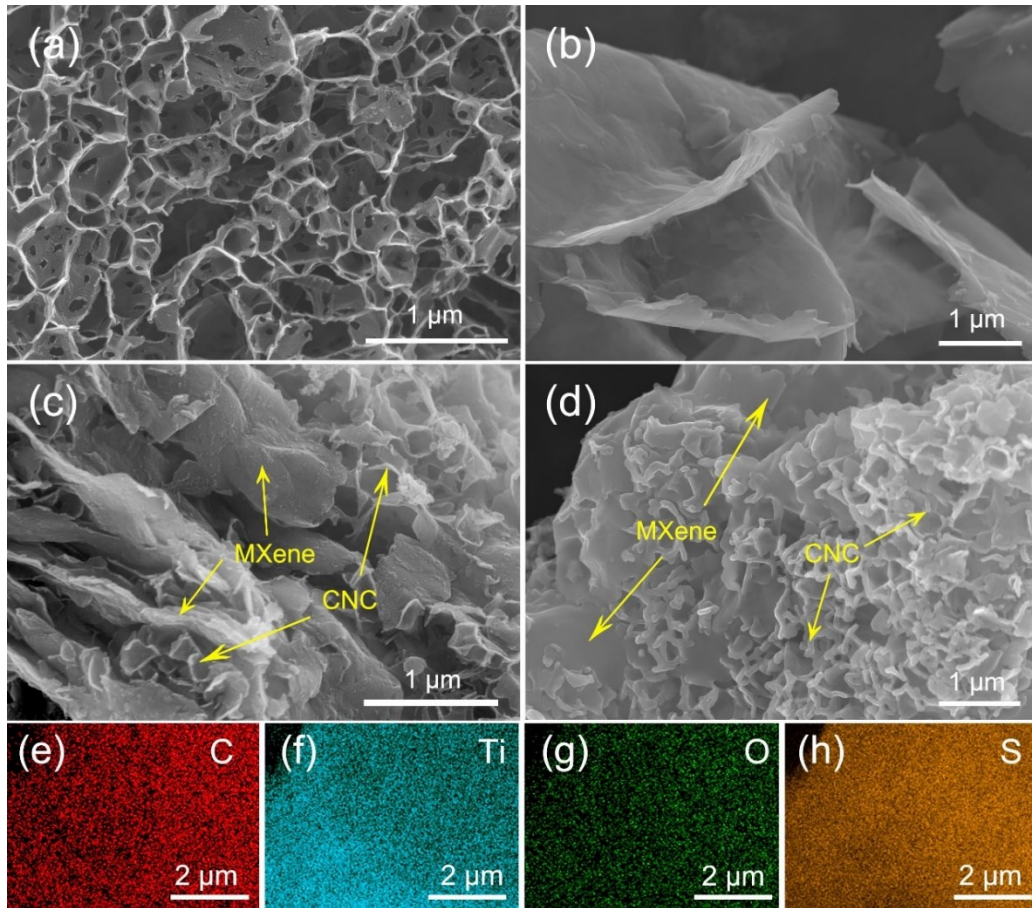


**Figure 4.3** (a) XRD patterns of MXene/S, CNC/S and S; (b) Raman spectrum of CNC.

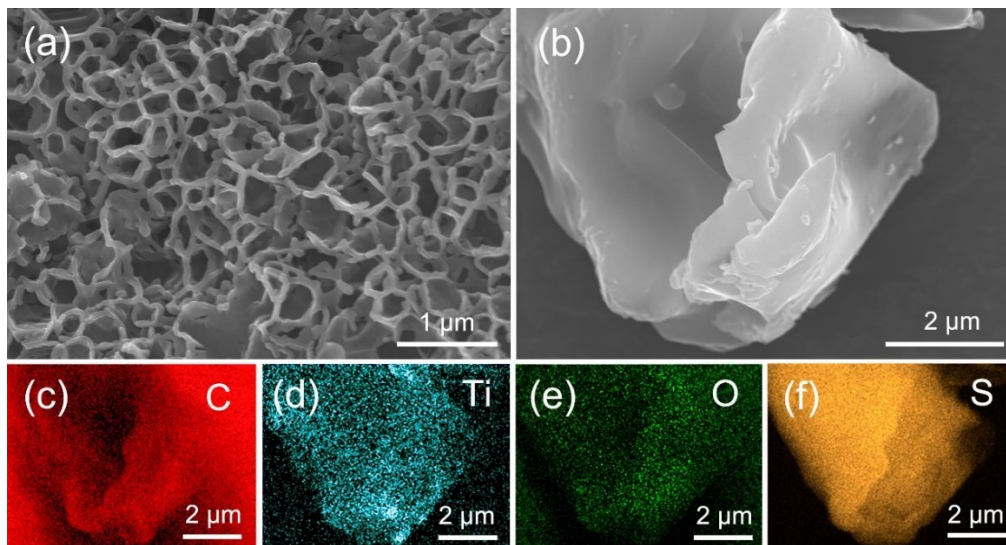
To reveal the morphological evolution of the MXene/CNC/S 7:3 composite, the FE-SEM images of CNC, MXene, MXene/CNC 7:3 and MXene/CNC/S 7:3 composites are collected. It is clear that the cage-shaped carbon skeletons are formed similar to the previous work [6] (as shown in **Figure 4.4a**). The size of CNC is range from 200 - 500 nm. The as-prepared  $\text{Ti}_3\text{C}_2\text{T}_x$  MXene material exhibits a curled-flake structure with several layered sheets (**Figure 4.4b**), which is further confirmed in the TEM images of **Figure 4.6b** and **Figure 4.7a**. In **Figure 4.4c**, it seems that after the ultrasonic process, MXene and CNC are dispersed uniformly and interlaced together.

When sulfur melts and grows on the MXene/CNC 7:3 composite, the surface of MXene/CNC/S 7:3 composite is covered by a layer of sulfur nanoparticles and appears more rounded (**Figure 4.4d**). The EDS mapping images of the area marked in **Figure 4.4d** correspond to the C, Ti, O and S elements as shown in **Figure 4.4e-h**. All the images clearly present a uniform distribution and the final MXene/CNC/S 7:3 composite yields a continuously conductive network of MXene and CNC.

The controlled groups of CNC/S and MXene/S composites are illustrated in **Figure 4.5**. In the case of CNC/S composite (**Figure 4.5a**), a thicker cage wall due to the sulfur melted on the CNC surface is observed, which is similar to the MXene/CNC/S 7:3 as shown in **Figure 4.4d**. Interestingly, the MXene/S composite in **Figure 4.5b** and **Figure 4.8a** displays a completely different morphology and a large particle with several micrometers is formed. The corresponding elemental mapping images of C, Ti, O and S (**Figure 4.5c-f** and **Figure 4.8c-f**) present a uniform distribution on the particle. However, MXene sheets tend to restack more easily when heating such as the melting sulfur process [3]. Hence, the layered structure of MXene is not preserved instead of aggregating to form large particles. These observations highlight that the introduction of CNC is important here to avoid restacking of MXene and retain a conductive network.



**Figure 4.4** FE-SEM images of (a) CNC, (b) MXene, (c) MXene/CNC 7:3 and (d) MXene/CNC/S 7:3. Corresponding EDS mappings of (d) area for elements of (e) C, (f) Ti, (g) O and (h) S, respectively.



**Figure 4.5** FE-SEM images of (a) CNC/S and (b) MXene/S. (c-f) Corresponding EDS mapping of (b) area for (c) C, (d) Ti, (e) O and (f) S elements.

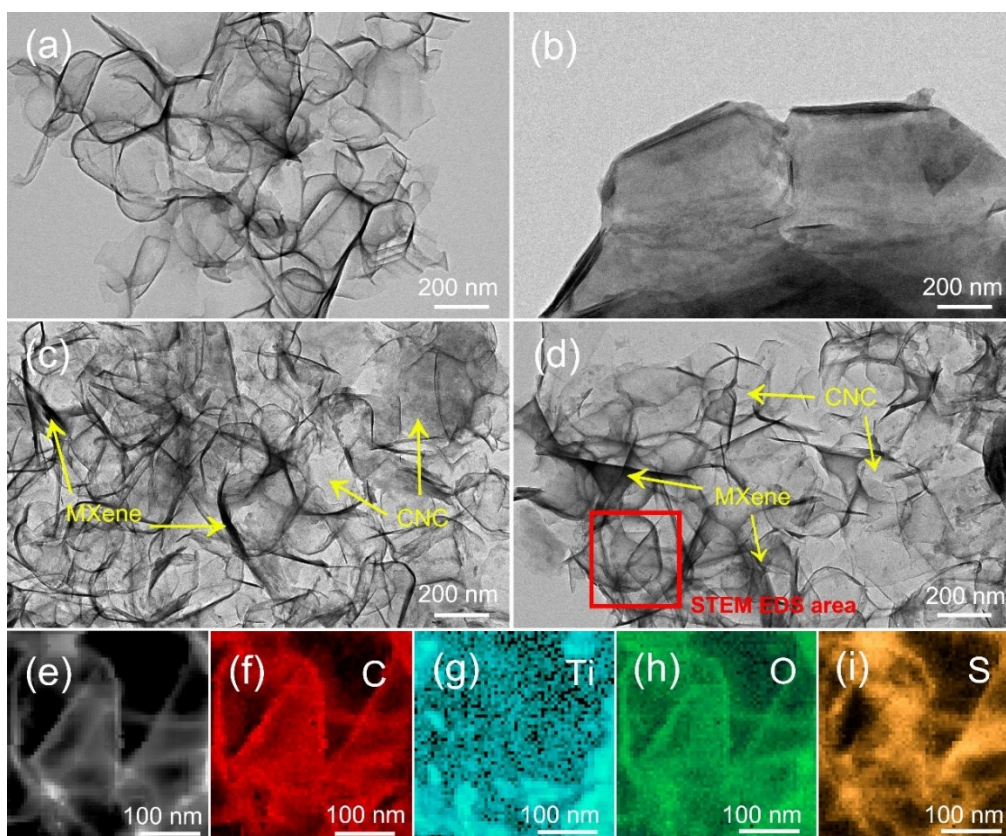
To observe the nanostructures of different samples more clearly, TEM, STEM and STEM EDS mapping are performed. In **Figure 4.6a**, the shape of CNC appears as a rough polygon, similar to the FE-SEM image (**Figure 4.4a**). Some small and thin nanosheets are attached to the CNC edge, which is consistent with the previous work [8]. **Figure 4.7b** shows the TEM image of CNC/S composite. We found no obvious change compared to pristine CNC. The STEM image and selected area of STEM mapping for CNC/S are presented in **Figure 4.7c** and **Figure 4.7d**. All the elements (C, O and S) are dispersed evenly in the composite (**Figure 4.7e-g**), indicating sulfur particles on the surface of CNC are relatively small.

The stacked structure of MXene sheets is seen in **Figure 4.6b**, while the enlarged image in **Figure 4.7a** presents several layered structure of MXene. Nevertheless, this structure is easy to collapse during the heating and drying process later, so mixing another material to support the structure of MXene is necessary [15]. For MXene/CNC 7:3 composite, many relatively large MXene sheets intersect and separate the CNC in a good dispersion manner (**Figure 4.6c**). These large MXene sheets appear different from those small sheets attached to CNC (**Figure 4.6a**). When the sulfur grows on the surface of MXene/CNC 7:3 composite, again there is no obvious change in TEM image (**Figure 4.6d**) where compared to the MXene/CNC/S 7:3 (**Figure 4.6c**). This result is in a good agreement with the observation of CNC/S composite, indicating the size of sulfur nanoparticle in the composite is tiny and it offers an effective way for the high utilization of sulfur. Indeed, the size of sulfur particles is less than 5 nm according to Barrett-Joyner-Halenda (BJH) data (shown later in Fig.6b). The uniform dispersion and

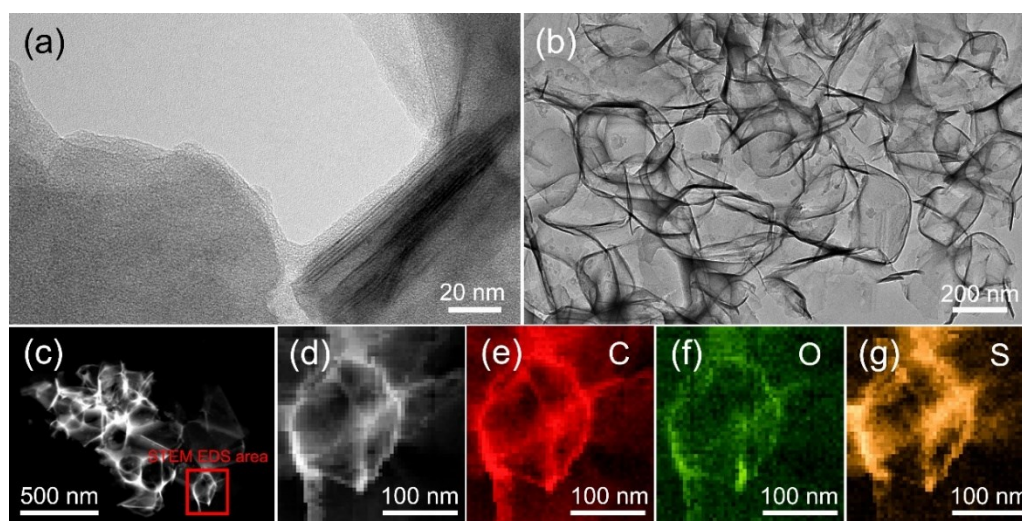
the nano size of sulfur particles are attributed to the high specific surface area and porous structure of MXene/CNC/S during the sulfur melting process [16-18].

**Figure 4.6e** is the selected area for STEM mapping of MXene/CNC/S 7:3. From **Figure 4.6f-i**, it is clear that C, Ti, O and S elements distribute uniformly in the composite. Corresponding SAED patterns of pristine MXene, CNC, MXene/CNC 7:3 and MXene/CNC/S 7:3 are presented in **Figure 4.9**. For CNC, **Figure 4.9a** shows two weak diffraction rings assigned to (100) and (002) of carbon, while for pure MXene sheets dense diffraction spots form several rings, probably from many stacked single-layered MXene (**Figure 4.9b**) [6, 19]. When MXene and CNC are mixed together, the diffraction spots of MXene become weaker, the overall diffraction pattern yields an overlaid rings of MXene and CNC (**Figure 4.9c**). In MXene/CNC/S 7:3 composite, as a large amount of amorphous sulfur was added, the feature of MXene diffraction spots gets further blur and there are no new diffraction signs of sulfur (**Figure 4.9d**) [20, 21].

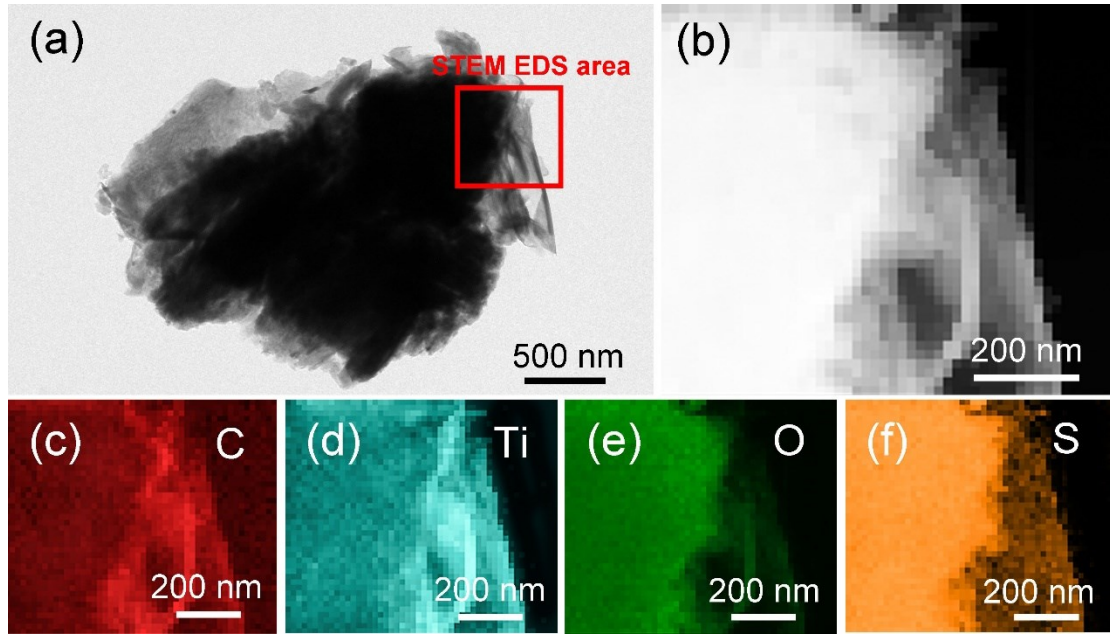




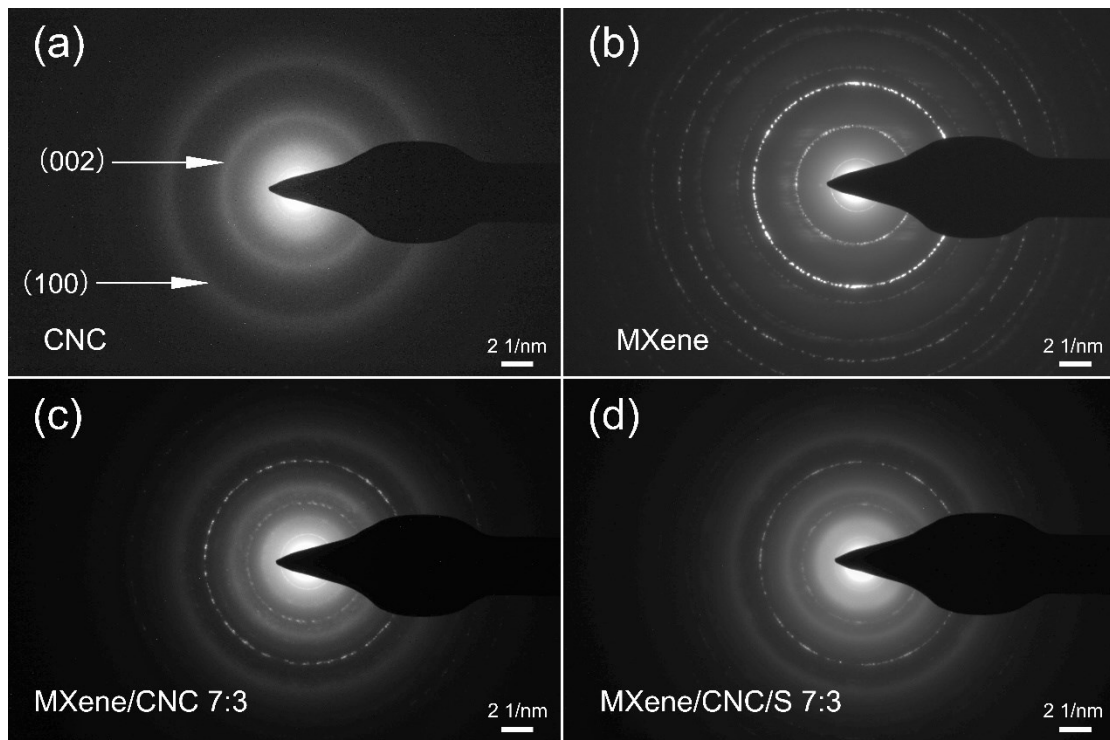
**Figure 4.6** TEM images of (a) CNC, (b) MXene, (c) MXene/CNC 7:3 and (d) MXene/CNC/S 7:3. (e) STEM EDS area (d); corresponding STEM EDS mapping for (f) C, (g) Ti, (h) O and (i) S elements.



**Figure 4.7** TEM images of (a) MXene and (b) CNC/S. (c) STEM image of CNC/S, (d) enlarged STEM EDS area from (c), (e-g) corresponding STEM EDS mapping of C, O and S elements.



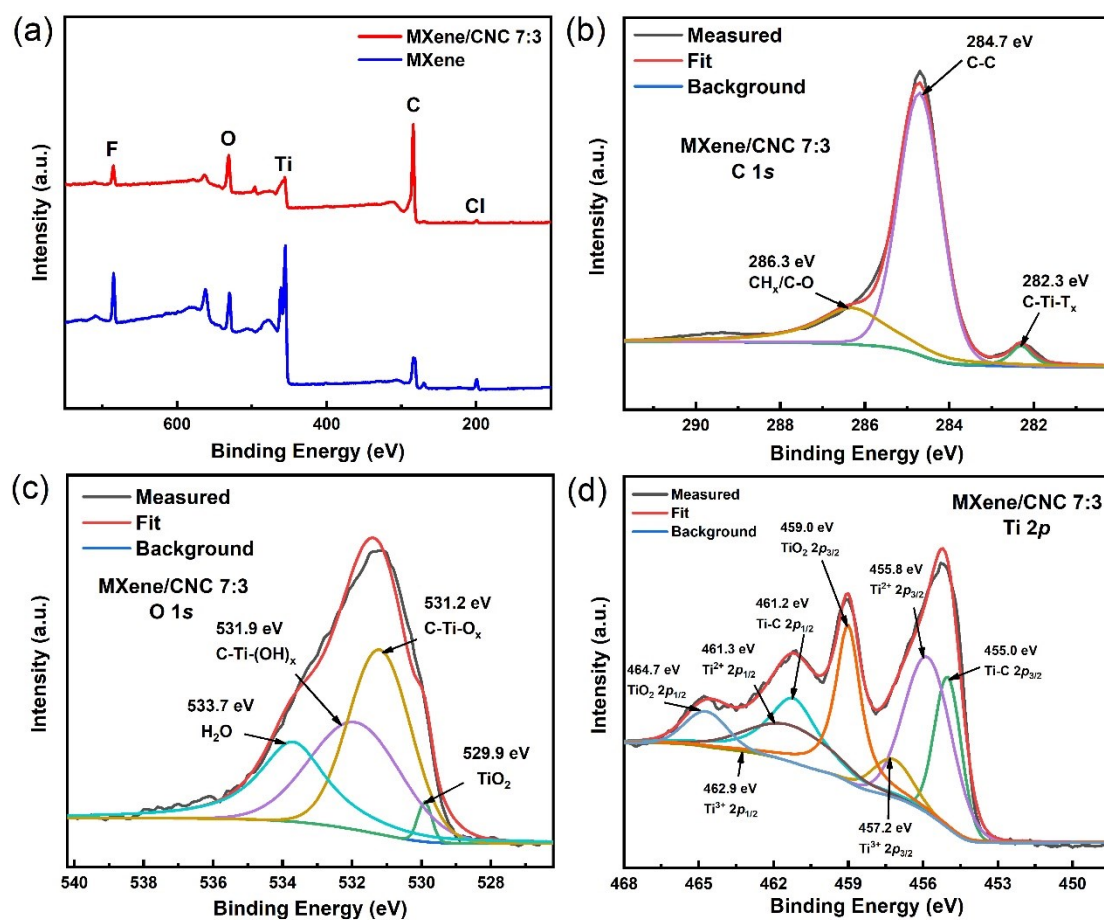
**Figure 4.8** TEM image of (a) MXene/S and (b) STEM EDS area of MXene/S, (c-f) corresponding STEM EDS mapping of C, Ti, O and S elements.



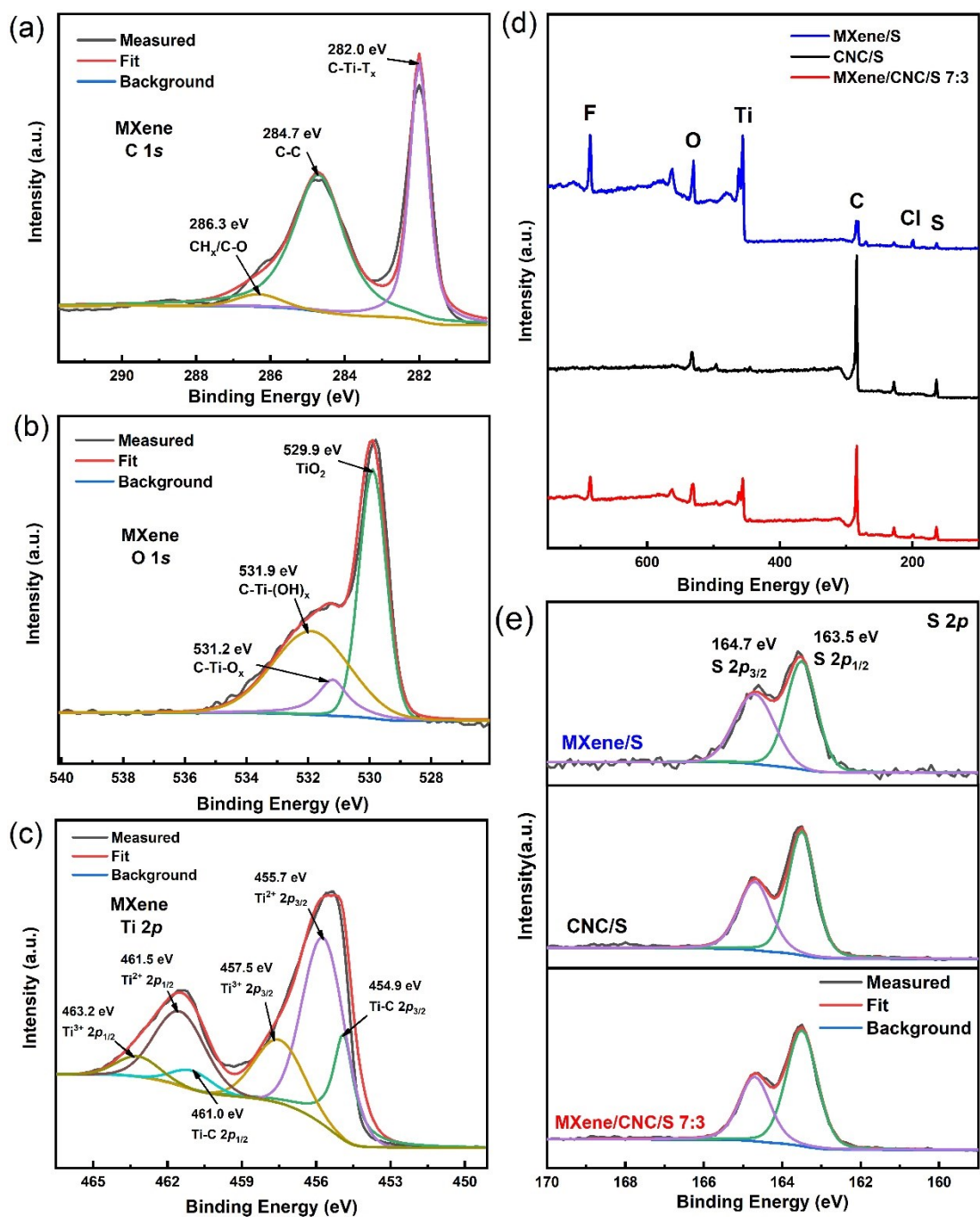
**Figure 4.9** SAED patterns of (a) CNC, (b) MXene, (c) MXene/CNC 7:3 and (d) MXene/CNC/S 7:3.

XPS spectroscopy is used to characterize the chemical environment of the composite. **Figure 4.10a** compares the XPS survey spectra of MXene/CNC 7:3 and MXene. Apparently, the MXene mainly consists of C, Ti and O elements, and other functional groups, such as F element and Cl element [2]. With the addition of CNC, the intensity of the C peak increases significantly and Ti peak reduces accordingly. Other elements are not affected. **Figure 4.10b-d** are the narrow scans of C 1s, O 1s, and Ti 2p for Mxene/CNC 7:3. For C 1s pattern, agreed with previous work [22], peaks at 282.3 eV, 284.7 eV and 286.3 eV are ascribed as C-Ti-Ti<sub>x</sub>, C-C and CH<sub>x</sub>/C-O bonds, respectively (**Figure 4.10b**). The high-resolution O 1s profile at 529.9 eV, 531.2 eV and 531.9 eV could be attributed to TiO<sub>2</sub>, C-Ti-O<sub>x</sub> and C-Ti(OH)<sub>x</sub> components. Meanwhile, the characteristic peak at 533.7 eV assigned to H<sub>2</sub>O is originated from the strong hydroscopicity of CNC with a high surface specific area [8]. (**Figure 4.10c**). The Ti 2p result is more complicated. There are three different components, which could be divided into three 2p<sub>1/2</sub> peaks and three 2p<sub>3/2</sub> peaks, confirming the formation of MXene (**Figure 4.10d**) [23]. The scan of different elements for pristine MXene is shown in **Figure 4.11a-c** as a comparison. Most functional groups are in accordance with Mxene/CNC 7:3, and just some contents are different. For example, without CNC, the content of the C-C bond in C 1s is less and there is no peak of H<sub>2</sub>O in O 1s spectrum. After melting the sulfur, characteristic peaks of sulfur are observed in all the composites as shown in **Figure 4.11d**. For the narrow scan of S 2p in **Figure 4.11e**, no S-Ti bond (162.3 eV) is observed. The peaks observed at 163.5 and 164.7 eV can be attributed to the S-S bond with 2p<sub>1/2</sub> and 2p<sub>3/2</sub> species. These results imply that no chemical bond

was formed during the melting process and the sulfur exists as an elemental form in these composites [15, 24].



**Figure 4.10** (a) The XPS survey spectra for MXene and MXene/CNC 7:3; XPS spectra for MXene/CNC 7:3 of (b) C 1s, (c) O 1s and (d) Ti 2p.



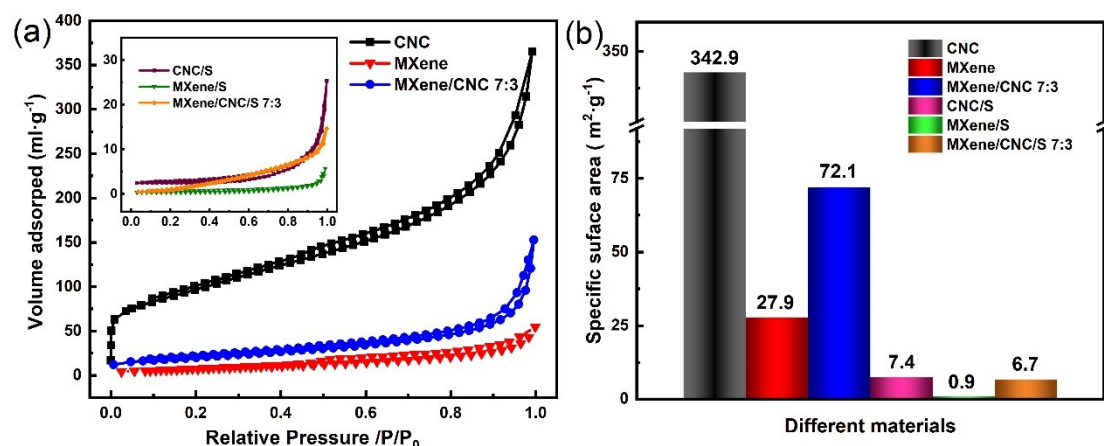
**Figure 4.11** The XPS spectra for MXene of (a) C 1s, (b) O 1s and (c) Ti 2p. (d) The XPS survey spectra, (e) S 2p narrow scans for MXene/S, CNC/S and MXene/CNC/S 7:3.

The specific surface areas of different materials are calculated by Brunauer-Emmett-Teller (BET) method. In Fig. **Figure 4.12b**, CNC presents the highest value of  $342.9 \text{ m}^2 \cdot \text{g}^{-1}$ , similar to the previous work [6]. The prepared MXene has a low specific

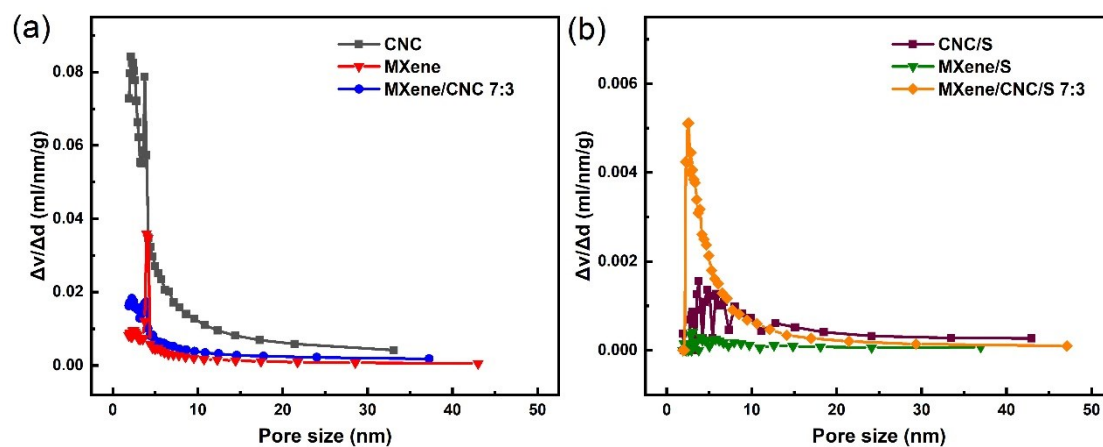
surface area of  $27.9 \text{ m}^2 \cdot \text{g}^{-1}$ , which is associated with the stacking and agglomeration of MXene sheets [3]. Interestingly, when the porous CNC is mixed into the composite, the MXene/CNC 7:3 composite shows a relatively high value of  $72.1 \text{ m}^2 \cdot \text{g}^{-1}$ . A higher specific surface area is beneficial to grow sulfur more uniformly, improve the utilization of sulfur as well as a high sulfur content [25, 26]. For comparison, the specific surface area of MXene/CNC/S 7:3 composite is only  $6.7 \text{ m}^2 \cdot \text{g}^{-1}$  (**Figure 4.12b**), indicating that most of the pores in the composite are filled and the sulfur nanoparticles are growing on the surface. This is supported by the FE-SEM observation as shown in **Figure 4.4d**. CNC/S has a slightly higher specific surface area ( $7.4 \text{ m}^2 \cdot \text{g}^{-1}$ ) but the value is only  $0.9 \text{ m}^2 \cdot \text{g}^{-1}$  for MXene/S. These results prove that a high specific area of host material and final composite can increase sulfur utilization and thus obtain high electrochemical performance.

**Figure 4.13a-b** show pore size distribution data for these six materials. The pore size of CNC mainly distributes from 1 to 5 nm, while MXene has fewer mesopores with just a characteristic 4 nm porous size [27]. For CNC/S, MXene/S and MXene/CNC/S 7:3, the number of micropores and mesopores is much less compared to the sample without sulfur. Particularly, there are no pores smaller than 2.2 nm in MXene/CNC/S 7:3 composite. This is explained by sulfur tends to melt in nano-sized micropores, which also helps to ensure sufficient contact between sulfur and host materials, thus improving the utilization of sulfur in the prepared structure [28, 29]. In addition, it is found that the content of micropores and mesopores is relatively high for MXene/CNC/S 7:3, suggesting mixed CNC and MXene host materials help to maintain

a high specific surface area even after melting sulfur, which further improves the battery performance.



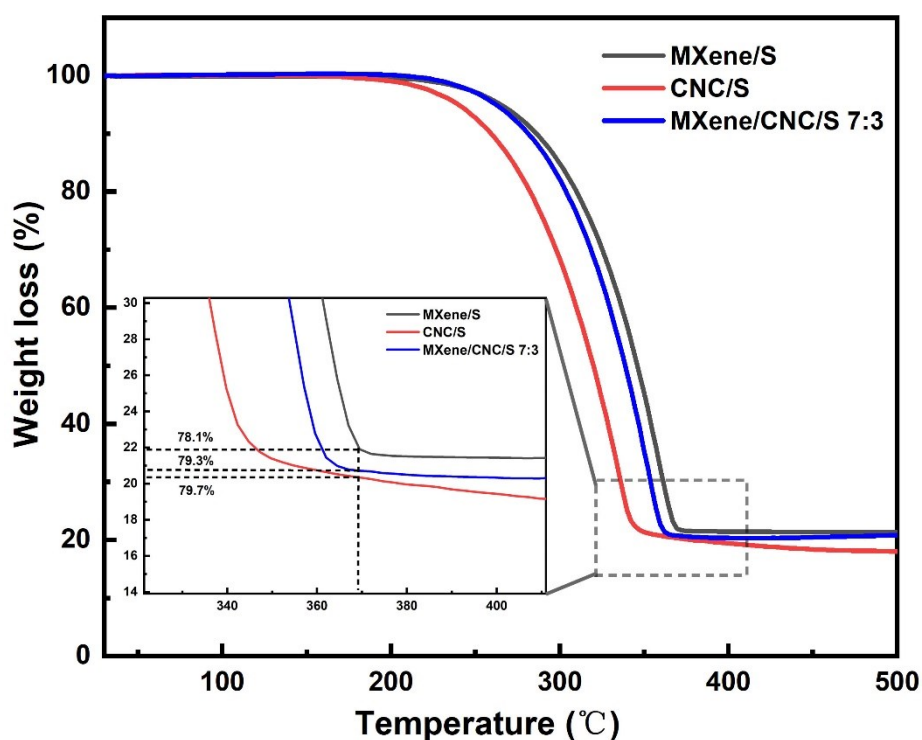
**Figure 4.12** (a)  $N_2$  adsorption/desorption isotherm of CNC, MXene and MXene/CNC 7:3; Insert: CNC/S, MXene/S and MXene/CNC/S 7:3. (b) Specific surface area comparison of six different composites.



**Figure 4.13** Pore size distribution of (a) CNC, MXene and MXene 7:3 and (b) CNC/S, MXene/S and MXene/CNC/S 7:3 after melting sulfur.

We next determine the sulfur content of the composite using thermogravimetric analysis. Based on 4:1 mass ratio of sulfur and host materials (MXene and CNC), the sulfur content of CNC/S, MXene/S and MXene/CNC/S 7:3 is calculated to be 79.7 %, 78.1 % and 79.3 % (**Figure 4.14**). CNC/S presents a slightly higher sulfur content

because CNC porous structure is beneficial to melt sulfur into it [30]. These three composites with sulfur contents of around 80 % are relatively high value in the Li-S batteries field, and it is beneficial to increase the high energy density for the achieved batteries [18].



**Figure 4.14** TGA curves of Mxene/S, CNC/S composite and MXene/CNC/S 7:3 composite. Insert: enlarged area.

The detailed electrochemical performance tests are performed to verify the functions of different materials in composite. **Figure 4.15a** is the first charge-discharge curve for six as-prepared electrodes. The curves for all electrodes appear relatively stable at the small current density of 0.1 C. The length ratio of the first and second discharge plateau is close to 1:3. Particularly, MXene/S shows a short second discharge plateau, indicating the reaction of the second discharge requires more Li ions and is not performed completely, and the stacking of MXene sheets may hinder the transfer of Li

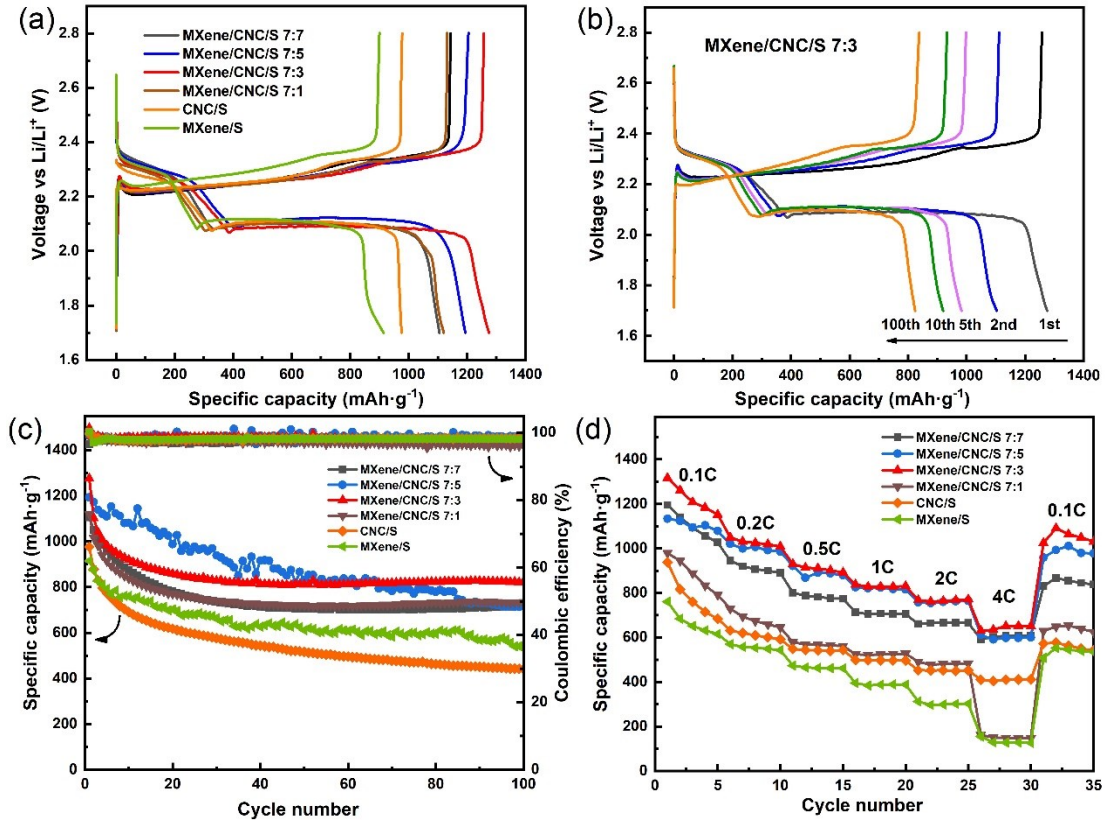


ions [27]. It delivers a low specific capacity of  $914.7 \text{ mAh}\cdot\text{g}^{-1}$ . Similarly, the CNC/S as an electrode yields a capacity below  $1000 \text{ mAh}\cdot\text{g}^{-1}$  and the utilization of sulfur is not satisfactory due to the insufficient polysulfides adsorption and potentially self-discharge, which is different from the CNC as an interlayer [6]. On the contrary, compared to the composites with other CNC amounts, MXene/CNC/S 7:3 has the highest capacity of  $1275.5 \text{ mAh}\cdot\text{g}^{-1}$ .

**Figure 4.15b** is the charge-discharge curves of the 1st, 2nd, 5th, 10th and 100th cycle for MXene/CNC/S 7:3. In the first several cycles, the capacity of the composite drops quickly, but the fading rate reduces significantly and the electrode becomes stable after the 100th cycle. This is rationalized by the fact that the active materials and electrolyte become homogeneous with the cycling process and the chemical reaction turns to be more stable [31]. The decreasing trend of capacity is shown in **Figure 4.15c**. All the composites maintain almost over 98 % coulombic efficiency. After 100 cycles at 0.1 C, MXene/CNC/S 7:3 has a capacity of  $823.8 \text{ mAh}\cdot\text{g}^{-1}$  with a 64.6 % high retention rate. This high and stable performance is attributed to that the addition of CNC promotes the dispersion of MXene and releases the stacking of MXene, which can be seen from the observation of FE-SEM and TEM images (**Figure 4.4** and **Figure 4.6**). On the other hand, MXene provides the extra active sites to adsorb polysulfides during the charge-discharge process and compensates for the insufficient adsorption of polysulfides of CNC [15]. Meanwhile, mixing hydrophilic MXene enables a uniform dispersion of CNC and alleviates the agglomeration of CNC. Such effect of MXene modification for improving cycling performance is similar as Li batteries modified by

metal oxide. Su et al. put forward morphology reconfiguration of manganese oxide hybrid materials to achieve good contact, and no collapsed/agglomerated was seen [32]. Song's group designed ZnO porous nanocomposite with *in-situ* surfaces/interfaces organic encapsulation [33]. Ultrasmall ZnO nanocrystals are crucial for the high initial coulombic efficiency and fully reversible conversion. In the case of MXene/S electrode, owing to large sulfur particles (seen in **Figure 4.5b**) and low sulfur utilization, it presents the lowest first capacity just over  $900 \text{ mAh}\cdot\text{g}^{-1}$ , but it remains  $531.5 \text{ mAh}\cdot\text{g}^{-1}$  with a 58.1 % retention rate after cycles due to strong adsorption of polysulfides of MXene. Due to the insufficient adsorption of polysulfides, the capacity of CNC/S decreases to a low capacity of  $441.0 \text{ mAh}\cdot\text{g}^{-1}$  with only a 45.1 % retention rate in the end.

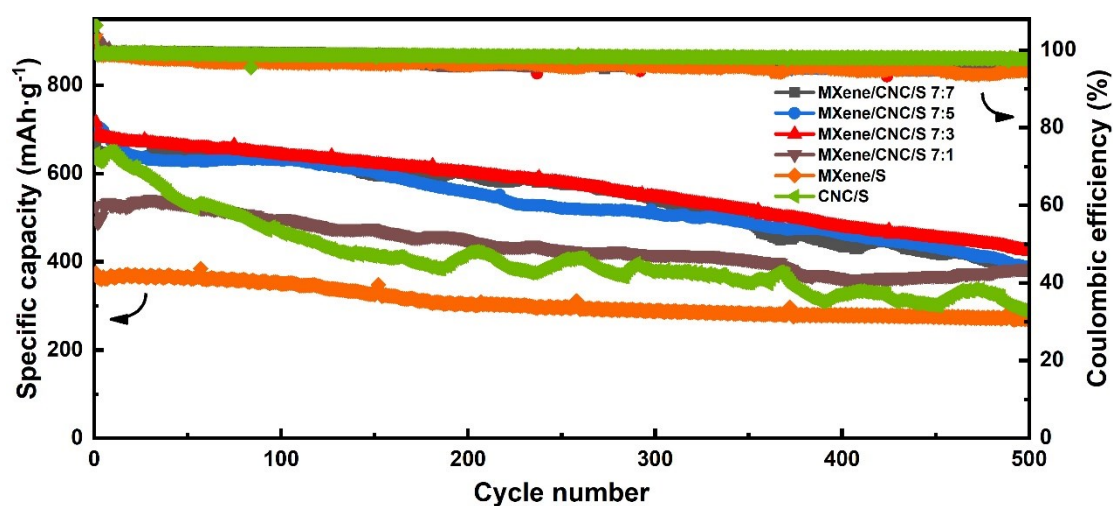
The MXene/CNC/S 7:3 composite also achieves the best rate performance (**Figure 4.15d**). When current density rises to 4 C, the capacity of MXene/CNC/S 7:3 composite remains at a high value of  $630.5 \text{ mAh}\cdot\text{g}^{-1}$  due to its high conductive network (seen in **Figure 4.4d**). By increasing the ratio of CNC in the electrode, the MXene/CNC/S 7:5 composite retains  $611.2 \text{ mAh}\cdot\text{g}^{-1}$  capacity, a slight drop compared to the MXene/CNC/S 7:3 composite. [6]. At the same high current density (4C), the MXene/CNC/S 7:1 and MXene/S composite have relatively low capacities of  $161.8 \text{ mAh}\cdot\text{g}^{-1}$  and  $155.3 \text{ mAh}\cdot\text{g}^{-1}$ , while the CNC/S composite obtains  $410.2 \text{ mAh}\cdot\text{g}^{-1}$ . Interestingly, increasing the amount of CNC in the composite, rather than a continuous increase, the capacity shows a discrete profile. This suggests that there is a threshold percentage of CNC loading to ensure the conductivity of electrodes with high sulfur content (~80%).



**Figure 4.15** (a) First discharge-charge curves of six different cathodes at 0.1 C; (b) The galvanostatic charge-discharge curves for MXene/CNC/S 7:3 at various cycle times; (c) Cyclic performances for six different cathodes at 0.1 C; (d) Rate performances for six different cathodes.

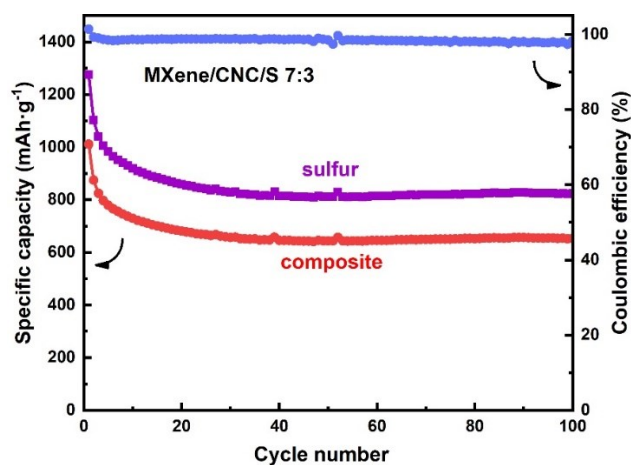
As expected, MXene/CNC/S 7:3 composite presents an outstanding performance for the long-cycle performance at 1 C large current density (**Figure 4.16**). It has 716.2 mAh·g<sup>-1</sup> at the first cycle and retains 423.9 mAh·g<sup>-1</sup> after 500 cycles. In the case of MXene/CNC/S 7:5, a similarly high initial capacity is seen but the decay rate is slightly faster. The CNC/S composite displays a high first-cycle capacity but experiences fast and unstable decay subsequently. When using the MXene/S composite, the initial capacity is at 374.4 mAh·g<sup>-1</sup> and it decays slowly to 270.8 mAh·g<sup>-1</sup> after 500 cycles. This analysis implies that CNC offers good conductivity and MXene is helpful for

polysulfides adsorption and long-time cycling stability. Due to the synergistic effect of CNC and MXene, we conclude that MXene:CNC=7:3 is the best ratio for the composite according to its high initial capacity, rate performance and stable long-cycle performance.



**Figure 4.16** Cyclic performance of six different cathodes at the large current density of 1 C.

According to a high ~80 % sulfur content in the composite, it is calculated that MXene/CNC/S 7:3 owns over 1000 mAh·g<sup>-1</sup> initial specific capacity towards the whole composite (**Figure 4.17**).



**Figure 4.17** Cyclic capacity of MXene/CNC/S 7:3 towards active sulfur and the whole composite.

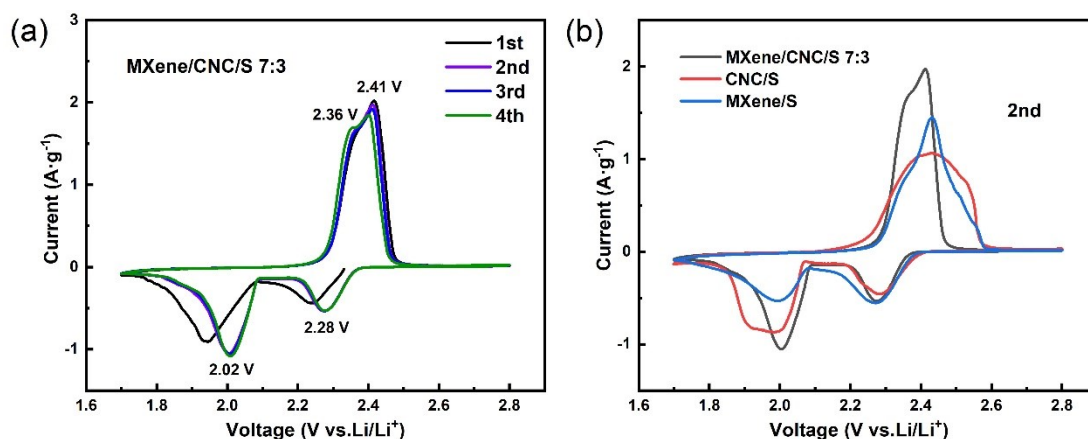
The electrochemical performance results can actually reflect the role of each component in a battery. As shown in **Table 4.1**, if there is only MXene or CNC in the composite, the capacity of MXene/S in the first cycle is very low while the decay rate of CNC/S is fast at 1 C. Further evidence could be referred to the CV curves in **Figure 4.18** and **Figure 4.19**. The large dynamic redox reaction of MXene/CNC/S 7:3 leads to a high specific capacity in cycle performance.

**Table 4.1** Comparison of different cycle performance and retention rates for three different batteries.

	<b>0.1 C (1<sup>st</sup>, 100 cycles retention)</b>	<b>1 C (1<sup>st</sup>, 500 cycles retention)</b>	<b>Rate (0.1 C, 4 C)</b>
<b>MXene/S</b>	914.7 mAh·g <sup>-1</sup> , 58.1 %	374.4 mAh·g <sup>-1</sup> , 72.3 %	760.9 mAh·g <sup>-1</sup> , 155.3 mAh·g <sup>-1</sup>
<b>CNC/S</b>	976.3 mAh·g <sup>-1</sup> , 45.1 %	645.5 mAh·g <sup>-1</sup> , 44.4 %	937.9 mAh·g <sup>-1</sup> , 410.2 mAh·g <sup>-1</sup>
<b>MXene/CNC/S 7:3</b>	1275.5 mAh·g <sup>-1</sup> , 64.6 %	716.2 mAh·g <sup>-1</sup> , 59.2 %	1316.8 mAh·g <sup>-1</sup> , 630.5 mAh·g <sup>-1</sup>

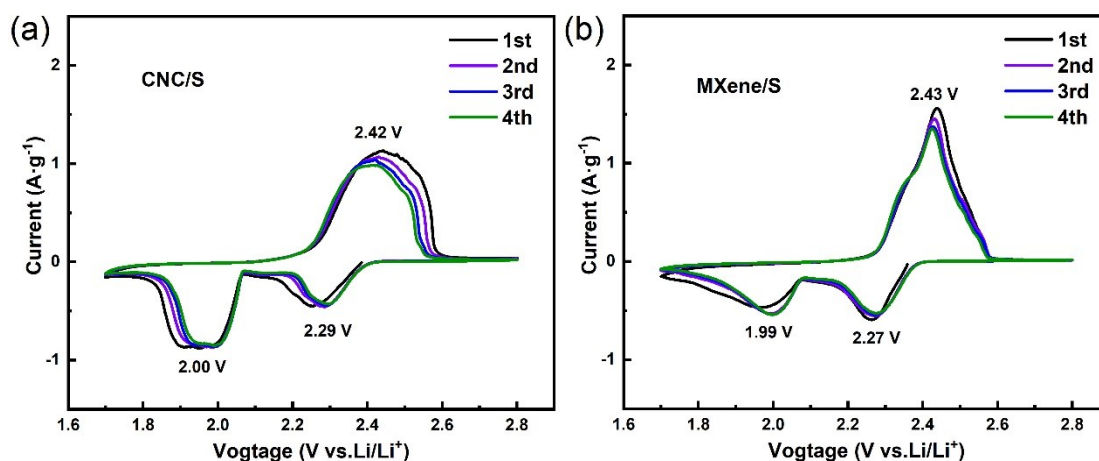
These results above suggest that MXene has high conductivity and strong polysulfides adsorption but tends to stack, therefore, the advantages of MXene are underutilized. CNC has high conductivity and specific surface area but lacks the sufficient ability of polysulfides adsorption, resulting in poor cycle performance. These drawbacks are significant to the battery performance of MXene/S and CNC/S when sulfur content is approaching ~ 80 % high.

In order to investigate the mechanism of the chemical reaction during the charge-discharge process, the cyclic voltammetry (CV) test was conducted. **Figure 4.18a** is the CV curves of MXene/CNC/S 7:3. It is clear that two reduction peaks are located at 2.28 V and 2.02 V, which refer to the two reductions of transferring sulfur to high order polysulfide, and further to  $\text{Li}_2\text{S}_2$  or  $\text{Li}_2\text{S}$ . Two peaks at 2.36 V and 2.41 V correspond to two oxidation reaction processes [34]. During the first discharge process, the polarization phenomenon of reduction is dominant due to the inhomogeneous electrolyte and the unstable chemical reaction. In the following 2-4th cycle, the polarization decreases significantly, and the overlapping features are excellent with sharp redox peaks, suggesting the charge-discharge process and reaction kinetics become stable gradually [35]. This is also a good indicator that this composite has better cycle performance. In **Figure 4.18b**, CNC/S presents relatively broad peaks, which might imply that the chemical reaction occurs slowly and the electrochemical kinetics proceed slowly. Moreover, the bad overlapping feature is related to the poor cycle reversibility of CNC/S [36]. The second reduction peak at 1.99 V of MXene/S is significantly wide and spanned until 1.7 V before disappearing. This phenomenon is explained by large agglomerated sulfur particles, stacking MXene sheets (several micrometers seen in **Figure 4.5b**) and consequently resulting in a slow transition of Li ions and insufficient conductivity of the composite [3], especially considering a 78.1% high sulfur content. It is also noted that MXene/CNC/S 7:3 exists two oxidation, whereas CNC/S and MXene/S exist only one peak, indicating less polarization and more sufficient oxidation in MXene/CNC/S 7:3 composite [10].



**Figure 4.18** (a) CV curves of the MXene/CNC/S 7:3 composite cathode at the scan rate of  $0.1 \text{ mV}\cdot\text{s}^{-1}$  for the 1-4th cycle. (b) Comparison of CV curves of the second cycle for MXene/CNC/S 7:3, CNC/S and MXene/S.

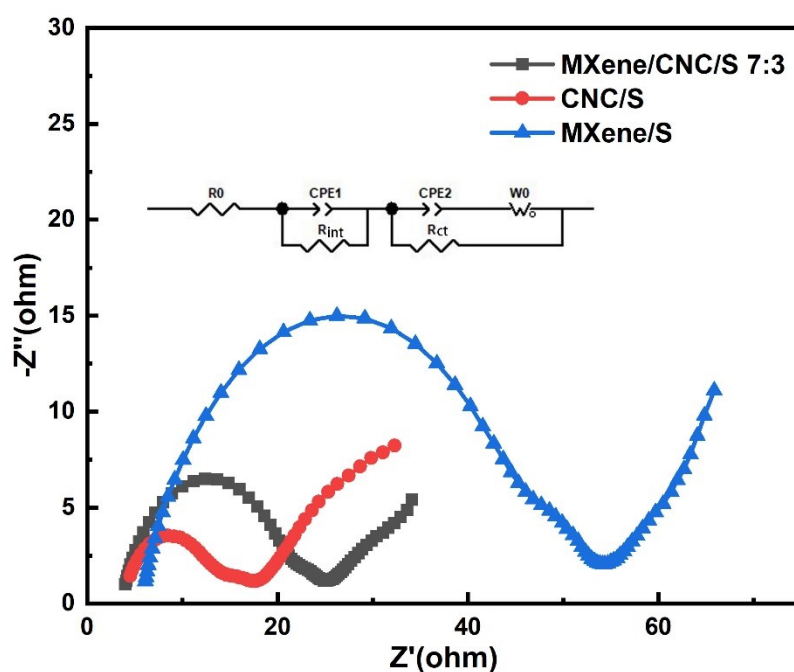
**Figure 4.19** is the CV curves of CNC/S and MXene/S composites at a scan rate of  $0.1 \text{ mV}\cdot\text{s}^{-1}$  for 1-4th cycles. For CNC/S and MXene/S composites, the positions of redox peaks are similar to the ones of MXene/CNC/S 7:3, although a slight shift is observed. Meanwhile, the overlapping feature of curves for MXene/S is better than CNC/S, indicating that the capacity decay of MXene/S is slower than CNC/S.



**Figure 4.19** CV curves of (a) CNC/S and (b) MXene/S cathode at a scan rate of  $0.1 \text{ mV}\cdot\text{s}^{-1}$  for 1-4th cycles.

The impedance results are provided by EIS data in **Figure 4.20**. The semicircle

locates at a high frequency and the extra small arc of a semicircle in the medium frequency correspond to the internal impedance ( $R_{int}$ ) and charge-transfer resistance ( $R_{ct}$ ) of electrodes, respectively. In the low-frequency region, the short line refers to Warburg resistance ( $W_0$ ), indicating the diffusion resistance of Li ions in electrodes [37]. The equivalent circuit is included in **Figure 4.20**. It is calculated that the order of  $R_{int}$  value for CNC/S, MXene/CNC/S 7:3 and MXene/S and composites is  $7.3 \Omega < 17.0 \Omega < 42.1 \Omega$ . This result suggests that CNC/S and MXene/CNC/S 7:3 have a better conductivity compared with MXene/S. Indeed, thanks to the porous structure of CNC and the forming conductive network of MXene/CNC, CNC/S and MXene/CNC/S 7:3 have preferable electrons transfer tunnel. While for the case of MXene/S, large non-conductive sulfur particles and seriously stacked MXene (as shown in **Figure 4.5b**) bring in a significant problem for hindering electrons transfer and limiting the effective conductivity of MXene [6, 15].



**Figure 4.20** Nyquist plots of MXene/CNC/S 7:3, CNC/S and MXene/S. Insert:



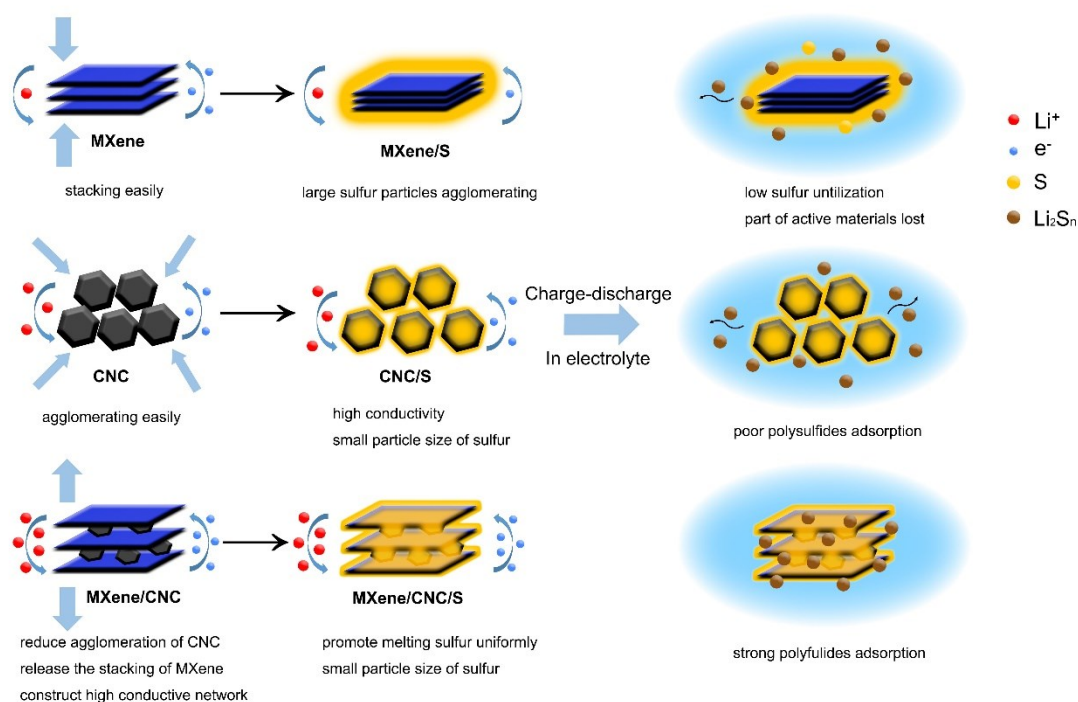
equivalent circuit.

Our experimental data have been considered an enhancing mechanism of battery performance (**Figure 4.21**). The cycle performance and retention rate for different batteries are listed in Table S1 as a comparison of the synergistic effect. Specifically, for the MXene/S sample, the high retention rate but low initial capacity is achieved, which is probably due to the better polysulfides absorption of MXene but low utilization of large sulfur particles. Meanwhile, the CNC/S sample, which possesses high sulfur utilization but insufficient polysulfides adsorption, presents a relatively high initial capacity and low retention rate. Hence, the MXene/CNC/S sample adopts the above good points and avoids the shortcomings, appearing excellent morphology reconfiguration, high conductivity, and strong polysulfides adsorption.

Furthermore, pristine MXene material shows a feature of stacking, which hinders the transfer of Li ions [24]. When melting with sulfur during the heating process, the stacking of MXene is even worse and consequently the surface of MXene is less exposed, making the melting sulfur wrap the stacked MXene sheets and form small particles initially. With the melting process continually proceeds, sulfur will grow on top of the original sulfur particles, eventually forming large sulfur particles (several micrometers, as seen in **Figure 4.5b**). This type of structure reflects the low utilization of sulfur and underutilized conductivity of MXene in MXene/S composite [27, 38]. For pristine CNC, this kind of carbon material with a high specific surface area is easy to agglomerate [39]. After sulfur is melted to form CNC/S composites, it presents poor polysulfides adsorption and thus some parts of active materials are lost during the

cycling. But for the particle size of sulfur, the CNC/S composite is significantly smaller than the MXene/S composite. This change represents the structural advantage of porous CNC with high specific surface area, leading to small sulfur particles. As revealed in **Figure 4.4a** and **Figure 4.13b**, CNC contains a large number of micropores and mesopores, which provides substantial thermal-activated sites to adhere sulfur in nanoscale. [36, 40]. In the case of MXene/CNC composite, the CNC acts as a layer separator to reduce the stacking of MXene while the agglomeration of CNC is significantly relieved as MXene intersected [8, 41]. The hydrophilic property of MXene also helps to achieve a good dispersion in water. When mixing with CNC, MXene and CNC material intercalate each other to form a high conductive network and reduce the impedance of transmission of Li-ions [2, 3]. In the sequential step, sulfur particles fuse on the surface of MXene/CNC composite, the sulfur particle size (several nanometers) of the resulting MXene/CNC/S composite (as confirmed by TEM image and STEM EDS mapping in **Figure 4.6d** and **Figure 4.6i**) is similar to the case of CNC/S (**Figure 4.7b** and **Figure 4.7g**). The sulfur particle size is an indicator of sulfur utilization for Li-S batteries [42]. To increase the sulfur utilization, it is desirable to have small sulfur particles in the electrode structure. The evolution of sulfur particle size when forming different composites has also been reported in previous work [43]. It was found that N-Ti<sub>3</sub>C<sub>2</sub>/S agglomerated to form large sulfur particles while N-Ti<sub>3</sub>C<sub>2</sub>@CNT microspheres/S displayed many small porous sulfur spheres. Another attractive feature of the MXene/CNC/S composite is its dual-ability of high conductivity and strong polysulfides adsorption. The conductive network between MXene/CNC provides

abundant tunnels of charge transfer and the multilayer structure of MXene sheets offers numerous adsorption sites to anchor the polysulfides. These data analysis highlights a good strategy of MXene-based Li-S batteries with improved electrochemical performance and fundamental studies of electrode materials at the nanoscale level.



**Figure 4.21** Proposed mechanism of synergistic effect between MXene and CNC.

#### 4.3.2 Parameters investigation for MXene/CNC/S composite

Since the mixed  $\text{TiC-TiO}_2/\text{SWCNT/S}$  composite just owns  $\sim 0.5 \text{ mg}\cdot\text{cm}^{-2}$  sulfur loading, it is necessary for exploring a relatively high and suitable sulfur loading for MXene/CNC/S composite, contributing to meet the requirements of commercial applications. Here, three typical values of  $0.5 \text{ mg}\cdot\text{cm}^{-2}$ ,  $1.5 \text{ mg}\cdot\text{cm}^{-2}$  and  $2.5 \text{ mg}\cdot\text{cm}^{-2}$ , with 80 % sulfur content representing low, medium and high sulfur loading, are tested for their battery performance. The extreme cases of  $0.5 \text{ mg}\cdot\text{cm}^{-2}$  sulfur loading with 60 % sulfur content and  $2.5 \text{ mg}\cdot\text{cm}^{-2}$  sulfur loading with 90 % sulfur content are

compared simultaneously.

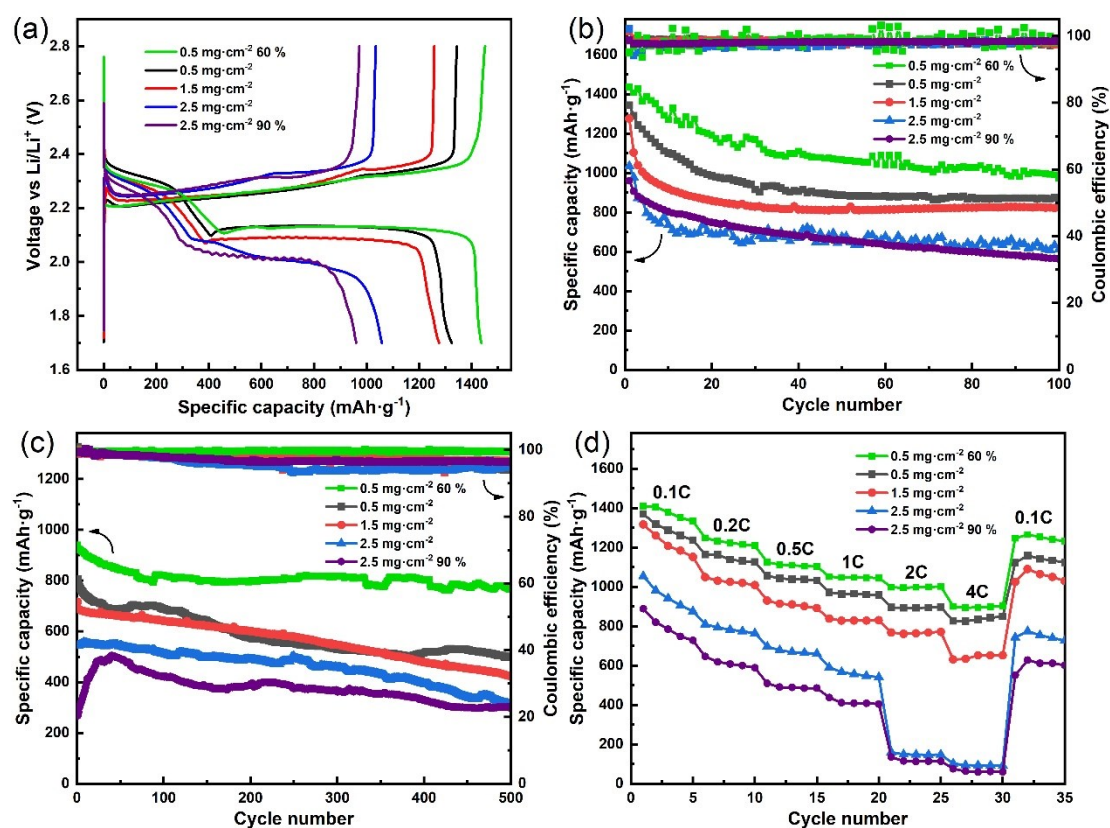
Generally, with the sulfur loading increasing, the comprehensive performance declines as predicted because the electrode thickness increases and the electronics impedance rises [44]. In the meantime, sulfur content is another key factor affecting performance. The specific capacity towards active sulfur declines along with the sulfur content growth in the composite because too less host material cannot effectively compensate conductivity of sulfur and poorly provide sufficient polysulfides adsorption. For the charge-discharge curves in **Figure 4.22a**, on account of high content host materials and more sufficient contact between it and active sulfur, sulfur utilization of the  $0.5 \text{ mg}\cdot\text{cm}^{-2}$  60 % composite presents the maximum value and its battery shows the greatest performance of  $1436.7 \text{ mAh}\cdot\text{g}^{-1}$  first capacity at 0.1 C, which is up to 85.8 % theoretical capacity. The  $0.5 \text{ mg}\cdot\text{cm}^{-2}$  composite has  $1343.3 \text{ mAh}\cdot\text{g}^{-1}$  capacity with a small voltage polarization, while the  $1.5 \text{ mg}\cdot\text{cm}^{-2}$  of relatively high sulfur content just owns a slightly low  $1275.5 \text{ mAh}\cdot\text{g}^{-1}$  capacity with a slightly larger polarization. As the sulfur loading continues to grow, however, the capacity decreases to a greater degree and the polarization deteriorates markedly because the thicker materials would cause a higher resistance in the electrode. As a result, the  $2.5 \text{ mg}\cdot\text{cm}^{-2}$  composite displays  $1035.1 \text{ mAh}\cdot\text{g}^{-1}$ , while  $2.5 \text{ mg}\cdot\text{cm}^{-2}$  90 % with less host material only remains  $960.6 \text{ mAh}\cdot\text{g}^{-1}$  at the first cycle. For the following cycles at 0.1 C in **Figure 4.22b**, the strong polysulfides adsorption of the more host materials contributes to the most stable performance of the  $0.5 \text{ mg}\cdot\text{cm}^{-2}$  60 % composite ( $971.5 \text{ mAh}\cdot\text{g}^{-1}$  after 100 cycles, 67.6 % retention).  $0.5 \text{ mg}\cdot\text{cm}^{-2}$  and  $1.5 \text{ mg}\cdot\text{cm}^{-2}$  composites show similar values, remaining

869.8 mAh·g<sup>-1</sup> and 823.8 mAh·g<sup>-1</sup> after cycling, while the other two capacities are below 650 mAh·g<sup>-1</sup> under 2.5 mg·cm<sup>-2</sup> high sulfur content.

At 1 C large current density, the performances of five different cathodes show a similar case (**Figure 4.22c**). Without a doubt, the large current cycling performance of the 0.5 mg·cm<sup>-2</sup> 60 % composite is extremely high (940.5 mAh·g<sup>-1</sup> at first cycle) as less content of sulfur and the thin electrode has excellent conductivity. Under strong polysulfides adsorption of sufficient contact between sulfur and host materials, it also presents an ultrahigh retention rate (81.5 %, 766.6 mAh·g<sup>-1</sup> after 500 cycles). Accompanied by rising sulfur content to ~80 %, the capacity declines obviously to 805.4 mAh·g<sup>-1</sup>, 716.2 mAh·g<sup>-1</sup> and 543.4 mAh·g<sup>-1</sup> for 0.5 mg·cm<sup>-2</sup>, 1.5 mg·cm<sup>-2</sup> and 2.5 mg·cm<sup>-2</sup> respectively, which can be ascribed as low content of host materials leads to the low conductivity of the composites. Noticeably, there is a different trend of the capacity for the 2.5 mg·cm<sup>-2</sup> 90 % composite. It is only 268.0 mAh·g<sup>-1</sup> at the first discharge, and the capacity gradually grows to a peak of 504.4 mAh·g<sup>-1</sup> at the 40th cycle. Due to the high sulfur loading and content, the polarization voltage during the charge-discharge at the initial several cycles is greatly large, leading to the inadequate redox reaction, incomplete platforms of the charge and discharge and early termination of the charge-discharge process. Followed by cycling, the electrolyte infiltrates fully by degrees, the conductivity is improved, the polarization decreases and thus the capacity grows. Owing to the loss of active sulfur, the capacity for the 2.5 mg·cm<sup>-2</sup> 90 % composite still declines at following cycles.

Rate performance reflects conductivity from the other side (**Figure 4.22d**).

Attributing to the high conductivity, low polarization and two whole discharge platforms, the  $0.5 \text{ mg}\cdot\text{cm}^{-2}$  60 %,  $0.5 \text{ mg}\cdot\text{cm}^{-2}$  and  $1.5 \text{ mg}\cdot\text{cm}^{-2}$  composites achieve an excellent capacity of  $900.2 \text{ mAh}\cdot\text{g}^{-1}$ ,  $826.3 \text{ mAh}\cdot\text{g}^{-1}$  and  $630.5 \text{ mAh}\cdot\text{g}^{-1}$  at 4 C current density, and recover to  $1247.3 \text{ mAh}\cdot\text{g}^{-1}$ ,  $1121.7 \text{ mAh}\cdot\text{g}^{-1}$  and  $1024.8 \text{ mAh}\cdot\text{g}^{-1}$  when current returns to 0.1 C. However, the performance from 0.1 C to 1 C of the  $2.5 \text{ mg}\cdot\text{cm}^{-2}$  and  $2.5 \text{ mg}\cdot\text{cm}^{-2}$  90 % composites is evidently low. Particularly, when the current increases to 2 C and 4 C, their capacity remains only around  $100 \text{ mAh}\cdot\text{g}^{-1}$  because extremely large polarization of discharge results in only one discharge plateau for them. When the current recovers to 0.1 C, the capacity still regains normal values of them.



**Figure 4.22** (a) First charge-discharge curves; (b) charge-discharge performance at 0.1 C, (c) charge-discharge performance at 1 C large current density and (d) rate performance from 0.1 C to 4 C of different sulfur loading and sulfur content for

MXene/CNC/S.

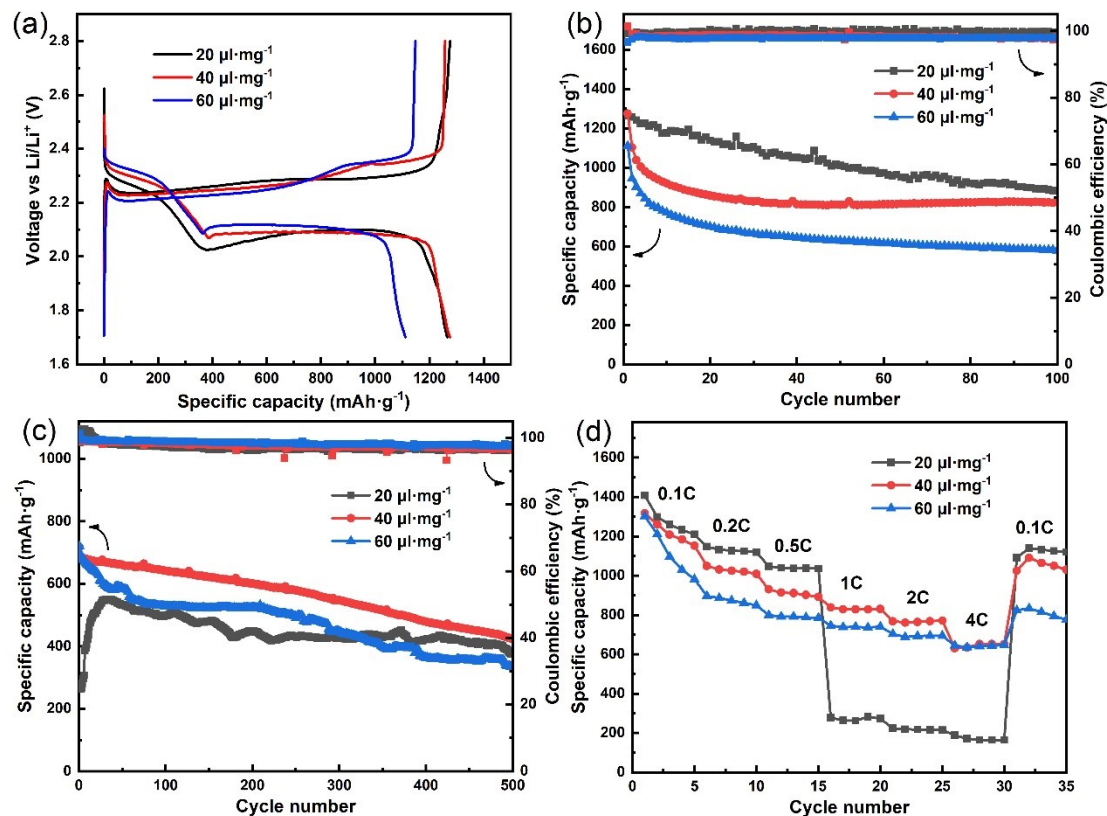
Another parameter that should be investigated is the ratio between the electrolyte and active sulfur (E/S ratio) since the electrolyte amount can affect the performance of Li-S batteries to a great extent. Our MXene/CNC/S 15 composite with three typical E/S ratios of  $20 \mu\text{l}\cdot\text{mg}^{-1}$ ,  $40 \mu\text{l}\cdot\text{mg}^{-1}$  and  $60 \mu\text{l}\cdot\text{mg}^{-1}$  are tested. As charge-discharge curves in **Figure 4.23a**, the electrode with  $20 \mu\text{l}\cdot\text{mg}^{-1}$  and  $40 \mu\text{l}\cdot\text{mg}^{-1}$  display an approximate capacity of about  $1270 \text{mAh}\cdot\text{g}^{-1}$  at the first cycle, while a low capacity of  $1110.9 \text{mAh}\cdot\text{g}^{-1}$  under  $60 \mu\text{l}\cdot\text{mg}^{-1}$ , because excessive electrolyte leads to the more serious self-discharge. Compared to  $40 \mu\text{l}\cdot\text{mg}^{-1}$ ,  $20 \mu\text{l}\cdot\text{mg}^{-1}$  shows a larger polarization in charge-discharge curves. This can be ascribed as insufficient electrolyte leads to incomplete infiltration for electrode materials and low conductivity. For the following cyclic performance in **Figure 4.23b**, it can be seen that the electrode with  $20 \mu\text{l}\cdot\text{mg}^{-1}$  presents the most stable cycle life with uniform slow descent of capacity, retaining a high  $882.7 \text{mAh}\cdot\text{g}^{-1}$  after 100 cycles at 0.1 C. Meanwhile, when using  $40 \mu\text{l}\cdot\text{mg}^{-1}$  electrolyte, the capacity decreases fast for the initial 10 cycles and the decay speed tends to be gentle later, also remaining over  $800 \text{mAh}\cdot\text{g}^{-1}$ . However, the  $60 \mu\text{l}\cdot\text{mg}^{-1}$  large amount of electrolyte results in a rapid capacity decay (merely  $579.4 \text{mAh}\cdot\text{g}^{-1}$ ) as polysulfides are easily dissolved in the electrolyte, and more polysulfides will promote more dissolution polysulfides.

A similar trend exists for 1 C large current density performance (**Figure 4.23c**). Although both composites with E/S ratios of  $40 \mu\text{l}\cdot\text{mg}^{-1}$  and  $60 \mu\text{l}\cdot\text{mg}^{-1}$  own a high initial capacity approach to  $720 \text{mAh}\cdot\text{g}^{-1}$ ,  $60 \mu\text{l}\cdot\text{mg}^{-1}$  displays a faster decline during

the cycling (only  $333.5 \text{ mAh}\cdot\text{g}^{-1}$  after 500 cycles) due to exceeding electrolyte and accelerated polysulfides dissolution. Comparatively,  $20 \mu\text{l}\cdot\text{mg}^{-1}$  has just  $280.5 \text{ mAh}\cdot\text{g}^{-1}$  at the start due to scarce electrolytes and low conductivity. With the cycling process and polarization relieving, the capacity reverts to a high point of  $550.5 \text{ mAh}\cdot\text{g}^{-1}$  at the 34th cycle. It descends slowly to  $375.8 \text{ mAh}\cdot\text{g}^{-1}$  later owing to the relatively less electrolyte amount and less loss of polysulfides.

In **Figure 4.23d**, sufficient electrolyte and high conductivity also contribute to the excellent rate performance of  $40 \mu\text{l}\cdot\text{mg}^{-1}$  and  $60 \mu\text{l}\cdot\text{mg}^{-1}$ , reaching  $630.5 \text{ mAh}\cdot\text{g}^{-1}$  and  $644.7 \text{ mAh}\cdot\text{g}^{-1}$ , respectively. Lack of sufficient electrolyte providing effective conductivity, the electrode with  $20 \mu\text{l}\cdot\text{mg}^{-1}$  just achieves high performance below 0.5 C small current density. When it enhances to over 1 C, the capacity drops distinctly to around  $200 \text{ mAh}\cdot\text{g}^{-1}$  because of the large polarization and incomplete discharge platforms.





**Figure 4.23** (a) First charge-discharge curves; (b) charge-discharge performance at 0.1 C, (c) charge-discharge performance at 1 C large current density and (d) rate performance from 0.1 C to 4 C of the different E/S ratio for MXene/CNC/S.

#### 4.4 Conclusions

In conclusion, we successfully synthesized a 3D MXene/CNC/S composite with a high-conductive network via a simple strategy with low-cost raw materials ( $\text{Ti}_3\text{AlC}_2$  and  $\text{C}_6\text{H}_5\text{Na}_3\text{O}_7$ ). MXene and CNC offer an interesting synergistic effect for simultaneously achieving superior cycle performance and outstanding rate performance. By combining both advantages, MXene/CNC/S 7:3 delivers a stable cycle performance with a high initial capacity of  $1275.5 \text{ mAh}\cdot\text{g}^{-1}$  at 0.1 C and a retention rate of 64.6 % of  $823.8 \text{ mAh}\cdot\text{g}^{-1}$  after 100 cycles. It maintains a  $630.5 \text{ mAh}\cdot\text{g}^{-1}$  capacity at the large current density of 4 C because of its excellent conductivity. For various mass ratios of

MXene and CNC, it is found that MXene: CNC = 7:3 shows the best electrochemical performance for the composites investigated. Moreover, sulfur loading, sulfur content and electrolyte ratio were explored to balance performance and energy density. The results indicate that  $1.5 \text{ mg}\cdot\text{cm}^{-2}$  sulfur is the best for MXene/CNC/S 7:3 cathode to achieve excellent performance and high energy density. Meanwhile,  $40 \text{ }\mu\text{l}\cdot\text{mg}^{-1}$  E/S ratio is the most suitable as insufficient electrolyte may lead to slow electronic transmission, but excessive electrolyte would result in fast loss of polysulfides. The designed electrode composite also achieves a high sulfur content ( $\sim 80 \%$ ), opens the perspectives for the host of sulfur and is potentially applied in commercial applications.

## 4.5 References

- [1] J. Liang, Z.H. Sun, F. Li, and H.M. Cheng, Carbon materials for Li-S batteries: Functional evolution and performance improvement, *Energy Storage Materials*, 2 (2016) 76-106.
- [2] C. Zhang, Y. Ma, X. Zhang, S. Abdolhosseinzadeh, H. Sheng, W. Lan, A. Pakdel, J. Heier, and F. Nüesch, Two-Dimensional Transition Metal Carbides and Nitrides (MXenes): Synthesis, Properties, and Electrochemical Energy Storage Applications, *Energy & Environmental Materials*, 3 (2020) 29-55.
- [3] C. Zhang, L. Cui, S. Abdolhosseinzadeh, and J. Heier, Two-dimensional MXenes for lithium-sulfur batteries, *InfoMat*, 2 (2020) 613-638.
- [4] L. Zhang, J. Bi, Z. Zhao, Y. Wang, D. Mu, and B. Wu, Sulfur@Self-assembly 3D MXene hybrid cathode material for lithium-sulfur batteries, *Electrochimica Acta*, 370 (2021) 137759.
- [5] K. Li, M. Liang, H. Wang, X. Wang, Y. Huang, J. Coelho, S. Pinilla, Y. Zhang, F. Qi, V. Nicolosi, and Y. Xu, 3D MXene Architectures for Efficient Energy Storage and Conversion, *Advanced Functional Materials*, 30 (2020) 2000842.
- [6] Z. Ma, F. Jing, Y. Fan, J. Li, Y. Zhao, and G. Shao, High electrical conductivity of 3D mesoporous carbon nanocage as an efficient polysulfide buffer layer for high sulfur utilization in lithium-sulfur batteries, *Journal of Alloys and Compounds*, 789 (2019) 71-79.
- [7] M. Alhabeab, K. Maleski, B. Anasori, P. Lelyukh, L. Clark, S. Sin, and Y. Gogotsi, Guidelines for Synthesis and Processing of Two-Dimensional Titanium Carbide

- ( $\text{Ti}_3\text{C}_2\text{T}_x$  MXene), *Chemistry of Materials*, 29 (2017) 7633-7644.
- [8] Z. Ma, G. Shao, Y. Fan, M. Feng, D. Shen, and H. Wang, Fabrication of High-Performance All-Solid-State Asymmetric Supercapacitors Based on Stable  $\alpha$ - $\text{MnO}_2$ @ $\text{NiCo}_2\text{O}_4$  Core-Shell Heterostructure and 3D-Nanocage N-Doped Porous Carbon, *ACS Sustainable Chemistry & Engineering*, 5 (2017) 4856-4868.
- [9] P. Simon, Two-Dimensional MXene with Controlled Interlayer Spacing for Electrochemical Energy Storage, *ACS nano*, 11 (2017) 2393-2396.
- [10] N. Li, Y. Xie, S. Peng, X. Xiong, and K. Han, Ultra-lightweight  $\text{Ti}_3\text{C}_2\text{T}_x$  MXene modified separator for Li-S batteries: Thickness regulation enabled polysulfide inhibition and lithium ion transportation, *Journal of Energy Chemistry*, 42 (2020) 116-125.
- [11] Y. Fu and A. Manthiram, Orthorhombic Bipyramidal Sulfur Coated with Polypyrrole Nanolayers As a Cathode Material for Lithium-Sulfur Batteries, *The Journal of Physical Chemistry C*, 116 (2012) 8910-8915.
- [12] C. Zu and A. Manthiram, Hydroxylated Graphene-Sulfur Nanocomposites for High-Rate Lithium-Sulfur Batteries, *Advanced Energy Materials*, 3 (2013) 1008-1012.
- [13] Q. Qi, H. Zhang, P. Zhang, Z. Bao, W. Zheng, W. Tian, W. Zhang, M. Zhou, and Z. Sun, Self-assembled sandwich hollow porous carbon sphere @ MXene composites as superior Li-S battery cathode hosts, *2D Materials*, 7 (2020) 025049.
- [14] Z. Pan and X. Ji, Facile synthesis of nitrogen and oxygen co-doped  $\text{C}@\text{Ti}_3\text{C}_2$  MXene for high performance symmetric supercapacitors, *Journal of Power Sources*, 439 (2019) 227068.

- [15] W. Bao, X. Xie, J. Xu, X. Guo, J. Song, W. Wu, D. Su, and G. Wang, Confined Sulfur in 3D MXene/Reduced Graphene Oxide Hybrid Nanosheets for Lithium-Sulfur Battery, *Chemistry*, 23 (2017) 12613-12619.
- [16] C. Li, X.L. Sui, Z.B. Wang, Q. Wang, and D.M. Gu, 3D N-doped graphene nanomesh foam for long cycle life lithium-sulfur battery, *Chemical Engineering Journal*, 326 (2017) 265-272.
- [17] R. Fang, K. Chen, L. Yin, Z. Sun, F. Li, and H.M. Cheng, The Regulating Role of Carbon Nanotubes and Graphene in Lithium-Ion and Lithium-Sulfur Batteries, *Advanced materials*, 31 (2019) 1800863.
- [18] A. Fu, C. Wang, F. Pei, J. Cui, X. Fang, and N. Zheng, Recent Advances in Hollow Porous Carbon Materials for Lithium-Sulfur Batteries, *Small*, 15 (2019) 1804786.
- [19] N.K. Chaudhari, H. Jin, B. Kim, D. San Baek, S.H. Joo, and K. Lee, MXene: an emerging two-dimensional material for future energy conversion and storage applications, *Journal of Materials Chemistry A*, 5 (2017) 24564-24579.
- [20] J. Zhang, P. Gu, J. Xu, H. Xue, and H. Pang, High performance of electrochemical lithium storage batteries: ZnO-based nanomaterials for lithium-ion and lithium-sulfur batteries, *Nanoscale*, 8 (2016) 18578-18595.
- [21] L. Fei, X. Li, W. Bi, Z. Zhuo, W. Wei, L. Sun, W. Lu, X. Wu, K. Xie, C. Wu, H.L. Chan, and Y. Wang, Graphene/sulfur hybrid nanosheets from a space-confined "sauna" reaction for high-performance lithium-sulfur batteries, *Advanced materials*, 27 (2015) 5936-5942.
- [22] J. Halim, K.M. Cook, M. Naguib, P. Eklund, Y. Gogotsi, J. Rosen, and M.W.

Barsoum, X-ray photoelectron spectroscopy of select multi-layered transition metal carbides (MXenes), *Applied Surface Science*, 362 (2016) 406-417.

[23] Y.T. Liu, P. Zhang, N. Sun, B. Anasori, Q.Z. Zhu, H. Liu, Y. Gogotsi, and B. Xu, Self-Assembly of Transition Metal Oxide Nanostructures on MXene Nanosheets for Fast and Stable Lithium Storage, *Advanced materials*, 30 (2018) 1707334.

[24] H. Tang, W. Li, L. Pan, K. Tu, F. Du, T. Qiu, J. Yang, C.P. Cullen, N. McEvoy, and C. Zhang, A Robust, Freestanding MXene-Sulfur Conductive Paper for Long-Lifetime Li-S Batteries, *Advanced Functional Materials*, 29 (2019) 1901907.

[25] C. Wang, K. Su, W. Wan, H. Guo, H. Zhou, J. Chen, X. Zhang, and Y. Huang, High sulfur loading composite wrapped by 3D nitrogen-doped graphene as a cathode material for lithium-sulfur batteries, *Journal of Materials Chemistry A*, 2 (2014) 5018-5023.

[26] C. Xiong, G.Y. Zhu, H.R. Jiang, Q. Chen, and T.S. Zhao, Achieving multiplexed functionality in a hierarchical MXene-based sulfur host for high-rate, high-loading lithium-sulfur batteries, *Energy Storage Materials*, 33 (2020) 147-157.

[27] Z. Xiao, Z. Li, X. Meng, and R. Wang, MXene-engineered lithium-sulfur batteries, *Journal of Materials Chemistry A*, 7 (2019) 22730-22743.

[28] R. Carter, L. Oakes, N. Muralidharan, and C.L. Pint, Isothermal Sulfur Condensation into Carbon Scaffolds: Improved Loading, Performance, and Scalability for Lithium-Sulfur Battery Cathodes, *The Journal of Physical Chemistry C*, 121 (2017) 7718-7727.

[29] Q. Wu, L. Yang, X. Wang, and Z. Hu, Carbon-Based Nanocages: A New Platform for Advanced Energy Storage and Conversion, *Advanced materials*, 32 (2020) 1904177.

- [30] Y. Chen, W. Zhang, D. Zhou, H. Tian, D. Su, C. Wang, D. Stockdale, F. Kang, B. Li, and G. Wang, Co-Fe Mixed Metal Phosphide Nanocubes with Highly Interconnected-Pore Architecture as an Efficient Polysulfide Mediator for Lithium-Sulfur Batteries, *ACS Nano*, 13 (2019) 4731-4741.
- [31] L. Li, G. Zhou, L. Yin, N. Koratkar, F. Li, and H.M. Cheng, Stabilizing sulfur cathodes using nitrogen-doped graphene as a chemical immobilizer for Li-S batteries, *Carbon*, 108 (2016) 120-126.
- [32] J. Su, H. Song, and C. Wang, Morphology Reshaping Enabling Self-Densification of Manganese Oxide Hybrid Materials for High-Density Lithium Storage Anodes, *Advanced Functional Materials*, 29 (2019) 1907154.
- [33] H. Song, J. Su, and C. Wang, In Situ Subangstrom-Thick Organic Engineering Enables Mono-scale, Ultrasmall ZnO Nanocrystals for a High Initial Coulombic Efficiency, Fully Reversible Conversion, and Cycle-Stable Li-Ion Storage, *Advanced Energy Materials*, 9 (2019) 1900426.
- [34] M. Yu, J. Ma, H. Song, A. Wang, F. Tian, Y. Wang, H. Qiu, and R. Wang, Atomic layer deposited TiO<sub>2</sub> on a nitrogen-doped graphene/sulfur electrode for high performance lithium-sulfur batteries, *Energy & Environmental Science*, 9 (2016) 1495-1503.
- [35] Y. Jiang, M. Lu, X. Ling, Z. Jiao, L. Chen, L. Chen, P. Hu, and B. Zhao, One-step hydrothermal synthesis of three-dimensional porous graphene aerogels/sulfur nanocrystals for lithium-sulfur batteries, *Journal of Alloys and Compounds*, 645 (2015) 509-516.

- [36] D. Xiao, Q. Li, H. Zhang, Y. Ma, C. Lu, C. Chen, Y. Liu, and S. Yuan, A sulfur host based on cobalt-graphitic carbon nanocages for high performance lithium-sulfur batteries, *Journal of Materials Chemistry A*, 5 (2017) 24901-24908.
- [37] Z. Cui, J. Yao, T. Mei, S. Zhou, B. Hou, J. Li, J. Li, J. Wang, J. Qian, and X. Wang, Strong lithium polysulfides chemical trapping of TiC-TiO<sub>2</sub>/S composite for long-cycle lithium-sulfur batteries, *Electrochimica Acta*, 298 (2019) 43-51.
- [38] R. Chen, T. Zhao, J. Lu, F. Wu, L. Li, J. Chen, G. Tan, Y. Ye, and K. Amine, Graphene-based three-dimensional hierarchical sandwich-type architecture for high-performance Li/S batteries, *Nano letters*, 13 (2013) 4642-4649.
- [39] Y.C. Jiarui He, Pingjian Li\*, Fei Fu, Zegao Wang, and Wanli Zhang, Three-Dimensional CNT Graphene-Sulfur Hybrid Sponges with High Sulfur Loading as Superior-Capacity Cathode for Lithium-Sulfur Batteries, *Journal of Materials Chemistry A*, 3 (2015) 18605-18610.
- [40] K. Zhang, Q. Zhao, Z. Tao, and J. Chen, Composite of sulfur impregnated in porous hollow carbon spheres as the cathode of Li-S batteries with high performance, *Nano Research*, 6 (2013) 38-46.
- [41] O. Salim, K.A. Mahmoud, K.K. Pant, and R.K. Joshi, Introduction to MXenes: synthesis and characteristics, *Materials Today Chemistry*, 14 (2019) 100191.
- [42] H. Chen, C. Wang, W. Dong, W. Lu, Z. Du, and L. Chen, Monodispersed sulfur nanoparticles for lithium-sulfur batteries with theoretical performance, *Nano letters*, 15 (2015) 798-802.
- [43] J. Wang, Z. Zhang, X. Yan, S. Zhang, Z. Wu, Z. Zhuang, and W.Q. Han, Rational



Design of Porous N-Ti<sub>3</sub>C<sub>2</sub> MXene@CNT Microspheres for High Cycling Stability in Li-S Battery, Nano-Micro Letters, 12 (2019) 1-14.

[44] M. Zhang, K. Amin, M. Cheng, H. Yuan, L. Mao, W. Yan, and Z. Wei, A carbon foam-supported high sulfur loading composite as a self-supported cathode for flexible lithium-sulfur batteries, Nanoscale, 10 (2018) 21790-21797.

# **Chapter 5 : Functionalized MXene/sulfur cathode with covalent adsorption mechanism for minimizing the “shuttle effect” of Li-S batteries**

## **5.1 Introduction**

The MXene/CNC/S cathode discussed in Chapter 4 presents a satisfactory effect of elevating sulfur loading for Li-S batteries with relatively high performance via a 3D conductive network. However, it still needs two types of host materials for active sulfur, and a mixed TiC-TiO<sub>2</sub>/SWCNT/S cathode in Chapter 3 requires three types. Those sophisticated composites also require complex fabrication processes or drastic reaction conditions. Herein, functionalized MXene as a single type of host material for sulfur is put forward to achieve a simplified method, gentle procedure and high stability of Li-S batteries.

Although the significance of pristine MXene has been recognized by most of the works, it seems that the suppression of the “shuttle effect” is fairly limited and the traditional physical absorption of polysulfides is inadequate to prevent the formation of high-order polysulfides, leading to active material lost during the charge-discharge. [1]. This work presents a chemical S-S bond breakage mechanism at first and polymerization via the covalent attachment of sulfur to the MXene sheets. The method not only maximizes the advantages of MXene but also significantly decreases the production of high-order polysulfides. It has been reported that copolymerization of S<sub>8</sub> with alkene or its derivative via inverse vulcanization can chemically cross-link polymeric sulfur cathode. Simmonds et al. prepared polymeric electrode materials via

this method for Li-S batteries, displaying enhanced capacity retention ( $1005 \text{ mAh}\cdot\text{g}^{-1}$  at 100 cycles) and battery lifetimes over 500 cycles at 0.1 C [2-4]. A moderate process was discovered through utilizing nitrile groups and  $\text{S}_8$  to promote dehydrogenation and ring formation [1].

In this work, three types of functionalized MXene and their cathodes: N-MXene/S, N, S-MXene/S and 3D MXene/S were fabricated. Then, two optimized strategies of chemical functionalization of MXene have been investigated. One is cysteamine hydrochloride (CH), another is 3-mercaptopropyltrimethoxysilane (MPTS) blended and reacted with MXene, because both can react with MXene on certain conditions and have sulfhydryl groups to achieve copolymerization with sulfur. After the modifying step, sulfur is grafted into sulfhydryl-modified MXene to form S-MXeneSH(CH) or MXeneSH(MPTS) under a high temperature, forming free radical copolymerization between ring-opening polymerization of elemental sulfur and sulfhydryl groups grafted on MXene. During the discharge process, both S-MXeneSH(CH) or S-MXeneSH(MPTS) composite only have low-order polysulfides after abundant insertion of Li [5]. High-order  $\text{Li}_2\text{S}_4$  was produced as intermediates and then consumed quickly, which can greatly suppress “shuttle effect” and significantly improves the stability of batteries. The as-prepared S-MXeneSH by two strategies presents different electrochemical performances. S-MXeneSH(CH) 15 achieves a more stable cycling and a higher rate performance. Despite a slightly low performance of S-MXeneSH(MTPTS), the milder and safer fabrication process might find its potential in practical applications.

The research work in chapter 5 was designed and carried out under the supervision

of Prof. Li Yang and Prof. Pengfei Song. The result shown in this chapter was published on *Electrochimica Acta*, 2023, 441: 141877 (DOI: 10.1016/j.electacta.2023.141877). The manuscript was drafted by me and corrected by Dr. Li Yang and Dr. Pengfei Song. The rest of the authors helped with some supplementary works, including idea guidance, data analysis, and experimental data checking.

## **5.2. Experiment part**

### **5.2.1 Preparation of MXene/S, N-MXene/S, N,S-MXene/S and 3D MXene/S**

Firstly, MXene solution and freeze-dried MXene powder were synthesized for reserve. Typically, 2 g  $\text{Ti}_3\text{AlC}_2$  powders were slowly added to the prepared solution, in which 2 g LiF was mixed with 40 mL HCl (12 M) under magnetic stirring for 30 min to synthesize a homogeneous delaminated MXene solution. Then, the above solution was continued to stir and heated to 35 °C for 24 h to etch Al atoms. After the reaction, the resultant was washed with DI water through several centrifugation-rinsing cycles (5500 rpm for 10 min) until its PH approached 6. Next, the washed product was dispersed in 40 ml ethanol via ultrasonication for 1.5 h. The dark green MXene solution ( $\sim 10 \text{ mg} \cdot \text{ml}^{-1}$ ) was collected by centrifugal treatment several times. Half of the solution was stored in dark glass bottles under 4 °C. Another half was freeze-dried for 48 h to obtain fluffy MXene powder. The powder was reserved under the same condition as the solution.

In order to fabricate nitrogen-doped MXene (N-MXene), the negatively charged MXene powder was added to the positively charged ammonium chloride ( $\text{NH}_4\text{Cl}$ ) solution. The positively charged ammonium ions will directly intercalate into the gap

between layers via electrostatic force. Functional groups with negative charges on MXene surface promoted the permeation process [6]. The  $\text{NH}_4\text{Cl}/\text{MXene}$  sheets solution was centrifuged at 5500 rpm, collected and dried at 60 °C for 24 h in a vacuum oven. Finally, the N-MXene sample was obtained after annealing at 600 °C for 4 h under  $\text{N}_2$  gas [7].

For nitrogen, sulfur-doped MXene (N, S-MXene), 100 mg MXene powder and 2 g thiourea were mixed uniformly and heated in an  $\text{N}_2$  atmosphere at 600 °C for 3 h at a heating rate of 2 °C  $\text{min}^{-1}$ . The N, S co-doped MXene was obtained after cooling down to room temperature naturally [8].

As prepared-MXene solution (diluted to 2  $\text{mg}\cdot\text{mL}^{-1}$ ) and the PMMA sphere dispersion (concentrate to 10  $\text{mg}\cdot\text{mL}^{-1}$ ) were mixed and then magnetically stirred for 10 min. The mass ratio of MXene to PMMA spheres was 1: 10. The mixture was then centrifuged at 4000 rpm for 10 min and the solid residue was washed with DI water and centrifuged at 4000 rpm for another 10 min. After that, the solid precipitate was collected and transferred to a vacuum oven to dry at 60 °C for 12 h to obtain MXene/PMMA hybrid. Then it was annealed at 450 °C under Ar flow for 1 h to remove the PMMA and left MXene hollow spheres [9].

To prepare four different cathodes, pristine MXene, N-MXene, N, S-MXene and 3D MXene were mixed with sublimed sulfur (mass ratio = 1:3), respectively. Then, these mixtures were heated at 155 °C for 12 h to achieve a sulfur fusion process. The ultimate products were denoted as MXene/S, N-MXene/S, N, S-MXene/S and 3D MXene/S, respectively.

### 5.2.2 Preparation of two different sulfhydryl-functionalized MXene/S electrodes

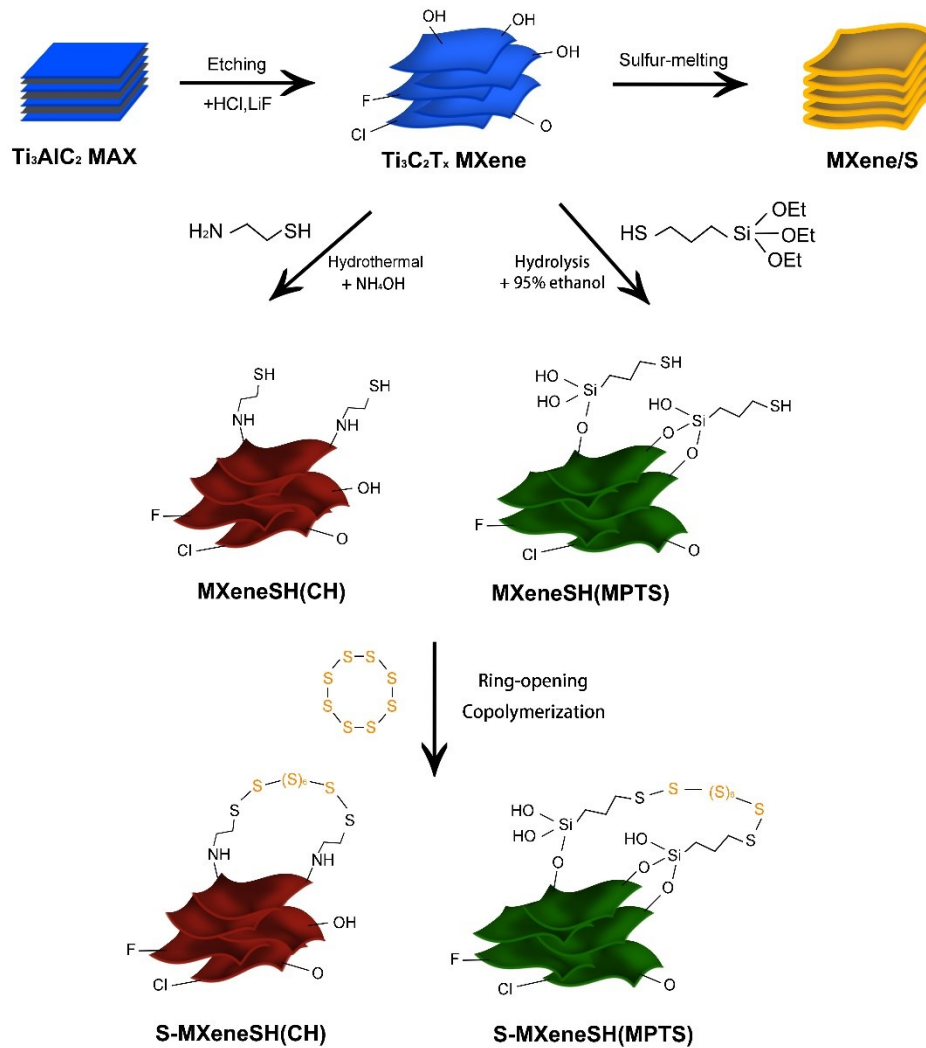
The MXeneSH(CH) electrode material was prepared via a one-step hydrothermal reaction in a muffle furnace by heating the mixture of MXene solution (90 ml, 1 mg·ml<sup>-1</sup>), ammonium hydroxide (1 ml), and CH powder at 90 °C for 6 h under Ar atmosphere. The mass ratios between CH and MXene (CH/MXene) were 5:1, 10:1, 15:1 and 20:1. Through vacuum filtration and washing by DI water several times, the resultants were freeze-dried for 24 h to obtain the porous MXeneSH(CH). For the different mass ratios between MXene and CH, these resultants were denoted as MXeneSH(CH) 5, MXeneSH(CH) 10, MXeneSH(CH) 15 or MXeneSH(CH) 20.

For comparison, the MXeneSH(MPTS) 15 composite was fabricated by means of a simple hydrolysis reaction. Specifically, freeze-dried MXene powder was added into ethanol (95 %) and ultrasonicated for 30 min to form a homogeneous MXene ethanol solution (~10 mg·ml<sup>-1</sup>). This process adopted ethanol containing a small amount of water to hydrolyze and was carried out under Ar gas to prevent oxidation of sulfhydryl. After MPTS and MXene were mixed in 15:1 mass ratio, a magnetic stirring was applied for 24 h under Ar atmosphere at room temperature. Then, the solution was centrifuged for 10 min at 10000 rpm, and the liquid above was poured out. Later, ethanol and DI water were used for washing the product in the same centrifugation condition several times. Finally, DI water was added to the cleaned product and was ultrasonicated for 10 min to form an aqueous dispersion of MXeneSH(MPTS) 15 (~10 mg·ml<sup>-1</sup>). Fluffy MXeneSH(MPTS) 15 powder was obtained by freeze-drying for 24 h.

In order to prepare S-MXeneSH(CH) composite, the mixture of MXeneSH(CH)

and sublimed sulfur was ground with the mass ratio of 1:3. Then, the mixture was heated to 185 °C for 10 h and further heated to 245 °C for 2 h under an Ar atmosphere in a muffle furnace, to stimulate the ring-opening polymerization of elemental sulfur (S<sub>8</sub>) into a linear polysulfane and minimize oxidation. After naturally cooling down to room temperature, S-MXeneSH(CH)/sulfur composite was fabricated. Next, the composite was transferred to a tubular furnace via heating at 155 °C for 3 h under an Ar gas stream to remove the insert sulfur, and S-MXeneSH(CH) composite was obtained [5]. The final products were denoted as S-MXeneSH(CH) 5, S-MXeneSH(CH) 10, S-MXeneSH(CH) 15 or S-MXeneSH(CH) 20. The synthesis procedures for preparing these materials are shown in **Figure 5.1**.

Similarly, MXeneSH(MPTS) 15 or MXene was mixed with sublimed sulfur for the same mass ratio. The heating process of MXeneSH(MPTS) 15 was identical to carrying out a ring-opening polymerization, while the mixture of MXene and sublimed sulfur was heated at 155 °C for 12 h to achieve a fusion process. The ultimate products were denoted as S-MXeneSH (MPTS) 15 or MXene/S.



**Figure 5.1** The schematic diagrams of different MXene and their corresponding sulfur-growing composites.

### 5.2.3 Materials characterization and electrochemical measurements

Scanning electron microscope (SEM, JEOL JSM-6510) and field emission scanning electron microscope (FE-SEM, Regulus SU8230) were used to characterize the microstructure and morphology of different composites. High-resolution images were characterized by transmission electron microscope (TEM, FEI Tecnai G2 F20) with scanning transmission electron microscopy (STEM) and elemental mapping function. The X-ray powder diffraction (D8 Advance, Bruker, with  $\text{Cu K}\alpha$  radiation,  $\lambda$



= 1.5406 Å) was used to record the crystal structure of the resultant materials. Elemental composition, functional groups and chemical bonds were measured with X-ray photoelectron spectroscopy (XPS, ESCALAB 250Xi, Thermo Scientific). The sulfur content in the composites was measured by a NETZSCH STA 449 F3 thermogravimetric analyzer (TGA) with a temperature ramp of 10 °C per minute under the N<sub>2</sub> gas atmosphere. The N<sub>2</sub> adsorption and desorption isotherms of the Brunauer-Emmett-Teller (BET) were taken on a 3H-2000PS2 at 77.3 K, and the pore size distributions were obtained by the Barrett-Joyner-Halenda (BJH) model.

**UV/Vis spectra tests:** The Genesys 10s UV-vis spectrometer was used to operate UV-Vis spectroscopy for polysulfides in cathodes at different discharge voltages. In this work, batteries discharged to three typical voltages (2.32 V, 2.07 V and 1.96 V) were chosen to disassemble and fetch out their separators. The voltages reflect the preliminary discharge, the end of the first discharge platform and the end of the second discharge platform, respectively. As long-chain polysulfides (e.g. Li<sub>2</sub>S<sub>4</sub>, Li<sub>2</sub>S<sub>6</sub> and Li<sub>2</sub>S<sub>8</sub>) are easily dissolved in the electrolyte, The separators were soaked in a small amount of electrolyte for several minutes to dissolve polysulfides. After that, the polysulfide-containing electrolyte was collected to take the liquid phase UV-vis test.

CR2032-type coin cells were assembled in an Ar-filled glove box (H<sub>2</sub>O, O<sub>2</sub> < 0.5 ppm) to characterize the electrochemical properties. To prepare the working electrodes, a uniform slurry was prepared by mixing the active material, conductive agent (super P), and polyvinylidene fluoride (PVDF) with a mass ratio of 8:1:1 in N-methyl-2-pyrrolidone (NMP). The electrolyte was lithium bis (trifluoromethanesulfonyl) imide

(1.0 M) dissolved in a mixture of a lithium salt (LiTFSI) in dioxolane (DOL) and dimethoxyethane (DME) (1:1 by volume) with a 1.0 wt% LiNO<sub>3</sub> additive. The active materials were used as the cathode, and lithium tablets were used as the anode, separated by the Celgard 2400 separator. The slurry was coated on the pure aluminum foil current collector and vacuum dried at 60 °C for 12 h.

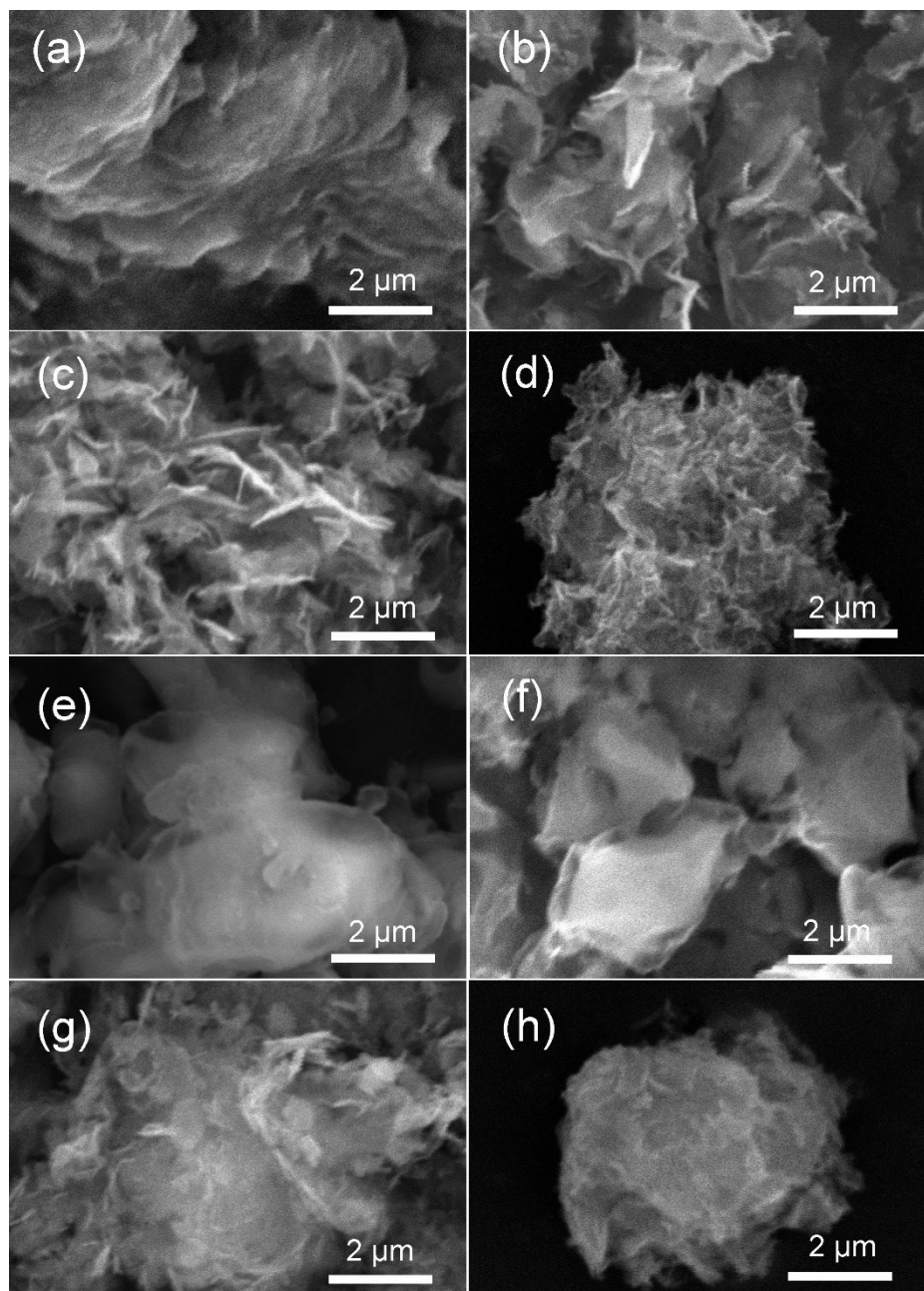
Galvanostatic charge-discharge cycling tests were conducted on a battery tester (Neware CT - 4008) with the voltage ranging from 1.7 V to 2.8 V versus Li<sup>+</sup>/Li at various current densities at room temperature. The cycling voltammetry (CV) was measured by using an electrochemical workstation (Metrohm Autolab PGSTAT302N) at the scanning rate of 0.1 mV s<sup>-1</sup> in a two-electrode system. The electrochemical impedance spectroscopy (EIS) was also measured from 15 mHz to 100 kHz on an Autolab PGSTAT302N electrochemical workstation.

## **5.3 Results and discussion**

### **5.3.1 Comparison of N-MXene/S, N,S-MXene/S and 3D MXene/S composites**

The research aim is to mainly prevent the stacking feature of MXene and expose more active sites for polysulfides adsorption, achieving an effective utilisation of the function of MXene. Therefore, we first tried three different methods to functionalize the pristine MXene. As a traditional thought, nitrogen sources such as NH<sub>4</sub>Cl could be chosen to synthesize nitrogen doped MXene, similar to the way of fabricating nitrogen-doped graphene [7, 10]. This scheme was applied for capacitive deionization and achieved a high SSA of over 300 m<sup>2</sup>·g<sup>-1</sup> in previous work [7], so it was considered suitable to apply our Li-S cathode. In **Figure 5.2b**, it is evident that this type of N-

MXene shows a wrinkled layered structure with less stacking compared to the pristine MXene in **Figure 5.2a**. After the sulfur fusion process, both MXene/S and N-MXene/S aggregate to large particles of several micrometer diameter size in **Figure 5.2e-f**, indicating  $\text{NH}_4\text{Cl}$  modified MXene can relieve staking of MXene to some extent but cannot prevent aggregation during the sulfur melting. Another N, S co-doped  $\text{V}_2\text{CT}_x$  MXene with more active sites for the adsorption of lithium ions provided improved ion transfer kinetics during the redox reaction, which was investigated for Li-S batteries in 2021 [8]. Similarly, thiourea as a nitrogen and sulfur source was used to doping  $\text{T}_3\text{C}_2\text{T}_x$  MXene. The resultant N, S-MXene presents a crumpled structure and a smaller flake size in **Figure 5.2c**. The N, S-MXene/S composite displayed a relatively slight aggregation when the sulfur melting was carried out, as it can be identified some layered sheets of MXene (**Figure 5.2g**). The last experiment is to prepare the 3D MXene via a PMMA template method to achieve high SSA and less stacking. In **Figure 5.2d**, 3D MXene demonstrates a stereoscopic view but does not own an expected sphere structure as in the previous work [9]. After sulfur melting, 3D MXene/S roughly keeps a primary structure with a thick sulfur layer on the surface (**Figure 5.2h**).

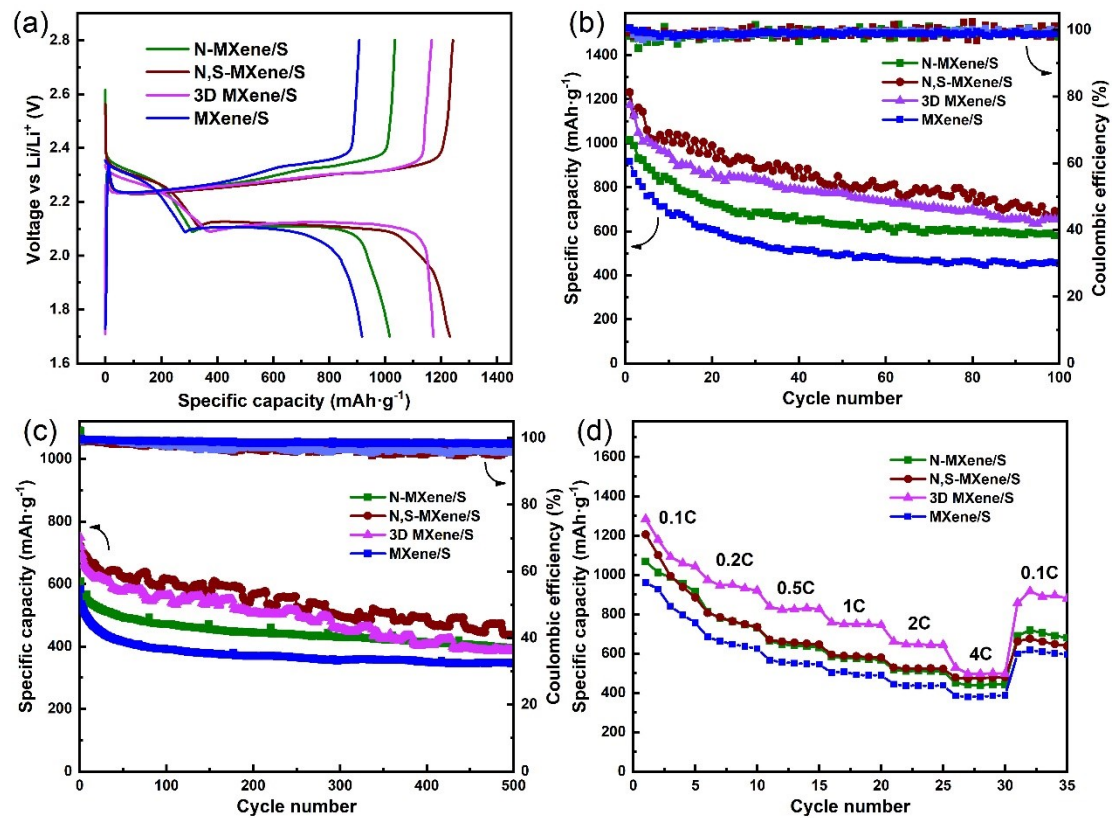


**Figure 5.2** (a-d) SEM images of pristine MXene, N-MXene, N, S-MXene and 3D MXene; (e-h) MXene/S, N-MXene/S, N, S-MXene/S and 3D MXene/S.

The different morphologies of these composites contribute to their distinct performance, shown in **Figure 5.3**. There is no doubt that MXene/S presents the lowest first specific capacity of merely  $917.5 \text{ mAh}\cdot\text{g}^{-1}$  at  $0.1 \text{ C}$ , refer to the charge-discharge curve in **Figure 5.3a**. The capacity rises slightly to over  $1000 \text{ mAh}\cdot\text{g}^{-1}$  after nitrogen

doping due to the increased active sites of MXene. For N, S-MXene/S and 3D MXene/S cathodes, they own about  $1200 \text{ mAh}\cdot\text{g}^{-1}$  high capacity because it could speculate N, S-MXene and 3D MXene have a relatively large SSA with smaller sized MXene sheets seen in SEM images in **Figure 5.2c-d**, and there is a less agglomeration of large particles for N, S-MXene/S and 3D MXene/S, which benefits to high utilization of sulfur. As shown in **Figure 5.3b** and **Table 5.1**, all the modified MXene/S possess a retention rate of about 55 % while the pristine MXene/S just owns 49 %, since nitrogen and sulfur doping can add active sites and 3D modification can expose more active sites of MXene, contributing to enhanced adsorption of polysulfides.

For the performance at 1 C large current density in **Figure 5.3c**, the situation has changed in some respects. 3D MXene/S has the highest initial capacity of  $748.3 \text{ mAh}\cdot\text{g}^{-1}$  owing to a high conductive network, but the capacity drops relatively fast after 200 cycles. On the contrary, element-doped MXenes display a more stable cycle performance (over 60 % retention after 500 cycles) though losing some conductivity. For the rate performance in **Figure 5.3d**, it is evident that 3D MXene/S and MXene/S with the highest and lowest conductivity present corresponding capacities of  $528.9 \text{ mAh}\cdot\text{g}^{-1}$  and  $384.1 \text{ mAh}\cdot\text{g}^{-1}$ , and the values of 3D MXene/S and MXene/S are in the middle.



**Figure 5.3** (a) First charge-discharge curves; (b) Charge-discharge performance at 0.1 C, (c) Charge-discharge performance at 1 C large current density and (d) Rate performance from 0.1 C to 4 C of four different cathodes.

**Table 5.1** Comparison of different performances for four different cathodes.

	<b>0.1 C (1<sup>st</sup>, 100 cycles retention)</b>	<b>1 C (1<sup>st</sup>, 500 cycles retention)</b>	<b>Rate (0.1 C, 4 C)</b>
<b>N-MXene/S</b>	1015.7 mAh·g <sup>-1</sup> 56.2%	608.2 mAh·g <sup>-1</sup> 64.7%	1067.4 mAh·g <sup>-1</sup> 450.3 mAh·g <sup>-1</sup>
<b>N,S-MXene/S</b>	1230.7 mAh·g <sup>-1</sup> 53.3%	721.9 mAh·g <sup>-1</sup> 60.4%	1205.1 mAh·g <sup>-1</sup> 477.4 mAh·g <sup>-1</sup>
<b>3D MXene/S</b>	1172.7 mAh·g <sup>-1</sup> 56.4%	748.3 mAh·g <sup>-1</sup> 51.3%	1283.9 mAh·g <sup>-1</sup> 528.9 mAh·g <sup>-1</sup>
<b>MXene/S</b>	917.5 mAh·g <sup>-1</sup> 49.4%	583.4 mAh·g <sup>-1</sup> 59.4%	960.9 mAh·g <sup>-1</sup> 384.1 mAh·g <sup>-1</sup>

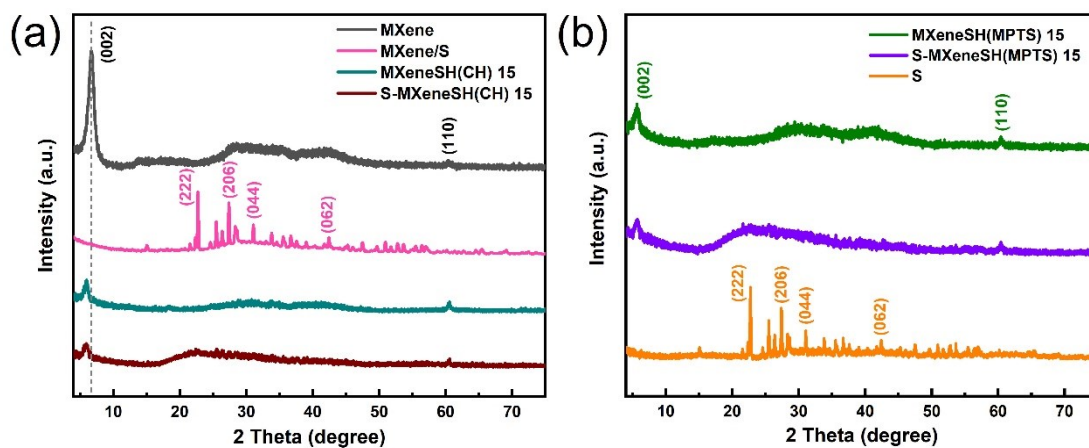
### 5.3.2 Comparison of different sulfydryl-modified methods

As seen in the morphology in **Figure 5.2** and battery performance in **Figure 5.3**, all the modified MXene/S cathodes do not possess regular shape and, more importantly, have just mediocre performance because simple and rough modification and traditional physical adsorption of MXene to sulfur are inadequate for requirements of Li-S batteries' development. Hence, the sulfydryl functionalized MXene and the chemical adsorption method are put forward to experiment.

In order to verify the phase structure, XRD patterns of different samples were shown in **Figure 5.4**. For the as-prepared MXene sheets (black line in **Figure 5.4a**), there is a strong peak of (002) at 6.6° and a weak peak of (110) at 61.0° [11, 12]. After growing sulfur on the MXene via the traditional melting method, the MXene/S shows

almost all the characteristic peaks of sulfur, such as (222), (206), (044) and (062), due to the formation of high-content crystalline sulfur (72.1 % in **Figure 5.11d**) in composite [13]. The characteristic peaks of MXene are not visible, which is probably attributed to the agglomerated large particles and the surface is mainly covered by the melting sulfur in **Figure 5.5b**. In contrast, the MXeneSH(CH) 15 shows peaks from MXene but a relatively lower intensity at  $6.6^\circ$ . The signal from S is not detectable due to a small quantity of sulfydryl (S-H peak in **Figure 5.10b**). When the element sulfur was connected to MXeneSH(CH) 15 via a ring-opening polymerization, the resultant S-MXeneSH(CH) 15 composite (brown line) displays a broad and weak peak at  $22.4^\circ$  approaching the crystal face (222), indicating the element sulfur exists mainly in an amorphous state [14]. For the S-MXeneSH(MPTS) 15 composite (purple line in **Figure 5.4b**), similar shapes and peaks as S-MXeneSH(CH) 15 are observed, suggesting that both strategies lead to similar chemical bonding with sulfur. It is also noted that for MXeneSH(CH) 15 composite, the diffraction peak (002) of MXene shifts from  $6.6^\circ$  to  $5.9^\circ$ , in line with its increased interlayer spacing as reported previous in ref [15]. While a lower diffraction peak of (002) at  $5.6^\circ$  is seen for MXeneSH(MPTS) 15 because the larger MPTS molecules contribute to a larger increment of interlayer spacing.



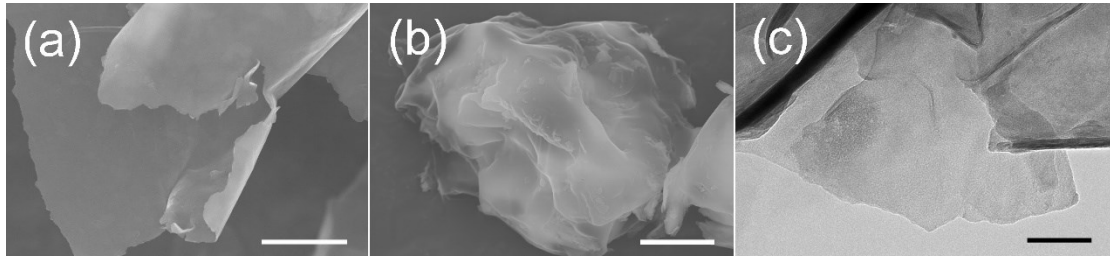


**Figure 5.4** XRD patterns of (a) MXene, MXene/S, MXeneSH(CH) 15 and S-MXeneSH(CH) 15; (b) MXeneSH(MPTS) 15, S-MXeneSH(MPTS) 15 and sublimed sulfur.

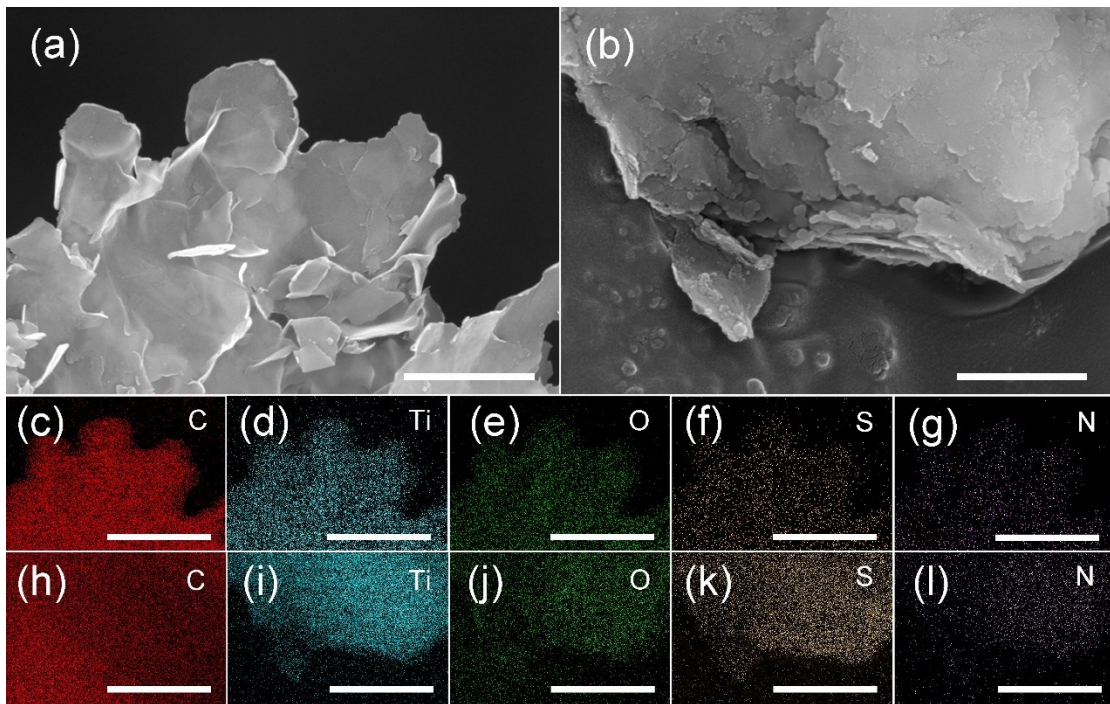
The morphology of different sulfydryl-modified MXene was examined by electron microscopy. FE-SEM image in **Figure 5.6a** and **Figure 5.8a** shows that due to the sulfydryl modification, MXeneSH(CH) 15 and MXeneSH(MPTS) 15 sheets present a wrinkled feature, while the pristine MXene sheets exhibit a smooth surface (**Figure 5.5a**). Particularly, MXeneSH(CH) 15 has a smaller size of flakes. **Figure 5.6c-g** are EDS mapping of different elements corresponding to the area of **Figure 5.6a**. It is clear that all the elements are dispersed well in the MXeneSH(CH) 15 sheets. A small quantity of the nitrogen element is referred to nitrogen atoms in CH molecules. After growing sulfur, as seen in **Figure 5.6a** and **Figure 5.8b** for S-MXeneSH(CH) 15 and S-MXeneSH(MPTS) 15, the flake structure (from the edge of the samples) is preserved. For EDS mapping of S-MXeneSH(CH) 15 in **Figure 5.6h-l**, all the elements are also dispersed uniformly, and an increased content of sulfur is seen as expected after the sulfur loading. In **Figure 5.6h**, the elemental carbon spanned the full area is due to the background of conducting resin. As a comparison, MXene/S was fabricated by a

traditional melting method of growing sulfur and a large particle with a diameter of several micrometers is observed (**Figure 5.5b**). Hence, the functional modification MXene can relieve agglomeration between MXene and sulfur during the high-temperature melting process and prevent sulfur attach to the composite, forming a large particle when cooling down.

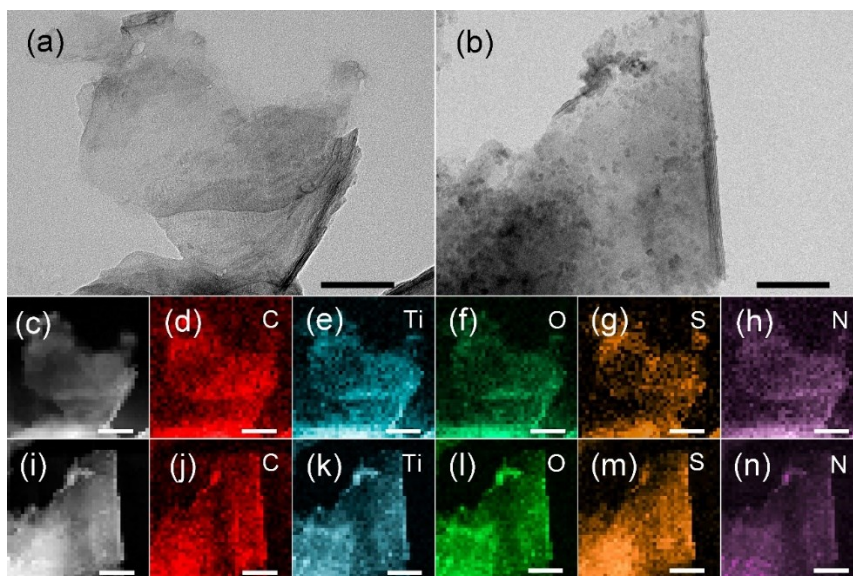
The morphology was further examined under high-resolution TEM. As shown in **Figure 5.7a-b**, MXeneSH(CH) 15 presents a few stacked sheet structure with size of around 300 nm. Meanwhile, the main structure of S-MXeneSH(CH) 15 sheets show almost no change, but it appears some nanoparticles on account of sulfur growing. This feature benefits effective and sufficient contact between sulfur and MXene sheets, which ensures a high utilization of sulfur and specific capacity. **Figure 5.7c,i** are STEM EDS mapping areas of MXeneSH(CH) 15 and S-MXeneSH(CH) 15. **Figure 5.7d-h** and **Figure 5.7j-n** prove all the elements dispersed evenly in corresponding composites. Noticeably in **Figure 5.7g**, the signal of sulfur appears weaker for MXeneSH(CH) 15 than that of S-MXeneSH(CH) 15, which agrees well to the result observed in SEM images (**Figure 5.6f,k**). A similar result is observed for the materials modified by MPTS. S-MXeneSH(MPTS) 15 becomes thicker with a few particles compared with MXeneSH(MPTS) 15 in **Figure 5.8c-d**. All the elements are also dispersed uniformly in **Figure 5.8f-j** and **Figure 5.8l-p**. The existence of the silicon element (**Figure 5.8j** and **5.8p**) is attributed to MPTS molecules.



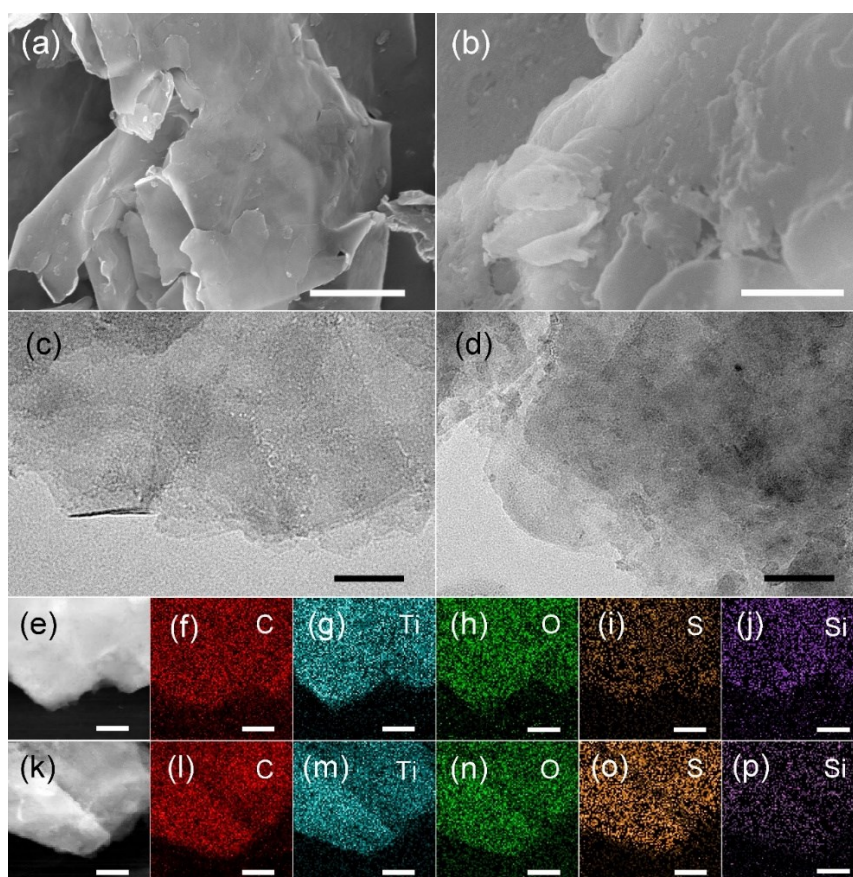
**Figure 5.5** FE-SEM images of (a) pristine MXene sheets and (b) MXene/S composite; (c) TEM image of pristine MXene sheets. Scale bars: (a) 1  $\mu\text{m}$ ; (b) 2 $\mu\text{m}$ ; (c) 100 nm.



**Figure 5.6** FE-SEM images of (a) MXeneSH(CH) 15 and (b) S-MXeneSH(CH) 15; Corresponding EDS mappings of (c-g) MXeneSH(CH) 15 and (h-l) S-MXeneSH(CH) 15. Scale bars: (a-b) 1  $\mu\text{m}$ ; (c-l) 2  $\mu\text{m}$ .



**Figure 5.7** TEM images of (a) MXeneSH(CH) 15 and (b) S-MXeneSH(CH) 15; STEM EDS mapping areas of (c) MXeneSH(CH) 15 and (i) S-MXeneSH(CH) 15; Corresponding STEM EDS mapping of (d-h) MXeneSH(CH) 15 and (j-n) S-MXeneSH(CH) 15. Scale bar: 100 nm.



**Figure 5.8** FE-SEM images of (a) MXeneSH(MPTS) 15 and (b) S-MXeneSH(MPTS)

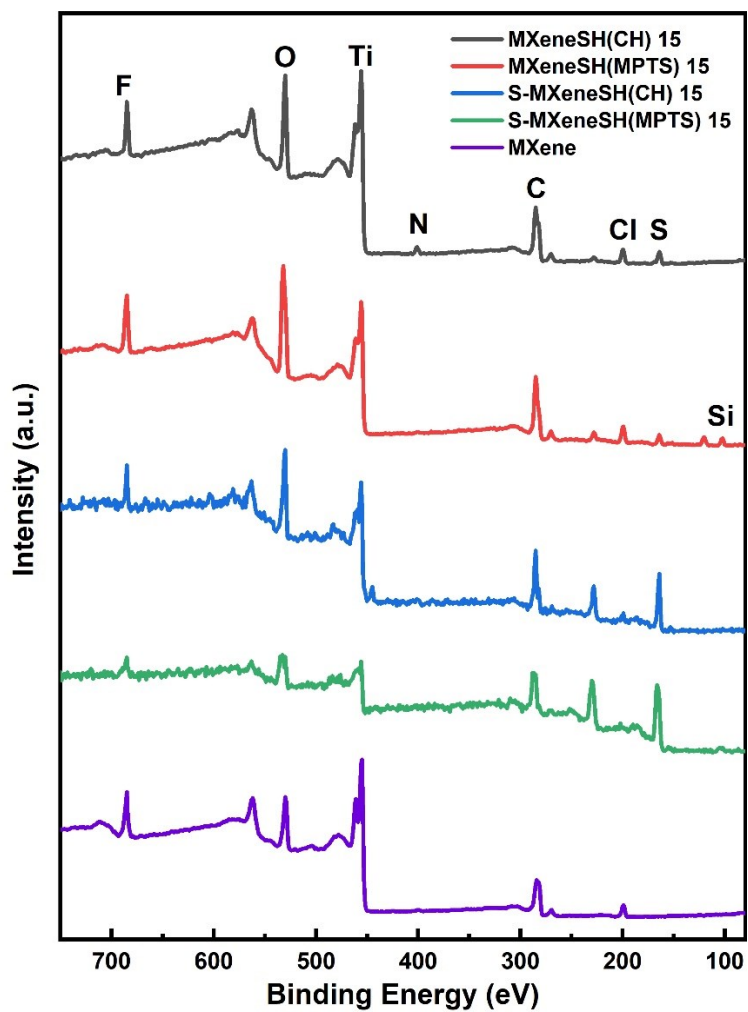
15; TEM images of (c) MXeneSH(MPTS) 15 and (d) S-MXeneSH(MPTS) 15; STEM EDS mapping area of (e) MXeneSH(MPTS) 15 and (k) S-MXeneSH(MPTS) 15; Corresponding STEM EDS mapping of (f-j) MXeneSH(MPTS) 15 and (l-p) S-MXeneSH(MPTS) 15. Scale bars: (a-b) 1  $\mu\text{m}$ ; (c-p) 100 nm.

To verify the chemical bondings of these composites, XPS analysis was performed. For the full scan in **Figure 5.9**, MXeneSH(CH) 15 owns the C 1s (285 eV), Ti 2p (456 eV) and O 1s (530 eV) peaks with high intensity assigned to the pristine MXene sheets (purple line), which has the main content of  $\text{Ti}_3\text{C}_2$  and a large amount of oxygen-containing functional groups. In addition, the existence of the F 1s (685 eV) and Cl 2p (200 eV) peaks corresponds to other fluorine-containing and chlorine-containing functional groups [15-17]. After the modification, the weak S 2p (164 eV) and N 1s (401 eV) peaks appear [8] because CH molecules replace hydroxyl groups on MXene sheets, and sulfydryl groups are exposed outside [5]. As a comparison, MXeneSH(MPTS) 15 shows no remarkable changes for most of peaks, except a Si 2p peak at 102 eV and no N 1s peak owing to the MPTS molecules [18]. According to the peak area, the sulfur content of MXeneSH(CH) 15 and MXeneSH(MPTS) 15 can be calculated as 2.97 % and 2.49 %, indicating that more sulfydryl groups are formed for MXeneSH(CH) 15 than MXeneSH(MPTS) 15. Therefore, more sulfydryl groups on MXeneSH(CH) 15 benefit to ring-opening polymerization of sulfur later. When the element sulfur grows on these two composites, the S-MXeneSH(CH) 15 and S-MXeneSH(MPTS) 15 show a noticeable increase in the intensity of S peak [5].

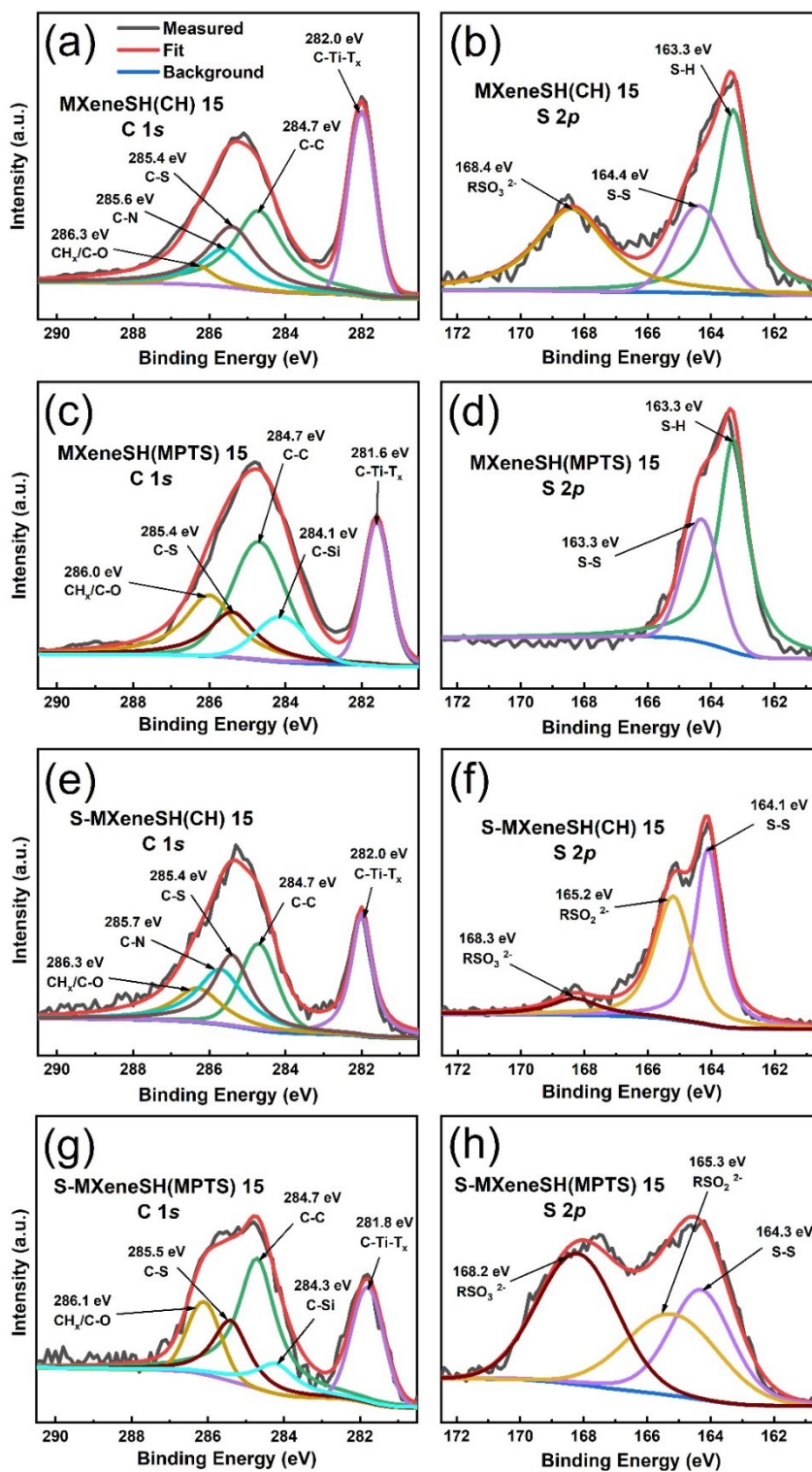
The more detailed fitting results are shown in **Figure 5.10**. For C 1s patterns of

MXeneSH(CH) 15 in **Figure 5.10a**, the peaks of C-C (284.7 eV), C-Ti-T<sub>x</sub> (282.0 eV) and CH<sub>x</sub>/C-O (286.3 eV) bonds correspond to the characteristic peaks of pristine MXene [19]. Moreover, the peaks of C-S and C-N bonds at 285.4 eV and 285.6 eV are due to adherence of CH molecules and sulfydryl modifying [5, 8, 20]. Particularly, the signal of the CH<sub>x</sub>/C-O peak is relatively weak due to its low content. During the hydrothermal process, a substitution reaction occurs and the CH molecules replace the hydroxyl groups [5]. It is found that MXeneSH(MPTS) 15 in **Figure 5.10c** presents a slightly stronger peak of CH<sub>x</sub>/C-O because MPTS molecules replace hydroxyl groups during the hydrolysis and connect in the form of C-O-Si bond. Therefore, the number of the C-O bond is higher than that of MXeneSH(CH) 15 while creating C-S (285.4 eV), as well as C-Si (284.1 eV) peaks [8, 18]. In **Figure 5.10e,g**, since the element sulfur connects directly to sulfydryl groups for both S-MXeneSH(CH) 15 and S-MXeneSH(MPTS) 15, their C 1s spectra are almost not affected by the process. For S 2p pattern of MXeneSH(CH) 15 in **Figure 5.10b**, there is a peak at 163.3 eV corresponding to the S-H bond due to the successful sulfydryl modification. The peak at 168.4 eV is associated with the RSO<sub>3</sub><sup>2-</sup> owing to partial oxidation in a hydrothermal reaction. MXeneSH(MPTS) 15 presents similar peaks but without RSO<sub>3</sub><sup>2-</sup> due to no oxidation when the hydrolysis occurs at room temperature. After growing sulfur via polymerization, S-MXeneSH(CH) 15 and S-MXeneSH(MPTS) 15 show markedly S-S bonds, and S-H bonds disappear because of S-H bonds breakage and chemical adsorption of element sulfur [5, 18]. In **Figure 5.10f** and **5.10h**, the quantity of RSO<sub>2</sub><sup>2-</sup> and RSO<sub>3</sub><sup>2-</sup> for S-MXeneSH(MPTS) 15 are higher than S-MXeneSH(CH) 15, implying

a higher level of oxidation for S-MXeneSH(MPTS) 15 during polymerization process at high temperature.



**Figure 5.9** Full scan of XPS survey for five different materials.



**Figure 5.10** XPS C 1s patterns of (a) MXeneSH(CH) 15, (c) MXeneSH(MPTS) 15, (e) S-MXeneSH(CH) 15 and (g) S-MXeneSH(MPTS) 15 ; XPS S 2p patterns of (b) MXeneSH(CH) 15, (d) MXeneSH(MPTS) 15, (f) S-MXeneSH(CH) 15 and (h) S-MXeneSH(MPTS) 15.

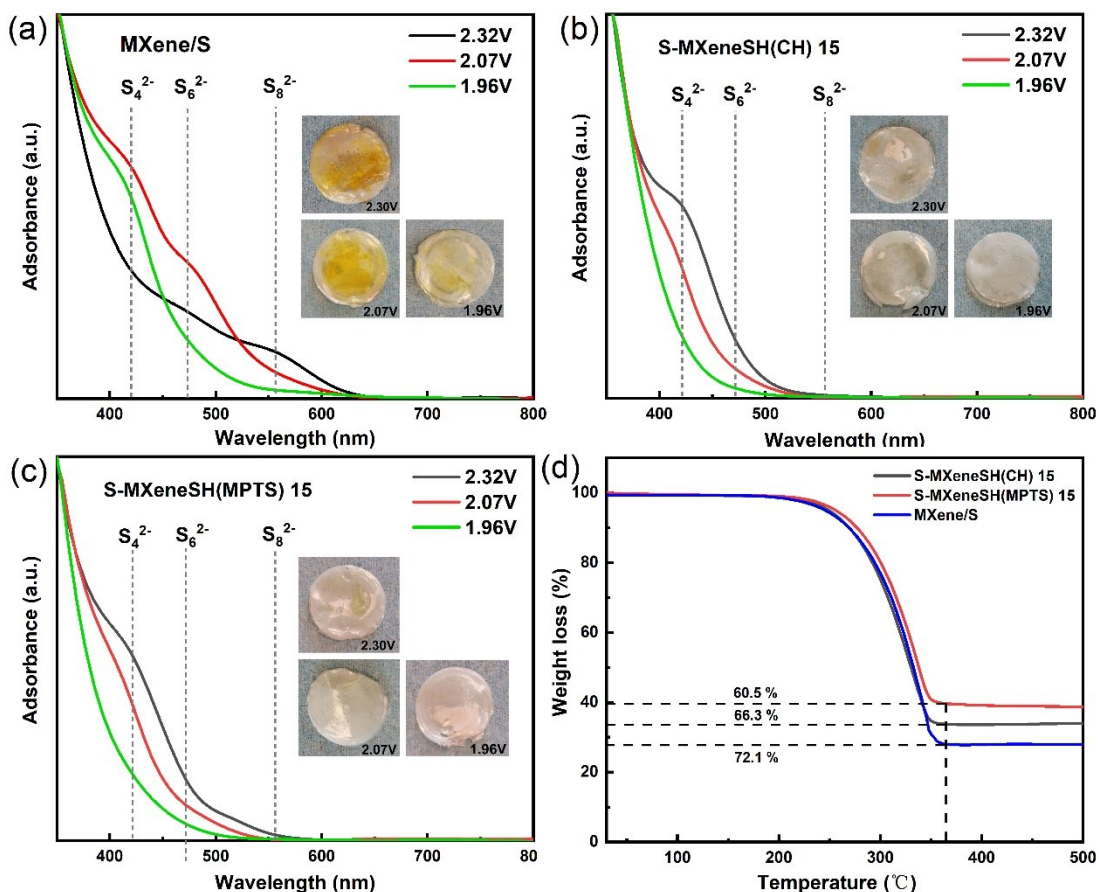


To clarify reaction mechanism and ingredient of polysulfides, UV-vis spectroscopy was performed by detecting the component variation in the electrolyte during the discharging. The UV-vis curves are shown in **Figure 5.11**, and optical images of corresponding soaked separators are inserted. As reported in previous work, the adsorption peaks of  $S_4^{2-}$ ,  $S_6^{2-}$  and  $S_8^{2-}$  are 420 nm, 470 nm and 560 nm, corresponding to  $Li_2S_4$ ,  $Li_2S_6$  and  $Li_2S_8$ , respectively [21]. For MXene/S in **Figure 5.11a**, the curve of 2.32 V appears an adsorption peak around 560 nm, suggesting its main component is  $Li_2S_8$ , while the curve of 2.07 V displays two weak adsorptions at about 420 nm and 470 nm, indicating polysulfides are transferred to  $Li_2S_6$  and  $Li_2S_4$ . When the discharge process continues to 1.96 V, the adsorption is shifted to only 420 nm, proving polysulfides are reduced to  $Li_2S_4$ . This phenomenon is in accordance with a general chemical reaction in Li-S batteries [22]. However, S-MXeneSH(CH) 15 shows a noticeably distinct state in **Figure 5.11b**. There are no adsorptions of  $S_8^{2-}$  and  $S_6^{2-}$  for three curves, while the curve of 2.30 V just has adsorption at around 420 nm of  $S_4^{2-}$ , demonstrating no high-order polysulfides ( $Li_2S_6$  and  $Li_2S_8$ ) are created. Only  $Li_2S_4$  is generated as the intermediate at the beginning of discharge process, which confirms the suppression of “shuttle effect” greatly. At the following discharging,  $Li_2S_4$  is gradually reduced to low-order polysulfides ( $Li_2S$ ,  $Li_2S_2$  and  $Li_2S_3$ ). According to previous work [5], Gibbs free energy can be used to explain the feature of no high-order polysulfides generated. Briefly, after sulfhydryl modification, the ring-opened  $S_8$  molecule is covalently stabilized on the MXene sheets by chemical bonding, which is much stronger than general physical adhesion. Consequently,  $Li_2S_4$  is the most probable

intermediate product to be produced with the lowest Gibbs free energy of  $-103.5 \text{ kcal}\cdot\text{mol}^{-1}$ , which prevent the production of high-order polysulfides ( $\text{Li}_2\text{S}_n, n>4$ ) at the first stage. Along with the continued insertion of  $\text{Li}^+$ , the  $\text{Li}_2\text{S}_4$  is reduced further and the final produced polysulfides are  $\text{Li}_2\text{S}$ ,  $\text{Li}_2\text{S}_3$  and  $\text{Li}_2\text{S}_2$ , with Gibbs free energy change of  $-57.5$ ,  $-66.3$  and  $-72.9 \text{ kcal}\cdot\text{mol}^{-1}$  [28]. For this reason, UV-vis curves of these three discharging voltages for S-MXeneSH(MPTS) 15 also exhibit a similar shape (**Figure 5.11c**) because it has ring-opened  $\text{S}_8$  stabilizing on the MXene surface via sulfydryl groups and the similar reaction [18].

To determine the sulfur content in composites, the TGA curves of three different cathodes under a nitrogen flow are illustrated in **Figure 5.11d**. Weight losses of S-MXeneSH(CH) 15, S-MXeneSH(MPTS) 15 and MXene/S over  $360 \text{ }^\circ\text{C}$  were 66.3 wt%, 60.5 wt% and 72.1 wt%, indicating the sulfur content in corresponding composites. Compared to sulfydryl-modified graphene with 60.7 % in previous work [5], the S-MXeneSH(CH) 15 presents a higher sulfur content because more abundant hydroxyl groups on MXene provide more anchor points for substitution reaction of sulfydryl groups, and more sulfydryl groups benefit to more sulfur grafted to MXene. In addition, the sulfur content of S-MXeneSH(CH) 15 is higher than S-MXeneSH(MPTS) 15. The reasons for this phenomenon can be explained as follows. During the substitution reaction for MXeneSH(CH) 15, a CH molecule is connected to MXene sheets by replacing a hydroxyl group [5]. Comparatively, when MXeneSH(MPTS) 15 occurs in a hydrolysis reaction, an MPTS molecule may consume one to three hydroxyl groups to connect to MXene sheets via a condensation reaction

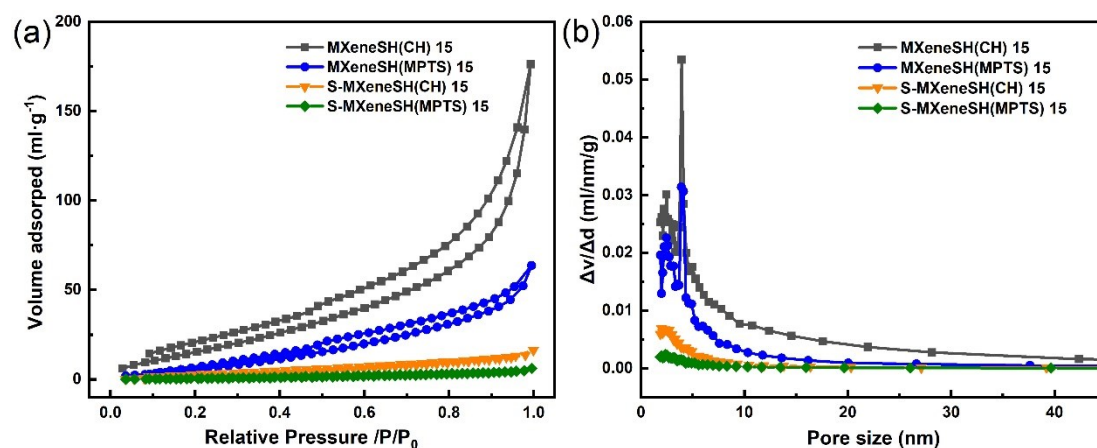
[18]. In fact, both the CH molecule and MPTS molecule just have a sulfydryl group. As a result, it could obtain more sulfydryl groups by consuming the same hydroxyl groups via the substitution reaction of CH molecules, which is agreed with sulfur content results via XPS characterization in Fig.S3. Therefore, the more sulfydryl groups contribute to the more sulfur molecules grafted on MXene sheets in the sulfur-growing process. As a reference, MXene/S possesses 72.1 % sulfur in the composite, since MXene and sublimed sulfur was mixed with the mass ratio of 1:3. Under the same mixing ratio, S-MXeneSH(CH) 15 has a slightly lower sulfur content because a small part of sulfur might not chemically connect to sulfydryl groups but exists in the form of physical adhesion. After the Ar gas stream in the tubular furnace at 155 °C, the physically adhered sulfur is removed, and the sulfur chemically bonded to sulfydryl groups remains in the system similar to the work reported previously [5]. The lower value of S-MXeneSH(MPTS) 15 suggests less sulfur grafted to the MXene with less sulfydryl groups on the surface.



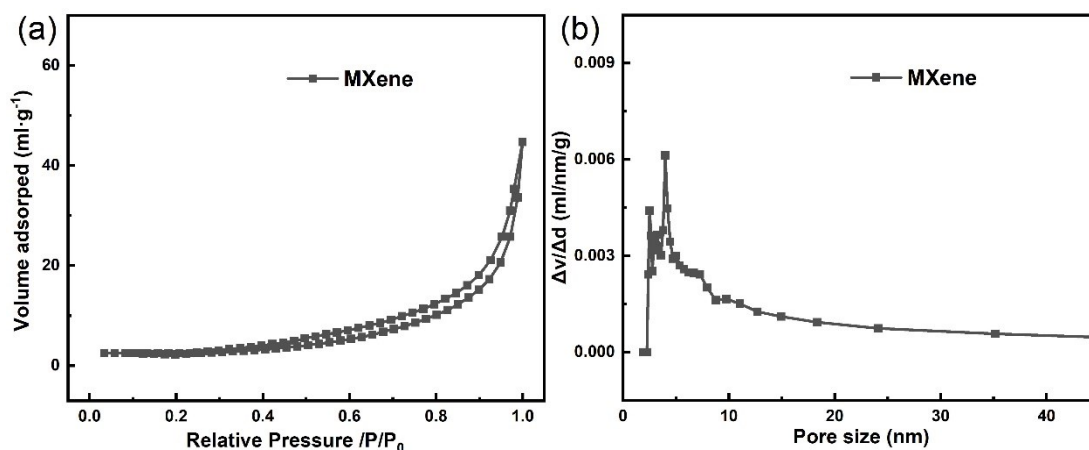
**Figure 5.11** The UV-vis spectra for polysulfides at different discharge voltages with a current rate of 0.1 C. (a) MXene/S, (b) S-MXeneSH(CH) 15. (c) S-MXeneSH(MPTS) 15. Inserts: separators taken from disassembled batteries at corresponding voltages. (d) TGA curves of S-MXeneSH(CH) 15, S-MXeneSH(MPTS) 15 and MXene/S.

Results of the BET approach and BJH pore size distribution analysis of four different composites are shown in **Figure 5.12**. The sulfhydryl modification can improve specific surface area (SSA) for MXene material because of preventing stacking of MXene and creating porous structure [23]. According to the nitrogen adsorption-desorption isotherms, it can be calculated that MXeneSH(CH) 15 has the highest SSA with  $72.6 \text{ m}^2 \cdot \text{g}^{-1}$ . The SSA of MXeneSH(MPTS) 15 is  $35.2 \text{ m}^2 \cdot \text{g}^{-1}$ , which is two times lower than MXeneSH(CH) 15 but still several times higher than  $7.9 \text{ m}^2 \cdot \text{g}^{-1}$  of pristine

MXene (**Figure 5.13a**). All of them have a characteristic pore size of 4 nm compared to MXene sheets, while MXeneSH(CH) 15 has more micropores than MXeneSH(MPTS) 15 [24]. After sulfur growing, the SSA of both S-MXeneSH(CH) 15 and S-MXeneSH(MPTS) 15 drops to  $19.7 \text{ m}^2 \cdot \text{g}^{-1}$  and  $3.2 \text{ m}^2 \cdot \text{g}^{-1}$ . This can be explained by heavy  $\text{S}_8$  molecules chemically bonded to MXeneSH(CH) 15 and MXeneSH(MPTS) 15, which significantly increase the weight of the composites. And the chain-like molecular structure formed outside MXene via  $\text{S}_8$  molecules has no extra pores and therefore no contribution to the surface area. Another reason is that the whole large-sized morphology of the composites is more compact as shown in **Figure 5.6b** and **Figure 5.8b**, leading to the low SSA. Nevertheless, S-MXeneSH(CH) 15 presents a relatively higher SSA compared to pure MXene, which can greatly increase the utilization of sulfur and the specific capacity of its batteries.



**Figure 5.12** (a) Nitrogen adsorption-desorption isotherms and (b) Pore-size distributions of four different composites.



**Figure 5.13** (a) Nitrogen adsorption-desorption isotherms and (b) pore-size distributions of pristine MXene.

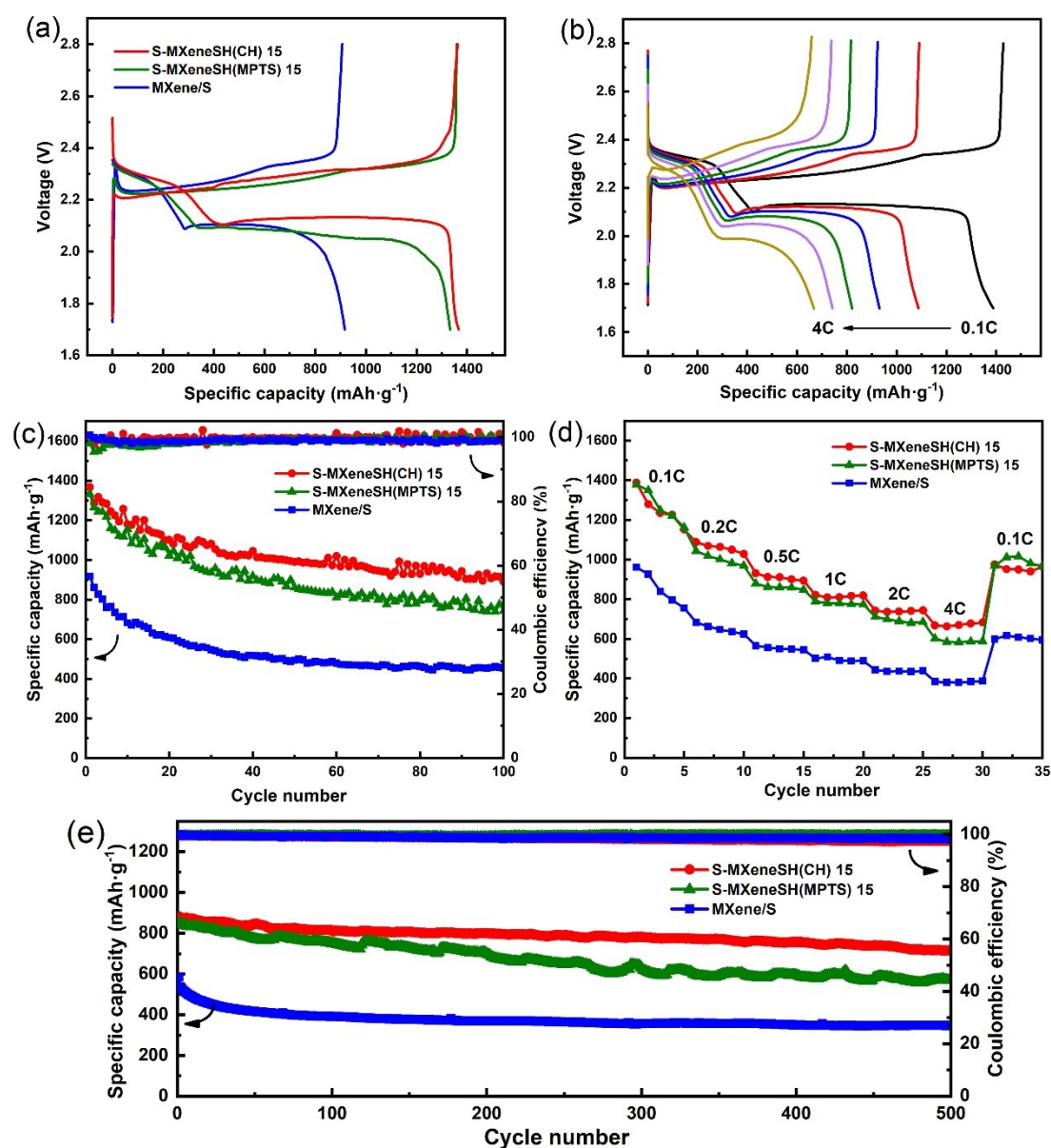
To test electrochemistry performance, galvanostatic discharge-charge behaviors with different batteries were first evaluated at 0.1 C. In **Figure 5.14a**, there is the highest initial discharge specific capacity of  $1367 \text{ mAh}\cdot\text{g}^{-1}$  for S-MXeneSH(CH) 15 while  $1333 \text{ mAh}\cdot\text{g}^{-1}$  for S-MXeneSH(MPTS) 15 owing to the uniform dispersion of sulfur in nanoscale and high utilization of sulfur (seen in Fig.4 and Fig.S2). However, MXene/S shows just  $918 \text{ mAh}\cdot\text{g}^{-1}$  capacity due to its large particles and low sulfur utilization (seen in Fig.S1b). Meanwhile, the polarization of S-MXeneSH(CH) 15 is the smallest, indicating that S-MXeneSH(CH) 15 owns sufficient active sites, electron transport channels and fast electron transport speed. For the following cycles at 0.1 C in **Figure 5.14c**, all the composites present a high coulombic efficiency ( $>98 \%$ ). S-MXeneSH(CH) 15 exhibits the most stable cycling performance and remains  $890 \text{ mAh}\cdot\text{g}^{-1}$  with 65.1 % retention after 100 cycles, which attributes to strong polysulfides adsorption of sulfydryl-modified MXeneSH(CH) 15 and suppression of high-order polysulfides intermediate products ( $\text{Li}_2\text{S}_6$  and  $\text{Li}_2\text{S}_8$ ) generated [5]. Therefore, the existence of more low-order polysulfides intermediate products ( $\text{Li}_2\text{S}_2$ ,  $\text{Li}_2\text{S}_3$ ) can

ensure cycling more stable due to the insolubility of low-order polysulfides [25]. On account of fewer sulfydryl groups, S-MXeneSH(MPTS) 15 displays a slightly fast decay rate with about 55.7 % retention ( $743 \text{ mAh}\cdot\text{g}^{-1}$  after 100 cycles). For MXene/S, it only delivers  $453 \text{ mAh}\cdot\text{g}^{-1}$  and 49.4 % capacity.

S-MXeneSH(CH) 15 also presents the highest capacity for the rate performance. In **Figure 5.14b** and **Figure 5.14d**, it maintains  $668 \text{ mAh}\cdot\text{g}^{-1}$  when the current density increases to 4 C and has no large polarization during this process, suggesting excellent conductivity of sulfydryl-modified MXeneSH(CH) 15. Likewise, S-MXeneSH(MPTS) 15 shows a slightly low capacity of  $601.1 \text{ mAh}\cdot\text{g}^{-1}$  at 4 C. However, the capacity is just  $384 \text{ mAh}\cdot\text{g}^{-1}$  for MXene/S because the formation of large particles of the composite reduces the transferable ability of electrons and the stacking of MXene hinders the transmission of Li-ions [26]. For the 1 C large current cycling in **Figure 5.14e**, it occurs a similar trend as 0.1 C. Owing to the high conductivity, S-MXeneSH(CH) 15 and S-MXeneSH(MPTS) 15 achieve  $880 \text{ mAh}\cdot\text{g}^{-1}$  and  $848 \text{ mAh}\cdot\text{g}^{-1}$  for the first capacity, and remain  $715 \text{ mAh}\cdot\text{g}^{-1}$  and  $569 \text{ mAh}\cdot\text{g}^{-1}$  with 81.3 % and 79.6 % retention respectively after 500 cycles. By comparison, MXene/S just has 59.3 % remaining after long cycles. Therefore, it can be concluded that sulfydryl modification avoids the production of high-order polysulfides and remarkably decreases the dissolution of polysulfides, contributing to the excellent cycling stability and retention rate [5, 18].

In general, S-MXeneSH(CH) has a higher performance because CH has a relatively short molecular structure with more effective sulfydryl groups to combine sulfur with MXene sheets covalently in the same weight (detailed analysis in TGA test

part). However, the hydrolysis reaction of S-MXeneSH(MPTS) is milder and safer because it occurs at room temperature, which may be desired in practical applications.

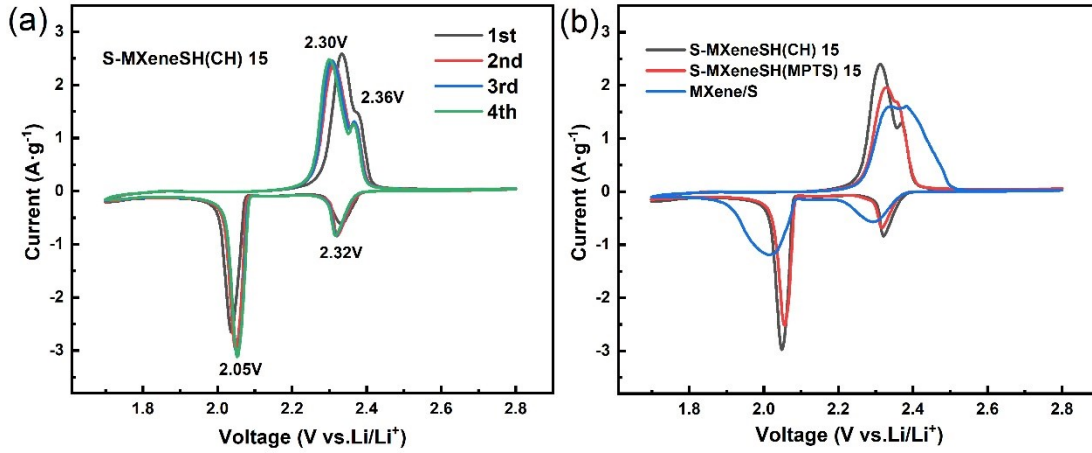


**Figure 5.14** (a) First discharge-charge curves of three different batteries at 0.1 C; (b) The discharge-charge curves with different current densities of S-MXeneSH(CH) 15; (c) Cyclic performances of three different batteries at 0.1 C; (d) Rate performances of three different batteries. (e) Cyclic performance of three different batteries at the large current density of 1 C.

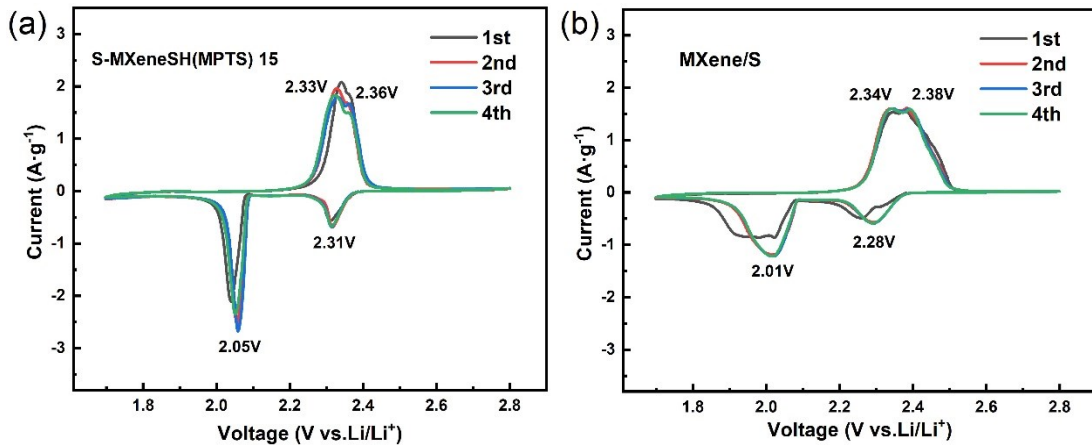
To further reveal the redox process during charge-discharge process, CV profiles



in a voltage window of 1.7 to 2.8 V at  $0.1 \text{ mV}\cdot\text{s}^{-1}$  are exhibited in **Figure 5.15** and **Figure 5.16**. In Fig. **Figure 5.15a**, it is evident that two reduction peaks are located at 2.32 V and 2.05 V, which refer to the two reductions of transferring sulfur to high-order polysulfides (mainly  $\text{Li}_2\text{S}_4$  in this work) and further to final products  $\text{Li}_2\text{S}_2$  or  $\text{Li}_2\text{S}$ . Two peaks at 2.30 V and 2.36 V correspond to two oxidation reactions [27]. During the first cycle, it is obvious that three composites have polarization voltages of redox peaks (**Figure 5.15a** and **Figure 5.16**), primarily because of the inhomogeneous electrolyte and the unstable chemical reaction. This phenomenon occurs more severely on MXene/S composite as it exists large particles with several micrometers (as seen in Fig.S1b), which need more standing or cycling to make electrolyte infiltrate fully. Hence, the polarization decreases, and the overlapping feature improves in the subsequent 2-4th cycles, indicating the charge-discharge of batteries and reaction kinetics become more stable [28, 29]. Based on this, we choose CV curves (**Figure 5.15b**) at the second cycle of three composites to compare performance. S-MXeneSH(CH) 15 shows the sharpest redox peaks with the lowest polarization, proving full redox reactions and the excellent conductivity of the composite to ensure fast electron transfer. In the meantime, S-MXeneSH(MPTS) 15 owns a similar shape (**Figure 5.16a**), while MXene/S displays broad redox peaks due to insufficient chemical reactions and delayed electron transportation (**Figure 5.16b**) [26, 30].



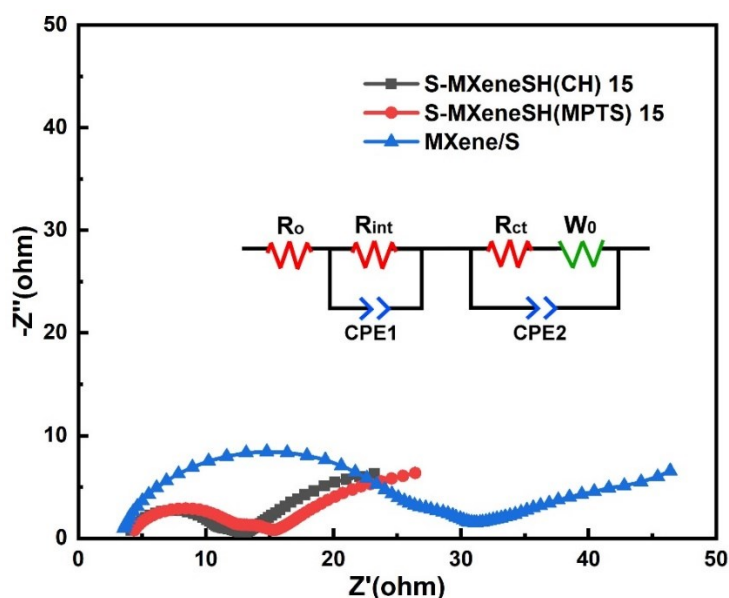
**Figure 5.15** (a) CV curves of the S-MXeneSH(CH) 15 composite at the scan rate of  $0.1 \text{ mV}\cdot\text{s}^{-1}$  for the 1-4th cycle. (b) Comparison of CV curves of the second cycle for S-MXeneSH(CH) 15, S-MXeneSH(MPTS) 15 and MXene/S composites.



**Figure 5.16** CV curves of (a) S-MXeneSH(MPTS) 15 and (b) MXene/S composites.

composites are listed in **Figure 5.17**. The semicircle in the high-frequency region refers to the internal impedance of the cathode ( $R_{\text{int}}$ ), and a small arc of a semicircle at the medium frequency range corresponds to the charge-transfer resistance ( $R_{\text{ct}}$ ). At low-frequency region, the short line is associated with a Warburg diffusion process ( $W_0$ ) of soluble lithium polysulfides in the electrolyte [31, 32]. An equivalent circuit is also included in Fig.10. The  $R_{\text{int}}$  values of the S-MXeneSH(CH) 15, S-MXeneSH(MPTS) 15 and MXene/S composites are calculated to be  $6.1 \text{ }\Omega$ ,  $7.0 \text{ }\Omega$  and  $21.9 \text{ }\Omega$ , respectively,

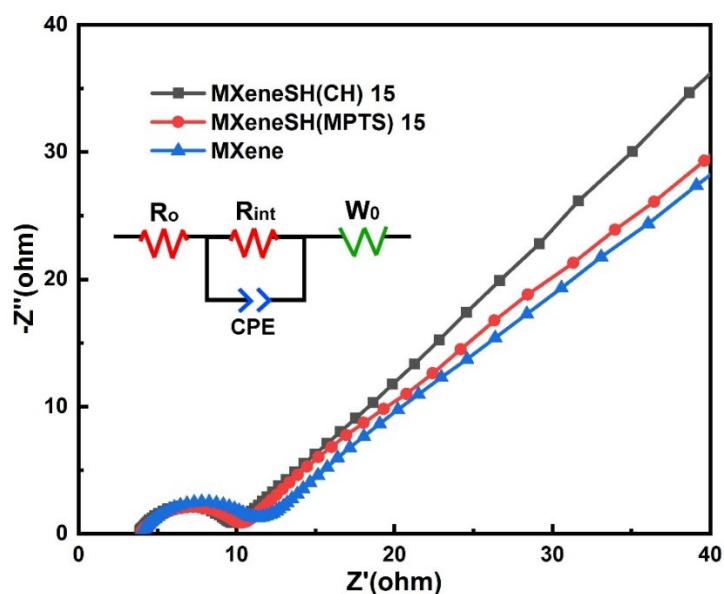
demonstrating the conductivity of S-MXeneSH(CH) 15 and S-MXeneSH(MPTS) 15 is significantly higher than MXene/S. The results align with rate performance and 1 C cycling performance as before (Fig.8d-e), indicating sulfydryl modification process increases the SSA of MXene, prevent its stacking and open more transportation tunnel for electrons [5, 18, 33]. On the contrary, large particles of agglomerated and restacked structure are harmful to MXene/S, which not only greatly reduces the utilization of sulfur but also hinders electrons transfer, thus seriously limiting the conductivity of MXene [34, 35].



**Figure 5.17** Nyquist plots of S-MXeneSH(CH) 15, S-MXeneSH(MPTS) 15 and MXene/S composites. Insert: equivalent circuit.

The impedance of the MXeneSH(CH) 15, MXeneSH(MPTS) 15 and MXene is calculated via fitting semicircle in the high-frequency region of **Figure 5.18**, with a value of 5.1  $\Omega$ , 5.8  $\Omega$  and 6.5  $\Omega$ , respectively. These results prove that the conductivity of MXeneSH(CH) 15 and MXeneSH(MPTS) 15 are slightly higher than pure MXene. It can be explained that sulfydryl modification of MXene relieves stacking and opens

more transmission channels for electrons. Combining the results in the Manuscript in Fig.10, it can be concluded that the impedance of S-MXeneSH(CH) 15 and S-MXeneSH(MPTS) 15 also retain a low impedance of 6.1  $\Omega$  and 7.0  $\Omega$  after sulfur chemical bonding because no insulated elemental sulfur is generated, the stacking of MXene is relieved to a great extent and their conductivity is utilized effectively. While the impedance of MXene/S increases drastically to 21.9  $\Omega$  compared to 6.5  $\Omega$  of MXene, due to the formation of MXene/S large particles and low conductivity utilization of MXene.



**Figure 5.18** Nyquist plots of MXeneSH(CH) 15, MXeneSH(MPTS) 15 and MXene composites. Insert: equivalent circuit.

Through the 4-point probes resistivity measurement system, the resistivity values of S-MXeneSH(CH), S-MXeneSH(MPTS) and MXene/S are 0.053  $\Omega \cdot \text{cm}$ , 0.058  $\Omega \cdot \text{cm}$  and 0.157  $\Omega \cdot \text{cm}$ . The corresponding host materials without sulfur: MXeneSH(CH), MXeneSH(MPTS) and MXene show the resistivity of 0.033  $\Omega \cdot \text{cm}$ , 0.039  $\Omega \cdot \text{cm}$  and 0.045  $\Omega \cdot \text{cm}$ . After unifying and converting, the comparative values of different

electrode materials are listed in **Table 5.2** below. MXeneSH(CH) and MXeneSH(MPTS) present an enhanced conductivity compared to pristine MXene. After growing sulfur, the conductivity of S-MXeneSH(CH) and S-MXeneSH(MPTS) declines slightly while MXene/S drops significantly.

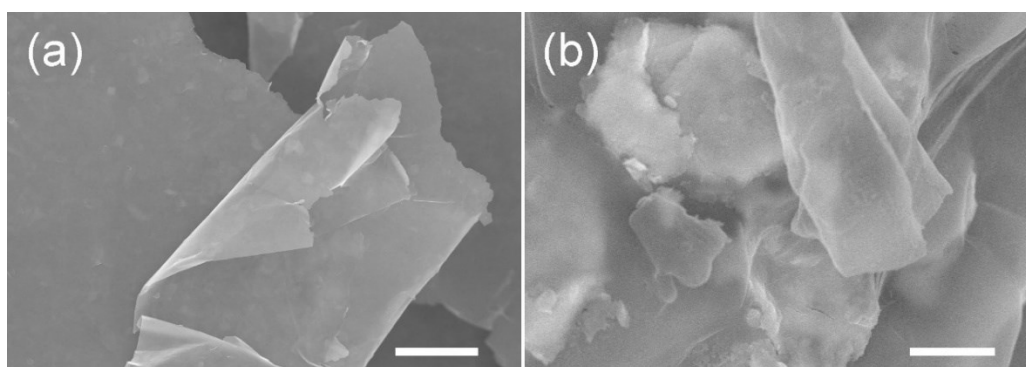
**Table 5.2** Tested resistivity and converted conductivity of different materials.

	Resistivity ( $\Omega \cdot m$ )	Conductivity (S/m)
S-MXeneSH(CH)	$5.3 \times 10^{-4}$	$1.89 \times 10^3$
S-MXeneSH(MPTS)	$5.8 \times 10^{-4}$	$1.72 \times 10^3$
MXene/S	$1.6 \times 10^{-3}$	$6.25 \times 10^2$
MXeneSH(CH)	$3.3 \times 10^{-4}$	$3.03 \times 10^3$
MXeneSH(MPTS)	$3.9 \times 10^{-4}$	$2.56 \times 10^3$
MXene	$4.5 \times 10^{-4}$	$2.22 \times 10^3$

### 5.3.3 Optimized ratio of CH for sulfydryl-modified MXene

The promising performance of the S-MXeneSH(CH) cathode promoted us to explore the optimal mixing ratio. First, MXene was mixed with CH of 5 times mass and carried out a hydrothermal reaction. The generated MXeneSH(CH) 5 (**Figure 5.19a**) displays similar morphology and size as pristine MXene (Fig.S1). When the usage of CH was increased to 15 and 20 times mass ratio of MXene, the created MXeneSH(CH) 15 and MXeneSH(CH) 20 both present a morphology similar to Fig.3a, which has a more crumpled structure and a smaller size. After growing sulfur via ring-opening polymerization, S-MXeneSH(CH) 5 exhibits a similar form of agglomerated large particles over  $2 \mu m$  (**Figure 5.19b**). At this ratio, it is likely that the available sulfydryl

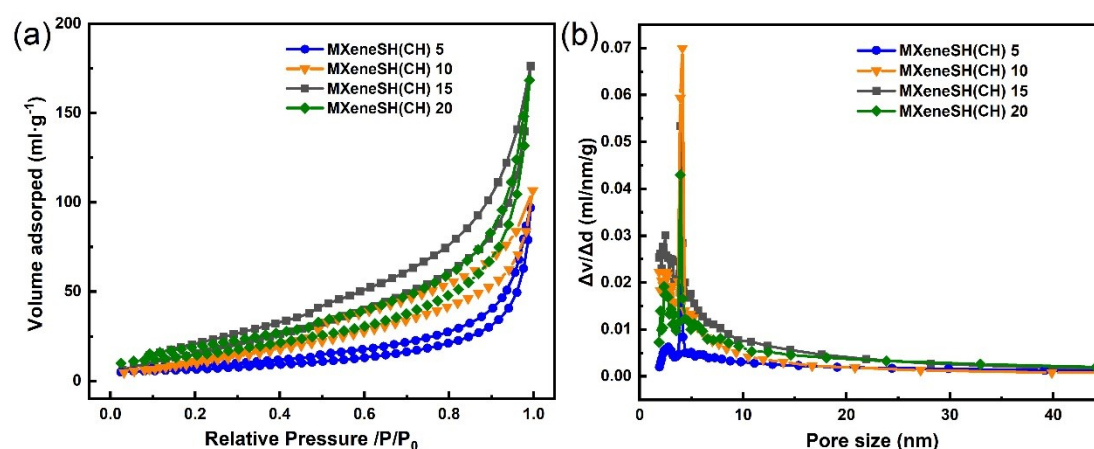
groups are sufficient to achieve fully covalent binding of sulfur and hence a large part of physical adhesion of sulfur remains agglomeration. After sulfur loading, S-MXeneSH(CH) 15 and S-MXeneSH(CH) 20 can be identified with a layered structure similar as Fig.3b because effective modification needs relatively affluent CH.



**Figure 5.19** FE-SEM images of (a) MXeneSH(CH) 5 and (b) S-MXeneSH(CH) 5 composites. Scale bar: 2  $\mu\text{m}$ .

In order to characterize the specific surface area and the generated pores, the BET test was conducted for four composites with different CH mixing ratios. In **Figure 5.20a**, the SSA of MXeneSH(CH) 5, MXeneSH(CH) 10, MXeneSH(CH) 15 and MXeneSH(CH) 20 are  $23.4 \text{ m}^2 \cdot \text{g}^{-1}$ ,  $47.9 \text{ m}^2 \cdot \text{g}^{-1}$ ,  $72.6 \text{ m}^2 \cdot \text{g}^{-1}$  and  $55.1 \text{ m}^2 \cdot \text{g}^{-1}$ , which are remarkably higher than  $7.9 \text{ m}^2 \cdot \text{g}^{-1}$  of pristine MXene (Fig.S4b). It is clear that the SSA boosts with the usage of CH increasing until 15 times the mass ratio of MXene. Further increasing CH may have a negative effect. In **Figure 5.20b**, all the composites possess a characteristic of 4 nm pore size of MXene. Consistent with the trend of SSA, MXeneSH(CH) 15 has the most micropores distribution, while MXeneSH(CH) 5 has the fewest micropores. As supported by a previous study [16], more CH mixing could prompt wrinkled shape formation and create more micropores. As a comparison, pristine MXene has no pore size distribution below 2 nm (Fig.S4b), and MXeneSH(CH)

15 owns the most pores in this range, which benefits the growth of sulfur more efficiently and uniformly.

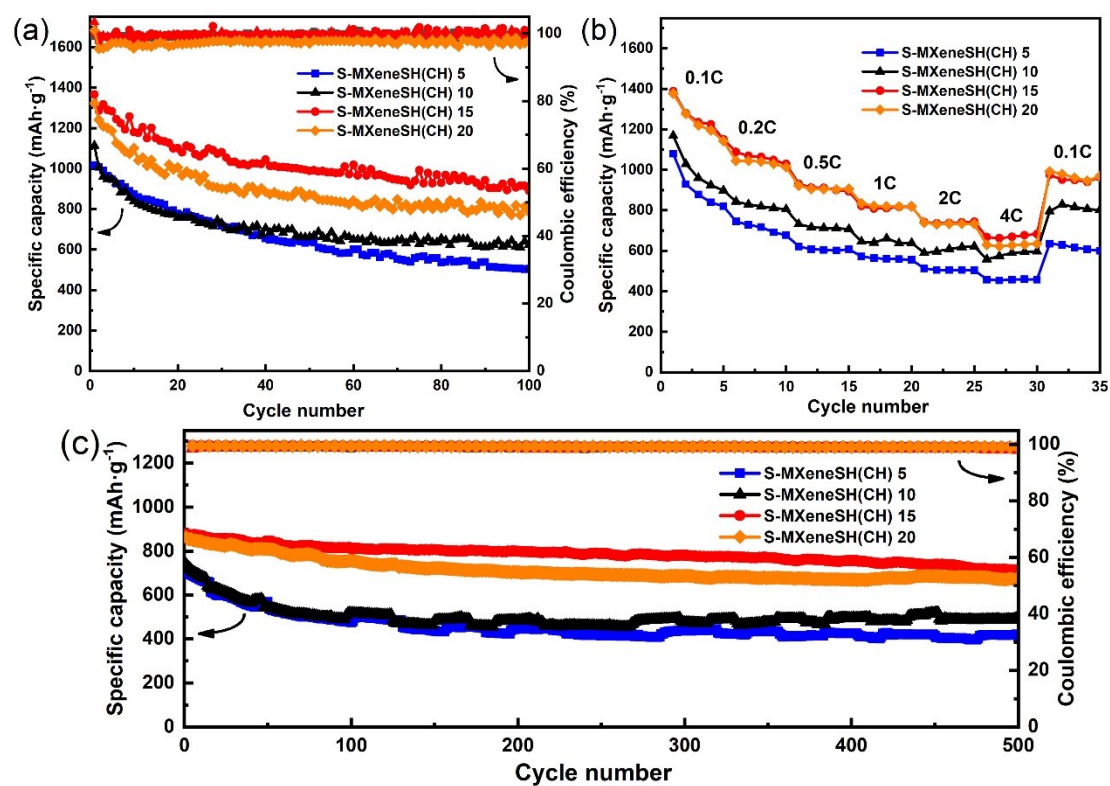


**Figure 5.20** (a) Nitrogen adsorption-desorption isotherms and (b) pore-size distributions of four composites with different CH mixing ratios.

For the cycle performance at 0.1 C in **Figure 5.21a**, S-MXeneSH(CH) 15 and S-MXeneSH(CH) 20 reach a high first capacity of  $1367 \text{ mAh}\cdot\text{g}^{-1}$  and  $1323 \text{ mAh}\cdot\text{g}^{-1}$ , and maintain  $890 \text{ mAh}\cdot\text{g}^{-1}$  and  $786 \text{ mAh}\cdot\text{g}^{-1}$  after 100 cycles. However, S-MXeneSH(CH) 10 and S-MXeneSH(CH) 5 just have  $1114 \text{ mAh}\cdot\text{g}^{-1}$  and  $1017 \text{ mAh}\cdot\text{g}^{-1}$  capacity, and drop to  $624 \text{ mAh}\cdot\text{g}^{-1}$  and  $505 \text{ mAh}\cdot\text{g}^{-1}$  respectively. Identically, S-MXeneSH(CH) 15 and S-MXeneSH(CH) 20 achieve over  $650 \text{ mAh}\cdot\text{g}^{-1}$  capacity after 500 long cycling at 1 C while S-MXeneSH(CH) 10 and S-MXeneSH(CH) 5 decline to beneath  $500 \text{ mAh}\cdot\text{g}^{-1}$  at the same stage in Fig.13c. These results indicate that sufficient sulfhydryl groups are beneficial to effectively reduce the generation of high-order polysulfides and the suppression of “shuttle effect”. Compared to rate performance under  $400 \text{ mAh}\cdot\text{g}^{-1}$  of MXene/S in Fig.8d, S-MXeneSH(CH) 5 and S-MXeneSH(CH) 10 display a gradually higher capacity of  $458 \text{ mAh}\cdot\text{g}^{-1}$  and  $558 \text{ mAh}\cdot\text{g}^{-1}$  at 4 C large current density with the increase of CH in **Figure 5.21b**. S-MXeneSH(CH) 15 and S-MXeneSH(CH) 20 present

an extremely approximate rate performance, but S-MXeneSH(CH) 15 delivers 668  $\text{mAh}\cdot\text{g}^{-1}$  at 4 C, which is slightly higher than 629  $\text{mAh}\cdot\text{g}^{-1}$  of S-MXeneSH(CH) 20. This is explained by preventing the restacking of MXene and increasing the interlayer gap. As a result, there are more electron transfer tunnels, and the conductivity of MXene is utilized more efficiently with the addition of CH [23, 35].

Summarizing the experimental results detailed above, the mass ratio of CH/MXene over 15:1 provide little benefit for performance, while adequate addition of CH is required for sufficient sulfydryl modification to achieve polymerization of sulfur. For the ratios studied, it is found the mass ratio of CH/MXene 15:1 offers the best performance overall, delivering a 1367  $\text{mAh}\cdot\text{g}^{-1}$  first capacity at 0.1 C and 715  $\text{mAh}\cdot\text{g}^{-1}$  after 500 cycles at 1 C with an excellent retention of 81.3 %.



**Figure 5.21** (a) Cyclic performances at 0.1 C and (c) 1 C; (b) Rate performances of four different batteries with different CH mixing ratios.



## 5.4 Conclusions

In summary, we successfully fabricated two types of sulfydryl-functionalized MXene and their sulfur cathodes: S-MXeneSH(CH) and S-MXeneSH(MPTS). Both achieve high conductivity and strong polysulfides adsorption. Compared to the physical adsorption of active sulfur, N-MXene/S, N, S-MXene/S and 3D MXene/S show relatively low performance. Chemically sulfydryl-modified MXene has higher stability and as a sulfur host, provides its cathode for a superb performance towards Li-S batteries. For the two modification strategies, S-MXeneSH(MPTS) 15 presents a slightly lower performance than S-MXeneSH(CH) 15. Among four different ratios between MXene and CH, S-MXeneSH(CH) 15 cathode achieves the highest first capacity of  $1367 \text{ mAh}\cdot\text{g}^{-1}$  at 0.1 C and retains  $668 \text{ mAh}\cdot\text{g}^{-1}$  at 4 C large current density. At the same time, it displays 500 stable cycles with 81.3 % capacity retention. Our results highlight that the covalent attachment is a promising strategy for designing functionalized carbon or metal-based materials and the “shuttle effect” in Li-S batteries can be greatly addressed.

## 5.5 References

- [1] S. Wei, L. Ma, K.E. Hendrickson, Z. Tu, and L.A. Archer, Metal-Sulfur Battery Cathodes Based on PAN-Sulfur Composites, *Journal of the American Chemical Society*, 137 (2015) 12143-12152.
- [2] W.J. Chung, J.J. Griebel, E.T. Kim, H. Yoon, A.G. Simmonds, H.J. Ji, P.T. Dirlam, R.S. Glass, J.J. Wie, N.A. Nguyen, B.W. Guralnick, J. Park, A. Somogyi, P. Theato, M.E. Mackay, Y.E. Sung, K. Char, and J. Pyun, The use of elemental sulfur as an alternative feedstock for polymeric materials, *Nature chemistry*, 5 (2013) 518-524.
- [3] A.G. Simmonds, J.J. Griebel, J. Park, K.R. Kim, W.J. Chung, V.P. Oleshko, J. Kim, E.T. Kim, R.S. Glass, C.L. Soles, Y.E. Sung, K. Char, and J. Pyun, Inverse Vulcanization of Elemental Sulfur to Prepare Polymeric Electrode Materials for Li-S Batteries, *ACS Macro Letters*, 3 (2014) 229-232.
- [4] J.J. Griebel, G. Li, R.S. Glass, K. Char, and J. Pyun, Kilogram scale inverse vulcanization of elemental sulfur to prepare high capacity polymer electrodes for Li-S batteries, *Journal of Polymer Science Part A: Polymer Chemistry*, 53 (2015) 173-177.
- [5] N. Xu, T. Qian, X. Liu, J. Liu, Y. Chen, and C. Yan, Greatly Suppressed Shuttle Effect for Improved Lithium Sulfur Battery Performance through Short Chain Intermediates, *Nano letters*, 17 (2017) 538-543.
- [6] W. Bao, L. Liu, C. Wang, S. Choi, D. Wang, and G. Wang, Facile Synthesis of Crumpled Nitrogen-Doped MXene Nanosheets as a New Sulfur Host for Lithium-Sulfur Batteries, *Advanced Energy Materials*, 8 (2018) 1702485.
- [7] A. Amiri, Y. Chen, C. Bee Teng, and M. Naraghi, Porous nitrogen-doped MXene-

based electrodes for capacitive deionization, *Energy Storage Materials*, 25 (2020) 731-739.

[8] Y. Zhang, J. Li, Z. Gong, J. Xie, T. Lu, and L. Pan, Nitrogen and sulfur co-doped vanadium carbide MXene for highly reversible lithium-ion storage, *Journal of Colloid and Interface Science*, 587 (2021) 489-498.

[9] M.Q. Zhao, X. Xie, C.E. Ren, T. Makaryan, B. Anasori, G. Wang, and Y. Gogotsi, Hollow MXene Spheres and 3D Macroporous MXene Frameworks for Na-Ion Storage, *Advanced materials*, 29 (2017).

[10] M. Yu, R. Li, M. Wu, and G. Shi, Graphene materials for lithium-sulfur batteries, *Energy Storage Materials*, 1 (2015) 51-73.

[11] P. Simon, Two-Dimensional MXene with Controlled Interlayer Spacing for Electrochemical Energy Storage, *ACS Nano*, 11 (2017) 2393-2396.

[12] N. Li, Y. Xie, S. Peng, X. Xiong, and K. Han, Ultra-lightweight  $Ti_3C_2T_x$  MXene modified separator for Li-S batteries: Thickness regulation enabled polysulfide inhibition and lithium ion transportation, *Journal of Energy Chemistry*, 42 (2020) 116-125.

[13] Y. Fu and A. Manthiram, Orthorhombic Bipyramidal Sulfur Coated with Polypyrrole Nanolayers As a Cathode Material for Lithium-Sulfur Batteries, *The Journal of Physical Chemistry C*, 116 (2012) 8910-8915.

[14] C. Wang, X. Wang, Y. Wang, J. Chen, H. Zhou, and Y. Huang, Macroporous free-standing nano-sulfur/reduced graphene oxide paper as stable cathode for lithium-sulfur battery, *Nano Energy*, 11 (2015) 678-686.

- [15] H.Y. Zhou, Z.Y. Sui, K. Amin, L.W. Lin, H.Y. Wang, and B.H. Han, Investigating the Electrocatalysis of a  $\text{Ti}_3\text{C}_2/\text{Carbon}$  Hybrid in Polysulfide Conversion of Lithium-Sulfur Batteries, *ACS applied materials & interfaces*, 12 (2020) 13904-13913.
- [16] P. Xu, H. Xiao, X. Liang, T. Zhang, F. Zhang, C. Liu, B. Lang, and Q. Gao, A MXene-based EDA- $\text{Ti}_3\text{C}_2\text{T}_x$  intercalation compound with expanded interlayer spacing as high performance supercapacitor electrode material, *Carbon*, 173 (2021) 135-144.
- [17] C. Zhang, Y. Ma, X. Zhang, S. Abdolhosseinzadeh, H. Sheng, W. Lan, A. Pakdel, J. Heier, and F. Nüesch, Two-Dimensional Transition Metal Carbides and Nitrides (MXenes): Synthesis, Properties, and Electrochemical Energy Storage Applications, *Energy & Environmental Materials*, 3 (2020) 29-55.
- [18] N.J. Huang, Q.Q. Xia, Z.H. Zhang, L. Zhao, G.D. Zhang, J.F. Gao, and L.C. Tang, Simultaneous improvements in fire resistance and alarm response of GO paper via one-step 3-mercaptopropyltrimethoxysilane functionalization for efficient fire safety and prevention, *Composites Part A: Applied Science and Manufacturing*, 131 (2020) 105797.
- [19] J. Halim, K.M. Cook, M. Naguib, P. Eklund, Y. Gogotsi, J. Rosen, and M.W. Barsoum, X-ray photoelectron spectroscopy of select multi-layered transition metal carbides (MXenes), *Applied Surface Science*, 362 (2016) 406-417.
- [20] R. Rajagopalan and J.O. Iroh, Characterization of polyaniline-polypyrrole composite coatings on low carbon steel: a XPS and infrared spectroscopy study, *Applied Surface Science*, 218 (2003) 58-69.
- [21] C. Barchasz, F. Molton, C. Duboc, J.C. Lepretre, S. Patoux, and F. Alloin,

Lithium/Sulfur Cell Discharge Mechanism: An Original Approach for Intermediate Species Identification, *Analytical chemistry*, 84 (2012) 3973-3980.

[22] L.F. Nazar, M. Cuisinier, and Q. Pang, Lithium-sulfur batteries, *MRS Bulletin*, 39 (2014) 436-442.

[23] J. Li, D. Yan, S. Hou, Y. Li, T. Lu, Y. Yao, and L. Pan, Improved sodium-ion storage performance of  $Ti_3C_2T_x$  MXenes by sulfur doping, *Journal of Materials Chemistry A*, 6 (2018) 1234-1243.

[24] C. Zhang, L. Cui, S. Abdolhosseinzadeh, and J. Heier, Two-dimensional MXenes for lithium-sulfur batteries, *InfoMat*, 2 (2020) 613-638.

[25] H. Yan, H. Wang, D. Wang, X. Li, Z. Gong, and Y. Yang, In Situ Generated  $Li_2S$ -C Nanocomposite for High-Capacity and Long-Life All-Solid-State Lithium Sulfur Batteries with Ultrahigh Areal Mass Loading, *Nano letters*, 19 (2019) 3280-3287.

[26] L. Zhang, J. Bi, Z. Zhao, Y. Wang, D. Mu, and B. Wu, Sulfur@Self-assembly 3D MXene hybrid cathode material for lithium-sulfur batteries, *Electrochimica Acta*, 370 (2021) 137759.

[27] M. Yu, J. Ma, H. Song, A. Wang, F. Tian, Y. Wang, H. Qiu, and R. Wang, Atomic layer deposited  $TiO_2$  on a nitrogen-doped graphene/sulfur electrode for high performance lithium-sulfur batteries, *Energy & Environmental Science*, 9 (2016) 1495-1503.

[28] D. Xiao, Q. Li, H. Zhang, Y. Ma, C. Lu, C. Chen, Y. Liu, and S. Yuan, A sulfur host based on cobalt-graphitic carbon nanocages for high performance lithium-sulfur batteries, *Journal of Materials Chemistry A*, 5 (2017) 24901-24908.

- [29] R. Chen, T. Zhao, J. Lu, F. Wu, L. Li, J. Chen, G. Tan, Y. Ye, and K. Amine, Graphene-based three-dimensional hierarchical sandwich-type architecture for high-performance Li/S batteries, *Nano letters*, 13 (2013) 4642-4649.
- [30] Z. Wu, T. Shang, Y. Deng, Y. Tao, and Q.H. Yang, The Assembly of MXenes from 2D to 3D, *Advanced Science*, 7 (2020) 1903077.
- [31] X. Gu, C. J. Tong, B. Wen, L.M. Liu, C. Lai, and S. Zhang, Ball-milling synthesis of ZnO@sulphur/carbon nanotubes and Ni(OH)<sub>2</sub> @sulphur/carbon nanotubes composites for high-performance lithium-sulphur batteries, *Electrochimica Acta*, 196 (2016) 369-376.
- [32] Z. Cui, J. Yao, T. Mei, S. Zhou, B. Hou, J. Li, J. Li, J. Wang, J. Qian, and X. Wang, Strong lithium polysulfides chemical trapping of TiC-TiO<sub>2</sub>/S composite for long-cycle lithium-sulfur batteries, *Electrochimica Acta*, 298 (2019) 43-51.
- [33] W. Bao, X. Xie, J. Xu, X. Guo, J. Song, W. Wu, D. Su, and G. Wang, Confined Sulfur in 3D MXene/Reduced Graphene Oxide Hybrid Nanosheets for Lithium-Sulfur Battery, *Chemistry*, 23 (2017) 12613-12619.
- [34] X. Liang, Y. Rangom, C.Y. Kwok, Q. Pang, and L.F. Nazar, Interwoven MXene Nanosheet/Carbon-Nanotube Composites as Li-S Cathode Hosts, *Advanced materials*, 29 (2017).
- [35] C. Xiong, G.Y. Zhu, H.R. Jiang, Q. Chen, and T.S. Zhao, Achieving multiplexed functionality in a hierarchical MXene-based sulfur host for high-rate, high-loading lithium-sulfur batteries, *Energy Storage Materials*, 33 (2020) 147-157.

## Chapter 6 : Conclusion and Future perspectives

### 6.1 Conclusion

The thesis focus on addressing the intrinsic problems of sulfur cathode for Li-S batteries through designing and preparing host materials. For carbon and titanium-based composite materials, they can offer preeminent electron and ion conductivity, strong adsorption of polysulfides, as well as their low-cost and easily accessible feature. Meanwhile, much research indicates that the synergistic effect between different types of materials can promote battery performance markedly.

Initially, different carbon and titanium-based materials are selected to combine with sulfur to prepare composite cathodes to enhance battery performance and investigate their diverse features. Based on understanding the strength and weaknesses of these materials, the TiC-TiO<sub>2</sub>/SWCNT/S modified cathode for Li-S batteries was proposed and fabricated with a high conductive network through 1D SWCNT connected. With a small addition of SWCNT (~2 % wt), TiC-TiO<sub>2</sub>/SWCNT/S 2 reaches an evidently increased 1324.2 mAh·g<sup>-1</sup> and shows 711.2 mAh·g<sup>-1</sup> at 4 C for rate performance, suggesting its higher conductivity and sulfur utilization. In the meantime, pouch cells with this cathode were fabricated successfully, presenting 1067.6 mAh·g<sup>-1</sup> high first capacity and retaining 639.9 mAh·g<sup>-1</sup> after 100 cycles at 0.1 C.

After a successful improvement in performance, a 3D MXene/CNC/S composite accommodates a higher 1.5 mg·cm<sup>-2</sup> sulfur loading and around 80 % sulfur content was fabricated by a simple method with low-cost raw materials, which has a high-conductive network. Contributing to the synergistic effect between MXene and CNC,

the cathode possesses a stable cycle performance with a retention rate of 64.6 % of 823.8 mAh·g<sup>-1</sup> after 100 cycles. It is found that MXene: CNC = 7:3 shows the best electrochemical performance for the composites investigated. Moreover, sulfur loading, sulfur content and electrolyte ratio were explored to balance performance and energy density. The electrolyte/sulfur (E/S) ratio of 40 μl·mg<sup>-1</sup> is the most suitable for ensuring conductivity and less loss of polysulfides.

In order to simplify the fabrication process and reduce the complexity of materials, Functionalized MXene and their cathodes: N-MXene/S, N, S-MXene/S and 3D MXene/S with physical adsorption of active sulfur were tried, but they presented the relatively low performance. Later, two types of sulfydryl-functionalized MXene and their sulfur cathodes: S-MXeneSH(CH) and S-MXeneSH(MPTS), with chemical adsorption were fabricated, demonstrating a obviously higher stability. S-MXeneSH(CH) 15 cathode obtains the highest initial capacity of 1367 mAh·g<sup>-1</sup> at 0.1 C and holds 668 mAh·g<sup>-1</sup> at 4 C large current density. Meanwhile, it owns over 81 % retention for 500 stable cycles. The results indicate that covalent attachment is a promising strategy for designing functionalized carbon or titanium-based materials to greatly suppress “shuttle effect” in Li-S batteries.



## 6.2 Future Perspectives

As cathode materials for Li-S batteries have been investigated intensively, particularly in most of the carbon-based materials or some general titanium-based materials, it can be concluded that a prominent host material should have excellent conductivity, effective trapping of polysulfides and the scaffold to overcome volume expansion. Nevertheless, some crucial issues need to be solved in commercial applications:

(1) compared to the 10-20  $\mu\text{l}\cdot\text{mg}^{-1}$  E/S ratio in some preferable works in the laboratory and below the requirement of 10 $\mu\text{l}\cdot\text{mg}^{-1}$  in practical application, the use of the amount of electrolyte is overweight (about 40  $\mu\text{l}\cdot\text{mg}^{-1}$  sulfur), which leads to the low energy density of the whole cell; (2) the sulfur loading (around 1.5  $\text{mg}\cdot\text{cm}^{-2}$ ) need to increase further, as 1-2  $\text{mg}\cdot\text{cm}^{-2}$  just is medium level in Li-S battery field in experiment stage and over 2  $\text{mg}\cdot\text{cm}^{-2}$  could be high sulfur loading; (3) originally, coin cells have been employed as the testing system in the majority of research to assess the impact on the cathode materials. However, some significant distinctions between the coin cells and pouch cells relate to the enlarged electrode area and active material mass. Consequently, it is essential to evaluate the application of materials in the pouch cell. (4) as a type of Li metal battery, the growth of dendritic lithium and crack of the Li plate are not negligible due to the safety issue of short circuits. In any case, all the cathode materials reported in the thesis possess high performance. These experiments may provide some innovative concepts and simple techniques to further promote the development of carbon and titanium-based materials as sulfur hosts for Li-S batteries.